TU Delft

Delft University of Technology

Corrosion and Corrosion Inhibition Studies of Aerospace Aluminium Alloys at the Nanoscale using TEM Approaches

Kosari, A.

DOI
10.4233/uuid:3706e467-dd4b-400d-a08e-1a5c57635775

Publication date
2021

Document Version
Final published version

Citation (APA)
Kosari, A. (2021). *Corrosion and Corrosion Inhibition Studies of Aerospace Aluminium Alloys at the Nanoscale using TEM Approaches*. [Dissertation (TU Delft), Delft University of Technology]. https://doi.org/10.4233/uuid:3706e467-dd4b-400d-a08e-1a5c57635775

Important note
To cite this publication, please use the final published version (if applicable).
Please check the document version above.

Copyright
Other than for strictly personal use, it is not permitted to download, forward or distribute the text or part of it, without the consent of the author(s) and/or copyright holder(s), unless the work is under an open content license such as Creative Commons.

Takedown policy
Please contact us and provide details if you believe this document breaches copyrights.
We will remove access to the work immediately and investigate your claim.

This work is downloaded from Delft University of Technology.
For technical reasons the number of authors shown on this cover page is limited to a maximum of 10.

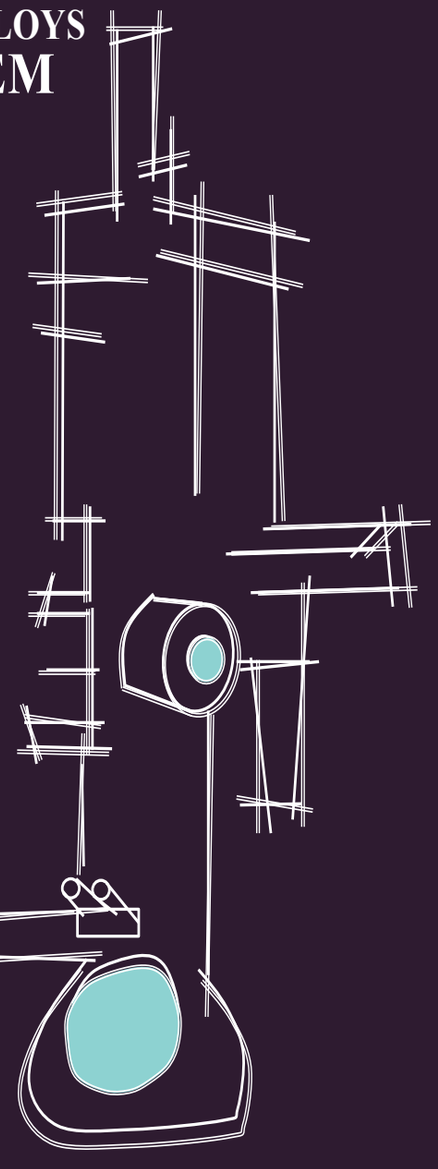


Delft University of Technology

Corrosion and Corrosion Inhibition Studies of Aerospace Aluminium Alloys at the Nanoscale using TEM Approaches

Ali Kosari

Corrosion and Corrosion Inhibition Studies of Aerospace Aluminium Alloys at the Nanoscale using TEM Approaches



Ali KOSARI

CORROSION AND CORROSION INHIBITION STUDIES OF AEROSPACE ALUMINIUM ALLOYS AT THE NANOSCALE USING TEM APPROACHES

Ph.D. thesis

ALI KOSARI





This work is part of the research program Understanding Processes using Operando Nanoscopy (UPON) with project number 14205 (B2), which is financed by the Dutch Research Council (NWO) and partially by AkzoNobel.





This research was performed as a research collaboration between the Corrosion Technology and Electrochemistry group in the department of Materials Science and Engineering at TU Delft and National Centre for High Resolution Electron Microscopy at Kavli Nanolab Delft.

Corrosion and Corrosion Inhibition Studies of Aerospace Aluminium Alloys at the Nanoscale using TEM Approaches

Dissertation

for the purpose of obtaining the degree of doctor

at Delft University of Technology

by the authority of the Rector Magnificus Prof.dr.ir. T.H.J.J. van der Hagen, chair of the

Board for Doctorates to be defended publicly on Wednesday October 6 2021at 12:30 o'clock

By

Ali KOSARI

Master of Science in Materials Engineering - Corrosion and Protection of Materials,

Ferdowsi University of Mashhad, Iran.

Born in Mashhad, Iran.

This dissertation has been approved by the promotors:

Prof. dr. ir. J.M.C Mol

Prof. dr. ir. H. Terryn

Composition of the doctoral committee:

Rector magnificus	Chairman
Prof. dr. ir. J.M.C. Mol	Delft University of Technology, promotor
Prof. dr. ir. H. Terryn	Vrije Universiteit Brussel/Delft University of Technology, promotor
Prof. dr. H.W. Zandbergen	Delft University of Technology

Independent members:

Prof. dr. Grace Burke	The University of Manchester, UK
Prof. dr. Philippe Marcus	École Nationale Supérieure de Chimie de Paris, France
Prof. dr. Mikhail Zheludkevich	Helmholtz-Zentrum Hereon, Germany
Prof. dr. ir. Jilt Sietsma	Delft University of Technology, the Netherlands
Prof. dr. Maria Santofimia Navarro	Delft University of Technology, the Netherlands (reserve member)

Keywords: *In-situ liquid-phase TEM; Quasi in-situ TEM; Ex-situ TEM; Local Corrosion; Corrosion inhibition; Intermetallic particles; Lithium-based salts; Cerium-based compounds*

Table of content

	Summary	VI
	Samenvatting	VIII
Chapter 1	Introduction	1
Chapter 2	Application of TEM in corrosion science (literature review)	15
Chapter 3	Development of the TEM approaches	45
Chapter 4	In-situ liquid-phase, quasi in-situ and ex-situ TEM observations of local corrosion induced by precipitates	63
Chapter 5	Quasi in-situ and ex-situ observations of local corrosion induced by intermetallic constituent particles and dispersoids	101
Chapter 6	Cross-sectional analytical TEM characterisation of the conversion layer formed on AA2024-T3 by a lithium-leaching coating	125
Chapter 7	Liquid-Phase TEM observations of lithium-based conversion layer formation	147
Chapter 8	FIB/SEM, TEM, and electrochemical studies of lithium-based conversion layer at the matrix and intermetallic particles	167
Chapter 9	Quasi in-situ and ex-situ TEM, and electrochemical investigations of local corrosion inhibition by a cerium-based inhibitor	191
Chapter 10	Conclusions	221
	Acknowledgements	231
	List of publications	235
	Curriculum Vitae	239

Summary

For many decades, corrosion and corrosion inhibition of high-strength aluminium alloys have been studied indirectly and through traditional and separately performed electrochemical, spectroscopic and microscopic techniques. These approaches employed to date commonly lack sufficient lateral and time resolution to unravel early stage events which is controlled at the nanoscopic levels at which microstructural heterogeneities actually steer local and dynamic electrochemical activities. Besides, techniques with appropriate resolution like transmission electron microscopy (TEM) have been applied to the field, but carried out ex-situ, normally providing no detailed on-site time-resolved information to investigate distinctive-but-consecutive stages of corrosion and corrosion inhibition phenomena. That is why theories of relevance are established through bridging and linking separately-obtained information and therefore are described in rather stochastic than deterministic terms. This is particularly the case for the legacy alloy AA2024-T3 which is prone to complicated forms of local corrosion resulting from extremely complex and heterogeneous local microstructures.

Local corrosion in AA2024-T3 is site-specific where complicated local degradation events predominantly take place at surface intermetallic particles (IMPs) dispersed in the alloy matrix and eventually lead to pitting and intergranular forms of corrosion. Thus, the detailed understanding of space- and time-resolved local corrosion mechanisms of engineered microstructures is of pivotal importance to developing reliable and active protection strategies. However, despite the high demand for time- and space-resolved mechanistic information of local corrosion, it has not yet been possible to unambiguously define the morphological and micro-electrochemical characteristics during local corrosion and corrosion inhibition owing to extremely demanding experimental challenges. Nevertheless, this thesis put efforts into carrying out dedicated TEM experimental approaches to provide time-resolved direct nanoscopic evidence of local corrosion and corrosion inhibition processes from early surface initiation to an advanced stage of propagation.

To this aim, Chapter 2 is devoted to briefly introducing TEM and its analytical techniques. Then, it discusses the challenges of a recently applicable technique in corrosion science namely in-situ liquid-phase TEM and besides reviews state-of-the-art achievements in the field of relevance. Subsequently in Chapter 3, the TEM experimental approaches employed and instrumentations developed are described, including the details on the implementation of ex-situ, quasi in-situ and in-situ liquid-phase TEM. Besides, the electrochemical liquid cells designed for liquid phase TEM corrosion studies and a unique developed protocol for preparing and transferring thin specimens for top- and cross-sectional-view observations of corrosion via liquid-phase TEM.

Chapter 4 and 5 (Part 1) are devoted to studying local corrosion phenomena with a focus on the role of different intermetallic phases in localised corrosion. In Chapter 4, in-situ top-view and cross-sectional-view liquid-phase TEM observations supported by quasi in-situ and ex-situ analytical TEM studies are performed on the hardening precipitations in AA2024-T3 (i.e., Al_2CuMg and Al_2Cu). In Chapter 5, a combination of quasi in-situ and ex-situ analytical TEM experiments are focused on local corrosion by

microscopic constituent intermetallic compounds and nanoscopic dispersoids. Thus, the pivotal role of dealloying attack to different IMPs as the precursor of local degradations is revealed. It is also evidenced the IMPs, regardless of their type, are in fact simultaneous anodic and cathodic sites as from the beginning of exposure. In fact, local corrosion stabilises through nanogalvanic interactions between the heterogeneities within the corroding IMPs themselves, and later with the closest neighbouring alloy matrix. It is directly shown that the IMPs can release copper into the solution (Cu redistribution) as soon as they get undercut from the alloy matrix. Al_2CuMg contributes to Cu redistribution process the most.

Development of novel eco-friendly active protective coatings for aluminium alloys is of pivotal importance to aerospace industry due to recent international legislative restrictions being imposed to the use of hexavalent chromium-based systems. Lithium-based active protective coating technology has been proposed recently as one of the most promising alternatives. Therefore, three chapters of the current thesis (Part 2) are devoted to performing cross-sectional liquid-phase TEM observations (Chapter 7) and systematic FIB/SEM and TEM studies (Chapter 8) of the lithium conversion layer on the alloy matrix and different IMPs, respectively. Besides, Chapter 6 characterises the grown-up lithium conversion layer in a 1-mm scribe in neutral salt spray environment in terms of morphology, structure and chemical composition. Remarkably, the supersaturation by $Al(OH)_4^-$ of the solution is found to be key to establishing the conversion layer and is fulfilled at the expense of the direct dissolution of the alloy substrate. The sublayer with a columnar morphology initially forms upon supersaturation and grows until the appearance of a porous morphology. The conversion process is completed by the formation of a thin dense layer closest to the substrate at advanced stages. The variant morphology of the sublayers is a direct consequence of the dissolution/precipitation kinetics at different stages. Although IMPs, except for Al_2CuMg, insignificantly interact with the lithium carbonate-containing solution, they are covered fully with a columnar layer. Al_2CuMg undergoes dealloying which assists the conversion process by local supersaturation providing $Al(OH)_4^-$ ions relatively rapidly.

Cerium-based compounds are one of the most studied candidates for hexavalent chromium-based compounds to hinder localised corrosion of AAs. This class of inhibitors precipitates in the form of cerium hydroxide via a chemical route and as a response to the local alkalinity due to electrochemical activity of individual IMPs. However, the literature still lacks an agreement when it comes to explaining the detailed mechanisms in relation to the morphology and sequence of cerium hydr(oxide) precipitation on individual intermetallic compounds. In Chapter 9, detailed top-view and cross-sectional analytical TEM investigations along with electrochemical evaluations of individual IMPs including Al_2CuMg, Al_2Cu, Al_7Cu_2Fe(Mn) and $Al_{76}Cu_6Fe_7Mn_5Si_6$ at different stages of exposure are carried out. With that, the critical role of dealloying in governing the rate of local cerium precipitation on different intermetallic phases is unravelled. The cerium-based inhibitor cannot inhibit dealloying of IMPs, thus Al_2CuMg as an active phase rapidly undergoing dealloying is found fully corroded but with a thick layer of cerium hydroxide.

Samenvatting

Gedurende vele decennia zijn corrosie en corrosiebescherming van hoge sterkte aluminiumlegeringen indirect en door middel van traditionele en afzonderlijk uitgevoerde elektrochemische, spectroscopische en microscopische technieken bestudeerd. De benaderingen die tot nu toe zijn gebruikt, missen gewoonlijk voldoende laterale en tijdresolutie om corrosieprocessen in een vroeg stadium te ontrafelen. Corrosie-initiatie wordt geactiveerd op nanoscopische niveaus waarbij lokale en dynamische elektrochemische activiteit door microstructurele heterogeniteiten wordt bepaald. Technieken met de juiste laterale resolutie zoals transmissie-elektronenmicroscopie (TEM) worden in het onderzoeksveld toegepast, maar ex-situ uitgevoerd waarbij normaal gesproken geen gedetailleerde tijdsgeresolveerde informatie ter plaatse wordt verkregen om onderscheidende en, opeenvolgende stadia van corrosie en corrosie-inhibitie te onderzoeken. Dat is de reden waarom tot op heden relevante theorieën met name tot stand zijn gekomen door het overbruggen en koppelen van afzonderlijk verkregen informatie en daarom worden beschreven in eerder stochastische dan deterministische termen. Dit is met name het geval voor de conventionele legering AA2024-T3 die vatbaar is voor gecompliceerde vormen van lokale corrosie als gevolg van een extreem complexe en heterogene lokale microstructuur.

Lokale corrosie in AA2024-T3 is locatie-specifiek waar gecompliceerde lokale degradatieprocessen voornamelijk plaatsvinden ter plaatse van intermetallische oppervlaktedeeltjes die in de legeringsmatrix zijn gedispergeerd en uiteindelijk leiden tot putcorrosie en interkristallijne vormen van corrosie. Het gedetailleerde begrip van in-de-ruimte en in-de-tijd geresolveerde lokale corrosiemechanismen van complexe microstructuren is dus van cruciaal belang voor het ontwikkelen van betrouwbare en actieve beschermingsstrategieën. Ondanks de grote vraag naar tijd- en ruimte-geresolveerde mechanistische informatie van lokale corrosie, is het echter nog niet mogelijk geweest om de morfologische en micro-elektrochemische kenmerken tijdens lokale corrosie en corrosiebescherming ondubbelzinnig te definiëren vanwege extreem veeleisende experimentele uitdagingen. Desalniettemin zijn in dit proefschrift inspanningen gerapporteerd om specifieke TEM-gebaseerde experimentele benaderingen uit te voeren om in-de-tijd geresolveerde en direct nanoscopisch bewijs te leveren van lokale corrosie en corrosiebeschermingsprocessen vanaf de vroege oppervlakte-initiatie tot een gevorderd stadium van propagatie.

Hoofdstuk 2 is gewijd aan een korte introductie van TEM en de gerelateerde analytische technieken. Vervolgens worden de uitdagingen besproken van een recent toepasbare techniek in de corrosiewetenschap, namelijk in-situ vloeistoffase TEM, en worden daarnaast tot op heden bereikte resultaten op relevante onderzoeksgebieden besproken. Vervolgens worden in Hoofdstuk 3 de gebruikte experimentele TEM-benaderingen en ontwikkelde instrumenten beschreven, inclusief de details over de implementatie van ex-situ, quasi in-situ en in-situ vloeistoffase TEM. Daarnaast zijn de elektrochemische vloeistofcellen ontworpen voor TEM-corrosiestudies in de vloeistoffase beschreven als ook een uniek ontwikkeld protocol voor het voorbereiden en overbrengen van dunne monsters voor observaties in bovenaanzicht en dwarsdoorsnede van corrosie via vloeistoffase TEM.

Hoofdstuk 4 en 5 (Deel 1) zijn gewijd aan het bestuderen van lokale corrosiefenomenen met een focus op de rol van verschillende intermetallische fasen in lokale corrosieprocessen. In Hoofdstuk 4 worden in-situ bovenaanzicht en dwarsdoorsnede TEM-waarnemingen in de vloeistoffase, ondersteund door quasi in-situ en ex-situ analytische TEM-onderzoeken, uitgevoerd op de intermetallische fasen in AA2024-T3 (d.w.z. Al_2CuMg en Al_2Cu). Hoofdstuk 5 beschrijft een combinatie van quasi in-situ en ex-situ analytische TEM-experimenten gericht op lokale corrosie geactiveerd door microscopisch kleine intermetallische verbindingen en nanoscopische dispersoïden. Zo wordt de cruciale rol onthuld van aantasting van verschillende 'intermetallische verbindingen als voorloper van verdergaande lokale degradatie. Er is ook aangetoond dat de intermetallische verbindingen, ongeacht hun type, in feite gelijktijdige anodische en kathodische locaties zijn vanaf het begin van de blootstelling aan een corrosief milieu. In feite initieert lokale corrosie door nanogalvanische interacties tussen de heterogeniteiten binnen de corroderende 'intermetallische deeltjes zelf, en later met de dichtstbijzijnde naburige legeringsmatrix. Er wordt aangetoond dat de 'intermetallische deeltjes koper in de oplossing kunnen afgeven (koper-herverdeling) zodra ze ondergraven worden en losgekoppeld van de legeringsmatrix. Al_2CuMg draagt het meest bij aan het herverdelingsproces van koper.

De ontwikkeling van nieuwe milieuvriendelijke, actieve beschermende coatings voor aluminiumlegeringen is van cruciaal belang voor de luchtvaartindustrie vanwege de recente internationale strenge wettelijke beperkingen die zijn opgelegd aan het gebruik van op zeswaardig chroom gebaseerde systemen. Op lithium gebaseerde actieve beschermende coatingtechnologie is recentelijk voorgesteld als een van de meest veelbelovende alternatieven. Daarom zijn drie hoofdstukken van het huidige proefschrift (Deel 2) gewijd aan het uitvoeren van vloeistoffase TEM-waarnemingen (Hoofdstuk 7) en systematische FIB/SEM- en TEM-onderzoeken (Hoofdstuk 8) van de lithium-conversielaag op de legeringsmatrix en verschillende intermetallische deeltjes. Bovendien karakteriseert Hoofdstuk 6 de volgroeide lithium-conversielaag in een coatingdefect van 1 mm breed in een neutrale zoutneveltest in termen van morfologie, structuur en chemische samenstelling. Opmerkelijk is dat de oververzadiging van de oplossing door $Al(OH)_4^-$ de sleutel blijkt te zijn voor het tot stand brengen van de conversielaag en wordt vervuld door de directe oplossing van het legeringssubstraat. De onderlaag met een kolomvormige morfologie vormt zich aanvankelijk bij oververzadiging en groeit tot het verschijnen van een poreuze morfologie. Het conversieproces wordt voltooid door de vorming van een dunne, dichte laag die zich in gevorderde stadia het dichtst bij het substraat bevindt. De veranderende morfologie van de sublagen is een direct gevolg van de oplossings-/precipitatiekinetiek in verschillende stadia. Hoewel intermetallische deeltjes, behalve Al_2CuMg, onbeduidend interageren met de lithiumcarbonaat-bevattende oplossing, zijn ze volledig bedekt met een kolomvormige laag. Al_2CuMg ondergaat een selectief oplosproces die het conversieproces ondersteunt door lokale oververzadiging waardoor relatief snel $Al(OH)_4^-$ ionen worden verkregen.

Op cerium gebaseerde verbindingen zijn een van de meest bestudeerde kandidaten voor vervanging van zeswaardig chroom om lokale corrosie van akuminiumlegeringen te voorkomen. Deze klasse

inhibitoren slaat neer in de vorm van ceriumhydroxide via een chemische route en als reactie op de lokale alkaliteit als gevolg van elektrochemische activiteit ter plaatse van individuele intermetallische verbindingen. Er is echter nog steeds geen overeenstemming in de literatuur als het gaat om het verklaren van de gedetailleerde mechanismen in relatie tot de morfologie en sequentie van ceriumhydr(oxide)precipitatie op individuele intermetallische verbindingen. In Hoofdstuk 9 wordt een gedetailleerd bovenaanzicht en transversaal analytisch TEM-onderzoek uitgevoerd, samen met elektrochemische evaluaties van individuele intemetallische deeltjes, waaronder Al_2CuMg, Al_2Cu, $Al_7Cu_2Fe(Mn)$ en $Al_{76}Cu_6Fe_7Mn_5Si_6$ in verschillende stadia van blootstelling. Daarmee wordt de cruciale rol van selectieve oplossing bij het bepalen van de snelheid van lokale ceriumprecipitatie op verschillende intermetallische fasen ontrafeld. De op cerium gebaseerde inhibitor kan de selectieve oplossing van 'intermetallische deeltjes niet remmen, dus wordt gevonden dat Al_2CuMg een actieve fase betreft die snel selectieve oplossing ondergaat, maar wel voorzien is van een relatief dikke laag ceriumhydroxide.

CHAPTER 1

INTRODUCTION

1.1. Motivation and industrial relevance

Aluminium is an essential metal for modern economies and is considered as a desired material for strategic applications in aerospace and automotive industries. Aluminium can be readily alloyed with magnesium, zinc, copper, and silicon having adequate solubility to serve as major alloying elements. A number of elements like manganese, chromium, zirconium, titanium, and scandium which have a total solubility of 1% are also added to modify different properties of the alloys. This diverse and facile alloying brings along a common feature that is a very high density of intermetallic particles in most of the aluminium alloys. In fact, the aluminium alloys reveal highly heterogeneous microstructures including desired phases (dispersed precipitation particles) and undesired phases (large constituent particles) in a wide range of morphology, structure and chemical composition. This heterogeneous character of aluminium alloys is most pronounced in members of the high strength alloys of the 2xxx, 6xxx, 7xxx and 8xxx [1, 2].

Up to now, aerospace industries have played a great role in the alloy development as the related applications demand for coexisting strength, toughness, light weight and corrosion resistance [3]. At present, the aluminium alloy used in aircraft structure in the world is mainly high-strength 2xxx series and ultra-high-strength 7xxx Series (see Fig. 1.1). Table 1 compares the typical chemical composition of aerospace aluminium alloys [4]. Known as legacy alloy AA2024-T3, the 2xxx aluminium alloys have a long history of utilisation in aerospace applications owing to their exceptional balance between high-strength and low weight. This has been fulfilled through additional alloying where a necessary high-strength-to-weight ratio is acquired [1, 2].

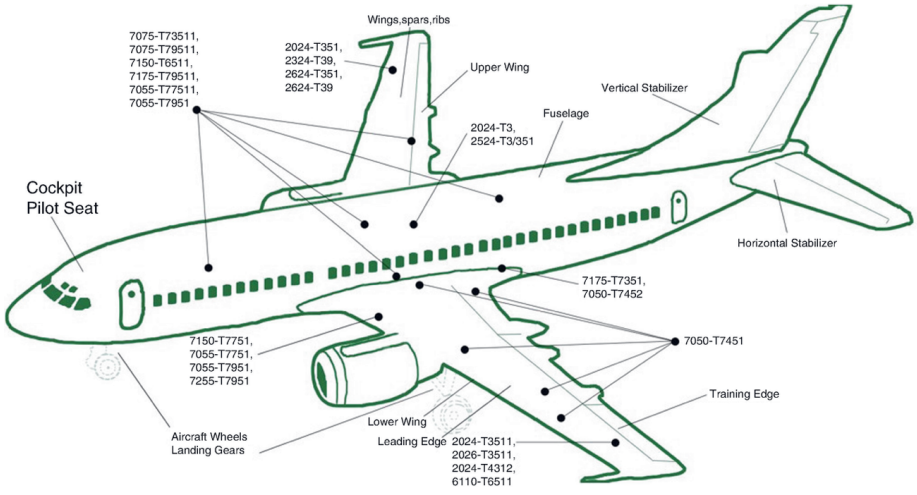


Fig. 1.1. Airframe materials distributions in an aeroplane. Typically, AA 2XXX, 6XXX and 7XXX = conventional aluminium alloys are used [5].

Table. 1.1. Chemical compositions (wt%) of aerospace aluminium alloys [4].

	Cu	Zn	Li	Mg	Mn	Fe	Si	Cr	Zr	Ti	Al
2024	4.4	-	-	1.5	0.6	≤0.5	≤0.5	0.1	-	0.15	Bal.
7075	1.2-2.0	5.1-6.1	-	2.1-2.9	0.3	0.5	0.4	0.18-0.28	-	0.2	Bal.
2099	2.4-3.0	0.4-1.0	1.6-2.0	0.1-0.5	0.1-0.5	0.07	0.05	0.1-0.5	0.05-0.12	0.1	Bal.
2199	2.0-2.9	0.2-0.9	1.4-1.8	0.05-0.4	0.1-0.5	0.07	0.05	-	0.05-0.12	0.1	Bal.
2050	0.7-1.3	0.25	3.2-3.9	0.2-0.6	0.2-0.5	0.1	0.08	0.05	0.06-0.14	0.1	Bal.

Intermetallic particles (IMPs) are an essential aspect of the microstructure of AA2024-T3 [6]. Given the length scale, they can be categorized into three groups of (a) hardening precipitates (< 200 nm), (b) dispersoids (100–500 nm) and (c) coarse constituent phase and impurity particles (> 0.5 μm) [7, 8]. Precipitates including Al_2CuMg (S-phase) with an orthorhombic crystal structure proposed by Perlitz and Westgren [9] and Al_2Cu (θ-phase) with a tetragonal crystal structure [10] emerge in response to age hardening processes and greatly contribute to the mechanical strength enhancement in aerospace AAs. They largely through a clustering root of either Cu and Mg or Cu into Guinier-Preston-Bagaratsky (Al-Cu-Mg) and Guinier-Preston (Al-Cu) zones. Next, the precipitates undergo the transformation patch of either $S''\rightarrow S'\rightarrow S$ for Al_2CuMg or $\theta''\rightarrow\theta'\rightarrow\theta$ for Al_2Cu [1, 2, 8]. In contrast with the precipitates, the dispersoids and constituent phase particles form during the ingot formation. They generally do not react to any further heat treatment, hence considered insoluble. The major dispersoid in AA2024-T3 is $Al_{20}Mn_3Cu_2$, which is are formed purposefully in the melt for grain refinement, commonly having a nodular shape. Constituent phases are formed during solidification at high temperatures and are quite variant in composition and crystal structure [1, 2, 8]. In contemporary AA2024-T3, constituent phases contain combinations of Al, Mn, Fe, Cu and Si in various ratios [11]. Table 1.2 presents crystal structure and compositions for main constituent phases particles containing Al, Cu, Fe, Mn, Si.

Table 1.2. Elemental compositions for different types of constituent particles containing Al, Cu, Fe Mn, and Si reported to be found in AA2024-T3; the table is modified from Ref [11].

Particle Name	Crystallography	Stoichiometry	Shape and Distribution
Type 1	Body centred cubic (BCC)	$Al_{77}Cu_{10}Fe_7Mn_5Si_2$	Large angular particles, most commonly present with Type 2 particles in larger constituents.
Type 2	Monoclinic	$Al_{76}Cu_6Fe_7Mn_5Si_6$	Large and Angular as individual particles or commonly present with Type 1 in larger constituents.
Type 5	Tetragonal Al_7Cu_2Fe*	$Al_{79}Cu_{13}Fe_5Mn_2Mg_{0.7}Si_{0.2}$	Rounded as isolated particles or angular on the boundary with the matrix in larger particles.

***** *The composition of this constituent is close to the nominal Al_7Cu_2Fe composition widely reported and so it is assumed that this particle type is representative/interchangeable with Al_7Cu_2Fe.*

Fig. 1.2 shows 3D reconstruction of heterogeneous AA2024-T3 microstructure revealing a variety of intermetallic particles distributed in the alloy matrix in a wide range of size and compositions. Such a

microstructural complexity is associated with a complicated corrosion behaviour, leading to consequently considerable literature merely dedicated to corrosion contribution to microstructural degradations; as a well-documented fact, copper-containing IMPs are most problematic in AA2024 corrosion [8, 11-15].

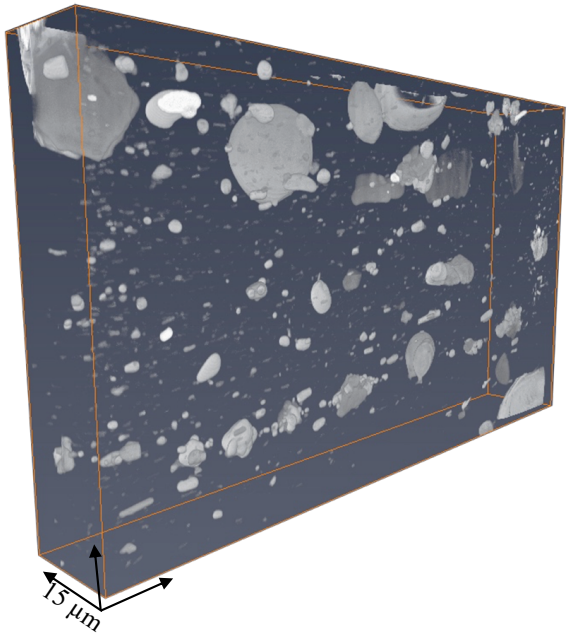


Fig. 1.2. 3D focused ion beam/scanning electron microscopy (FIB/SEM) reconstruction revealing heterogeneous microstructure of AA2024-T3. A variety of intermetallic particles in a wide range of size are distributed in the alloy matrix.

Given individual intermetallic phases (IMPs) as potential pit initiation sites (see Fig. 1.3), corrosion normally initiates as a consequence of selective dissolution of some constituent elements (dealloying) within the active phases like Al_2CuMg. Based on the microgalvanic concept, S-phase which is the most abundant IMP in AA2024 has an anodic activity to its adjacent matrix which is covered with an aluminium oxide passive layer. Upon exposure to neutral aqueous solutions, it quickly enriches in copper as a consequence of preferential magnesium and aluminium dissolution toward formation of a porous copper-rich remnant. A corroding Al_2CuMg particle progressively attains nobility and at a certain time, it can turn into an opposite particle (nobility inversion) accommodating cathodic reactions that produce OH^- ions. Then, the gradual build-up of alkalinity results in destabilisation of the aluminium oxide passive layer and trenching the neighbouring matrix [1]. The S-phase is associated with numerous copper clusters (redistributed copper) that nestle in the trench and neighbouring matrix

[13]. Redistributed copper, which plays a great role in further propagation of corrosion, is believed to be mainly a consequence of mechanically-detached clusters from the corroding S-phase that can non-faradaically liberate Cu ions, followed by re-plating at surface flaws [13].

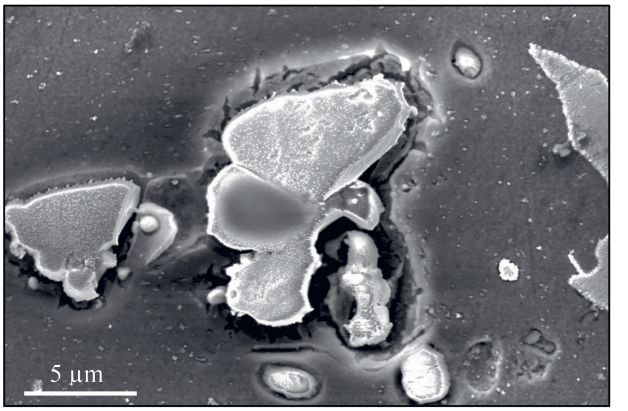


Fig. 1.3. SEM image of a corroded AA2024-T3 sample exposed to 0.01 M NaCl for 6 h, revealing the local corrosion attack at/around the intermetallic particles.

Comparatively, local corrosion induced by cathodic particles like Al_2Cu, Al_7Cu_2Fe and $Al_{76}Cu_6Fe_7Mn_5Si_6$ has less complication as supposedly this phase cathodically behaves to the matrix and other IMPs. Cathodic particles support cathodic reactions like oxygen reduction reaction (ORR) upon exposure, owing to a higher corrosion potential than that of the alloy matrix [8, 16-18]. This process will establish a locally basic solution chemistry in which the aluminium oxide passive layer is undermined gradually. Such electrolyte conditions can give rise to local dissolution of the surrounding matrix commonly in the form of a circumferential trench around the IMP. This form of local dissolution is known as trenching [19, 20].

There are numerous works reporting the effect of IMPs and their role in localised corrosion of A2024; however, the literature is still in need of a through mechanism elucidating the entire degradation process from initiation to stable propagation. In fact, none of the aforementioned events are evidenced directly and at this stage, the arguments are focused on determining anode-to-cathode transition and trenching initiation times and also explaining controversial ways of non-faradaic liberation of copper.

AA2024-T3 alloy needs a reliable active protection otherwise pitting corrosion readily takes place at IMPs locations in a short period of exposure. In the presence of mechanical stress, pit to crack transition can occur, which is quite detrimental to the safety of the alloy structure. As shown in Fig. 1.4, one approach is to apply the organic coatings in which inhibitors are incorporated. Upon any damage to the coating during the service, inhibitors can be released (leaching process) at the place protecting the substrate from the corrosion attack [4]. Such a scheme has been fulfilled for decades by the application

of hexavalent chromate-based inhibitors [21-24]. However, being recognised to be toxic and carcinogenic, the urgent need has risen to be replaced by non-toxic systems due to increasingly strict international health and safety legislation [25]. In this case, two important potential candidates are lithium-based and cerium-based technologies. The lithium salts bring the protection through formation of a ubiquitous conversion layer over the alloy matrix and IMPs [26]. However, the cerium-based inhibitors locally interact with individual IMPs, precipitating as (hydro)oxide layer as a consequence of the local alkalinisation due to electrochemical activity of the IMPs [27]. Since the inhibition is a process taking place through nanoscopic interaction events of inhibitors with individual phases in the substrate over time, time-resolved direct nanoscopic morphological and compositional evidence of the entire process is of crucial importance for development and improvement of currently available systems.

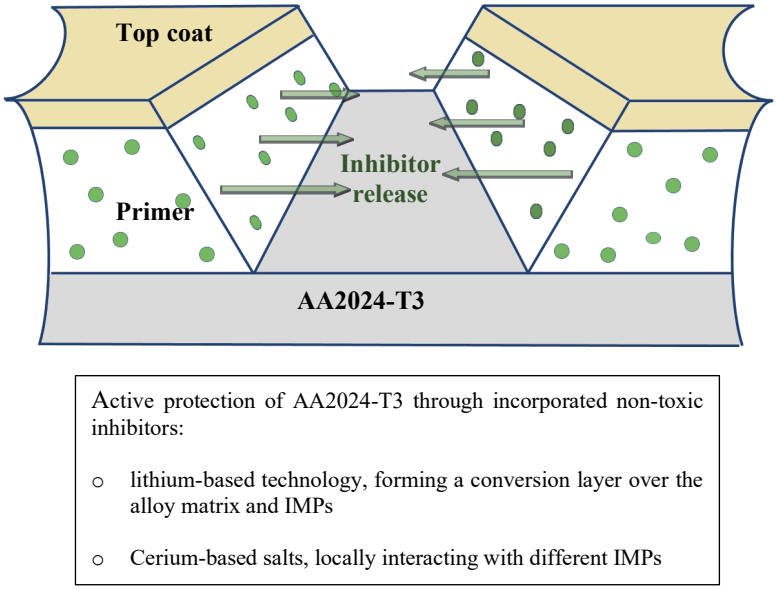


Fig. 1.4. Schematic representation of active corrosion protection of AA2024-T3. In this scheme, inhibitors are incorporated into organic coatings. If the coating is damaged, the inhibitors are released within the area and provide active protection.

1.2. Research aim

The scientific objective of this work is to provide time-resolved nanoscopic direct evidence of local corrosion and inhibition phenomena in AA2024-T3, through dedicated TEM approaches. This study firstly explores the role of different intermetallic particles (IMPs) in prompting local corrosion in this class of structural materials. Subsequently, inhibition mechanisms by lithium-

based technology and cerium-based salts are explored in detail. Therefore, the investigations of the thesis can be divided into three main parts:

a) *On the local corrosion mechanisms induced by IMPs in AA2024-T3*
b) *On the formation mechanism of protective conversion layer on AA2024-T3 by lithium-based technology*
c) *On the local corrosion inhibition mechanisms of AA2024-T3 by a cerium-based compound*

Aerospace industries would definitely benefit from a comprehensive knowledge and understanding of corrosion and corrosion inhibition phenomena in order to develop reliable anticorrosion systems protecting aerospace aluminium alloys. Therefore, this thesis attempts to comes up with deterministic descriptors fully explaining mechanisms of relevance in the legacy alloy AA2024-T3.

1.3. Research approach

TEM and its analytical techniques can provide information at high resolutions down to atomic scale that can directly be correlated to a morphology, structure, and composition of an object [28]. Given the vacuum operating conditions, practical TEM corrosion studies are generally performed ex-situ. This means that the TEM examinations are carried out on regions of interest in pre-corroded samples [29-35]. Thus, ex situ TEM approach is very helpful in the case of long-term studies of alloy corrosion even in harsh environments. However, concluding statements are sometimes uncertain and debatable when compared to the real-life conditions since active solid/electrolyte interfaces cannot be assessed. In addition, ex-situ characterisations include end results, [36, 37] and always lack time-resolved information on the degradation of an identical sample.

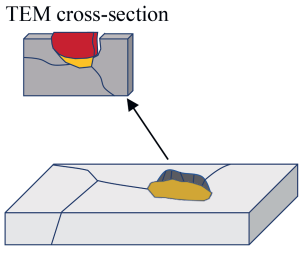
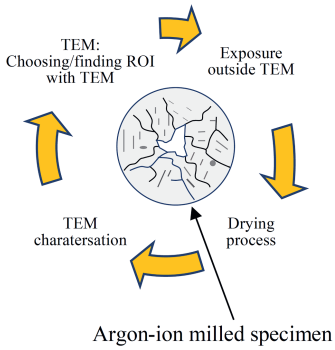
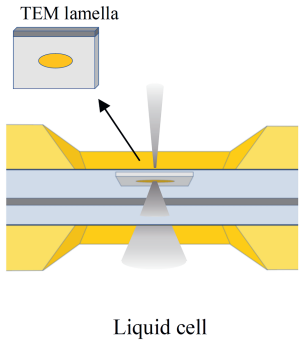
Quasi in-situ TEM is another approach in which an identical location on a thin sample is exposed intermittently to a corrosive environment outside the microscope and subsequently examined with TEM. Although characterisations still need to be done statically in vacuum, this method has so far delivered valuable insights mainly into early stages of corrosion in many alloys as morphological and chemical evolutions can directly be evidenced at the nanoscale [38]. Nevertheless, there are still potential drawbacks to this approach. For instance, the solution chemistry at sites experiencing localised corrosion attack normally develop differently with time than the bulk solution chemistry. Therefore, these specific sites might never become active again subsequent to the drying process or at least not reach the same conditions over the next rounds of exposure as compared to an undisturbed exposure case. Furthermore, artefacts and particularly carbon contaminations may be introduced into the system during handling and analysing the specimens, leading to beam-induced carbon depositions which can

deviate and change the corrosion mechanism and kinetics differently as compared to the uninterrupted exposure case [39].

In-situ liquid-phase TEM is implemented using thin-window liquid cells which elegantly isolate the specimen and its liquid surrounding from vacuum [40-43]. The samples loaded in electrochemical liquid cells can now be biased externally, whereby local dissolution events can be correlated directly to the corresponding morphological changes [44-47]. This development allows for studying morphological and even compositional evolutions of alloy specimens real time and in-situ as a consequence of interaction with corrosive environments at a desired temperature (operando) [48]. This ambition strongly demands optimised experimental conditions for liquid-phase TEM, that can simultaneously provide a high spatial and temporal resolution [49-53]. In-situ TEM movies can capture insightful corrosion events to understand mechanisms behind local corrosion attack in real specimens exposed to inhibited/uninhibited solutions. However, liquid-phase TEM is still not straightforward in implementation and there are limitations and challenging experimental considerations like beam effects, challenging sample preparation and transfer [54-57].

Table 1.3 schematically shows the basic principle of different TEM approaches and summaries their advantages and disadvantages. Since every TEM approach has its own pros and cons, the current work puts efforts into doing a combination of them in order to take advantage of TEM as a powerful technique for providing direct evidence of corrosion and corrosion inhibition phenomena. In this case, time-resolved nanoscopic information which is crucial for reliable and active corrosion protection of aerospace structures are indeed charming.

Table 1.3. Advantages and disadvantages of TEM-based approaches in corrosion studies.

Ex-situ TEM	Quasi in-situ TEM	In-situ liquid-phase TEM
		
○ **Advantage:** Long term experiments, Flexibility of corrosion conditions ○ **Disadvantage:** End results, No on-site time-resolved information, De-hydrated surfaces	○ **Advantage:** Time-resolved high-resolution structural and chemical information ○ **Disadvantage:** Needs proper exposure time, Carbon contamination, Deterioration of local solution chemistry upon drying, Useful for studying corrosion at early stages, De-hydrated surfaces	○ **Advantage:** Real-time nanoscopic imaging of dynamic process, Simultaneous electrochemical and TEM investigations ○ **Disadvantage:** Beam effects, Challenging sample preparation and transfer, Lack of detailed chemical information, Degraded resolution, Useful for studying corrosion at early stages

1.4. Outline

The structure of the thesis is illustrated graphically in Fig. 1.5. Chapter 1 gives an introduction to the motivation and industrial relevance of the work and brings up research questions and briefly described the research approach. Subsequently, Chapter 2 (literature review) is devoted to briefly introducing TEM and its analytical techniques. Then, it discusses the challenges of in-situ liquid-phase TEM whereas relevant state-of-the-art achievements in the field are reviewed. Given a dedicated TEM study, the details on the implementation of ex-situ, quasi in-situ and in-situ liquid-phase TEM are presented in Chapter 3. Moreover, a home-made electrochemical liquid cell for liquid-phase TEM corrosion studies is introduced where a protocol for preparing thin specimens to be used for top- and cross-sectional-view observations of corrosion in thin TEM specimens is presented. Chapter 4 and 5 are devoted to studying local corrosion phenomena in AA2024-T3. Chapter 4 is focused on providing direct evidence of the role of precipitations in local corrosion while Chapter 5 deals with the impact of

constituent phases and dispersoids. Chapter 6, 7 and 8 are concentrated on elucidating the formation mechanism of a protective conversion layer from leaching lithium-based salts. The lithium conversion layers grown at different locations of a 1-mm-wide coating defect are fully characterised in terms of morphology, structure and chemical composition in Chapter 6. Chapter 7 explores the formation mechanism of a protective conversion layer from a lithium salt-based solution on the alloy matrix while Chapter 8 is more oriented towards the local lithium-based conversion layer formation on different IMPs. Chapter 9 studies the interaction mechanisms of different IMPs in AA2024-T3 with cerium nitrate. Finally, overall conclusions and recommendations relevant to the current research are provided in Chapter 10.

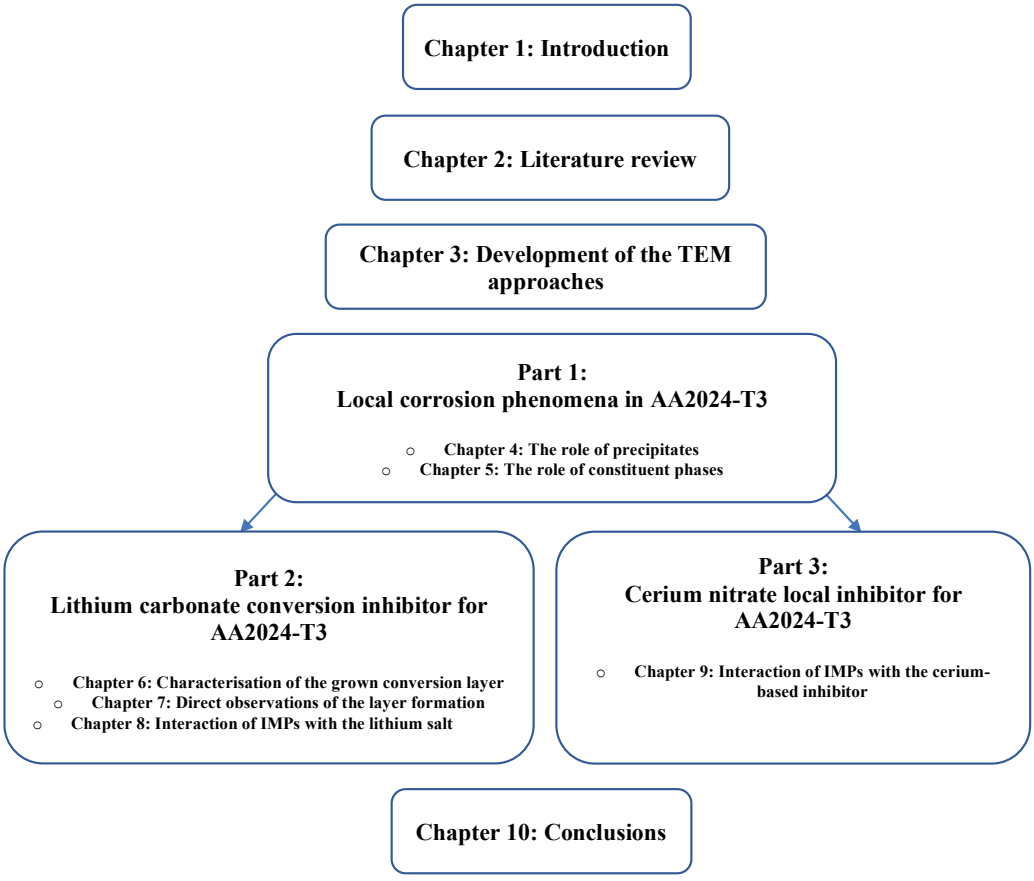


Fig. 1.5. Graphic representation of the thesis outline.

References

[1] N. Birbilis, T.H. Muster, R.G. Buchheit, Corrosion of Aluminum Alloys, in: P. Marcus (Ed.) Corrosion mechanisms in theory and practice, Crc Press, London, 2011.
[2] A.E. Hughes, N. Birbilis, J.M.C. Mol, S.J. Garcia, X. Zhou, G.E. Thompson, High Strength Al-Alloys: Microstructure, Corrosion and Principles of Protection, in: Z. Ahmad (Ed.) Recent Trends in Processing and Degradation of Aluminium Alloys, IntechOpen 2011.
[3] J. Liu, Advanced aluminium and hybrid aerostructures for future aircraft, in: Materials Science Forum, Trans Tech Publ, 2006, pp. 1233-1238.
[4] P. Visser, H. Terryn, J.M. Mol, Aerospace Coatings, in: Active Protective Coatings, Springer, 2016, pp. 315-372.
[5] https://www.aircraft-aluminium.com/, Aircraft aluminum sheets.
[6] G.S. Frankel, 2015 W.R. Whitney Award Lecture: The Effects of Microstructure and Composition on Al Alloy Corrosion, CORROSION, 71 (2015) 1308-1320.
[7] N. Birbilis, R. Buchheit, Electrochemical characteristics of intermetallic phases in aluminum alloys an experimental survey and discussion, Journal of The Electrochemical Society, 152 (2005) B140-B151.
[8] A.E. Hughes, R. Parvizi, M. Forsyth, Microstructure and corrosion of AA2024, Corrosion Reviews, 33 (2015) 1-30.
[9] S. Wang, M. Starink, N. Gao, Precipitation hardening in Al–Cu–Mg alloys revisited, Scripta Materialia, 54 (2006) 287-291.
[10] S. Hu, M. Baskes, M. Stan, L. Chen, Atomistic calculations of interfacial energies, nucleus shape and size of θ′ precipitates in Al–Cu alloys, Acta materialia, 54 (2006) 4699-4707.
[11] N. Birbilis, Y. Zhu, S. Kairy, M. Glenn, J.-F. Nie, A. Morton, Y. Gonzalez-Garcia, H. Terryn, J. Mol, A. Hughes, A closer look at constituent induced localised corrosion in Al-Cu-Mg alloys, Corrosion Science, 113 (2016) 160-171.
[12] A. Boag, R. Taylor, T. Muster, N. Goodman, D. McCulloch, C. Ryan, B. Rout, D. Jamieson, A. Hughes, Stable pit formation on AA2024-T3 in a NaCl environment, Corrosion Science, 52 (2010) 90-103.
[13] R. Buchheit, R. Grant, P. Hlava, B. McKenzie, G. Zender, Local dissolution phenomena associated with S phase (Al2CuMg) particles in aluminum alloy 2024-T3, Journal of the Electrochemical Society, 144 (1997) 2621-2628.
[14] M.-L. de Bonfils-Lahovary, L. Laffont, C. Blanc, Characterization of intergranular corrosion defects in a 2024 T351 aluminium alloy, Corrosion Science, 119 (2017) 60-67.
[15] Z. Wang, P. Chen, H. Li, B. Fang, R. Song, Z. Zheng, The intergranular corrosion susceptibility of 2024 Al alloy during re–ageing after solution treating and cold–rolling, Corrosion Science, 114 (2017) 156-168.
[16] N. Birbilis, M.K. Cavanaugh, R.G. Buchheit, Electrochemical behavior and localized corrosion associated with Al7Cu2Fe particles in aluminum alloy 7075-T651, Corrosion Science, 48 (2006) 4202-4215.
[17] B. Mazurkiewicz, A. Piotrowski, The electrochemical behaviour of the Al2Cu intermetallic compound, Corrosion Science, 23 (1983) 697-707.
[18] L. Yin, Y. Jin, C. Leygraf, N. Birbilis, J. Pan, Numerical Simulation of Micro-Galvanic Corrosion in Al Alloys: Effect of Geometric Factors, Journal of the Electrochemical Society, 164 (2017) C75-C84.
[19] O. Schneider, G. Ilevbare, J. Scully, R. Kelly, In situ confocal laser scanning microscopy of AA 2024-T3 corrosion metrology II. Trench formation around particles, Journal of The Electrochemical Society, 151 (2004) B465-B472.
[20] A. Boag, A. Hughes, A. Glenn, T. Muster, D. McCulloch, Corrosion of AA2024-T3 Part I: Localised corrosion of isolated IM particles, Corrosion Science, 53 (2011) 17-26.
[21] P. Campestrini, H. Terryn, J. Vereecken, J. De Wit, Chromate conversion coating on aluminum alloys: III. Corrosion protection, Journal of the Electrochemical Society, 151 (2004) B370.
[22] M. Kendig, R. Buchheit, Corrosion inhibition of aluminum and aluminum alloys by soluble chromates, chromate coatings, and chromate-free coatings, Corrosion, 59 (2003) 379-400.

[23] G. Ilevbare, J. Scully, J. Yuan, R. Kelly, Inhibition of pitting corrosion on aluminum alloy 2024-T3: effect of soluble chromate additions vs chromate conversion coating, Corrosion, 56 (2000) 227-242.
[24] A. Hughes, R. Taylor, B. Hinton, Chromate conversion coatings on 2024 Al alloy, Surface and Interface Analysis: An International Journal devoted to the development and application of techniques for the analysis of surfaces, interfaces and thin films, 25 (1997) 223-234.
[25] R. Saha, R. Nandi, B. Saha, Sources and toxicity of hexavalent chromium, Journal of Coordination Chemistry, 64 (2011) 1782-1806.
[26] P. Visser, Y. Liu, X. Zhou, T. Hashimoto, G.E. Thompson, S.B. Lyon, L.G. van der Ven, A.J. Mol, H.A. Terryn, The corrosion protection of AA2024-T3 aluminium alloy by leaching of lithium-containing salts from organic coatings, Faraday discussions, 180 (2015) 511-526.
[27] P. Rodič, I. Milošev, Corrosion inhibition of pure aluminium and alloys AA2024-T3 and AA7075-T6 by cerium (III) and cerium (IV) salts, Journal of The Electrochemical Society, 163 (2015) C85.
[28] D.B. Williams, C.B. Carter, The transmission electron microscope, in: Transmission electron microscopy, Springer, 1996, pp. 3-17.
[29] E. Hamada, K. Yamada, M. Nagoshi, N. Makiishi, K. Sato, T. Ishii, K. Fukuda, S. Ishikawa, T. Ujiro, Direct imaging of native passive film on stainless steel by aberration corrected STEM, Corrosion Science, 52 (2010) 3851-3854.
[30] S. Malladi, Q. Xu, F. Tichelaar, H. Zandbergen, F. Hannour, J. Mol, H. Terryn, Early stages during localized corrosion of AA2024 TEM specimens in chloride environment, Surface and Interface Analysis, 45 (2013) 1619-1625.
[31] K. Oh, S. Ahn, K. Eom, K. Jung, H. Kwon, Observation of passive films on Fe–20Cr–xNi (x= 0, 10, 20 wt.%) alloys using TEM and Cs-corrected STEM–EELS, Corrosion Science, 79 (2014) 34-40.
[32] R.P. Wei, C.-M. Liao, M. Gao, A transmission electron microscopy study of constituent-particle-induced corrosion in 7075-T6 and 2024-T3 aluminum alloys, Metallurgical and Materials Transactions A, 29 (1998) 1153-1160.
[33] B. Zhang, J. Wang, B. Wu, X. Guo, Y. Wang, D. Chen, Y. Zhang, K. Du, E. Oguzie, X. Ma, Unmasking chloride attack on the passive film of metals, Nature communications, 9 (2018) 2559.
[34] D. Sun, Y. Jiang, Q. Xiang, C. Zhong, J. Gong, L. Zhang, J. Li, Ex situ TEM observation of localized attack on AA 6061, Materials and corrosion, 61 (2010) 105-110.
[35] Y. Zhou, Y. Wang, S. Zheng, B. Zhang, X. Ma, Strain-induced preferential dissolution at the dislocation emergences in MnS: an atomic scale study, Philosophical Magazine, 95 (2015) 2365-2375.
[36] S. Persaud, S. Ramamurthy, A. Korinek, G. Botton, R. Newman, The influence of the high Fe and Cr contents of Alloy 800 on its inter-and intragranular oxidation tendency in 480° C hydrogenated steam, Corrosion Science, 106 (2016) 117-126.
[37] S. Persaud, J. Smith, A. Korinek, G. Botton, R. Newman, High resolution analysis of oxidation in Ni-Fe-Cr alloys after exposure to 315° C deaerated water with added hydrogen, Corrosion Science, 106 (2016) 236-248.
[38] B. Zhang, X. Ma, A review-pitting corrosion initiation investigated by TEM, Journal of Materials Science & Technology, (2019).
[39] A. Glenn, A. Hughes, T. Muster, D. Lau, N. Wilson, A. Torpy, C. MacRae, J. Ward, Investigation into the influence of carbon contamination on the corrosion behavior of aluminum microelectrodes and AA2024-T3, Journal of The Electrochemical Society, 160 (2013) C119-C127.
[40] N. De Jonge, F.M. Ross, Electron microscopy of specimens in liquid, Nature nanotechnology, 6 (2011) 695.
[41] K.L. Klein, I.M. Anderson, N. De Jonge, Transmission electron microscopy with a liquid flow cell, Journal of microscopy, 242 (2011) 117-123.
[42] H.-G. Liao, H. Zheng, Liquid cell transmission electron microscopy, Annual review of physical chemistry, 67 (2016) 719-747.
[43] M. Williamson, R. Tromp, P. Vereecken, R. Hull, F. Ross, Dynamic microscopy of nanoscale cluster growth at the solid–liquid interface, Nature materials, 2 (2003) 532.
[44] F.M. Ross, Quantifying Electrochemical Processes Using Liquid Cell TEM, in: F.M. Ross (Ed.) Liquid Cell Electron Microscopy, Cambridge University Press, Cambridge, 2016, pp. 210-236.

[45] B.L. Mehdi, J. Qian, E. Nasybulin, C. Park, D.A. Welch, R. Faller, H. Mehta, W.A. Henderson, W. Xu, C.M. Wang, Observation and quantification of nanoscale processes in lithium batteries by operando electrochemical (S) TEM, Nano letters, 15 (2015) 2168-2173.
[46] A. Radisic, P.M. Vereecken, J.B. Hannon, P.C. Searson, F.M. Ross, Quantifying electrochemical nucleation and growth of nanoscale clusters using real-time kinetic data, Nano Letters, 6 (2006) 238-242.
[47] J.H. Park, N.M. Schneider, D.A. Steingart, H. Deligianni, S. Kodambaka, F.M. Ross, Control of Growth Front Evolution by Bi Additives during ZnAu Electrodeposition, Nano letters, 18 (2018) 1093-1098.
[48] K. Jungjohann, C.B. Carter, In situ and operando, in: Transmission Electron Microscopy, Springer, 2016, pp. 17-80.
[49] J.E. Evans, K.L. Jungjohann, N.D. Browning, I. Arslan, Controlled growth of nanoparticles from solution with in situ liquid transmission electron microscopy, Nano letters, 11 (2011) 2809-2813.
[50] M. Tanase, J. Winterstein, R. Sharma, V. Aksyuk, G. Holland, J.A. Liddle, High-resolution imaging and spectroscopy at high pressure: A novel liquid cell for the transmission electron microscope, Microscopy and Microanalysis, 21 (2015) 1629-1638.
[51] E.R. White, S.B. Singer, V. Augustyn, W.A. Hubbard, M. Mecklenburg, B. Dunn, B.C. Regan, In situ transmission electron microscopy of lead dendrites and lead ions in aqueous solution, Acs Nano, 6 (2012) 6308-6317.
[52] T. Xu, L. Sun, Investigation on material behavior in liquid by in situ TEM, Superlattices and Microstructures, 99 (2016) 24-34.
[53] M.R. Hauwiller, X. Zhang, W.-I. Liang, C.-H. Chiu, Q. Zhang, W. Zheng, C. Ophus, E.M. Chan, C. Czarnik, M. Pan, Dynamics of Nanoscale Dendrite Formation in Solution Growth Revealed Through in Situ Liquid Cell Electron Microscopy, Nano letters, 18 (2018) 6427-6433.
[54] L.R. Parent, E. Bakalis, M. Proetto, Y. Li, C. Park, F. Zerbetto, N.C. Gianneschi, Tackling the challenges of dynamic experiments using liquid-cell transmission electron microscopy, Accounts of chemical research, 51 (2017) 3-11.
[55] N. Hodnik, G. Dehm, K.J. Mayrhofer, Importance and challenges of electrochemical in situ liquid cell electron microscopy for energy conversion research, Accounts of chemical research, 49 (2016) 2015-2022.
[56] F.M. Ross, Opportunities and challenges in liquid cell electron microscopy, Science, 350 (2015) aaa9886.
[57] T.J. Woehl, K.L. Jungjohann, J.E. Evans, I. Arslan, W.D. Ristenpart, N.D. Browning, Experimental procedures to mitigate electron beam induced artifacts during in situ fluid imaging of nanomaterials, Ultramicroscopy, 127 (2013) 53-63.

CHAPTER 2

APPLICATION OF TEM IN CORROSION SCIENCE (LITERATURE REVIEW)[1]

Identifying corrosion initiation events in metals and alloys demands techniques that can provide temporal and spatial resolution simultaneously. Transmission electron microscopy (TEM) enables to obtain microstructural and chemical descriptors of materials at atomic/nanoscopic level and has been used in corrosion studies of many metal-electrolyte combinations. Conventionally, ex-situ and quasi in-situ TEM studies of pre- and post-corroded samples were performed, but possible experimental artefacts such as dehydrated surfaces might not fully represent the real interfacial conditions as compared to those when actually immersed in the electrolyte. Recent advances in liquid cell transmission electron microscopy (LC-TEM) allows for in-situ monitoring morphological and even compositional evolutions in materials resulting from interaction with gas or liquid environments. Corrosion science, as a challenging field of research, can benefit from this unparalleled opportunity to investigate many complicated corroding systems in aqueous environments at high resolution. However, 'real life' corrosion with LC-TEM is still not straightforward in implementation and there are limitations and challenging experimental considerations for conducting reliable examinations. Thus, this chapter has been devoted to briefly introducing TEM and its analytical techniques. Then, it discusses the challenges of in-situ LC-TEM whereas state-of-the-art achievements in the field of relevance are reviewed.

Keywords: Aqueous corrosion; Analytical TEM; In-situ liquid cell TEM**;** Initiation events**;** Electron beam effect; Specimen preparation**;** (S)TEM imaging mode

[1] **A. Kosari**, H. Zandbergen, F. Tichelaar, P. Visser, H. Terryn, A. Mol, Application of In Situ Liquid Cell Transmission Electron Microscopy in Corrosion Studies: A Critical Review of Challenges and Achievements, CORROSION, 76 (2020) 4-17.

2.1. Introduction

Detailed understanding of local corrosion events and processes in alloys at very early-stages of exposure to a corrosive environment are of pivotal importance to developing timely and effective inhibition strategies to avoid premature failures [1, 2]. Techniques to probe corrosion initiation are limited where concurrent chemical, electrochemical and morphological characterizations at a high resolution are essential [3-5]. That is why theories have traditionally been established through bridging and linking information obtained from separately performed experiments involving multiple techniques [6-8]. Transmission electron microscopy (TEM) can provide information at atomic resolution that can be correlated to a structure, morphology, and composition of an object directly [9]. However, due to limiting factors such as a thin object size (5-300 nm) and the vacuum operating conditions, practical TEM corrosion studies were ex-situ typically, i.e., after the corrosion event, and of dehydrated surfaces (post-mortem characterizations) [10-16]. Thus, concluding statements are sometimes uncertain and debatable when compared to the real-life conditions since active solid/electrolyte interfaces cannot be evaluated real-time in such ex-situ studies. In addition, ex-situ characterizations, in case of long term studies of alloy corrosion in harsh environments [17, 18], always suffer from the lack of time-resolved information on the degradation kinetics of samples.

As an alternative, quasi in-situ TEM approaches have been applied to corrosion studies recently [19-23]. 'Quasi in-situ' implies that an identical location on a thin sample is exposed intermittently to a corrosive environment outside the microscope and subsequently examined with TEM. Although characterisations still need to be done statically in vacuum, this method has so far delivered valuable insights mainly into early stages of corrosion in many alloys as morphological and chemical evolutions can directly be evidenced at the nanoscale [21]. Nevertheless, there are still potential drawbacks to this approach. For instance, the solution chemistry at sites undergoing localised corrosion attack normally develop differently with time than the bulk solution chemistry. Therefore, these specific sites might never become active again subsequent to the drying process or at least not reach the same conditions over the next rounds of exposure as compared to an undisturbed exposure case. Furthermore, artefacts and particularly carbon contaminations may be introduced into the system during handling and analysing the specimens, leading to beam-induced carbon depositions which can steer and change the corrosion mechanism and kinetics differently as compared to the uninterrupted exposure case [24].

Nowadays, in-situ TEM can be implemented for corrosion studies by means of thin-window cells which elegantly isolate the specimen and its liquid surrounding from vacuum [25-28]. This development allows for studying morphological and even compositional evolutions of alloy specimens real time and in-situ as a consequence of interaction with corrosive environments at a desired temperature (operando) [29]. This ambition strongly demands optimised experimental conditions for in-situ LC-TEM, that can simultaneously provide a high spatial and temporal resolution [30-34], as initiation processes take place dynamically and relatively fast at the metal/electrolyte interface [35]. In fact, corrosion initiation often occurs at surface heterogeneities where microstructure and composition variations result in

electrochemical interaction and reactivity [21, 35-39]. In-situ TEM movies can capture insightful events to understand mechanisms behind local corrosion attack in real specimens exposed to inhibited/uninhibited solutions. Impressively, the samples loaded in electrochemical liquid cells can now be biased externally, whereby local dissolution events can be correlated directly to the corresponding morphological changes [40-43]. This can be utilised to conduct several studies using in-situ LC-TEM to probe dynamic nanoscale phenomena such as transition from metastable events to stable pitting corrosion at the nanoscale in many metallic systems like stainless steels, Al, Ti and Mg alloys [39, 44-51].

Even though LC-TEM provides an unprecedented opportunity of studying many complicated corroding systems at the nanoscopic level, it has raised demanding technical implications and concerns during interpretation of electrochemical events [52-55]. This chapter discusses limitations and challenges of in-situ LC-TEM applied to aqueous corrosion. Furthermore, noteworthy achievements in the field of relevance are reviewed.

2.2. Transmission Electron Microscopy (TEM) and its analytical techniques[2]

Transmission electron microscopy (TEM) is a powerful characterisation approach that can provide information down to atomic scale correlated to a structure, morphology, and composition of an object directly. TEM principally works as a consequence of electron beam interaction with nanometrically-thick materials, leading to numerous elastic and inelastic scattering events. Fig. 2.1 schematically shows the products of electron beam/specimen interaction taking place when the electrons travel through thin specimens. In general, a large portion of the travelling electrons get elastically-scattered; it can be a coherent elastic scattering (Bragg scattering) or an incoherent elastic scattering (Rutherford scattering). However, the energy-losing electrons endure inelastic scattering that cause several other characteristic signals such as X-rays and inelastically scattered electrons. Thus, different scattered electrons can be analysed within TEM columns in order to characterise materials in term of atomic structure, morphology, chemical composition and oxidation state. Thus, a TEM microscope normally come with different analytical techniques as the attachments. Examples of the applications have been shown in Fig. 2.2. A TEM microscope is mainly composed of three optical sections of illumination, objective lenses (image forming) and magnification. Besides, it can be equipped with monochromators, aberration correctors, beam and image deflection coils and several type of detectors.

[2] This section has mostly been adapted from reference [9]

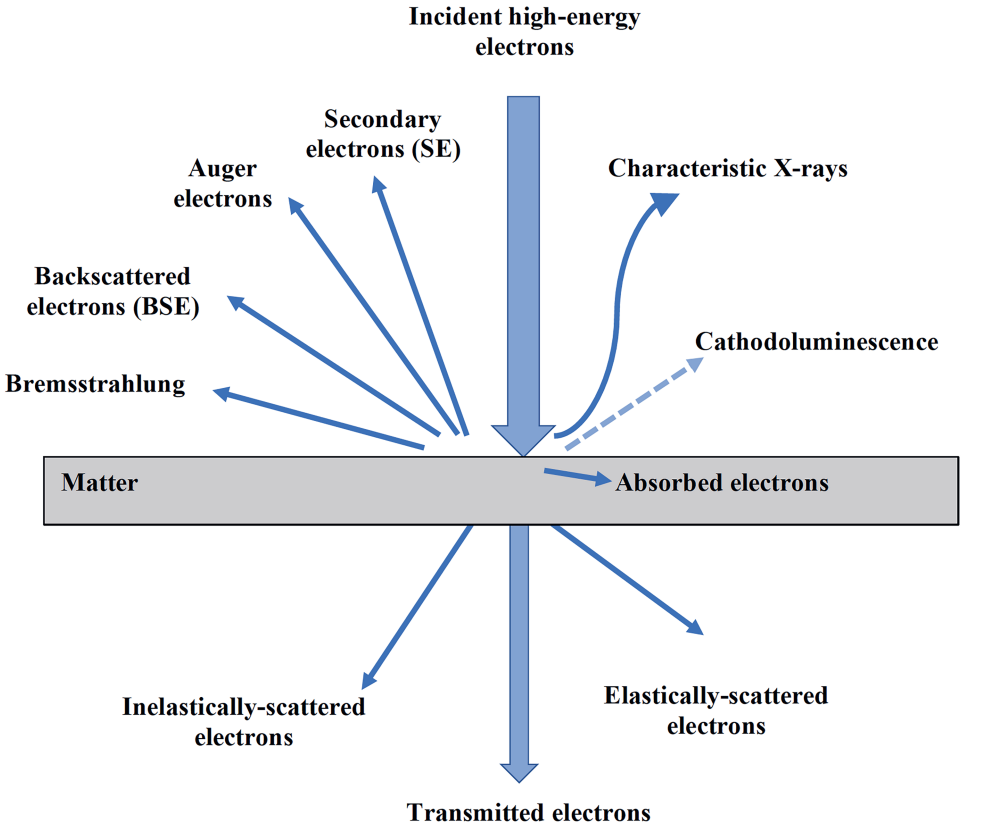


Fig. 2.1. Characterising products when a high-energy electron-beam interacts with a nanometrically-thick specimen. TEM columns are normally equipped with specific detectors that can detect and analyse most of these signals.

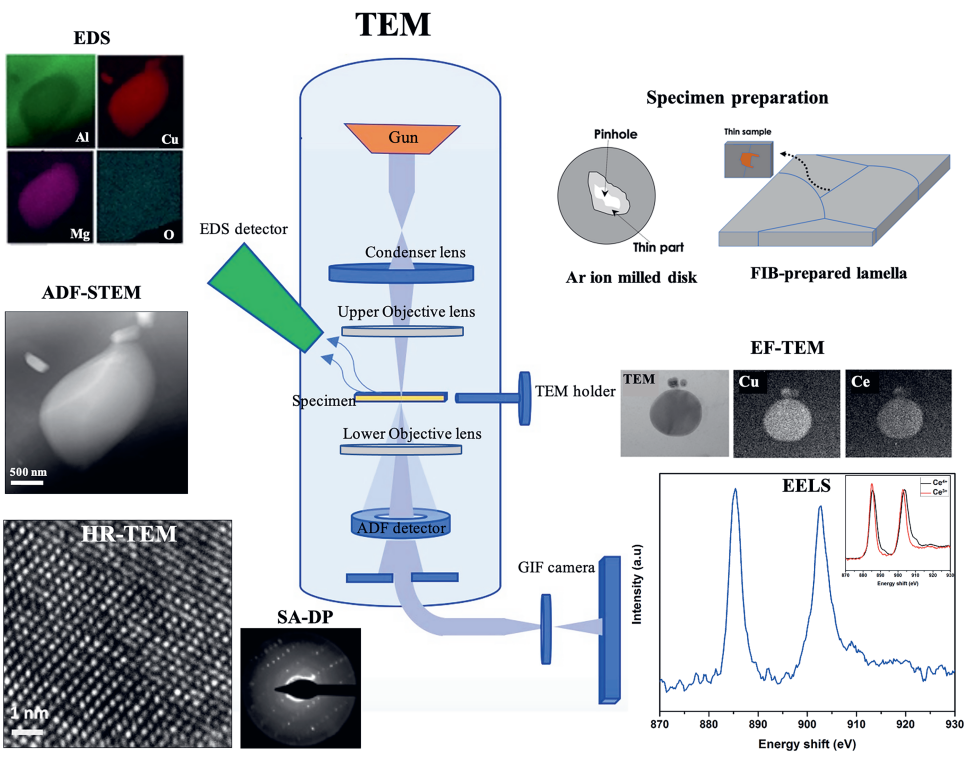


Fig. 2.2. Simplified schematic view of a typical transmission electron microscope together with its analytical techniques; the specimen is being illuminated in Scanning TEM (STEM) mode. Thin samples can be fabricated out of a "region of interest" either by argon-ion milling of approx. 50-µm thick disks or using focus ion beam (FIB) and lift-out procedures. TEM holders are used to mount electron-transparent samples (specimens) for examinations. The specimens can directly be imaged down to atomic level either with a broad static beam (TEM mode) or a scanning electron probe of typical 0.1 – 0.05 nm (STEM mode). An Annular Dark Field (ADF) detector (a ring) or Bright Field (BF) detector (a disc) is used for STEM imaging. An Energy Dispersive Spectroscopy (EDS) detector is used to collect X rays from the sample where the electron beam is. In STEM mode, elemental maps can be generated with a spatial resolution down to the electron probe size. High Resolution TEM (HR-TEM) allows for direct imaging of atomic arrangements in materials (phase contrast imaging). A Selected Area (SA) aperture can be inserted to collect diffraction patterns (DP) of different locations on a specimen. By collecting and analysing the inelastic transmitted electrons, it is possible to acquire information about elemental distribution and thickness variation within the specimen through Energy Filtered TEM (EF-TEM). The electronic structure like bonding and valence state of different phases can be analysed using Electron Energy Loss Spectroscopy (EELS).

2.2.1. Imaging and diffraction. The conventional application of TEM is to perform imaging and diffraction analysis. A diffraction pattern (DP) is formed due to scattering the electrons traveling through a crystalline at specific angles according to Bragg's law. Diffraction patterns are characteristic features through which lattice parameters can be estimated; a powerful approach of characterising materials. Field limiting apertures called selected area (SA) apertures are normally used to collect the diffraction pattern of specific regions in the specimen. In TEM imaging mode, the specimen can directly

be imaged down to atomic level either with a broad static beam while in STEM mode, an electron probe is scanned over the specimen. In TEM mode, image can be formed by diffraction, mass and phase contrast of the scattered electrons. Bright field (BF), dark field (DF), weak-beam dark field imaging (diffraction contrast) and high-resolution electron microscopy (HR-TEM) are the main techniques. The appearance of lattice fringe (i.e., HR-TEM) is a consequence of the primary beam/the diffracted beams interference along a low-index zone axis. The mass contrast is caused by the difference in the scattering powers of different regions in the specimen.

In STEM mode, the electron beam is concentrated on the specimen to make a probe of 0.1 – 0.05 nm. In general, STEM detectors usually have an annular geometry and record a single value per probe position. For instance, bright-field (BF) detector collects the intensities of the un-scattered direct beam (collection angle < 10 mrads). Annular bright-field (ABF) detector gives a unique contrast effect as it is the outer ring of the BF disk. Annular dark-field (ADF) concerns the intensities of the scattered electrons (10 mrads < collection angle < 50 mrads). And high-angle ADF (HAADF), commonly called Z-contrast imaging, is responsible for collecting highly scattered electrons, thus minimising the Bragg scattered electrons compared to ADF (collection angle > 50 mrads). HAADF-STEM (Z-contrast) technique is often used for atomic-scale imaging. It should be mentioned that the phase relationship of scattered beams and their interference, which are important considerations for HRTEM imaging, are irrelevant for HAADF- STEM imaging.

2.2.2. Energy Dispersive Spectroscopy (EDS). Accelerated electrons can ionise an atom in a specimen, thus any of possible transitions within the internal shells of the atom is associated with a characteristic X-ray emission. The specific detectors can collect the emitted X-ray photons, plotting the X-ray counts as a function of X-ray energy. Furthermore, the quantification and estimation of the elemental composition of a specimen can be acquired from the intensities of the characteristic peaks of different elements. In fact, the amounts of elements existing in the specimen can be estimated by relating the weight fraction and generated intensities (ionisation cross-section), according to the Cliff-Lorimer equation; $(W_a/W_b) = K_{ab} (I_a/I_b)$. In this equation, W_a, W_b, I_a, I_b are the weight fractions and the intensities of the element a and b. Most importantly, K_{ab} is the Cliff-Lorimer factor which is related to sensitivity and has to experimentally be obtained from a specimen of known composition. It is worth mentioning that fluorescence and absorption can affect the Cliff-Lorimer factor. However, their effects are negligible if the samples are rather thin (TEM specimens), thus the Cliff-Lorimer would be valid.

2.2.3. Electron Energy Loss Spectroscopy (EELS) and Energy-Filtered Transmission Electron Microscopy (EF-TEM). The electrons that have lost some energy during the interaction with the specimen (inelastically scattered) are considered. Although, the events related to losing energy negatively affect the image quality, they bring along valuable information about electronic structure of the specimen atoms like bonding, valence state and band-gap. In energy filtering, the forward scattered inelastic electrons are separated based on their energies while travelling through a magnetic prism. Then, the electrons are arranged according to their energies to an energy spectrum, normally consisted

of zero-loss, low-loss and core-loss (characteristic ionisation edges) sections. The low-loss region has been considered up to around 50 eV, comprising information in relation to dielectric response, the plasmon peaks, band gap and specimen thickness. These separated electrons can be restored to form an image through a lens by varying the settings of magnetic prism and a slit. By selecting a suitable energy window around an ionisation edge, 2-dimensional energy distribution maps of the specimen can be collected, (i.e., EFTEM imaging).

2.2.4. Specimen preparation technique. Thin samples can be fabricated out of a "region of interest" either by argon-ion milling of approx. 50-µm-thick polished disks or using focus ion beam (FIB) and lift-out procedures. Argon-ion milling machine bombards the thin samples with the ion energies of 0.5-5 kV at various glancing angles. The best result is achieved with a low ion-incident angle such as 3-50, although little implantation of argon ions still takes place. It should be noted that the thinning time can be long if the machine is operated at low angles, thus thin polished samples are more useful.

Nowadays, focused ion beam (FIB) microscopes are widely used to prepare TEM specimens out of regions of interest very efficiently. A FIB system is normally combined with an SEM, called FIB/SEM in order to facilitate the process of milling and imaging. In fact, the electron beam is used for conventional SEM imaging while the ion beam enables engraving the sample surface. The majority of FIBs have a gallium (Ga) ion source, although plasma sources like Xe are gradually becoming popular. The FIB microscopes are typically operated at accelerating voltage of 0.5-30 kV; apertures and lens are responsible for controlling the probe current density ranging from a few pA to nA. In principle, accelerated heavy Ga ions colliding the sample surface cause atoms or molecules sputtering. The FIB/SEM microscope are additionally equipped with nano-manipulators that can be used to precisely transfer the prepared cross-sections out of a region of interest to half-grids. Gallium implantation and amorphization that can occur during the specimen preparation are the main drawbacks of the approach. Thus, final cleaning process at a low voltage and current is recommended to mitigate these types of artefacts.

2.3. Application of Liquid-Cell Transmission Electron Microscopy (LC-TEM) in corrosion science

2.3.1. Instrumentation for in-situ LC-TEM. Towards practical liquid phase TEM studies, the recent technological advances have led to the development of dedicated microelectronic mechanical systems (MEMS) and TEM specimen holders [56]. In the contemporary designs, liquid cells are comprised of assembled top and bottom chips by which the liquid can be separated from the TEM column environment [57]. The electron-transparent windows (membranes) are usually made of amorphous Si_xN_y on silicon support substrates; the thickness of membranes usually varies from 20 to 50 nm to reach a balance between mechanical properties and imaging resolution [25]. As a key character that enables electrochemical measurements, Pt electrodes including working (WE), reference (RE) and

counter electrodes (CE) can be integrated onto the chips [40] (Fig. 2.3a). This provides a practical opportunity to apply anodic or cathodic potentials externally by a potentiostat [58]. In addition, a heating resistive pattern can also be designed on the chip to control the solution and sample temperature [59].

In practice, liquid cells (LCs) must be assembled manually in a way that rectangular windows overlap, allowing electron beam transmission through the LC. Si_xN_y membranes are usually hydrophobic as manufactured, repelling water to flow into the liquid cell. To make the membranes hydrophilic, the chips should be treated prior to assembling by either glow discharge or O_2 plasma cleaning. Such treatments are of additional benefit to get rid of carbon contaminations introduced during handling the specimens [55]. Spacers are patterned onto one of the chips to regulate the minimum distance between the top and bottom membranes; they are usually defined to be 150-500 nm tall. Despite the detailed design of the LCs, there will still be bulging of thin membranes when inserted into the high vacuum column, giving rise to higher water thickness than the desired spacing [60, 61]. The liquid cell needs to be leak-tight and this usually can be fulfilled either by gluing the cell or using sealing O-rings [62]. The assembled cell is placed on the specific TEM holder that can convey liquid to the inlet through a tubing system (Fig. 2.3b and c). To mitigate carbon deposition on the samples and membranes while illuminating the liquid cell, the solutions should be filtered to remove long hydrocarbon molecules in the solutions. In a prepared liquid cell loaded with a thin sample, the electron beam can readily travel through if the total path length is suitably short. In addition, a stagnant or flowing electrolyte is controlled by a syringe or pressure-based pump. Although the interaction of electrons with LC components can be used for dynamically recording and analysis of the specimen evolution with exposure, it might give rise to electrolyte radiolysis (Fig. 2.3d). In fact, the electron-beam effect is the main challenge of in-situ LC-TEM and must be well considered and understood to avoid any erroneous conclusion [53, 54, 63].

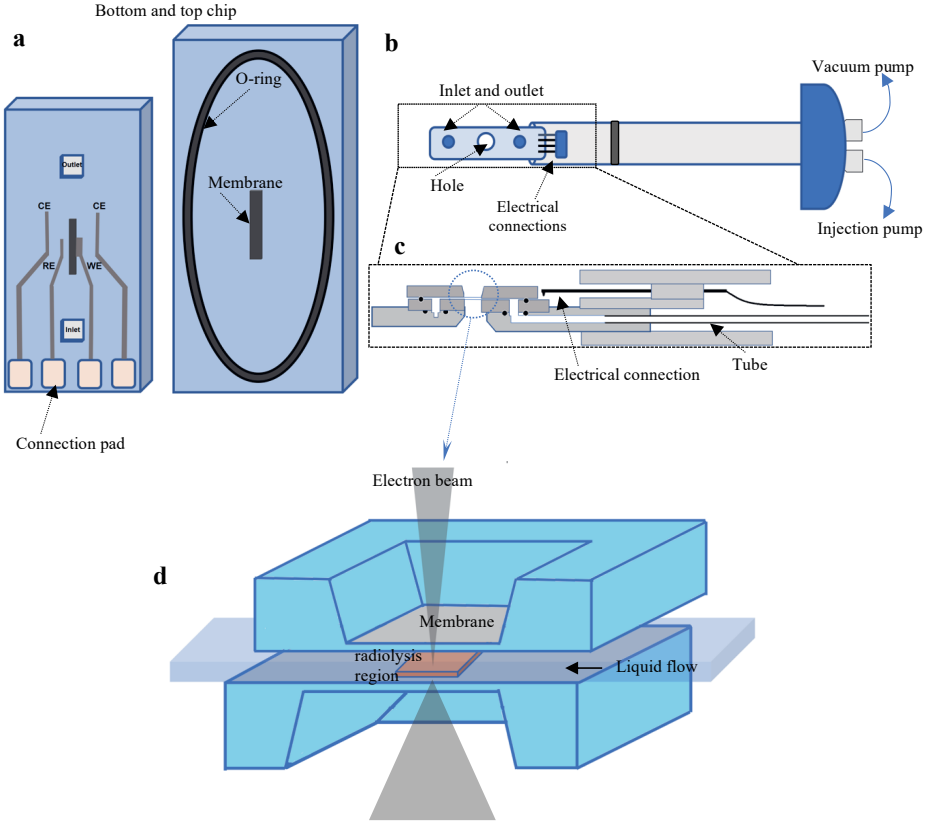


Fig. 2.3. (a) Schematic of bottom and top chip of a liquid cell for TEM. The Pt electrodes are patterned onto the chips to make electrochemical measurements in the liquid cell possible; counter electrode CE, reference electrode RE and working electrode WE. The rectangular membranes facilitate the alignment of the electron transparent windows when clamping them together. (b) A dedicated TEM holder with a specific tip to place the liquid cell (assembled bottom and top chips) and make electrical connections to the liquid cell. It consists of a tubing system, conveying electrolyte to run into the liquid cell through the inlet. A pressure difference between the inlet and outlet is applied by injection and vacuum pumps to have a controlled flow through the liquid cell. (c) Cross-sectional sketch of the holder tip loaded with a liquid cell. The inlet and outlet tubes go the entire distance from the injection pump to the other side of the holder, where they are attached to a vacuum pump; redrawn from Erdamar et al., [62] with permission from Springer Nature. (d) Cross-sectional view of a liquid cell loaded with a thin sample being irradiated (herein STEM mode). The incident beam can deposit energy into water which triggers radiolysis. Flowing the liquid can be an effective way to refresh the affected liquid.

2.3.2. Challenges of LC-TEM. Since the advent of the liquid phase TEM, image resolution and electron beam effect have been addressed as two major challenging factors [63, 64]. Furthermore, specimen preparation from the material to be studied and the transfer process can be considered as additional challenging issues during which the specimens are cut out of a 'region of interest' and positioned onto the fragile membranes.

2.3.2.1. Specimen preparation and transfer to liquid cells. One of the most crucial and time-consuming stages of the liquid cell setup is to delicately place a thin TEM specimen over the brittle windows

necessarily with a micron range precision. This should be done precisely otherwise even hairline damages to the membrane during transfer may lead to failure of the liquid cell during the operation in the high vacuum of a TEM column. As an added challenge, the overall thickness of specimens must fit within a 100-500 nm distance determined by spacers. Amongst conventional techniques, Ga^+ focused ion beam (FIB) preparation has been popular as thin specimens (lamellae) can selectively be fabricated out of 'regions of interest' in real bulk metals/alloys [65, 66]. In the case of liquid cells, a specific site is milled down to electron transparency. Next, the lamella is extracted from the trench and positioned on the chip either with ex-situ micro-manipulators under a light microscope, or with in-situ internal nano-manipulators installed on the FIB machines [67]. Reported as a drawback, Ga^+ ions can be implanted into the lamellae surface during ion sputtering and thinning; this phenomenon can induce structural and compositional surface modifications according to the primary ion-beam energy [67, 68]. Since corrosion initiation events are highly dependent on surface heterogeneities, a final cleaning process using a low-energy ion beam should be performed to mitigate Ga^+ ion impact and avoid probable erroneous conclusions. In addition, the Pt overlays, normally deposited to protect the top part of lamella from Ga damage, can be an issue when the specimen is in contact with an aqueous electrolyte, providing a galvanic couple with the region of interest.

Taking into account these concerns, a hybrid sample preparation procedure dedicated to liquid cells has recently been established [69, 70]. In this methodology, which is comprised of three basic steps, electropolished TEM thin-foil disks are initially prepared. Then, the region of interest is selected from an electron transparent area, followed by cutting it from the disk. Next, the plan-view section is lifted, positioned and finally fixed to the liquid cell using a FIB/SEM machine (see steps in Fig. 2.4). However, electropolished specimens are not recommended for corrosion studies as the samples undergo a pre-corrosion process during electropolishing, especially in the case of alloys prone to dealloying [71, 72]. As an alternative, argon ion-milled specimens are more favoured in LC-TEM corrosion studies.

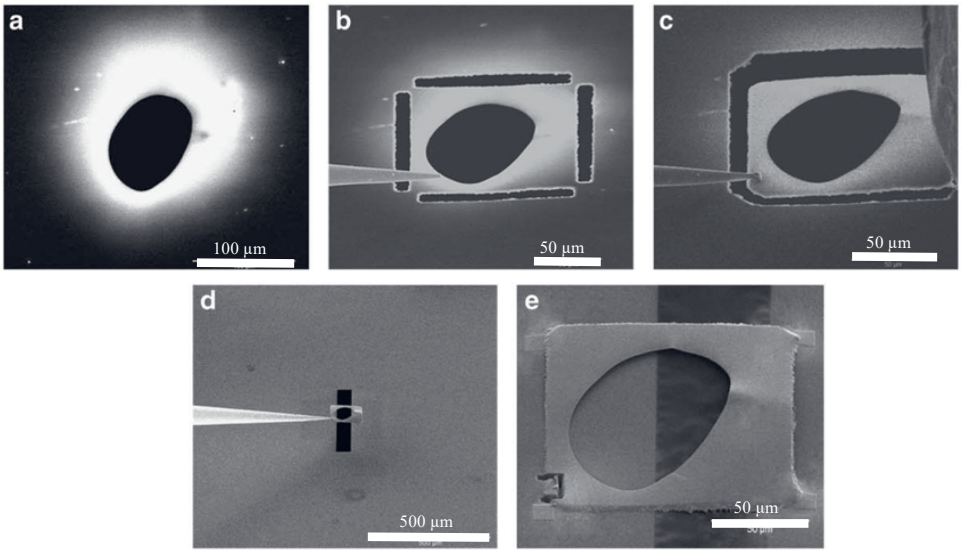


Fig. 2.4. Steps to cut and attach a thin specimen to the liquid cell (a) Dark-field STEM image showing the electron-transparent region on an electropolished disk (bright area), (b) cutting around the periphery of the transparent region, with corner attachments still in place. (c) Attaching the micromanipulator to the area of interest to be freed by milling off supporting material, (d) positioning the specimen above the window, (e) cutting off the micromanipulator and welding the specimen to the liquid cell by organometallic Pt deposition. Reprinted from Zhong et al., [69] with permission from Cambridge University Press.

2.3.2.2. Illumination modes and specimen configurations. Two illumination modes are available for in-situ LC-TEM corrosion studies: TEM and STEM. In both modalities, the image resolution is degraded by the multiple scattering of electrons in the liquid which depends strongly on the position of the specimen relative to the enclosing membranes of the LC [25, 64], although it is also limited by the specifications of the employed microscope like acceleration voltage, detectors, cameras, spherical and chromatic aberrations [55, 73-75]. Since the specimen must be attached to one of the membranes two possibilities exist: the specimen is positioned at the top or entrance membrane where the electron beam enters the LC, or the specimen is positioned at the bottom, or exit membrane. The dependency of image resolution for both imaging modes on these locations is called the top-bottom effect [52], and is illustrated in Fig. 2.5 for a corroded part of an AA2024-T3 alloy.

In TEM mode, a better resolution is achieved when the specimen is close to the beam exit side of the liquid cell (see Fig. 2.5a and b); the corrosion features and intermetallic phases are well distinguishable. The reason is that any further elastic scattering of electrons in the electrolyte between the exit membrane and the specimen generates additional blurring [25]. Thus, in TEM mode, the objects further from the exit side of the liquid layer are imaged with poorer resolution. Comparatively, in STEM mode, the highest resolution is acquired when the specimen is placed on the top chip (at the entrance side of the beam). In STEM mode, image resolution is highly determined by the probe diameter; however, the

beam progressively undergoes broadening while passing through the liquid cell as a result of multiple scattering [76]. For optimising an in-situ corrosion study, the specimen needs to be as bulk-like as possible, i.e., relatively thick samples are preferred. For such samples, STEM mode is reported to provide better quality of images than TEM, in particular, bright field STEM where beam broadening effect is less critical because of the detector characteristics [77]. In addition, annular dark field STEM, which, depending on the camera length, can be quite sensitive to differences in the atomic number (Z) of atoms and even diffraction contrasts within the specimen, has the benefit of showing Z-contrast and local thickness information more clearly. However, the spatial resolution is typically limited to the signal-to-noise ratio (SNR). This is observed in Fig. 2.5 in which dispersoids phases in AA2024-T3 matrix and localised attacks are well revealed with ADF-STEM. The detailed information about optimisation of the parameters like dose rate, detectors etc. for STEM imaging can be found in the recent paper published by De Jonge [77].

In contemporary liquid cells, the gap between the top and bottom chips is controlled by the height of the spacers. However, when the liquid cell is introduced into a high vacuum area, the pressure difference between the inside and the outside of the cell leads to an outward bowing of the membranes (bulging effect) [57]. As schematically depicted in Fig. 2.6a, the liquid thickness increases considerably from the edges towards the centre of the membrane, highly depending on the window width and membrane thickness. As an example, for 40-µm-wide membranes that are orthogonally oriented to each other and gapped with 500-nm-tall spacers, the bulging varies across the membrane from almost zero around the corners to approx. 500 nm in the centre [78]. It is worth noting that electron energy loss spectroscopy (EELS) enables to estimate the thickness of the liquid layer in terms of the mean free path based on the primary electron beam energy [79]. Thus, as a practical note, the lamella should be positioned close to the edges where the degree of bowing is smallest. Fig. 2.6b shows the spatial resolution in TEM and STEM to be strongly dependent of the liquid thickness; it is theoretically estimated for imaging Au nanoparticles [25]. According to the plot, the resolution in STEM is less dependent on the liquid thickness, as compared to TEM. This fact supports the STEM mode to be used in corrosion studies in which a wider range of possible electrolyte thicknesses is preferred to allow various and possibly varying realistic atmospheric corrosion conditions to be studied.

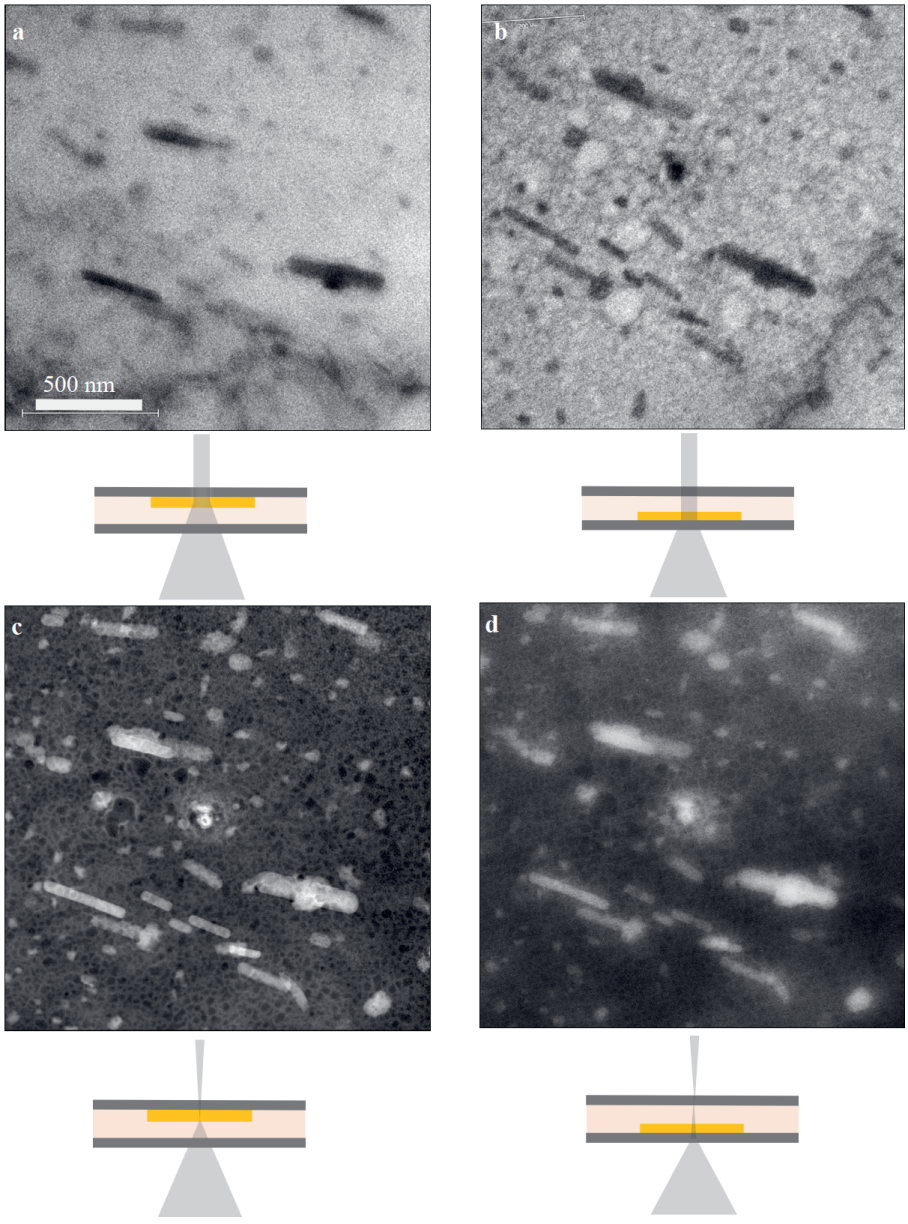


Fig. 2.5. Top–bottom effect on resolution in TEM and STEM imaging modes. The specimen is an approx. 200-nm-thick piece of AA2024-T3 corroded in 0.01 M NaCl for 1 hr. Images were recorded with liquid cell filled up with 1 bar air at 300 kV. The windows gap was about 700 nm, estimated by EELS. The thickness of top and bottom membranes was 60 nm. In TEM mode, the objective aperture was inserted. In STEM mode, an annular dark filed (ADF) detector (Camera length 185 mm) was used. (a) TEM image, the specimen at the entrance. (b) TEM image, the specimen at the exit. (c) STEM image, the specimen at the entrance. (d) STEM image, the specimen at the exit. Cross-sectional schematics illustrate the geometries applied.

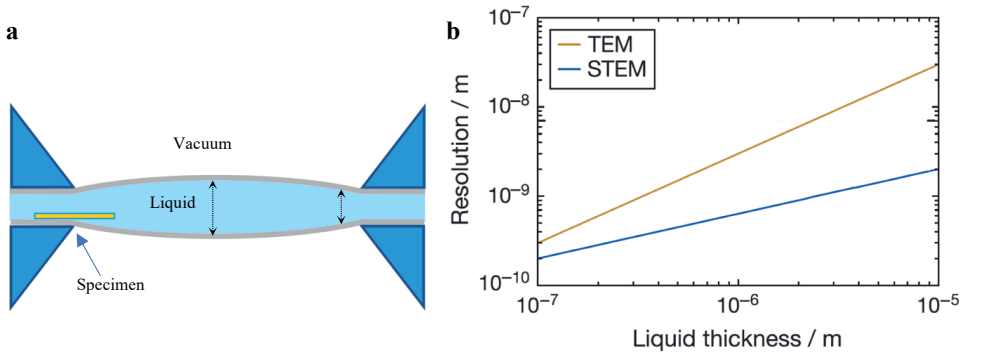


Fig. 2.6. (a) Schematic cross-section of a liquid cell placed in vacuum, showing bulging of the membranes which gives rise to a location-dependent liquid thickness. Therefore, TEM lamellae should be placed close to the edge of the window where bulging is minimum. (b) Maximum resolution versus thickness of water in TEM and STEM. The resolution is theoretically calculated for typical instrument parameters at 200 keV to image Au nanoparticles at the bottom of a layer of water for TEM, and at the top of the layer for STEM. Adapted from De Jonge and Ross [25] with permission from Springer Nature.

2.3.2.3. The effects of electron beam on solution chemistry. Radiolysis occurs when electrons travelling through a liquid cell interact with water molecules, delivering energy to the irradiated region mostly as a consequence of inelastic scattering of electrons [80]. While the transferred energy slightly heats the liquid cell, it may also convert water molecules and its constitutive atoms into various radical species like hydrated electrons eh^-, hydrogen radicals $H^\bullet$, hydroxyl radicals $OH^\bullet$ and more as follows [63]:

$$H_2O \rightarrow eh^-, H^\bullet, OH^\bullet, H_2, H_2O_2, H_3O^+, HO_2^\bullet$$

TEM and STEM imaging are performed typically at dose rates of 10^5–10^7 Gy s^{-1}, providing steady-state concentrations of the aqueous radicals [81, 82]. Therefore, the illuminated volume may suffer from a different local chemistry, in particular pH, highly dependent on the beam energy and intensities. For de-aerated water, the steady state pH is a function of dose rate and initial pH [82]. As shown in Fig. 2.7, the pH of the solution is less affected by irradiation at very low dose rates; acidic solutions do not or only at relatively high dose rates change their pH whereas alkaline solutions might get more acidic in the presence of the beam. Compared to aerated solutions, the electron beam can produce a slightly higher concentration of H^+ in initially moderate pH ($5 < pH < 9$) neutral solutions and almost equal in acidic and basic environments. In addition, other radicals are of particular importance since the hydrated electrons (eh^-) and the hydrogen radicals $H^\bullet$ as strong reducing species and hydroxyl radicals $OH^\bullet$ as strong oxidising agent can interact with the specimens [81]. Thus, it would be beneficial to deliberately add species that scavenge radicals, mitigating their impact on solution chemistry; a list of possible scavengers for various radicals are listed by Woehl and Abellan [81].

In TEM and STEM imaging modes, the electron beams pass the aqueous electrolyte in different configurations. In STEM illumination, point excitation occurs while rastering the focused electron probe over the liquid cell at each scan point, generating local radical concentrations highly dependent

on the pixel dwell time and magnification. In opposite, a broad static beam in TEM imaging continuously irradiates the specimen, typically delivering a higher cumulative dose rate than STEM. For quick dynamic processes, TEM imaging is capable of fast capturing although it often gives rise to bubbling [80]. Furthermore, the energy of the incident electrons can affect the delivered dose rate to the liquid cell; the higher accelerating voltages (i.e. 300 keV) are observed to create less radicals owing to lower electron stopping power in water [83]. In reality, the liquid cells are not uniform in terms of geometry and materials, thus there would be a spatial variation in dose rate due to a varying exchange of dose at the solid/liquid interface. In fact, secondary and backscattered electrons emitted out of the membranes and specimens, which have higher atomic number and density than water, can also contribute to the total dose rate. This phenomenon can increase the dose rate by several times within nanometric proximity of, for example, a water/electrode interface [84].

Regarding corrosion studies, the solution chemistry is of critical importance as it can modify dissolution events and passive surface layers. In fact, corrosion of many alloys is highly pH dependent; for instance, passive layers are undermined in acidic solutions where aggressive species like chloride may readily cause breakdown of the protective surface layers [37, 38, 85-87]. In addition, formation of species like $Cl^{\cdot}$, $Cl_2^{\cdot-}$ and $HClO^{\cdot-}$ [88] are plausible which add to other oxidising species like H_2O_2 and O_2 formed by water radiolysis, although Cl^- is reported to be $OH^{\bullet}$ and $H^{\bullet}$ scavenger in acidic solutions [81]. The electron beam effect is even more pronounced for corrosion inhibitor-containing solutions as some inhibitor molecules respond differently to pH variations where they can form local deposits over local anodes and cathodes [89]. For example, cerium-based compounds are known as cathodic inhibitors which can deposit a protective layer based on local alkalinity [90, 91]. On the other hand, inhibited systems with reducible species like cerium ions can undergo beam-induced deposition through reduction reactions with hydrated electrons or hydrogen radicals. In such systems, TEM mode imaging is preferred [92] as STEM illumination can generate a large local radical concentration by point excitation to the liquid at each scan point, providing a high local threshold electron dose for reduction nucleation [93]. Thus, the electron beam effect and imaging mode should be well considered otherwise the mechanisms observed would be misunderstood with LC-TEM. As a straightforward approach, lowering the dose rate can highly reduce the beam effect, however it induces noise on images and as a consequence a lower temporal resolution in LC-TEM. Noise in low-dose imaging is minimised with the new generation of imaging cameras and direct electron detectors, but can still reduce the spatial resolution, in particular for specimen-loaded liquid cells which are normally thick [75]. It should be noted that the spatial resolution in both TEM and STEM scales with dose rate to the power -1/4. It indicates that even slightly improved resolution would be at the expense of a huge rise of the electron dose, but on the other hand, a large decrease of the electron dose insignificantly affect the resolution [77].

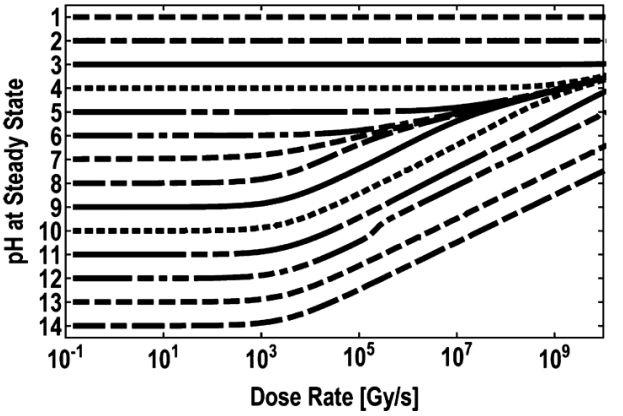


Fig. 2.7. Influence of initial pH prior to irradiation and dose rate on steady state pH of the radiated region. The values are theoretically calculated for de-aerated water. The gray per second (Gy/s) is defined as the absorption of one joule per kilogram of matter per unit time. Reprinted from Schneider et al., [82] with permission from American Chemical Society.

2.3.2.4. Electrochemical measurements in liquid cells. Nowadays, liquid cells for in-situ TEM are highly developed and can be linked to an external source like a potentiostat for biasing electrochemical reactions at electrode/electrolyte interface while the corresponding morphological evolutions are recorded [41]. The grounding configuration of the potentiostat and microscope is important to diminish noise within the system [94]. Electrochemical data recorded in a liquid cell can be affected by either the thin electrolyte or the electron beam [40]. The former giving rise to a potentially considerable ohmic-drop, and mass-controlled reactions should be managed by smart patterning of a platinum reference electrode quite close to the working electrode and flowing electrolyte, respectively [40]. However, the effect of the electron beam on the electrochemical processes is yet to be understood. Open circuit potential (OCP) measurements are reported to be largely influenced by the beam [94, 95]. Fig. 2.8b shows variations in the OCP of a Pt electrode recorded when the beam is intermittently blanked or de-blanked; it is excited up to 500mV in the stagnant solution. In comparison, the OCP of an austenitic stainless steel 0.001 M H_2SO_4 is almost unaffected by the beam, particularly when it is approaching the steady state (see Fig. 2.8c). In fact, the liquid cell configuration can function as a plate capacitor while an electrically conductive electrolyte allows for the exchange of charges, resulting in such behaviour; more information can be found in Ref [95]. Interestingly, hysteresis analysis of cyclic voltammetry curves has shown independency of the recorded currents in the presence of the STEM beam scanning over a glassy carbon electrode (see Fig. 2.8d) [96]. Furthermore, electrochemical impedance spectroscopy (EIS) has revealed the effect of mass-transfer on electrochemical reactions in the liquid cell. As can be seen in Fig. 2.8e, the low frequency loop related to mass-controlled events gets significantly smaller by increasing the flow rate [96].

The liquid cells are mainly designed for battery or electrodeposition applications which normally are conducted by inert working electrodes like Pt and Au. To conduct electrochemical corrosion evaluations, the alloy specimens need to be electrically connected to the electrode. Since both the specimen and the electrode are in contact with the electrolyte, galvanic coupling may influence and essentially fully disturb the corrosion mechanism and kinetics of the system. Moreover, quasi-Pt reference electrodes that are used in liquid cells have a potential highly dependent on the solution chemistry. Thus, before the in-situ LC-TEM measurement, potential measurements should be performed with respect to conventional reference electrodes in bulk-scale to calibrate the potential of the Pt reference electrode in a specific solution chemistry. However, the electron beam can still have an undesirable effect as the solution chemistry can be changed by the beam, causing modifications in the quasi-reference electrode potential which cannot be distinguished from real OCP evolutions of the specimen.

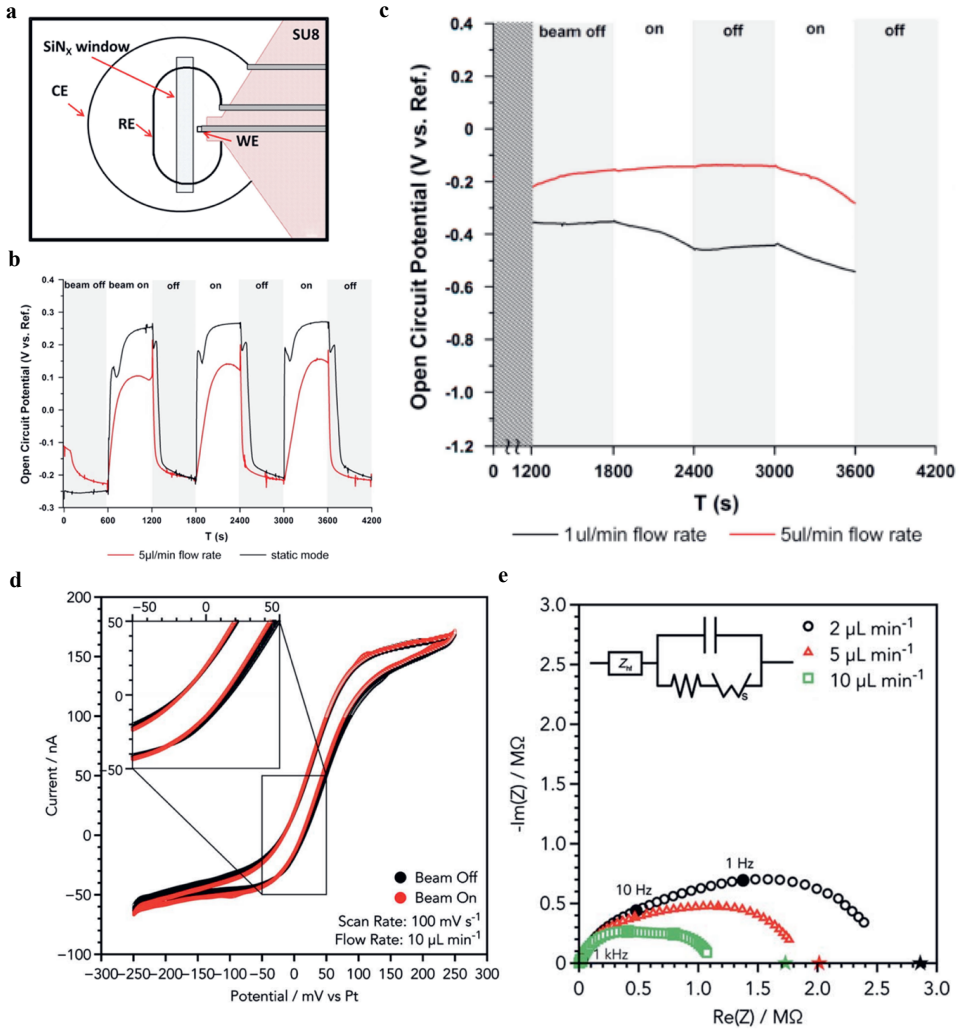


Fig. 2.8. Schematic top-view of a three-electrode configuration patterned on the chip. The working electrode (WE) is normally made of Pt or glassy carbon whereas the reference (RE) and counter (CE) electrodes are Pt. The similar configuration has been used for the experiments shown below. (b) Effect of electron beam on open circuit potential of a Pt electrode in aerated distilled water. (c) In-situ open circuit potential measurement of an austenitic stainless steel connected to a Pt electrode in 0.001M H_2SO_4. (a-c) are reprinted from Schilling et al., [95] with permission from Cambridge University Press. (d) Cyclic voltammetry of the $[Fe(CN)_6]^{4-}/Fe(CN)_6]^{3-}$ redox couple with the STEM beam on and beam off. STEM imaging has been done at 300 keV, giving electron dose of (154 e^-/nm^2 s). (e) Effect of flow rate on Nyquist plot of $[Fe(CN)_6]$ acquired with a glassy carbon WE at the constant potential of 0 V. (d, e) are reprinted from Unocic et al., [96] with permission from Cambridge University Press.

2.3.3. Recent achievements of LC-TEM in corrosion science. In recent years, the in-situ LC-TEM has been applied to a variety of research fields; corrosion is also one of the potential fields to take advantage

of this opportunity to unravel yet-to-be-resolved aspects in corrosion initiation and inhibition phenomena. Actually, this has just begun in 2013 by investigating localised corrosion of AA2024-T3, albeit in a vapor phase of a HCl/water mixture [97]. However, contemporary liquid cells and holders have paved the way to investigate many complicated corroding systems in liquid. Herein, state-of-the-art achievements of liquid cell TEM investigations in the field of corrosion studies are discussed.

2.3.3.1. In-situ liquid cell TEM corrosion of metal thin films. Preliminarily works in corrosion science have focused on corrosion of metal thin films due to simplicity of the system; the results of in-situ LC-TEM can be compared with bulk-scale findings [98-102]. In practice, thin films can directly be patterned with conventional techniques onto the chips or even further modified by ion implantations. Real-time morphological evaluations on Cu thin films exposed to a flowing NaCl solution have shown preferential dissolution of individual grains [100]. Preferential attacks to the grains, in particular, adjacent to an abnormally grown grain have been observed in Fe thin films [102]. Time-resolved TEM images, shown in Fig. 2.9a-f, reveal a high reactivity of grains with high surface area to volume ratio, while the large grain remains unaffected during 25 min exposure to 20% acetic acid. In another interesting study, Al thin films were biased to study their progressive morphological response to polarisation with in-situ LC-TEM. Illustrated in Fig. 2.9g-j, cathodic polarisation does not change the morphology while dissolution of individual grains, distinguished as dark regions, is observed in the anodic region of the curve. Recently, dissolution events of thin films are also studied at elevated solution temperatures [101]. Although, metal thin film studies can rarely mimic real-life corrosion of alloys, they are still beneficial to understand the beam impact on dissolution events and radiolysis of solutions with a complex chemistry.

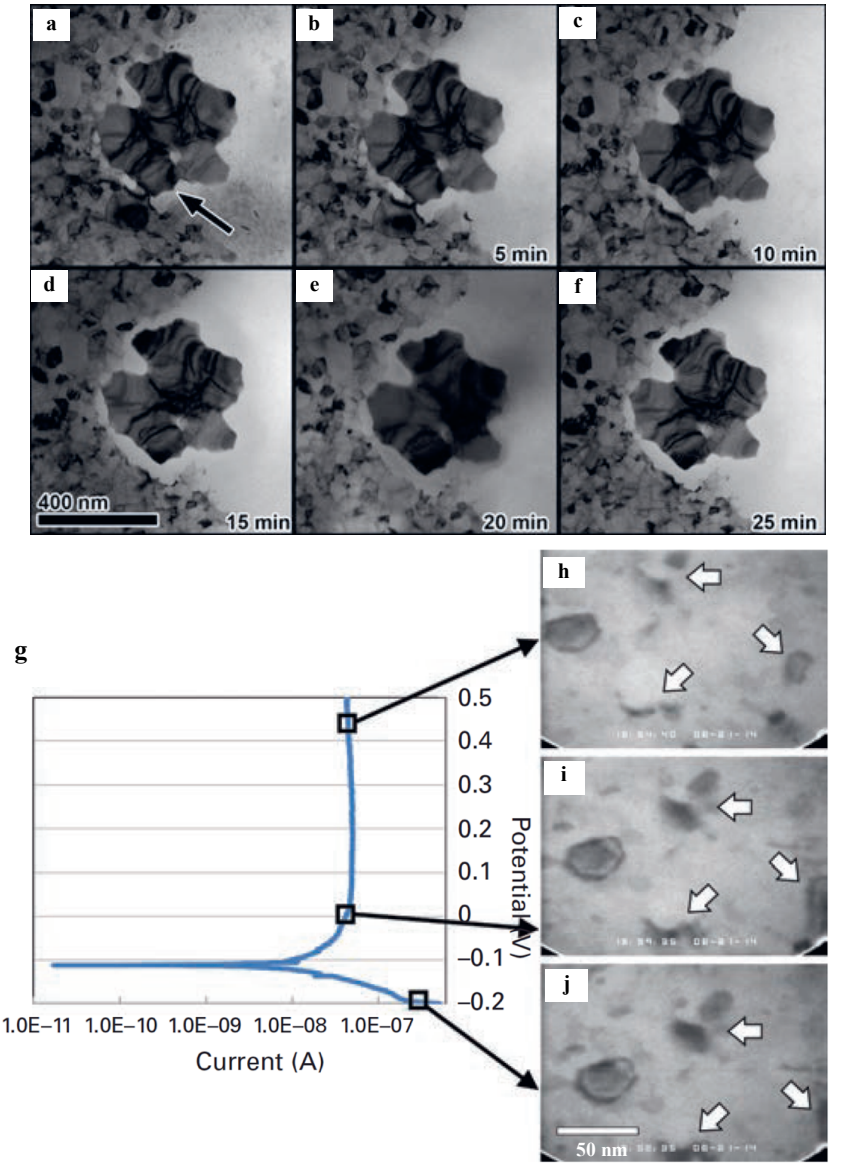


Fig. 2.9. (a-f) Time-resolved TEM images showing preferential dissolution of small grains, leaving the adjacent grown gain isolated. Reprinted from Gross et al., [102] with permission from John Wiley and Sons. (d) Polarization curve of an Al thin film (from -200 mV to 500 mV) in 0.1 M Na_2SO_4 and 0.001 M NaCl solution. (g-j) Snapshots of microstructural evolutions at different points of the curve revealing the dissolution of single grains (indicated with white arrows). Note that this is the second time that the sample has been polarized in the solution. Reprinted from Chee et al., [98] with permission from Cambridge University Press.

2.3.3.2. Analytical in-situ liquid TEM of austenitic stainless steel. Stainless steels are very resistive to uniform corrosion but highly susceptible to pitting corrosion [103]. MnS inclusions are mostly liable

for pit initiation by releasing sulphur species which can give rise to de-passivation in the presence of chloride [104-106]. Crevice formation at the edge of dissolving inclusions is proposed as a main mechanism of pit nucleation on stainless steels [107, 108]. Therefore, in-situ liquid TEM would be suitable to show evidence of dissolution of MnS inclusions that trigger breakdown of the passive film in chloride containing solutions. Although it is challenging to observe the passive film on a stainless steel in the liquid phase due to limited resolution, progressive dissolution around the inclusions can clearly be observed. In recent years, electrochemical liquid cells equipped with a resistive heater were also developed to investigate pitting corrosion of modern stainless steels with a high pitting potential and critical pitting temperature (CPT) [109].

In a recent study, thin pieces of type 304 stainless steel containing MnS inclusions have been studied with in-situ LC-TEM. Initial chemical and morphological characterizations have been done in 1 bar air, followed by exposing to distilled water for 24 h [95]. Fig. 2.10 shows that the dissolution of a specific MnS inclusion takes place as an initial corrosion event whereas no dissolution of the steel has been observed because of the absence of chloride. However, direct evidence still needs to be provided with in-situ LC-TEM showing an MnS inclusion to induce active dissolution at the adjacent passive region.

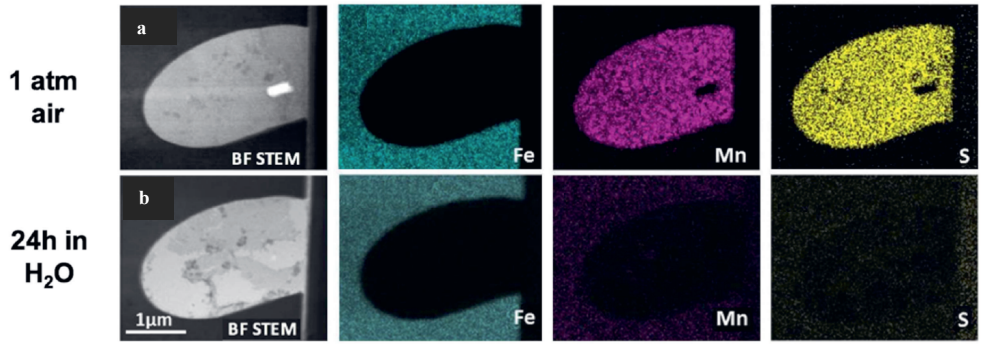


Fig. 2.10. Bright filed STEM images together with EDS maps of type 304 stainless steel revealing dissolution of a MnS inclusion after 24 h in flowing deionised H_2O at the room temperature. Adapted from Schilling et al., [95] with permission from Cambridge University Press.

2.3.3.3. Corrosion of low-carbon steel at the nanoscale. Corrosion of plain steel in oil and gas industry is a challenging concern as premature failure occasionally happens due to localized attack highly dependent on the environment [110, 111]. Having studied generally with ex-situ evaluations, insights into dynamic nanoscopic phenomena at heterogeneities are essential to establish models that can fully predict all the uniform and non-uniform corrosion processes [112-114]. In a very interesting paper, it has been shown with in-situ LC-TEM that initiation events can take place at triple junctions formed by cementite confined by ferrite grains [115]. Time-resolved bright field STEM has shown that local dissolution progressively propagates along the cementite/ferrite interface (see Fig. 2.11b-e) while no

further evolution of localised corrosion has been observed during short term exposure. The amount of uniform corrosion in steel has also been evaluated in the lamella before and after exposure to the electrolyte (see Fig. 2.11g and h). Post-corrosion analysis has been conducted by mapping the relative thickness via an EF-TEM approach, revealing selective dissolution of ferrite neighbouring cementite (Fig. 2.11i). Further support for determining the type of corrosion products has been obtained by EELS analysis, suggesting formation of iron oxide over ferrite grains [115].

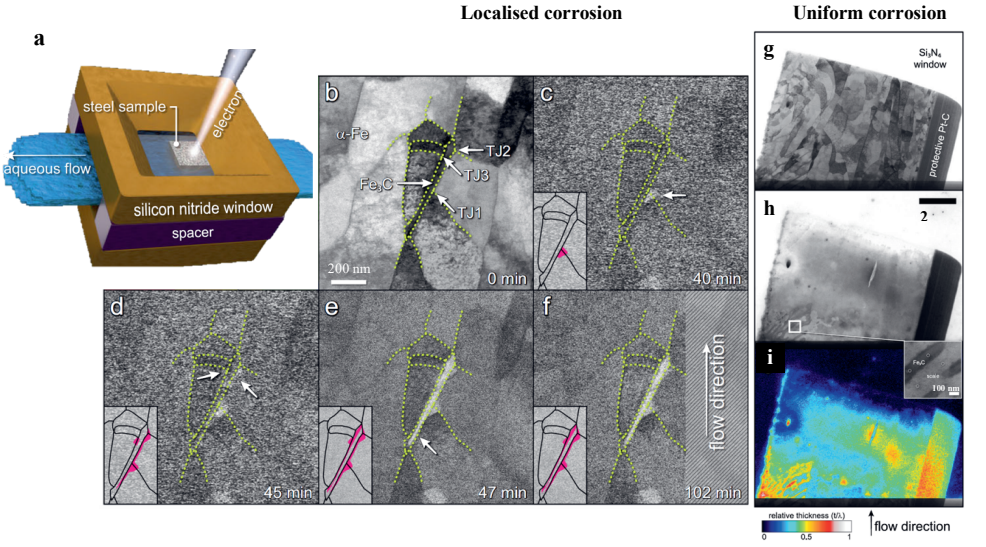


Fig. 2.11. (a) Schematic of the liquid cell loaded with a 1018 steel lamella. (b) Bright field STEM image of a region that was microstructurally and chemically characterized before exposure to 2.78 µM Na_2SO_4 solution. A cementite grain inclusion fully confined by a ferrite matrix and different triple junctions TJ1, TJ2, and TJ3 indicated by white arrows. (c–f) Time-resolved bright field STEM images of the region during exposure to the flowing solution. Having initiated at TJ1, localized corrosion took place in the 1018 steel sample at the phase boundary between ferrite and cementite. (g-i) Concurrent occurrence of uniform corrosion revealed by bright field STEM micrograph of the lamella (g) before, and (h) after 1025 min exposure. (i) Energy filtered TEM to relatively map the thickness of the corroded specimen. Reproduced from Hayden et al., [115] with permission from Springer Nature. The images were originally published as parts of three distinct figures.

2.4. Conclusions

Promising and exciting years are ahead of us in corrosion science with the rise and availability of in-situ liquid cell TEM to explore many complicated corroding systems. Real thin specimens can be prepared with FIB/SEM techniques or hybrid approaches. However, artefacts like Ga damage which can change the chemical composition of the specimens might be introduced into the system during sample preparation and handling; proper approaches must be selected to alleviate their impact. The specimens can partly be masked with inert materials to restrict corrosion processes to the field of view. Both TEM and STEM can be used in liquid cell imaging; the STEM operation mode is preferred for

thick liquid cells whereas the TEM mode provides higher frame rates in imaging videos. When an electrolyte is introduced in the liquid cell, both the resolution and image contrast are considerably decreased; its effect can largely be reduced with a favourable sample position in the LC corresponding to either imaging mode. Minimising the effect of the electron beam on solution chemistry is crucial to reduce its effect on the corrosion mechanisms and kinetics, in particular for complex solutions. As a direct result of irradiation at high dose rates, the formation of oxidising radiolytic species might change the solution pH and thus modify the nature and kinetics of corrosion events. In addition, for NaCl solutions, species like $Cl^{\bullet}$, $Cl_2^{\bullet-}$ and $HClO^{\bullet-}$ are possibly formed by radiolysis; therefore, running beam-off experiments, in parallel, is needed to study possible beam influences. The beam effect can be highly diminished by conducting low-dose rate imaging or flowing electrolyte experiments but at the expense of image resolution and corrosion-induced local chemistry, respectively. To conduct electrochemical measurements in liquid cells, alloy specimens must be in contact with noble electrodes like Pt where galvanic corrosion would highly be plausible at contact locations. This requires the design of electrochemical chips with the specific application of corrosion science in mind. Moreover, the potential of quasi-Pt reference electrodes is highly dependent on the solution chemistry. They should be patterned away from the irradiated region; however, this would give rise to a higher ohmic drop. Analytical TEM characterisations with EDS and EELS can be done on the post-corroded specimens to gain insights into the type of corrosion products. In the case of uniform corrosion, no significant contrast variation is seen, thus post EF-TEM analysis would be helpful to observe thickness reductions due to the metal dissolution.

In-situ liquid cell TEM has the potential to be applied in a wide range of corrosion studies, however, thickness limitations of specimens make it more appropriate for studying early-stage corrosion phenomena. Pitting in many alloy systems like stainless steels, aluminium, titanium and copper alloys are yet to be either understood or evidenced directly to establish mechanisms well explaining the initiation processes. LC-TEM can be utilised to link morphological evolutions and electrochemical responses caused by corrosion. For instance, in an electrochemical liquid cell, morphological changes as a consequence of local attack can produce transient currents that can be recorded externally with a potentiostat. Thus, in-situ LC-TEM, granting a good temporal and spatial resolution can discriminate between stable and metastable processes. In the current stage, it is possible to conduct electrochemical and morphological evaluations of corrosion at desired temperatures. In the future with ongoing technological advancements, it might be even practical to do complicated corrosion studies like mechanically influenced corrosion such as stress corrosion cracking within the liquid cell while beam effects are highly avoided.

References

[1] J.R. Scully, Future Frontiers in Corrosion Science and Engineering, Part I, in, NACE International, 2018.
[2] J.R. Scully, Future Frontiers in Corrosion Science and Engineering, Part II: Managing the Many Stages of Corrosion, in, NACE International, 2019.
[3] V. Maurice, P. Marcus, Progress in corrosion science at atomic and nanometric scales, Progress in Materials Science, 95 (2018) 132-171.
[4] R. Parvizi, M.Y. Tan, A.E. Hughes, Recent Insights Into Corrosion Initiation at the Nanoscale, in: Fundamentals of Aluminium Metallurgy, Elsevier, 2018, pp. 525-551.
[5] F. Renner, A. Stierle, H. Dosch, D. Kolb, T.-L. Lee, J. Zegenhagen, Initial corrosion observed on the atomic scale, Nature, 439 (2006) 707.
[6] N. Badwe, X. Chen, D.K. Schreiber, M.J. Olszta, N.R. Overman, E. Karasz, A. Tse, S.M. Bruemmer, K. Sieradzki, Decoupling the role of stress and corrosion in the intergranular cracking of noble-metal alloys, Nature materials, 17 (2018) 887-893.
[7] M. Bettayeb, V. Maurice, L.H. Klein, L. Lapeire, K. Verbeken, P. Marcus, Combined in situ microstructural study of the relationships between local grain boundary structure and passivation on microcrystalline copper, Electrochimica Acta, (2019).
[8] R. Parvizi, A.E. Hughes, M.Y. Tan, R.K. Marceau, M. Forsyth, P. Cizek, A.M. Glenn, Probing corrosion initiation at interfacial nanostructures of AA2024-T3, Corrosion Science, 116 (2017) 98-109.
[9] D.B. Williams, C.B. Carter, The transmission electron microscope, in: Transmission electron microscopy, Springer, 1996, pp. 3-17.
[10] E. Hamada, K. Yamada, M. Nagoshi, N. Makiishi, K. Sato, T. Ishii, K. Fukuda, S. Ishikawa, T. Ujiro, Direct imaging of native passive film on stainless steel by aberration corrected STEM, Corrosion Science, 52 (2010) 3851-3854.
[11] S. Malladi, Q. Xu, F. Tichelaar, H. Zandbergen, F. Hannour, J. Mol, H. Terryn, Early stages during localized corrosion of AA2024 TEM specimens in chloride environment, Surface and Interface Analysis, 45 (2013) 1619-1625.
[12] K. Oh, S. Ahn, K. Eom, K. Jung, H. Kwon, Observation of passive films on Fe–20Cr–xNi (x= 0, 10, 20 wt.%) alloys using TEM and Cs-corrected STEM–EELS, Corrosion Science, 79 (2014) 34-40.
[13] R.P. Wei, C.-M. Liao, M. Gao, A transmission electron microscopy study of constituent-particle-induced corrosion in 7075-T6 and 2024-T3 aluminum alloys, Metallurgical and Materials Transactions A, 29 (1998) 1153-1160.
[14] B. Zhang, J. Wang, B. Wu, X. Guo, Y. Wang, D. Chen, Y. Zhang, K. Du, E. Oguzie, X. Ma, Unmasking chloride attack on the passive film of metals, Nature communications, 9 (2018) 2559.
[15] D. Sun, Y. Jiang, Q. Xiang, C. Zhong, J. Gong, L. Zhang, J. Li, Ex situ TEM observation of localized attack on AA 6061, Materials and corrosion, 61 (2010) 105-110.
[16] Y. Zhou, Y. Wang, S. Zheng, B. Zhang, X. Ma, Strain-induced preferential dissolution at the dislocation emergences in MnS: an atomic scale study, Philosophical Magazine, 95 (2015) 2365-2375.
[17] S. Persaud, S. Ramamurthy, A. Korinek, G. Botton, R. Newman, The influence of the high Fe and Cr contents of Alloy 800 on its inter-and intragranular oxidation tendency in 480° C hydrogenated steam, Corrosion Science, 106 (2016) 117-126.
[18] S. Persaud, J. Smith, A. Korinek, G. Botton, R. Newman, High resolution analysis of oxidation in Ni-Fe-Cr alloys after exposure to 315° C deaerated water with added hydrogen, Corrosion Science, 106 (2016) 236-248.
[19] S. Kairy, P. Rometsch, C. Davies, N. Birbilis, On the electrochemical and quasi in situ corrosion response of the Q-phase (AlxCuyMgzSiw) intermetallic particle in 6xxx series aluminum alloys, Corrosion, 73 (2016) 87-99.
[20] S. Malladi, F. Tichelaar, Q. Xu, M. Wu, H. Terryn, J. Mol, F. Hannour, H. Zandbergen, Quasi in situ analytical TEM to investigate electrochemically induced microstructural changes in alloys: AA2024-T3 as an example, Corrosion Science, 69 (2013) 221-225.
[21] B. Zhang, X. Ma, A review-pitting corrosion initiation investigated by TEM, Journal of Materials Science & Technology, (2019).

[22] B. Zhang, J. Wang, B. Wu, Y. Zhou, X. Ma, Quasi-in-situ ex-polarized TEM observation on dissolution of MnS inclusions and metastable pitting of austenitic stainless steel, Corrosion Science, 100 (2015) 295-305.
[23] Y. Zhang, P. Gore, W. Rong, Y. Wu, Y. Yan, R. Zhang, L. Peng, J.-F. Nie, N. Birbilis, Quasi-in-situ STEM-EDS insight into the role of Ag in the corrosion behaviour of Mg-Gd-Zr alloys, Corrosion Science, 136 (2018) 106-118.
[24] A. Glenn, A. Hughes, T. Muster, D. Lau, N. Wilson, A. Torpy, C. MacRae, J. Ward, Investigation into the influence of carbon contamination on the corrosion behavior of aluminum microelectrodes and AA2024-T3, Journal of The Electrochemical Society, 160 (2013) C119-C127.
[25] N. De Jonge, F.M. Ross, Electron microscopy of specimens in liquid, Nature nanotechnology, 6 (2011) 695.
[26] K.L. Klein, I.M. Anderson, N. De Jonge, Transmission electron microscopy with a liquid flow cell, Journal of microscopy, 242 (2011) 117-123.
[27] H.-G. Liao, H. Zheng, Liquid cell transmission electron microscopy, Annual review of physical chemistry, 67 (2016) 719-747.
[28] M. Williamson, R. Tromp, P. Vereecken, R. Hull, F. Ross, Dynamic microscopy of nanoscale cluster growth at the solid–liquid interface, Nature materials, 2 (2003) 532.
[29] K. Jungjohann, C.B. Carter, In situ and operando, in: Transmission Electron Microscopy, Springer, 2016, pp. 17-80.
[30] J.E. Evans, K.L. Jungjohann, N.D. Browning, I. Arslan, Controlled growth of nanoparticles from solution with in situ liquid transmission electron microscopy, Nano letters, 11 (2011) 2809-2813.
[31] M. Tanase, J. Winterstein, R. Sharma, V. Aksyuk, G. Holland, J.A. Liddle, High-resolution imaging and spectroscopy at high pressure: A novel liquid cell for the transmission electron microscope, Microscopy and Microanalysis, 21 (2015) 1629-1638.
[32] E.R. White, S.B. Singer, V. Augustyn, W.A. Hubbard, M. Mecklenburg, B. Dunn, B.C. Regan, In situ transmission electron microscopy of lead dendrites and lead ions in aqueous solution, Acs Nano, 6 (2012) 6308-6317.
[33] T. Xu, L. Sun, Investigation on material behavior in liquid by in situ TEM, Superlattices and Microstructures, 99 (2016) 24-34.
[34] M.R. Hauwiller, X. Zhang, W.-I. Liang, C.-H. Chiu, Q. Zhang, W. Zheng, C. Ophus, E.M. Chan, C. Czarnik, M. Pan, Dynamics of Nanoscale Dendrite Formation in Solution Growth Revealed Through in Situ Liquid Cell Electron Microscopy, Nano letters, 18 (2018) 6427-6433.
[35] G. Burstein, C. Liu, R. Souto, S. Vines, Origins of pitting corrosion, Corrosion Engineering, Science and Technology, 39 (2004) 25-30.
[36] N. Casillas, S. Charlebois, W.H. Smyrl, H.S. White, Pitting corrosion of titanium, Journal of the Electrochemical Society, 141 (1994) 636-642.
[37] G. Frankel, Pitting corrosion of metals a review of the critical factors, Journal of the Electrochemical Society, 145 (1998) 2186-2198.
[38] Z. Szklarska-Smialowska, Pitting corrosion of aluminum, Corrosion science, 41 (1999) 1743-1767.
[39] G.L. Song, A. Atrens, Corrosion mechanisms of magnesium alloys, Advanced engineering materials, 1 (1999) 11-33.
[40] F.M. Ross, Quantifying Electrochemical Processes Using Liquid Cell TEM, in: F.M. Ross (Ed.) Liquid Cell Electron Microscopy, Cambridge University Press, Cambridge, 2016, pp. 210-236.
[41] B.L. Mehdi, J. Qian, E. Nasybulin, C. Park, D.A. Welch, R. Faller, H. Mehta, W.A. Henderson, W. Xu, C.M. Wang, Observation and quantification of nanoscale processes in lithium batteries by operando electrochemical (S) TEM, Nano letters, 15 (2015) 2168-2173.
[42] A. Radisic, P.M. Vereecken, J.B. Hannon, P.C. Searson, F.M. Ross, Quantifying electrochemical nucleation and growth of nanoscale clusters using real-time kinetic data, Nano Letters, 6 (2006) 238-242.
[43] J.H. Park, N.M. Schneider, D.A. Steingart, H. Deligianni, S. Kodambaka, F.M. Ross, Control of Growth Front Evolution by Bi Additives during ZnAu Electrodeposition, Nano letters, 18 (2018) 1093-1098.
[44] M. Moayed, R. Newman, Evolution of current transients and morphology of metastable and stable pitting on stainless steel near the critical pitting temperature, Corrosion science, 48 (2006) 1004-1018.

[45] P. Pistorius, G. Burstein, Metastable pitting corrosion of stainless steel and the transition to stability, Philosophical Transactions of the Royal Society of London. Series A: Physical and Engineering Sciences, 341 (1992) 531-559.
[46] S. Pride, J. Scully, J. Hudson, Metastable pitting of aluminum and criteria for the transition to stable pit growth, Journal of the Electrochemical Society, 141 (1994) 3028-3040.
[47] G. Frankel, L. Stockert, F. Hunkeler, H. Boehni, Metastable pitting of stainless steel, Corrosion, 43 (1987) 429-436.
[48] S. Virtanen, C. Curty, Metastable and stable pitting corrosion of titanium in halide solutions, Corrosion, 60 (2004) 643-649.
[49] Y. Tang, Y. Zuo, J. Wang, X. Zhao, B. Niu, B. Lin, The metastable pitting potential and its relation to the pitting potential for four materials in chloride solutions, Corrosion Science, 80 (2014) 111-119.
[50] N. Birbilis, R.G. Buchheit, Electrochemical characteristics of intermetallic phases in aluminum alloys an experimental survey and discussion, Journal of The Electrochemical Society, 152 (2005) B140-B151.
[51] N. Birbilis, Y. Zhu, S. Kairy, M. Glenn, J.-F. Nie, A. Morton, Y. Gonzalez-Garcia, H. Terryn, J. Mol, A. Hughes, A closer look at constituent induced localised corrosion in Al-Cu-Mg alloys, Corrosion Science, 113 (2016) 160-171.
[52] L.R. Parent, E. Bakalis, M. Proetto, Y. Li, C. Park, F. Zerbetto, N.C. Gianneschi, Tackling the challenges of dynamic experiments using liquid-cell transmission electron microscopy, Accounts of chemical research, 51 (2017) 3-11.
[53] N. Hodnik, G. Dehm, K.J. Mayrhofer, Importance and challenges of electrochemical in situ liquid cell electron microscopy for energy conversion research, Accounts of chemical research, 49 (2016) 2015-2022.
[54] F.M. Ross, Opportunities and challenges in liquid cell electron microscopy, Science, 350 (2015) aaa9886.
[55] T.J. Woehl, K.L. Jungjohann, J.E. Evans, I. Arslan, W.D. Ristenpart, N.D. Browning, Experimental procedures to mitigate electron beam induced artifacts during in situ fluid imaging of nanomaterials, Ultramicroscopy, 127 (2013) 53-63.
[56] N. de Jonge, F.M. Ross, Past, Present, and Future Electron Microscopy of Liquid Specimens, in: F.M. Ross (Ed.) Liquid Cell Electron Microscopy, Cambridge University Press, Cambridge, 2016, pp. 3-34.
[57] E. Jensen, K. Mølhave, Encapsulated Liquid Cells for Transmission Electron Microscopy, in: F.M. Ross (Ed.) Liquid Cell Electron Microscopy, Cambridge University Press, Cambridge, 2016, pp. 35-55.
[58] A.J. Leenheer, J.P. Sullivan, M.J. Shaw, C.T. Harris, A Sealed Liquid Cell forIn SituTransmission Electron Microscopy of Controlled Electrochemical Processes, Journal of Microelectromechanical Systems, 24 (2015) 1061-1068.
[59] M. Denoual, V. Menon, T. Sato, O. De Sagazan, A. Coleman, H. Fujita, Liquid cell with temperature control for in situ TEM chemical studies, Measurement Science and Technology, 30 (2018) 017001.
[60] J. Yang, O. Paul, Fracture properties of LPCVD silicon nitride thin films from the load–deflection of long membranes, Sensors and Actuators A: Physical, 97 (2002) 520-526.
[61] T. Alan, J. Gaspar, O. Paul, H.W. Zandbergen, F. Creemer, P.M. Sarro, Characterization of ultrathin membranes to enable TEM observation of gas reactions at high pressures, in: ASME 2009 International Mechanical Engineering Congress and Exposition, American Society of Mechanical Engineers, 2009, pp. 327-331.
[62] A. Erdamar, S. Malladi, F. Tichelaar, H. Zandbergen, Closed cell systems for in situ TEM with gas environments ranging from 0.1 to 5 bar, in: Controlled Atmosphere Transmission Electron Microscopy, Springer, 2016, pp. 165-210.
[63] N.M. Schneider, Electron Beam Effects in Liquid Cell TEM and STEM, in: F.M. Ross (Ed.) Liquid Cell Electron Microscopy, Cambridge University Press, Cambridge, 2016, pp. 140-163.
[64] N. de Jonge, N.D. Browning, J.E. Evans, S.W. Chee, F.M. Ross, Resolution in Liquid Cell Experiments, in: F.M. Ross (Ed.) Liquid Cell Electron Microscopy, Cambridge University Press, Cambridge, 2016, pp. 164-188.

[65] L.A. Giannuzzi, F.A. Stevie, A review of focused ion beam milling techniques for TEM specimen preparation, Micron, 30 (1999) 197-204.
[66] M. Schaffer, B. Schaffer, Q. Ramasse, Sample preparation for atomic-resolution STEM at low voltages by FIB, Ultramicroscopy, 114 (2012) 62-71.
[67] J. Mayer, L.A. Giannuzzi, T. Kamino, J. Michael, TEM sample preparation and FIB-induced damage, MRS bulletin, 32 (2007) 400-407.
[68] K.A. Unocic, M.J. Mills, G. Daehn, Effect of gallium focused ion beam milling on preparation of aluminium thin foils, Journal of microscopy, 240 (2010) 227-238.
[69] X.L. Zhong, S. Schilling, N.J. Zaluzec, M.G. Burke, Sample preparation methodologies for in situ liquid and gaseous cell analytical transmission electron microscopy of electropolished specimens, Microscopy and Microanalysis, 22 (2016) 1350-1359.
[70] X. Zhong, M. Burke, S. Schilling, S. Haigh, N. Zaluzec, Novel hybrid sample preparation method for in situ liquid cell TEM analysis, Microscopy and Microanalysis, 20 (2014) 1514-1515.
[71] S.-J. Lee, J.-J. Lai, The effects of electropolishing (EP) process parameters on corrosion resistance of 316L stainless steel, Journal of Materials Processing Technology, 140 (2003) 206-210.
[72] M. Yu, J. Yi, J. Liu, S. Li, G. Wu, L. Wu, Effect of electropolishing on electrochemical behaviours of titanium alloy Ti-10V-2Fe-3Al, Journal of Wuhan University of Technology-Mater. Sci. Ed., 26 (2011) 469-477.
[73] N. de Jonge, L. Houben, R.E. Dunin-Borkowski, F.M. Ross, Resolution and aberration correction in liquid cell transmission electron microscopy, Nature Reviews Materials, (2018) 1.
[74] N. De Jonge, D.B. Peckys, G. Kremers, D. Piston, Electron microscopy of whole cells in liquid with nanometer resolution, Proceedings of the National Academy of Sciences, 106 (2009) 2159-2164.
[75] N.D. Browning, J.E. Evans, The Potential for Imaging Dynamic Processes in Liquids with High Temporal Resolution, in: F.M. Ross (Ed.) Liquid Cell Electron Microscopy, Cambridge University Press, Cambridge, 2016, pp. 456-475.
[76] R. Ramachandra, H. Demers, N. de Jonge, The influence of the sample thickness on the lateral and axial resolution of aberration-corrected scanning transmission electron microscopy, Microscopy and microanalysis, 19 (2013) 93-101.
[77] N. de Jonge, Theory of the spatial resolution of (scanning) transmission electron microscopy in liquid water or ice layers, Ultramicroscopy, 187 (2018) 113-125.
[78] M.E. Holtz, Y. Yu, J. Gao, H.D. Abruña, D.A. Muller, In situ electron energy-loss spectroscopy in liquids, Microscopy and Microanalysis, 19 (2013) 1027-1035.
[79] R.F. Egerton, Electron energy-loss spectroscopy in the electron microscope, Springer Science & Business Media, 2011.
[80] J.M. Grogan, N.M. Schneider, F.M. Ross, H.H. Bau, Bubble and pattern formation in liquid induced by an electron beam, Nano letters, 14 (2013) 359-364.
[81] T. Woehl, P. Abellan, Defining the radiation chemistry during liquid cell electron microscopy to enable visualization of nanomaterial growth and degradation dynamics, Journal of microscopy, 265 (2017) 135-147.
[82] N.M. Schneider, M.M. Norton, B.J. Mendel, J.M. Grogan, F.M. Ross, H.H. Bau, Electron–water interactions and implications for liquid cell electron microscopy, The Journal of Physical Chemistry C, 118 (2014) 22373-22382.
[83] P. Abellan, T. Woehl, L. Parent, N. Browning, J. Evans, I. Arslan, Factors influencing quantitative liquid (scanning) transmission electron microscopy, Chemical Communications, 50 (2014) 4873-4880.
[84] T. Gupta, N.M. Schneider, J.H. Park, D. Steingart, F.M. Ross, Spatially dependent dose rate in liquid cell transmission electron microscopy, Nanoscale, 10 (2018) 7702-7710.
[85] B. Zaid, D. Saidi, A. Benzaid, S. Hadji, Effects of pH and chloride concentration on pitting corrosion of AA6061 aluminum alloy, Corrosion Science, 50 (2008) 1841-1847.
[86] N. Schiff, B. Grosgogeat, M. Lissac, F. Dalard, Influence of fluoride content and pH on the corrosion resistance of titanium and its alloys, Biomaterials, 23 (2002) 1995-2002.
[87] Y. Feng, K.-S. Siow, W.-K. Teo, K.-L. Tan, A.-K. Hsieh, Corrosion mechanisms and products of copper in aqueous solutions at various pH values, Corrosion, 53 (1997) 389-398.
[88] E. Atinault, V. De Waele, U. Schmidhammer, M. Fattahi, M. Mostafavi, Scavenging of es− and OH radicals in concentrated HCl and NaCl aqueous solutions, Chemical Physics Letters, 460 (2008) 461-465.

[89] S. Garcia, T. Markley, J. Mol, A. Hughes, Unravelling the corrosion inhibition mechanisms of bi-functional inhibitors by EIS and SEM–EDS, Corrosion Science, 69 (2013) 346-358.
[90] A. Hughes, T. Markley, S. Garcia, J. Mol, Comparative study of protection of AA 2024-T3 exposed to rare earth salts solutions, Corrosion Engineering, Science and Technology, 49 (2014) 674-687.
[91] K.A. Yasakau, M.L. Zheludkevich, S.V. Lamaka, M.G. Ferreira, Mechanism of corrosion inhibition of AA2024 by rare-earth compounds, The Journal of Physical Chemistry B, 110 (2006) 5515-5528.
[92] M.S.A. Asghar, B.J. Inkson, G. Möbus, Giant Radiolytic Dissolution Rates of Aqueous Ceria Observed in Situ by Liquid-Cell TEM, ChemPhysChem, 18 (2017) 1247-1251.
[93] T.J. Woehl, J.E. Evans, I. Arslan, W.D. Ristenpart, N.D. Browning, Direct in situ determination of the mechanisms controlling nanoparticle nucleation and growth, ACS nano, 6 (2012) 8599-8610.
[94] E. Fahrenkrug, D.H. Alsem, N. Salmon, S. Maldonado, Electrochemical measurements in in situ TEM experiments, Journal of The Electrochemical Society, 164 (2017) H358-H364.
[95] S. Schilling, A. Janssen, N.J. Zaluzec, M.G. Burke, Practical aspects of electrochemical corrosion measurements during in situ analytical transmission electron microscopy (TEM) of austenitic stainless steel in aqueous media, Microscopy and Microanalysis, 23 (2017) 741-750.
[96] R.R. Unocic, R.L. Sacci, G.M. Brown, G.M. Veith, N.J. Dudney, K.L. More, F.S. Walden, D.S. Gardiner, J. Damiano, D.P. Nackashi, Quantitative electrochemical measurements using in situ ec-S/TEM devices, Microscopy and Microanalysis, 20 (2014) 452-461.
[97] S. Malladi, C. Shen, Q. Xu, T. de Kruijff, E. Yücelen, F. Tichelaar, H. Zandbergen, Localised corrosion in aluminium alloy 2024-T3 using in situ TEM, Chemical Communications, 49 (2013) 10859-10861.
[98] S.W. Chee, J.-H. Park, A. Pinkowitz, B. Engler, F.M. Ross, D. Duquette, R. Hull, Liquid Cell TEM of Al Thin Film Corrosion under Potentiostatic Polarization, Microscopy and Microanalysis, 21 (2015) 973-974.
[99] S.W. Chee, D.J. Duquette, F.M. Ross, R. Hull, Metastable structures in Al thin films before the onset of corrosion pitting as observed using liquid cell transmission electron microscopy, Microscopy and Microanalysis, 20 (2014) 462-468.
[100] S.W. Chee, S.H. Pratt, K. Hattar, D. Duquette, F.M. Ross, R. Hull, Studying localized corrosion using liquid cell transmission electron microscopy, Chemical Communications, 51 (2015) 168-171.
[101] J.H. Park, T. Watanabe, A. Pinkowitz, D.J. Duquette, R. Hull, D.A. Steingart, F.M. Ross, In situ EC-TEM Studies of Metal Thin Film Corrosion in Liquid Solutions at Elevated Temperatures, Microscopy and Microanalysis, 24 (2018) 254-255.
[102] D. Gross, J. Kacher, J. Key, K. Hattar, I.M. Robertson, In situ TEM observations of corrosion in nanocrystalline Fe thin films, Processing, Properties, and Design of Advanced Ceramics and Composites II, 261 (2017) 329.
[103] M.P. Ryan, D.E. Williams, R.J. Chater, B.M. Hutton, D.S. McPhail, Why stainless steel corrodes, Nature, 415 (2002) 770.
[104] Y. Tsutsumi, A. Nishikata, T. Tsuru, Pitting corrosion mechanism of Type 304 stainless steel under a droplet of chloride solutions, Corrosion science, 49 (2007) 1394-1407.
[105] A. Chiba, I. Muto, Y. Sugawara, N. Hara, Pit initiation mechanism at MnS inclusions in stainless steel: synergistic effect of elemental sulfur and chloride ions, Journal of The Electrochemical Society, 160 (2013) C511-C520.
[106] T.S.L. Wijesinghe, D.J. Blackwood, Real time pit initiation studies on stainless steels: the effect of sulphide inclusions, Corrosion Science, 49 (2007) 1755-1764.
[107] R. Ke, R. Alkire, Surface analysis of corrosion pits initiated at MnS inclusions in 304 stainless steel, Journal of the Electrochemical Society, 139 (1992) 1573-1580.
[108] R. Ke, R. Alkire, Initiation of corrosion pits at inclusions on 304 stainless steel, Journal of the Electrochemical Society, 142 (1995) 4056-4062.
[109] N. Laycock, R. Newman, Temperature dependence of pitting potentials for austenitic stainless steels above their critical pitting temperature, Corrosion science, 40 (1998) 887-902.
[110] B. Brown, S.R. Parakala, S. Nesic, CO2 corrosion in the presence of trace amounts of H2S, CORROSION/2004, paper, (2004).

[111] W. Tait, Effect of physical parameters on the pitting corrosion of mild steel in low total dissolved solids, oxygen bearing waters: A nonpassivating metal/environment system, corrosion, 35 (1979) 296-300.
[112] S. Nešic, J. Postlethwaite, A Predictive Model for Localized Erosion—Corrosion, Corrosion, 47 (1991) 582-589.
[113] W. Sun, S. Nesic, A mechanistic model of H2S corrosion of mild steel, CORROSION 2007, (2007).
[114] S. Nešić, Key issues related to modelling of internal corrosion of oil and gas pipelines–A review, Corrosion science, 49 (2007) 4308-4338.
[115] S.C. Hayden, C. Chisholm, R.O. Grudt, J.A. Aguiar, W.M. Mook, P.G. Kotula, T.S. Pilyugina, D.C. Bufford, K. Hattar, T.J. Kucharski, Localized corrosion of low-carbon steel at the nanoscale, npj Materials Degradation, 3 (2019) 17.

CHAPTER 3

DEVELOPMENT OF THE TEM APPROACHES[1,2]

The TEM experimental approaches and instrumentation relevant to this work are explained fully in this chapter. Being a dedicated TEM study on local corrosion and corrosion inhibition of an aerospace aluminium alloy, the details on the implementation of ex-situ, quasi in-situ and in-situ liquid-phase TEM are presented here. This chapter introduces the home-made electrochemical liquid cells for LP-TEM corrosion studies. Moreover, it presents a protocol for preparing thin specimens to be used for top- and cross-sectional-view observations of corrosion using liquid-phase TEM.

Keywords: Ex situ TEM, Quasi in-situ TEM, In-situ liquid-phase TEM; Electrochemical liquid cell; FIB/SEM; Sample preparation and Transfer; Specimen selective masking

[1] A part of this chapter was published as Supplementary Martials for:
A. Kosari, H. Zandbergen, F. Tichelaar, P. Visser, P. Taheri, H. Terryn, J.M.C. Mol, In-situ nanoscopic observations of dealloying-driven local corrosion from surface initiation to in-depth propagation, Corrosion Science, 177 (2020) 108912.

[2] **A. Kosari**, H. Zandbergen, P. Visser, H. Terryn, J.M.C. Mol, Challenges to electrochemical evaluation of nanometric sandwiched thin specimens using liquid cells designed for application in liquid-phase TEM corrosion studies, Corrosion Science (2021).

3.1. Cross-sectional ex-situ TEM approach

For ex situ TEM studies, 2-mm-thick sheets of AA2024-T3 are hand-ground down to 1200 emery paper in water, followed by polishing using 0.5 and 0.05 μm alumina slurry in a non-aqueous solution on a soft cloth. Then the polished samples are immersed in solutions of interest, depending on the target of study, for different exposure times, followed by rinsing with distilled water. Subsequently, the regions of interest on the exposed samples are examined with SEM normally collecting secondary electrons. Afterwards, thin cross-sections of specific corroded particles are fabricated with a Thermo Fisher Helios G4 FIB (see Fig. 3.1) and positioned on copper half grids for later TEM examinations using a dedicated lift-out procedure (see Fig. 3.2) [1]. To protect the corroded surfaces while gallium ion-milling, a 200-nm-thick layer of carbon was deposited initially with a 2-keV electron beam, followed by ion-beam deposition until reaching a carbon thickness of approx. 1 μm. The cross-sectional investigations have the benefit of studying corrosion and corrosion inhibition for longer periods of exposure.

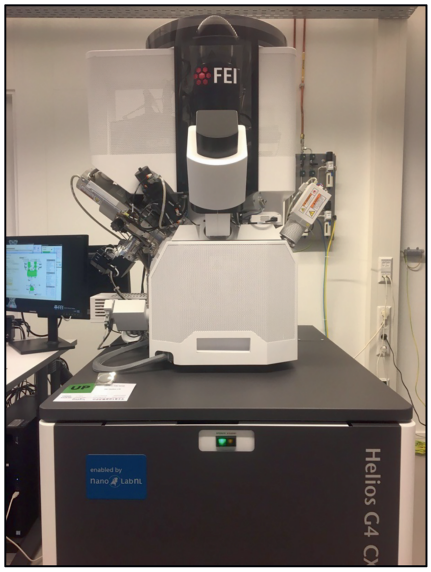


Fig. 3.1. Photograph showing Thermo Fisher Helios G4 FIB used in this study.

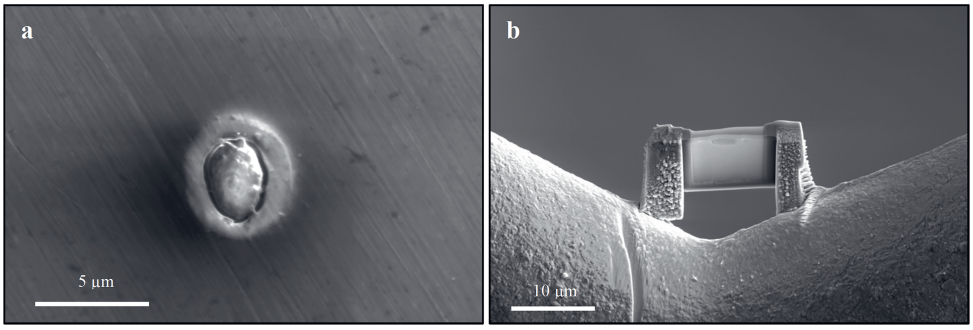


Fig. 3.2. (a) SEM image of a corroded S-phase particle covered with a layer of cerium (hydr)oxide. (b) SEM image of the TEM cross-section of the identical particle fabricated with FIB. The TEM specimen is mounted on a copper half-gride.

3.2. Top-view quasi in-situ TEM approach

This type of the experiments is performed by intermittently observing an identical location on argon ion-milled thin specimens exposed to solutions of interest outside the electron microscope. Here, ion milled specimens are 3 mm discs of AA2024-T3 which are mechanically polished down to 20-50 µm thickness. Then a Gatan precision ion polishing system (PIPS) is used to further thin them down by bombarding with a beam of argon ions at low energies of 2-5 kV. The ions normally hit the sample at a low incidence angle of 5 - 10° make the electron transparent area as large as possible. It should be mentioned that a series of electropolished samples were initially prepared and examined. However, pre-corroded intermetallic particles were always observed during the initial selection of regions of interest. Thus, electropolished specimens are not used here and consequently are not recommended too for quasi in-situ corrosion studies in particular for alloys prone to dealloying as the samples undergo a pre-corrosion process during electropolishing.

After each exposure event, the specimens are rinsed off with distilled water for a few seconds. Then, water on the specimens is immediately absorbed by delicate-task wipes and dried under a lamp. The specimens were subjected to plasma-cleaning for 5 min right before re-inserting into the TEM column. We found plasma-cleaning so critical in order to avoid carbon deposition during the TEM investigations. However, one has to make sure of fully dried samples otherwise the plasma environment might cause oxidation of the samples. The specimens are loaded on a single-tilt TEM holder as this type of holders gives better flexibility in terms of handling the specimens intermittently exposed and examined. Fig. 3.3a shows an argon ion-milled sample loaded on a single-tilt holder. As shown by an orange arrow, there is a pinhole in the middle of the disk around which the thickness meets electron transparency. A Tecnai F20ST/STEM 200 keV is employed to carry out typical high-angle annular dark field/scanning TEM (HAADF/STEM) imaging, energy dispersive spectroscopy (EDS) elemental mapping and also high resolution TEM imaging. Note that HAADF-STEM images are highly sensitive

to variations in the effective atomic numbers (Z-contrast and local thickness) in the studied regions [2]. For energy dispersive spectroscopy (EDS) elemental mapping, an Oxford Instruments X-Max^N 100TLE windowless detector was used. Fig. 3.3b shows a low-magnification TEM image of the pinhole in an argon ion-milled specimen. As is evident, there are features in the image which can serve as fiducial markers, helping us find the location of region of interest after each round of exposure.

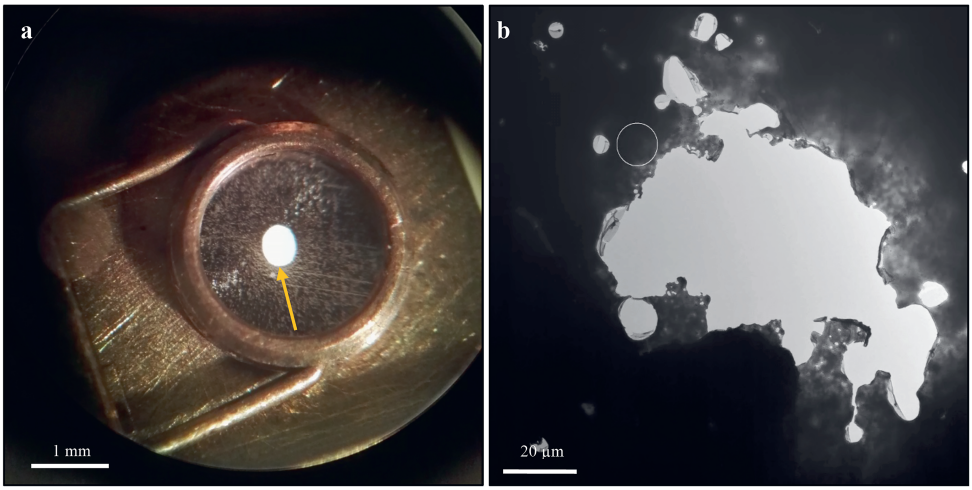


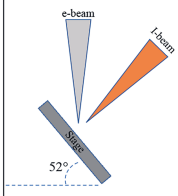
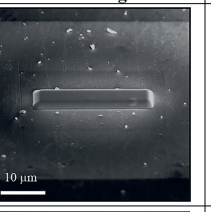
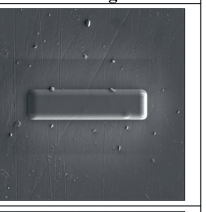
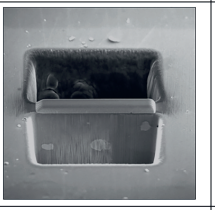
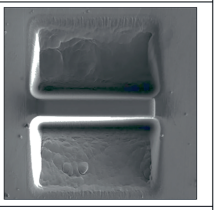
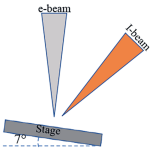
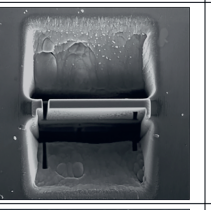
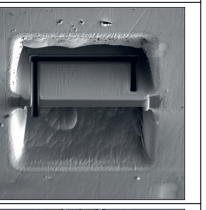
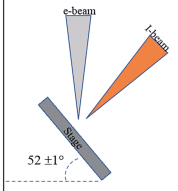
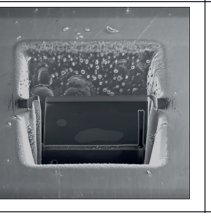
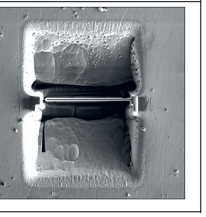
Fig. 3.3. (a) Photograph showing the tip of a single-tilt TEM holder loaded with an argon ion-milled specimen. (b) TEM image taken at a low magnification revealing the pinhole in an argon ion-milled specimen.

3.3. In-situ liquid-phase TEM approach

Electrochemical liquid phase-transmission electron microscopy (LP-TEM) has recently been an emerging facility that brings along an unparalleled opportunity to explore corrosion phenomena in situ and at the nanoscale [3, 4]. Thanks to the developed liquid cells, it is possible to polarise (bias) electrochemical reactions taking place at the specimen/electrolyte interface while the corresponding morphological/compositional are captured [5-9]. However, this significant prospect in relation to the approach and its application in corrosion science comes with inherent outstanding challenges and concerns [10-15]. This mainly includes the preparation of representing thin specimens of industrial alloys and the subsequent challenging transfer to the delicate liquid cells [16], in particular, when simultaneous electrochemical/morphological investigations are planned [17].

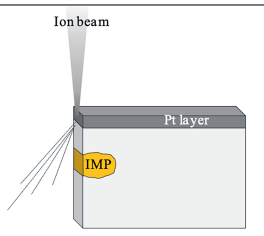
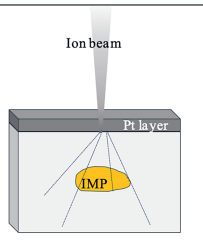
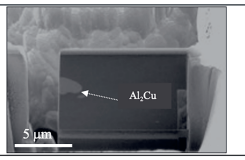
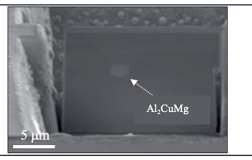
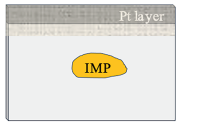
3.3.1. Specimen preparation and transfer procedure. Here, we use the Thermo-Fisher Helios G4 FIB/SEM armed with EasyLift NanoManipulator system to fabricate the thin TEM specimens (lamellae). To do so, we initially developed a methodology composed of three basic steps including preparation, masking and transfer. Table 3.1 shows the sequences to make a lamella out of a mirror-like polished AA2024-T3 sheet. Note that this is a dummy specimen; the desired size is 10 µm×20 µm.

Table 3.1. Specimen preparation step. Sequences to fabricate a lamella out of region of interest. Images are taken with the electron and ion beam at each stage.

Stage	Process	SEM images	FIB images
	Deposition of 1-µm-thick Pt layer using ion-beam to protect the sample from Ga damage while thinning down.		
	Rough milling to trench around the region of interest. The thickness of the sample is at least 4 µm at this stage.		
	Cleaning the specimen down to 3 µm followed by an undercutting process. Note that the specimen is still attached to the bulk on the right side. The ion-beam images are shown here to better explain the process from different views. For true specimens, the ion-beam is used just for cutting and would be off for imaging.		
	Thinning down, followed by cleaning at reduced currents to a desired electron transparency thickness. It is 200 nm for the samples used for top-view observations and 300 nm for cross-sectional-view examinations.		

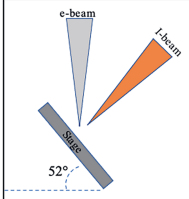
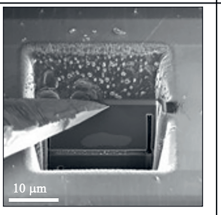
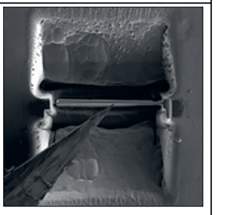
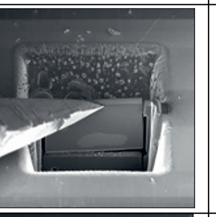
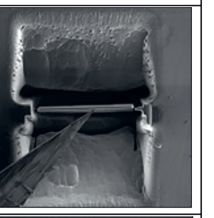
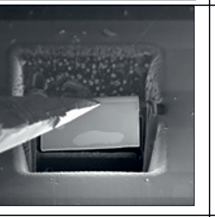
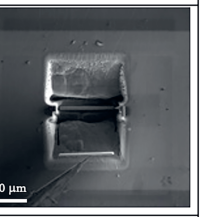
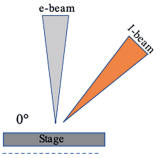
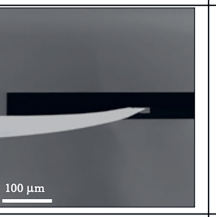
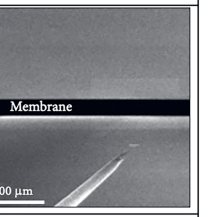
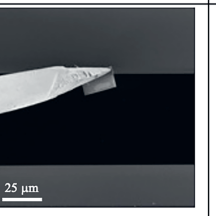
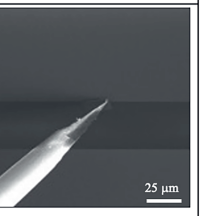
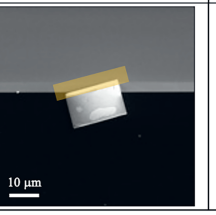
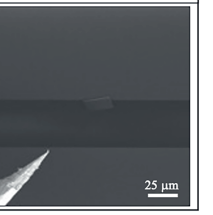
After preparing the lamella, we mask it in a targeted way (see Table 3.2) with tetraethyl orthosilicate (TEOS) layers using 2-keV electron-beam deposition at a beam current of 1.4 nA, dwell time of 1 µs and overlap X, Y of 60% being deposited dynamically in all directions. The mask thickness of 25-30 nm was chosen as it would not deteriorate the resolution, but sticks enough to the lamella surface to withstand corrosion. It should be noted that the mask layer is electrically inert and would not disturb the corrosion process through galvanic coupling with the lamella. In general, a mixture of TEOS and water is released from gas injection systems (GIS) on the FIB to form hydrated SiO_2 and ethanol as a by-product. However, we do TEOS deposition without adding water to avoid any pre-corrosion. Later, when the deposited TEOS layer is in contact with the aqueous electrolyte, the SiO_2 formation reaction will proceed sluggishly as the layer is densely deposited. On the other hand, even if reacting with the electrolyte, it would produce SiO_2 and ethanol that are a corrosion barrier and radical scavengers [12], respectively. Table 3.2 shows the sample configuration and masking condition of the lamella for top-view and cross-sectional-view observations.

Table 3.2. Milling and masking process. Schematic representations of milling and masking process for cross-sectional- and top-view observations.

Process	Cross-sectional-view configuration	Top-view configuration
The milling and thinning configuration to locate the intermetallic particle at the desired position in the lamella. For cross-sectional-view samples, the specimen is thinned down at the sides and shortened at the intermetallic side to have it right at the edge. Note that the side thinning is done when the specimen is still approx. 3 µm thick. For cross-sectional specimens, final edge cleaning is performed as the last step after final cleaning of the sides. For top-view sample, the process is identical to normal lamellae preparation.		
SEM images of two prepared lamellae which show the location of IMPs on the edge for cross-sectional observations and in the middle of the lamella for top-view studies.		
At this stage, the cross-sectional lamella is sandwiched between two 25-nm-thick TEOS layers while the top-view one is masked with the same layer merely on one side. The deposition parameters are explained in the text. Note that the Pt layer is masked as well to prevent galvanic corrosion between the Pt layer and the lamellae.		
Schematic of the final prepared lamellae. The cross-sectional lamellae interact with the electrolyte at the edge while the top-view just have it on one side.		

The most critical step is to delicately place the prepared lamellae over the brittle membrane of the liquid cell. This must be done precisely as any damage to the Si_xN_y membrane may result in failure of the liquid cell during the operation in the high vacuum. In general, to lift the specimen out of the trench, the needle of the manipulator installed on the FIB is Pt-welded to the lamella. We find this process inappropriate in this work as it limits the movement flexibility of the lamella while positioning on the liquid cell chip. In addition, when the lamella is landed on the chip, one needs to cut the needle off the lamella with ion-beam, normally resulting in Ga contamination and also damaging the Si_xN_y membrane. Instead, we found out that the electrostatic forces between the needle tip and the lamella are sufficient for extracting the lamella from the trench; note that the FIB chamber is in high vacuum (there is no air drag while moving the specimen). In the case of thick lamellae, the needle can be welded to the prepared specimen with a 100-nm thick TEOS layer using the electron beam. Interestingly, there is no need to cut off the TEOS weld and it smoothly detaches itself upon landing the lamella on the chip and the electron transparent membrane. Thus, we can implement the lift-out and transfer process without any welding; this gives a good flexibility of the sample movement while laying it down on the chip. Table 3.3 shows the sequences to transfer the prepared lamella from the trench to the liquid cell; note the stage tilt angles while extracting and landing throughout the process.

Table 3.3. Sample transfer. Sequences to lift out a lamella from the trench and position on the chip.

Stage	Process	SEM images	FIB images
	Bringing the manipulator down to touch slightly the lamella. We normally push the lamella back a little (50 nm) just to make sure of the contact. Note that the needle tip should be treated beforehand for an easier transfer process. Ion-beam imaging can be used to better guide the manipulator, at this stage. Note that the ion-beam is in parallel with the lamella and is blocked by the protective Pt layer, although low-current quick snapshots are recommended.		
	Cutting the lamella off the bulk. A high ion-beam current should be used (i.e., 25 nA) at this stage. As you can see, the lamella is suspended and kept from falling by electrostatic forces.		
	Bring the lamella up gradually to assure that it does hit the wall, resulting in the detachment from the needle. As soon as the lamella is out of the trench entirely, the needle can be fully retracted.		
	Setting the stage back at zero tilt to position the lamella on the chip. From now on, the ion-beam is always off for the true specimens. Now, the needle is brought down gradually from a point 200 µm above the chip. The distance between the sample and chip can be estimated by individually focusing at the lamella and chip.		
	Steps of the manipulator should be shortened as the lamella gets closer to the chip (i.e., 50-200 nm). Since the electrostatic forces between the lamella and chip is much stronger than that between the lamella and needle, as soon as the lamella is close enough to the surface, the chip drags it down like a magnet.		
	SEM image shows the lamella successfully landed on the chip. Note that the region of interest is close to the membrane edge where the bulging would be minimum. Finally, the top part of the lamella (rectangular region) is covered with a 200-nm-thick TEOS layer using the electron-beam to fix the lamella in place.		

3.3.2. Design and development of liquid cell. In this work, home-made liquid TEM holders and chips are used; they are specifically designed for conducting the experiments in scanning STEM mode. Fig. 3.4 shows the schematics of the bottom chip and also the macrographs of the top and bottom chips. As can be seen in Fig. 3.4a-c, there are four Pt electrodes integrated into the chips which can be reached by 4 connection pads. The two electrodes patterned on the sides of the chip (patterns coloured in blue) are approx. 300-500 nm tall. In the case of doing electrochemical measurements, one of each can serve either as the reference electrode (RE) or the counter electrode (CE). Moreover, these side electrodes function as spacers and can actually define the channel through which the electrolyte can pass; it is 250 µm wide around the membrane (Fig. 3.4b). The Pt electrodes patterned in the middle (coloured in blue) can be used as the electrical connection path to attach the thin TEM specimens (lamellae) for applying external bias. Unlike side electrodes, the middle Pt patterns are covered by 30-nm Si_xN_y; this can simply be implemented by including different steps during the chip manufacturing process [18]. Thus, they cannot interfere the electrochemical response of the TEM specimens when external biasing is applied. However, the Si_xN_y cover has to be removed locally in order to acquire the electrical connection; this process will be described later in this chapter. It should be noted that covering the middle Pt electrodes with TEOS using the FIB/SEM microscope is not possible because the scale of the Pt electrodes is too large for such a microscope to handle; hence, local removal of an externally and earlier applied Si_xN_y cover is more practical than later coverage within the microscope. Besides, there are on-chip inlet and outlet through which the electrolyte can run into and out the liquid cell, allowing us to have a real flow of electrolytes. Note that a liquid cell is composed of a top and bottom chip; the top chip here which includes no specific features except a 50-µm-wide Si_xN_y membrane (see Fig. 3.4d). The top chip is bare and only has a membrane of 50-100 µm wide in the middle. The membranes are 25 nm thick and made of Si_xN_y.

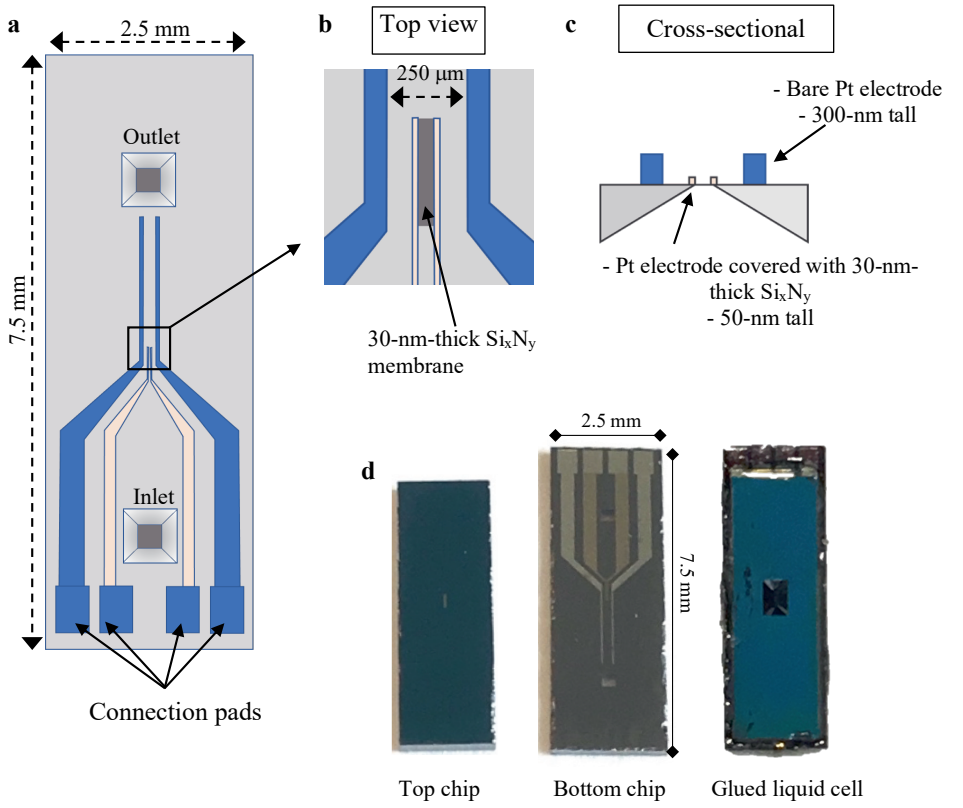


Fig. 3.4. (a) Schematic representation of the bottom chip. Note that a liquid cell is composed of a top and bottom chip. (b) Top and (c) cross-sectional view of the chip around the membrane. (d) Macrographs of the top and bottom chips before and after assembling.

Before assembling the chips, they are plasma cleaned for 1.5 min to get rid of contaminations and also to make the surfaces hydrophilic whereby the electrolyte can easily run into the liquid cell [19]. After putting the top and bottom chip together with the alignment tools, they are glued to seal in using an epoxy resin. Then the assembled liquid cell is placed on the home-made holder shown in Fig. 3.5a and then the holder is checked for being leak-tight. In order to introduce the electrolyte into the liquid cell, a diffusion vacuum pump sucks it from one side while the other side is at one bar pressure (Fig. 3.5b). Such a condition leads to a gentle electrolyte flow (a few µL/min) and a minimised membrane bulging [20]. Note that we used a liquid cell with defined microchannel through which the electrolyte can pass through; the electrolyte comes in from the inlet and goes out fully via the outlet. We should mention that the electrolyte is introduced after fully inserting the loaded holder in the TEM microscope and checking the specimen. Fig. 3.5c shows the liquid TEM holder once inserted into the microscope. The orange arrow indicates the electrolyte bottle, open to 1 bar air pressure, channelling down to the inlet in the liquid cell. The holder is designed so that the electron probe travels first through the specimen

and then the electrolyte. Such configuration can effectively lessen the beam broadening effect [14, 21], providing a good resolution despite a thick electrolyte.

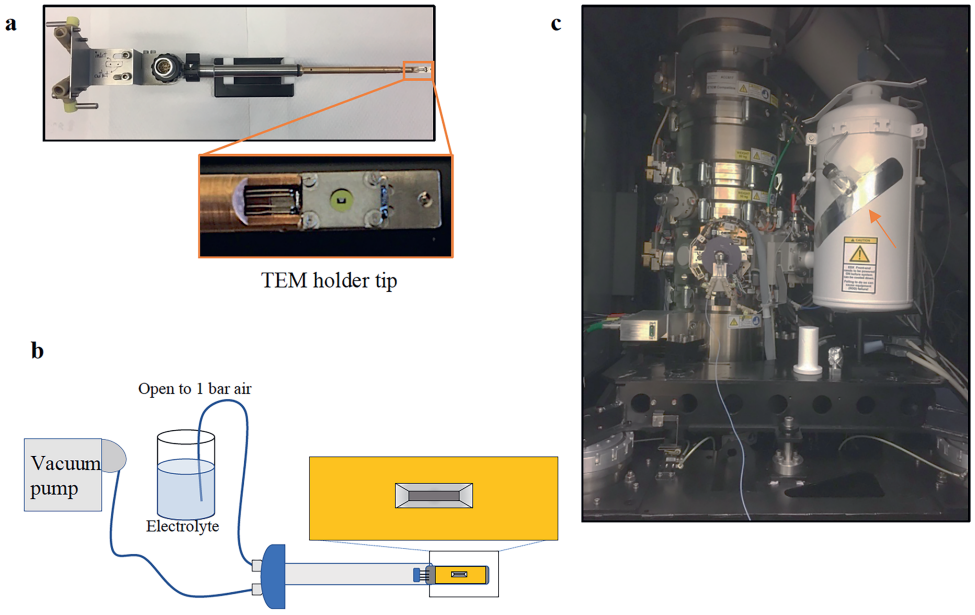


Fig. 3.5. In-situ liquid cell instrumentation. (a) Macrograph of the home-made liquid TEM holder. The inset shows the tip of the holder loaded with the liquid cell. (b) Schematic representation of the setup to inject the electrolyte into the liquid cell and also to minimise the bulging. (c) Macrograph of the liquid TEM holder once inserted into the microscope. The orange arrow indicates the electrolyte bottle, open to 1 bar air pressure, channelling down to the inlet in the liquid cell.

3.3.3. Electrochemical evaluations of nanometric sandwiched thin specimens. Contemporary liquid cells are typically composed of a top and bottom silicon-based chip assembly by which the specimen and its liquid surrounding are isolated from the ultra-high vacuum TEM column [18]. In addition, electrodes including working (WE), reference (RE) and counter electrodes (CE) are patterned on one of the chips mostly for batteries, catalysts and electrodeposition applications [8, 22]. They are normally made of Pt in order to facilitate the micromechanical fabrication process [18]. In the case of corrosion studies, the thin alloy specimens have to be electrically connected to the Pt WE electrode in order to conduct electrochemical measurements [17]. Since Pt is electrochemically active and highly noble with respect to many metals and alloys, this can result in huge galvanic corrosion of the TEM specimens once in contact with the electrolyte. It should be mentioned that Pt WE electrodes on the electrochemical chips have a significantly higher surface area than the prepared thin specimens. This phenomenon particularly causes a considerably accelerated corrosion of the thin specimens, in particular when reactive materials such as common aluminium, zinc and magnesium engineering alloys are of interest.

This challenge which can potentially limit applicability and reliability of the electrochemical measurements has not been considered in the design of the currently available commercial electrochemical TEM liquid cells if intended for corrosion studies. Moreover, electrochemical liquid-phase TEM studies of corrosion face several experimental considerations in relation to intricate sample preparation to be representative for realistic conditions of bulk samples. For instance, selective masking of the TEM specimen can be used to restrict the surface area involved in the electrochemical process, enabling top- or cross-sectional studies of corroding thin specimens [23]. Thus, this section is devoted to examining the developed electrochemical chips and sample protocols for a reliable LP-TEM studies of corrosion.

As explained already, several preparation stages that are shown in Fig. 3.6 have to be carried out. Here, we perform sandwiching the lamellae to control the oxidation direction, allowing cross-sectional observations of local corrosion. We have recently used this form of specimen preparation for studying local corrosion phenomena in freely-corroding AA2024-T3 samples (not biased) [23]. As shown in Fig. 3.6a, a lamella is sandwiched by applying two thin layers of tetraethyl orthosilicate (TEOS) (approx. 30 nm) on the sides of the specimen via the 2-keV electron beam. TEOS is electrochemically inert and does not disturb the system through galvanic coupling. We have demonstrated that TEOS with a thickness of 30-40 nm can resist even severe alkaline environments, protecting TEM specimens when sandwiched between two layers of TEOS [24]. To get an electrical connection between the specimen and chip, the Si_xN_y layer has to be removed locally before positioning the lamella. Fig. 3.6b shows a region of 5 µm × 20 µm at which the Si_xN_y layer has been removed by Ga ion milling. The Ga ion milling should be performed for approx. 30s (30 keV, 30 pA) to make certain of the Si_xN_y removal. As is evident in Fig. 3.6b, the bare region shows a brighter contrast compared to the covered regions. The next stage is to transfer the prepared lamella to the chip and position it at the membrane where the Si_xN_y is removed (Fig. 3.6c). The electrical connection can be obtained by ion-beam Pt deposition as shown in Fig. 2d. Thus, care should be taken during this process in order to avoid potential Ga ion-beam damage and Pt contaminations. In practice, it is usually preferable to perform Pt ion deposition at a relatively low ion-beam current (smaller ion beam size), allowing deposition to occur just on the region of interest. The electrical connection can be obtained by ion-beam Pt deposition as shown in Fig. 3.6d. Afterwards, three edges are covered by TEOS layers of 200- or 300-nm thick to leave the clean edge bare interacting with the electrolyte.

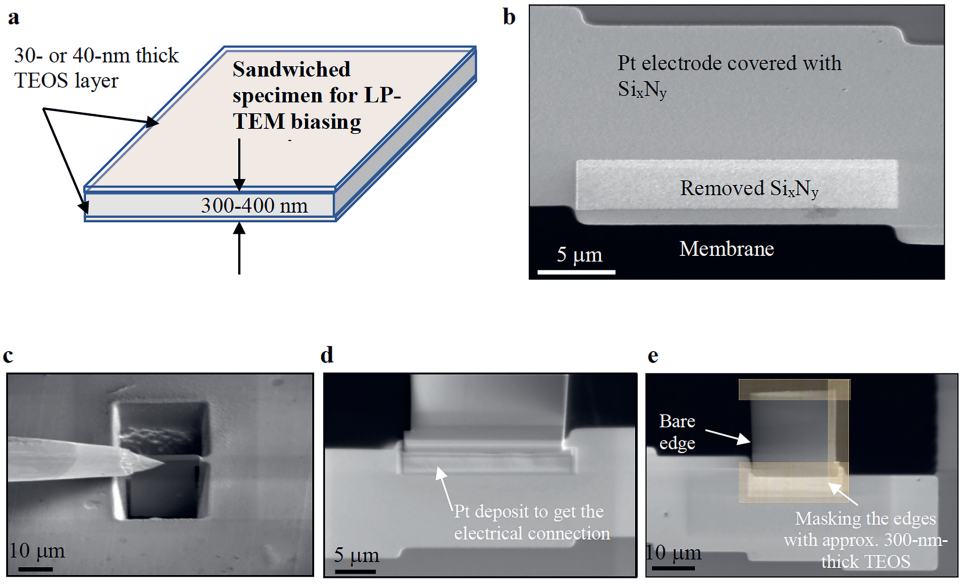


Fig. 3.6. Different stages of loading the chip with a lamella electrically connected. (a) Schematic of an AA2024-T3 sandwiched thin specimen of (approx.12 µm × 20 µm). (b) Local removal of Si_xN_y on the Pt WE. (c) Transfer of the prepared specimen to chips using the nano-manipulator. (d) Ion-beam Pt deposition to connect the specimen to the Pt WE. (e) Coverage of the three edges shown in yellow with TEOS and leaving the clean edge bare for electrochemical experiments.

In this part, two sandwiched specimens from AA2024-T3 are loaded on the designed chips and studied by open circuit potential (OCP) and anodic potentiodynamic polarisation (scan rate 2 mV/s) measurements. Fig. 3.7 shows the open-cell setup for electrochemical evaluation of nanometric sandwiched thin specimens. The chips were initially oxygen plasma-cleaned for 1 min in order to make them hydrophilic [10]. As shown, the experiments were performed ex-situ by putting the bottom chip on a home-made holder connected to an Ivium potentiostat. Then, a tiny droplet (a couple of µl) of 0.01 M NaCl solution (open to air) was dropped in the central region of the chip before conducting electrochemical measurements.

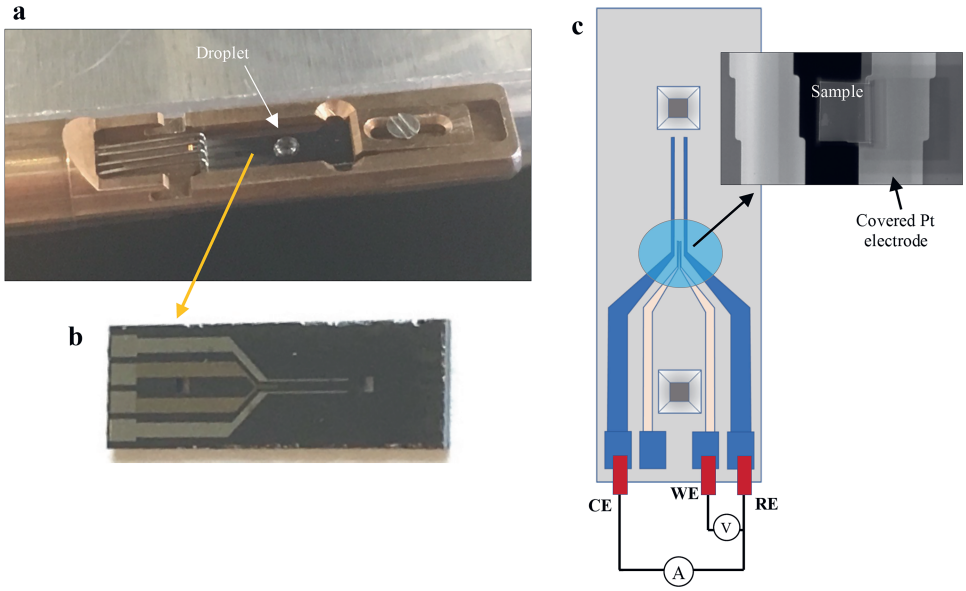


Fig. 3.7. Open-cell setup for electrochemical evaluations of nanometric sandwiched thin specimens. (a) Macrograph of the tip of the home-made TEM holder. (b) Macrographs the developed chip loaded on the holder. (c) Schematic of the chip and the configuration of the electrodes when connected to a potentiostat. As shown, a droplet of 0.01 M NaCl solution is used as the electrolyte. The inset shows the SEM image of the specimen connected to one of the covered Pt electrodes.

Fig. 3.8 shows the SEM morphological and electrochemical evaluations of the sandwiched 400-nm-thin specimens. As can be seen in Fig. 3.8a, the first lamella contains several grains indicated by the white dashed lines while the second specimen (Fig. 3.8b) contains three large Al_2CuMg (S-phase) intermetallic particles. The specimens are covered at three edges leaving a clean edge bare to the electrolyte (indicated by the white arrows). It should be mentioned that S-phase is highly reactive to the aqueous environments undergoing dealloying due to preferential dissolution of aluminium and magnesium [23, 25].

The OCP values were being recorded versus one of the side Pt electrodes while the other one was serving as the counter electrode. As can be seen in Fig. 3.8c, the Si_xN_y-covered Pt electrode (no sample) shows a stable OCP values around 70 mV during a 3-min recording indicating its inherently high electrochemical inertness. Interestingly, the OCP shows very negative values when the specimens are loaded. The specimen without S-phase shows an initial OCP values of approx. -700 mV with several fluctuations down to -900 mV related to possible morphological and compositional evolutions within the specimen. And then the OCP increases and stabilises to approx. -550 mV. Comparatively, the specimen with S-phase particles shows lower initial OCP values around -1200 mV due to the presence of S-phase at the edge of the specimen [25]. Afterwards, the OCP rises to -700 mV possibly owing to the Cu-enrichment of the specimen as a consequence of selective dissolution of aluminium and

magnesium (dealloying) [25]. The OCP remains almost stable over the next 60 s and again starts to increase to -600 mV after 150 s. Fig. 3.8d compares anodic polarisation curves for the two specimens. As can be seen, the specimen with S-phase particles shows higher anodic activity than the one without the intermetallic particles, owing to the presence of S-phase particles. It should be noted that the sandwiched TEM specimens are merely representative for the electrochemical behaviour of only a very local region (i.e., a single intermetallic phase embedded in a relatively small alloy matrix region). In contrast, bulk sample experiments may reveal the electrochemical response of a broader, representative AA2024-T3 microstructure comprising all the matrix-embedded intermetallic particles of different sizes and chemical compositions. Thus, the potentiodynamic polarisation of a thin TEM specimen cannot be compared to that of bulk samples, in particular for the heterogeneous and complex alloy microstructure studied. Furthermore, the geometry of the TEM specimens (i.e., size, thickness, and here confinement between two TEOS layers) has a significant impact on the kinetics of electrochemical processes, as also evidenced by two liquid-phase TEM studies on the local corrosion mechanism [23] and the formation of lithium-based conversion layers [24] in AA2024-T3. In fact, the main benefit of electrochemical liquid-phase TEM is the ability to directly correlate the electrochemical response of a thin TEM sample to the corresponding nanoscopic morphological and compositional evolutions.

The post-mortem SEM analysis shown in Fig. 3.8e and f reveals different corrosion-attack morphologies for the specimens after potentiodynamic polarisation testing. In the specimen without S-phase, some of the grains have been fully corroded while there are grains that are less attacked. Furthermore, the grain boundaries are preferential pathways for propagation of corrosion. It can be postulated that the corrosion has initiated at the edge S-phase particle (indicated by the red arrow), after which it has further penetrated into the grain, reaching another S-phase particle partly located at the grain boundaries. Besides, we can observe that one of the grains in this specimen is completely dissolved. This can be attributed to the different electrochemical activities of the grains due to different crystal orientation [26]. However, the detailed mechanism related to the corrosion initiation in the presence of different phases and grains are to be obtained by complete electrochemical liquid cell TEM experiments. This study shows the importance of real-time electrochemical measurements by liquid-phase TEM to be able to correlate microstructural evolution to the electrochemical response of individual phases, which are to be executed in a follow-up study.

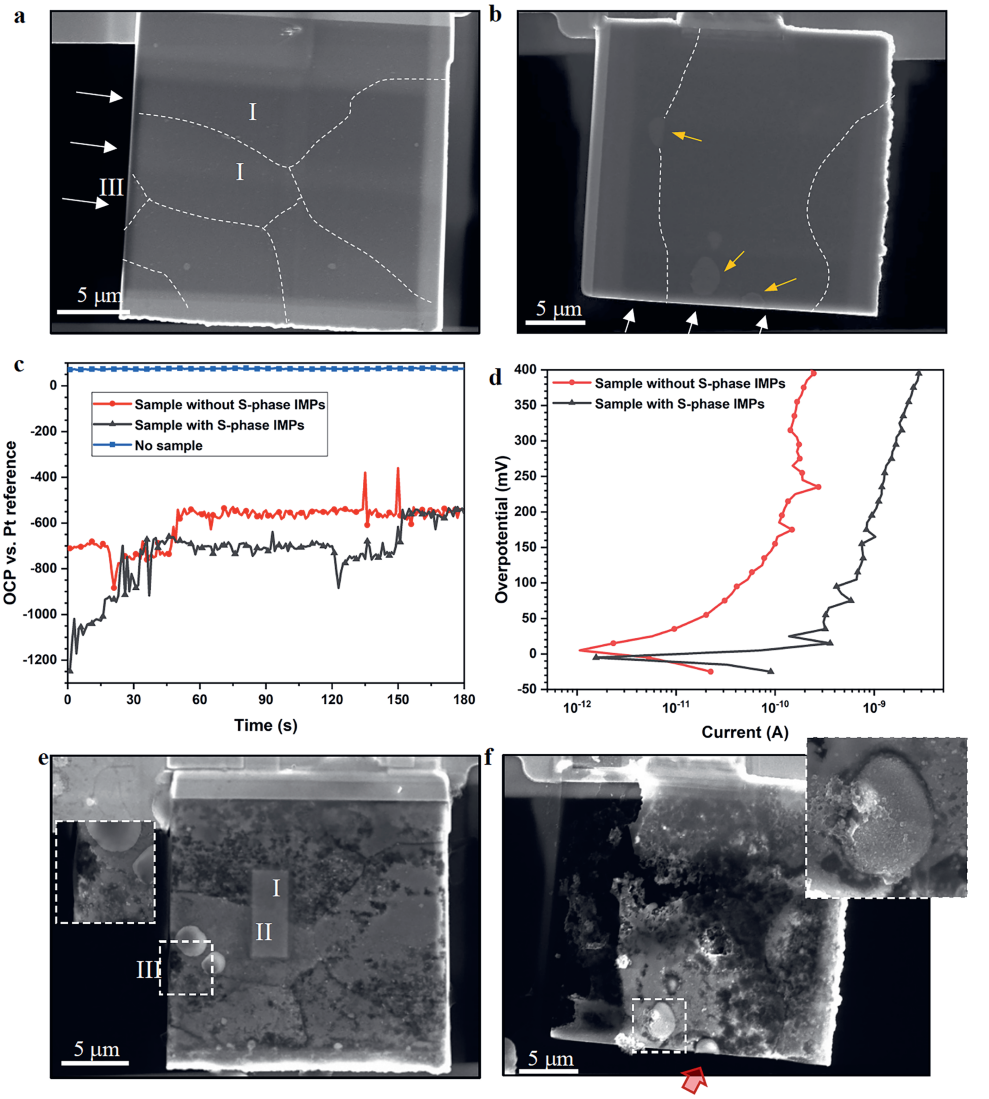


Fig. 3.8. SEM morphological and electrochemical evaluations of the sandwiched 400-nm-thin specimens. (a and b) SEM images of the specimens prior to the electrochemical measurements. (a) SEM mage of the sandwiched specimen containing several grains and nanoscopic intermetallic particles and (b) the sandwiched specimen comprising coarse Al_2CuMg particles before exposure. The white arrows indicate the bare edge interacting with the electrolyte. (c) Open circuit potential (OCP) values of the different specimens recorded for 180 s. (d) Potentiodynamic polarisation of the specimens -25 mV up +400 mV versus the OCP. The scan rate was 2 mV/s. (e and f) SEM images of the specimens subsequent to the electrochemical measurements. SEM image of (e) the corroded sandwiched specimen shown in Fig. 3.8a and (f) the sandwiched specimen shown in Fig. 3.8b. The insets are zoomed-in images of the corresponding rectangular regions.

Here we discussed the challenging limitations of the current commercial liquid cells for biased electrochemical response experiments in corrosion studies. As a remedy, we covered the Pt WE

electrodes with Si_xN_y to avoid galvanic coupling between the electrode and the specimens subjected to electrochemical measurements. We successfully used Si_xN_y covered Pt electrodes to study the electrochemical response of sandwiched thin AA2024-T3 specimens exposed to a corrosive aqueous NaCl solution. Sandwiched TEM specimens are recommended since they are able to guide the oxidation direction, mimicking cross-sectional propagation of corrosion. With the practical strategies taken here, the precise correlation of morphological evolutions to the electrochemical response of the corresponding corroding system are possible. Thus, the challenges should be well considered for the future corrosion studies with electrochemical LP-TEM.

References

[1] J. Mayer, L.A. Giannuzzi, T. Kamino, J. Michael, TEM sample preparation and FIB-induced damage, MRS bulletin, 32 (2007) 400-407.
[2] D.B. Williams, C.B. Carter, The transmission electron microscope, in: Transmission electron microscopy, Springer, 1996, pp. 3-17.
[3] S.W. Chee, M.G. Burke, Applications of Liquid Cell TEM in Corrosion Science, in: F.M. Ross (Ed.) Liquid Cell Electron Microscopy, Cambridge University Press, Cambridge, 2016, pp. 258-275.
[4] F.M. Ross, Opportunities and challenges in liquid cell electron microscopy, Science, 350 (2015) aaa9886.
[5] S.W. Chee, J.-H. Park, A. Pinkowitz, B. Engler, F.M. Ross, D. Duquette, R. Hull, Liquid Cell TEM of Al Thin Film Corrosion under Potentiostatic Polarization, Microscopy and Microanalysis, 21 (2015) 973-974.
[6] S.W. Chee, S.H. Pratt, K. Hattar, D. Duquette, F.M. Ross, R. Hull, Studying localized corrosion using liquid cell transmission electron microscopy, Chemical Communications, 51 (2015) 168-171.
[7] D. Gross, J. Kacher, J. Key, K. Hattar, I.M. Robertson, In situ TEM observations of corrosion in nanocrystalline Fe thin films, Processing, Properties, and Design of Advanced Ceramics and Composites II, 261 (2017) 329.
[8] F.M. Ross, 10 Quantifying Electrochemical Processes Using Liquid Cell TEM, Liquid Cell Electron Microscopy, (2016) 210.
[9] S.C. Hayden, C. Chisholm, R.O. Grudt, J.A. Aguiar, W.M. Mook, P.G. Kotula, T.S. Pilyugina, D.C. Bufford, K. Hattar, T.J. Kucharski, Localized corrosion of low-carbon steel at the nanoscale, npj Materials Degradation, 3 (2019) 1-9.
[10] A. Kosari, H. Zandbergen, F. Tichelaar, P. Visser, H. Terryn, A. Mol, Application of In Situ Liquid Cell Transmission Electron Microscopy in Corrosion Studies: A Critical Review of Challenges and Achievements, Corrosion, 76 (2020) 4-17.
[11] P. Abellan, T. Woehl, L. Parent, N. Browning, J. Evans, I. Arslan, Factors influencing quantitative liquid (scanning) transmission electron microscopy, Chemical Communications, 50 (2014) 4873-4880.
[12] T. Woehl, P. Abellan, Defining the radiation chemistry during liquid cell electron microscopy to enable visualization of nanomaterial growth and degradation dynamics, Journal of microscopy, 265 (2017) 135-147.
[13] N.M. Schneider, Electron Beam Effects in Liquid Cell TEM and STEM, in: F.M. Ross (Ed.) Liquid Cell Electron Microscopy, Cambridge University Press, Cambridge, 2016, pp. 140-163.
[14] N. de Jonge, Theory of the spatial resolution of (scanning) transmission electron microscopy in liquid water or ice layers, Ultramicroscopy, 187 (2018) 113-125.
[15] N. de Jonge, N.D. Browning, J.E. Evans, S.W. Chee, F.M. Ross, Resolution in Liquid Cell Experiments, in: F.M. Ross (Ed.) Liquid Cell Electron Microscopy, Cambridge University Press, Cambridge, 2016, pp. 164-188.
[16] X.L. Zhong, S. Schilling, N.J. Zaluzec, M.G. Burke, Sample preparation methodologies for in situ liquid and gaseous cell analytical transmission electron microscopy of electropolished specimens, Microscopy and Microanalysis, 22 (2016) 1350.
[17] S. Schilling, A. Janssen, N.J. Zaluzec, M.G. Burke, Practical aspects of electrochemical corrosion measurements during in situ analytical transmission electron microscopy (TEM) of austenitic stainless steel in aqueous media, Microscopy and Microanalysis, 23 (2017) 741-750.
[18] E. Jensen, K. Mølhave, Encapsulated Liquid Cells for Transmission Electron Microscopy, in: F.M. Ross (Ed.) Liquid Cell Electron Microscopy, Cambridge University Press, Cambridge, 2016, pp. 35-55.
[19] T.J. Woehl, K.L. Jungjohann, J.E. Evans, I. Arslan, W.D. Ristenpart, N.D. Browning, Experimental procedures to mitigate electron beam induced artifacts during in situ fluid imaging of nanomaterials, Ultramicroscopy, 127 (2013) 53-63.
[20] S. Keskin, P. Kunnas, N. de Jonge, Liquid-Phase Electron Microscopy with Controllable Liquid Thickness, Nano Letters, (2019).
[21] N. De Jonge, F.M. Ross, Electron microscopy of specimens in liquid, Nature nanotechnology, 6 (2011) 695.

[22] A.F. Beker, H. Sun, M. Lemang, J.T. van Omme, R.G. Spruit, M. Bremmer, S. Basak, H.H.P. Garza, In situ electrochemistry inside a TEM with controlled mass transport, Nanoscale, 12 (2020) 22192-22201.
[23] A. Kosari, H. Zandbergen, F. Tichelaar, P. Visser, P. Taheri, H. Terryn, J. Mol, In-situ nanoscopic observations of dealloying-driven local corrosion from surface initiation to in-depth propagation, Corrosion Science, 177 (2020) 108912.
[24] A. Kosari, F. Tichelaar, P. Visser, P. Taheri, H. Zandbergen, H. Terryn, J. Mol, Nanoscopic and in-situ cross-sectional observations of Li-based conversion coating formation using liquid-phase TEM, npj Materials Degradation, 5 (2021) 1-9.
[25] N. Birbilis, R.G. Buchheit, Electrochemical characteristics of intermetallic phases in aluminum alloys an experimental survey and discussion, Journal of The Electrochemical Society, 152 (2005) B140-B151.
[26] X. Zhang, X. Zhou, T. Hashimoto, B. Liu, Localized corrosion in AA2024-T351 aluminium alloy: Transition from intergranular corrosion to crystallographic pitting, Materials Characterization, 130 (2017) 230-236.

CHAPTER 4

IN-SITU LIQUID-PHASE, QUASI IN-SITU AND EX-SITU TEM OBSERVATIONS OF LOCAL CORROSION INDUCED BY PRECIPITATES[1]

Dealloying is involved in materials science responsible for fabrication of nano-scale structures beneficially but for corrosion degradations detrimentally. Detailed understanding related to the latter is critical for designing corrosion-resistance alloys and dedicated inhibition systems. Thus, direct nanoscopic observations of nano-structural and compositional evolutions during the process are essential. In this chapter, we show, for the first time, dynamic evolution of intricate site-specific local corrosion linked to intermetallic particles (IMPs) in aerospace aluminium alloys using liquid phase-transmission electron microscopy (LP-TEM). To thoroughly probe degradation events, oxidation direction is controlled by purposefully masking thin specimens, allowing for observing top-view surface initiation to cross-sectional depth propagation of local degradations. Real-time capturing validated and supported by post-mortem examinations shows a dealloying-driven process that initiates at IMPs and penetrates into the depth of the alloy, establishing macroscopic corrosion pits. Besides, controversial mechanisms of noble-metal redistribution are finally elucidated.

Keywords: Aerospace aluminium alloys; In-situ liquid-phase TEM; Dealloying; Pitting corrosion; Copper redistribution

[1] **A. Kosari**, H. Zandbergen, F. Tichelaar, P. Visser, P. Taheri, H. Terryn, J.M.C. Mol, In-situ nanoscopic observations of dealloying-driven local corrosion from surface initiation to in-depth propagation, Corrosion Science, 177 (2020) 108912.
* *All the movies related to this chapter can be found in the relevant paper.*

4.1. Introduction

High-strength-to-weight ratio in aluminium alloys (AAs) is key to many transport industries like aerospace as it reduces dead-weight and energy consumption and beneficially increases loading capacity [1]. The main contributors to mechanical properties are nano-to microscale intermetallic compounds that are introduced to the aluminium-based systems by specific alloying followed by precipitation hardening processes [2-6] (Fig. 4.1 and Movie S1), but they are typically undesirably detrimental to the corrosion resistance [7]. Contemporary aerospace AAs benefit from a comprehensive metallurgical knowledge of tuning the microstructure towards desirable mechanical properties [8]. However, the detailed understanding to unambiguously describe how the engineered microstructures affect the corrosion properties is deficient to date. In particular, complicated site-specific local degradation events that predominantly take place at surface intermetallic particles (IMPs) dispersed in the AAs matrix eventually lead to progressive pitting and intergranular corrosion [9]. Furthermore, mechanical stress during imposed operating conditions may give rise to pit-to-crack transition, jeopardizing the integrity of the aluminium alloy structure [10]. Thus, the comprehensive primary knowledge of microstructure-affected corrosion properties is absolutely essential to designing and developing intrinsically corrosion resistant AAs.

Intermetallic compounds are electrochemically instable phases in aqueous environments and generally undergo dealloying due to selective removal of less-noble metal components towards formation of a nanoporous noble-metal morphology [11, 12]. The dealloying process of binary or ternary systems is very complicated in terms of mechanism [13-16]. However, the mechanisms would be even more intricate when IMPs are confined in alloys as they can electrochemically interact (galvanic coupling) with the surrendering matrix [17-21]. Problematically, this circumstance leads to ambiguous local degradation phenomena including initiation, propagation [22-27] and noble-metal redistribution process (i.e., Cu) [28-30] over a nanoscopic length scale. A reliable approach of finding deterministic descriptors is to directly observe the nano-structural and compositional evolutions during local corrosion [31]. However, the challenges coming along with such research approaches have hampered experimental studies due to lack of experimental approaches that can probe the local degradation from early surface initiation to depth propagation in-situ and at a high spatial and temporal resolution. Therefore, the current understanding has been acquired through bridging and linking individual electrochemical and physicochemical studies [32-35] along with modelling and simulation studies [36-38], hence still explained in hypothetical terms.

Liquid phase TEM (LP-TEM) provides an unprecedented but challenging opportunity [39-44] to enhance the mechanistic understanding of interactions or dynamic in martials and particularly local corrosion at the nano-scale for complicated corroding systems [45, 46]. However, it has contributed little to corrosion science up to now and it is mainly due to the lack of representing thin specimens of industrial alloys [47-50] and the subsequent challenging transfer to the delicate liquid cells [46, 51, 52]. Furthermore, the thin specimens can merely represent very early stages and this would be insufficiently

informative for establishing comprehensive corrosion mechanisms. Here, we therefore treat specimens fabricated out of an industrial aerospace AA2024-T3 for a dedicated in-situ liquid phase transmission electron microscopy (LP-TEM), allowing for not only representative top-view (surface initiation) but also cross-sectional-view (depth propagation) observations of corrosion in-situ and at the nanoscopic level.

A schematic illustration of the methodology is shown in Fig. 4.1. As depicted, the oxidation direction is controlled by covering the specimens either on one side (in case of top view) or on both sides (cross-sectional view) by 25-nm-thick layers of tetraethyl orthosilicate (TEOS). The specimens that encompass precipitates of either Al_2CuMg (as a compound with a very complicated corrosion [53-56]) or Al_2Cu (a phase reported with a high cathodic electrochemical activity [21, 57]) are fabricated with focused ion beam (FIB). The mask layer is electrochemically inert and promote no galvanic corrosion with the alloy specimen. The prepared specimens are transferred to the home-made liquid cell via a self-developed intricate procedure and each specimen is placed at the entrance side of the electron probe to mitigate the beam-broadening effect [58]. Top-view experiments show very early initiation events whilst the cross-sectional experiments provide insights into moderate stages of corrosion attack when the degradation propagates into the depth. In parallel, quasi in-situ and ex-situ TEM experiments are performed to obtain detailed chemical and structural analysis, and additionally to validate the in-situ results (Supplementary Materials). With that, we evidence that dynamics of local corrosion in AAs that are largely governed by dealloying attack to IMPs.

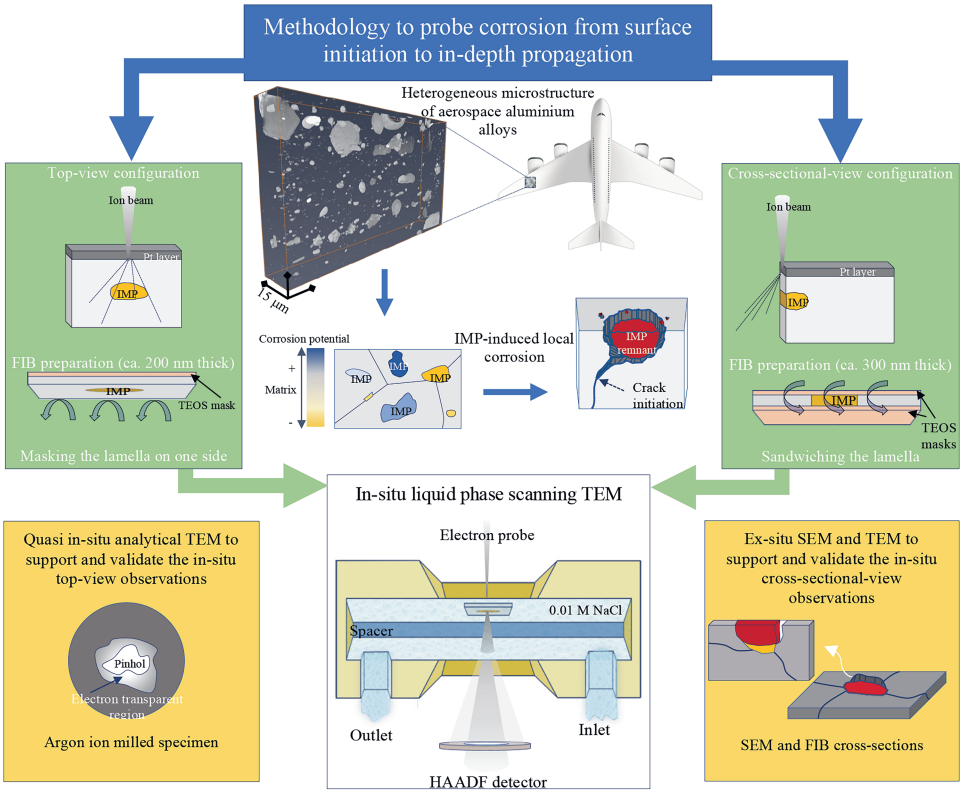


Fig. 4.1. Methodology for examining IMPs-induced corrosion degradation in aerospace aluminium alloys from surface initiation to in-depth propagation at the nano-scale. Three-dimensional reconstruction of aerospace AA2024-T3 microstructure (Movie S1) which leads to complicated corrosion. IMPs acquiring different corrosion potential and electrochemical activity in aqueous solutions are potential pit initiation sites. In-situ LP-TEM are performed in in HAADF-STEM mode on the treated lamellae of approx. 10µm×20µm, representing 'real-life' corrosion. Top-view observations are provided by depositing a 25-nm-thick layer of tetraethyl orthosilicate (TEOS) using 2-keV electron-beam deposition; the corresponding schematic depicts the location of intermetallic particle (IMP) on the lamellae. For cross-sectional observations, the TEM specimen sandwiched between two 25-nm-thick layers of TEOS; note the location of intermetallic particle (IMP) on the lamellae. The prepared specimens are transferred to the home-made liquid cell using a FIB-based procedure, and each specimen is placed at the entrance side of the electron probe to mitigate the beam-broadening effect. Quasi in-situ analytical TEM experiments are conducted, in parallel, on argon ion-milled specimens (3-mm disk) to provide in-situ top-view observations with detailed structural and compositional information. Ex-situ examinations are carried out on FIB cross-sections to support cross-sectional in-situ observations.

4.2. Material and Methods

4.2.1. In-situ liquid-phase Scanning TEM (LP-TEM). A Thermo-Fisher Helios G4 FIB/SEM armed with EasyLift NanoManipulator system was used to fabricate the TEM specimens (lamellae) out of regions of interest. To do so, high-current ion milling of a polished AA2024-T3 sheet was conducted until the appearance of an intermetallic particle within the milled region. To have the specimens more

representative of bulk state microstructures, 200- to 300-nm-tick lamellae that were either masked on one-side or sandwiched by applying 25-nm-thick tetraethyl orthosilicate (TEOS) layers with 2-keV electron beam, giving either top- or cross-sectional-views to the electron beam. The deposition parameters are presented in Supplementary Materials. A novel sample transfer procedure was established to lift out and position the lamellae on the home-made chips without damaging the 25-nm thin Si_xN_y membrane (see Supplementary Materials). The chips were plasma cleaned for 1-1.5 min before assembling to get rid of contaminations and to make the surfaces hydrophilic, so that the electrolyte can easily run into the liquid cell. The electrolyte was 0.01 M NaCl open to 1 bar air pressure while the outlet was being sucked by a vacuum pump to have a very gentle flow during the experiments and also mitigate the bulging of the membranes [59]. The specimens were positioned at the entrance side of the electron probe to effectively mitigate the beam-broadening effect on the resolution in STEM mode. A home-made TEM holder that are specially designed for corrosion studies was used. A Cs corrected Thermo-Fisher Titan 300 kV TEM was employed to perform in-situ studies. High angle annular dark field (HAADF)-STEM imaging that has the advantage of showing Z-contrast and local thickness information was carried out at the probe current of 1.409 nA measured in vacuum. Snapshots of critical stages were taken at a fame time of 10 s^{-1} at various magnifications (either 20,000X or 28,500X) of 2048 × 2048 pixels using TEM Imaging and Analysis (TIA) software. Simultaneously, the movies were captured over the corrosion period with a fame time of 1 s^{-1} at various magnifications of 2048 × 2048 pixels using a screen recorder. The challenges in relation to the electron beam effect and sample artifacts on this part are discussed in Supplementary Materials.

4.2.2. Quasi in-situ analytical TEM. Quasi in-situ experiments were performed by repeatedly examining an identical location on argon ion-milled thin samples exposed intermittently to 0.01 M NaCl outside the microscope. After each cycle of exposure, the specimen was first rinsed off with distilled water for a few seconds and dried out carefully, followed by plasma-cleaning for 5 min before inserting to the TEM column. A Tecnai F20ST/STEM 200 kV was used for typical high resolution TEM imaging and scanning transmission electron microscopy/energy dispersive spectroscopy (STEM/EDS) elemental mapping and selected area electron diffraction (SAED) analysis. For EDS measurements, an Oxford Instruments X-MaxN 100TLE Windowless detector was used.

4.2.3. Ex-situ characterisations. AA2024-T3 sheets were hand-ground down to 1200 emery paper, followed by polishing using 0.5 and 0.05 μm alumina slurry in a non-aqueous solution on a soft cloth. Then the samples were exposed to 0.01 M NaCl for different exposure times. The surface morphology of the corroded samples was examined with secondary electron SEM. The thin cross-sections were fabricated out of corroded particles of interest with FIB and lift-out procedure, then examined with HRTEM, STEM-EDS and SAED methods.

4.3. Results and Discussion

4.3.1. Local corrosion by S-phase (Al_2CuMg). Time-resolved top-view morphological evolutions of S-phase as a result of interaction with 0.01 M NaCl are shown in Fig. 4.2a (Movie S2). High angle annular dark field-scanning TEM (HAADF-STEM), taken at 0 min in the absence of the electrolyte, shows a large bright particle of Al_2CuMg embedded in the alloy matrix. Note that HAADF-STEM images are highly sensitive to changes in spatial differences in atomic composition (Z-contrast). The Al_2CuMg particle consists of two grains and as indicated by the white arrow, a grain boundary can be distinguished inside the particle. After 5 min of exposure, the centre of the Al_2CuMg particle shows darker, implying less electron scattering due to material removal (corrosion). Note that the contrast becomes a bit poorer after introducing the electrolyte at t= 5 min due to scattering of electrons while traveling through the liquid. With prolonged exposure to the electrolyte (t= 8 min), the central corroded region radially grows in the same morphology which is ultra-finely porous. As indicated by the white arrow, a part of the adjacent matrix has partially dissolved (trenching initiation), showing up dark in the HAADF-STEM image. At t= 11 min, the dissolution has extended more into the alloy matrix and the granular contrast variations are now visible over the whole corroding Al_2CuMg particle. The digitally-magnified view of the rectangular region shown in Fig. 4.2b reveals that the initially-corroded zone (Region I) is finely porous in morphology (pore size <9 nm) whereas Region II has coarser porosities (15 nm< pore size <20 nm). After 16 min, although no change in the particle morphology is seen (the grain boundary is not distinguishable any longer), the dark regions become evident further around the particle and into the alloy matrix, indicating a trench-shaped local dissolution. Furthermore, a bright spot that is circled in yellow appears at the edge of the matrix but it vanishes later (Movie S2). Besides, comparison of the circled-in-white region at 11 and 16 min reveals that a nanosized dispersoid ($Al_{20}Mn_3Cu_2$) has undergone corrosion and left a nano-pit behind. After 19 min, the matrix dissolution has entirely trenched all around the particle, indicating that the particle is electrically disconnected from the neighbouring matrix. At 21 min, numerous bright particles emerge all over the edge of the matrix, shown later by diffraction analysis to be clusters of nano-scale Cu particles. In addition, the Al_2CuMg particle size has considerably reduced between 19 and 21 min due to copper dissolution at this stage. With prolonged exposure (t= 28 min), we observe that some of the clusters of nano-scale Cu-rich particles which are deposited around the trench rim disappear; we discuss this phenomenon later.

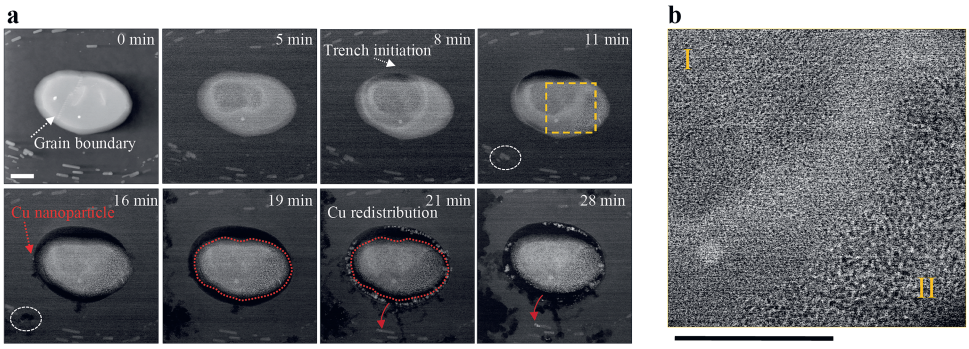


Fig. 4.2. In-situ top-view observations of local corrosion by S-phase (Al_2CuMg). (a) Time-resolved top-view HAADF-STEM images of an Al_2CuMg particle, showing morphological evolutions of the particle and its adjacent matrix (Movie S2; Probe current in vacuum 1.409 nA, Convergence angle 13.7 mrad, Camera length 185 mm, Magnification 20000X). The lamella is approximately 225 nm thick, in total. The electrolyte is 0.01 M NaCl (pH 6.5). The image taken at 0 min is in the absence of the electrolyte. The red dashed-lines border the particle area before and after the detachment from the alloy matrix. (b) Digitally-magnified view of the rectangular region shown in the STEM image taken at 11 min. The scale bar is 500 nm.

In-situ liquid phase HAADF-STEM clearly showed the evolution of a nanoporous morphology within S-phase caused by corrosion. In parallel, we have conducted complementary quasi in-situ TEM examinations on argon ion-milled disk specimens to acquire detailed compositional information at critical stages of corrosion. This also allows for assessing the potential effect of electron beam on the whole process, as discussed in Supplementary Materials. Fig. 4.3a shows HAADF-STEM imaging and energy-dispersive spectroscopy (EDS) mapping over the corroded parts of an Al_2CuMg particle after 10 min exposure to 0.01 M NaCl (see also Fig. S4.6). As can be seen, a nanoporous morphology has been established at some zones of the particle. Given the EDS results, we conclude that the selective dissolution of magnesium and to a lesser extent aluminium has occurred. The oxygen map is also a clear indication of corrosion taken place at morphologically-evolved zones; it also suggests the presence of aluminium hydroxide residing inside the pitted area.

To figure out what happens to copper at this very early stage of corrosion, further quasi in-situ investigations have been performed. Fig. 4.3b shows a STEM image of the pitted regions on an Al_2CuMg particle exposed to distilled water for 20 min (Fig. S4.5); this solution was chosen to slow down the corrosion process at very early stages. As is evident, the pits and the intact region are boarded by the bright narrow rims which are actually surface-diffused copper (see Fig. S4.5). Note that the pits appear darker in the HAADF-STEM image due to local mass loss by selective dissolution. Thus, dealloying attack is clearly responsible for corrosion initiation on S-phase. In fact, dealloying selectively depletes active elemental components of the phase (herein aluminium and magnesium) to evolve a nanoporous Cu morphology.

Fig. 4.3c shows a HAADF-STEM image of an Al_2CuMg particle intermittently exposed to 0.01 M NaCl for a total exposure of 30 min. The EDS analysis reveals that the particle is depleted from magnesium and aluminium (see Fig. S4.6); it is almost empty of magnesium (0.2 at%) and contains approx. 6.3 at% after 30 min. Note that the particle is still connected to the alloy matrix and the copper redistribution process has not occurred. As can be seen, the copper dendrites are formed at the trench region (Fig. 4.3c_1). Further analysis including EDS mapping and HRTEM imaging identify them as clusters of the nano-scale Cu_2O particles (Fig. 4.3c_2). This form of copper is sourced from solid solution, which holds 0.2-0.5 at% copper, as a consequence of the simultaneous matrix dissolution and surface diffusion [11]. In fact, the copper in the matrix solid solution gradually accumulates during the trenching to form sub-micron copper particles. However, they later become electrically isolated in the aluminium oxide products and undergo oxidation themselves. Looking at the oxygen map corresponding to the rectangular region, we see some local corrosion spots on the alloy matrix. As shown in Fig. 4.3c_3, these are nano-pits that are formed due to the passive layer breakdown. The corresponding EDS map reveals the surface-diffused solid-solution copper as a rim around the pit where the alloy matrix is locally dissolved.

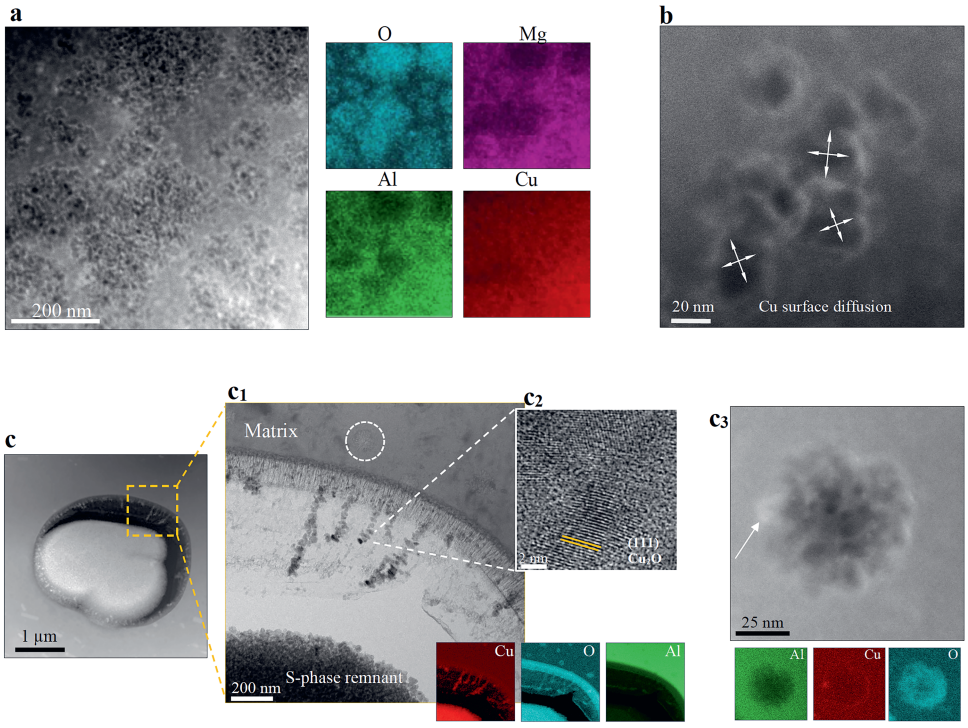


Fig. 4.3. Analysis of corroded S-phase intermediately exposed to 0.01 M NaCl. (a) STEM/EDS analysis of an Al_2CuMg particle exposed to 0.01 M NaCl for 10 min; the elemental map reveals selective dissolution of aluminium and magnesium to different extents (Fig. S4.6). (b) HAADF-STEM image of an Al_2CuMg particle exposed to distilled water for 20 min, revealing the single pits and copper surface diffusion (Fig. S4.5). (c) HAADF-STEM image of an Al_2CuMg particle taken after 30 min of exposure to 0.01 M NaCl (Fig. S4.6). (c_1) TEM image and corresponding EDS map are related to the dashed rectangular region shown in the STEM image. (c_2) High resolution TEM (HRTEM) image of the region indicated by the white dashed lines. (c_3) STEM/EDS analysis of a single pit on the alloy matrix where the region is circled in the TEM image, revealing redistribution of solid-solution Cu as a rim around the pit. Notice that the results are obtained via quasi in-situ TEM experiments on thin argon ion-milled specimens (Fig. S4.5 and Fig. S4.6).

Cross-sectional-view HAADF-STEM sequences of a sandwiched S-phase being exposed in-situ to 0.01 M NaCl solution are shown in Fig. 4.4a (Movie S3). The image taken in the absence of the electrolyte (t= 0 min) shows an Al_2CuMg particle which is confined in the alloy matrix. The snapshot taken after 15 min reveals some contrast variations on the upper part of the particle which is bare and interacting with the electrolyte. As can be seen, corrosion has slightly dissolved the surrounding alloy matrix while it has propagated more into the particle than the matrix, resulting in a nanoporous morphology. After 20 min, the corrosion process changes in morphology. It penetrates deeper at the particle/matrix interface associated with the extensive matrix dissolution. The snapshot taken at 25 min shows the deep corrosion propagation equally into the matrix and the interfacial regions of the particle but shallower into the middle part of the particle. The trench grows in width and depth during the corrosion process

until it is about to undercut the particle after 28 min; the middle part of the particle is not fully corroded at this point. Fig. 4.4b compares the digitally-magnified view of the rectangular region at 15 and 28 min, revealing formation of the nanoparticles at the top of the corroding particle which have considerably grown in size and number since the beginning of the exposure. The snapshot taken at 31 min shows that the particle disconnected from the alloy matrix. Like the top-view findings, the latest-corroded region shows up in a course nanoporous morphology. Due to rapid dealloying at this stage (Movie S3), a breakdown crack takes place near the top of the particle, indicated by the yellow arrow. At t= 34 min, numerous nanoparticles are formed at the edge of the matrix whereas the particle has decreased in size and also the bright layer atop the corroding particle has disappeared. Fig. 4.4c shows the involvement of a deep intermetallic particle in corrosion propagation at an advanced stage. As is evident, the corrosion has penetrated quite deep induced by the redistributed sub-micron Cu-rich particles until reaching another Al_2CuMg particle underneath. This can well explain how corrosion further propagates into the depth with prolonged exposure time. In addition, comparison of the particle size before corrosion (t= 0 min) and after 37 min reveals a considerable shrinkage due to selective aluminium and magnesium dissolution and following copper liberation.

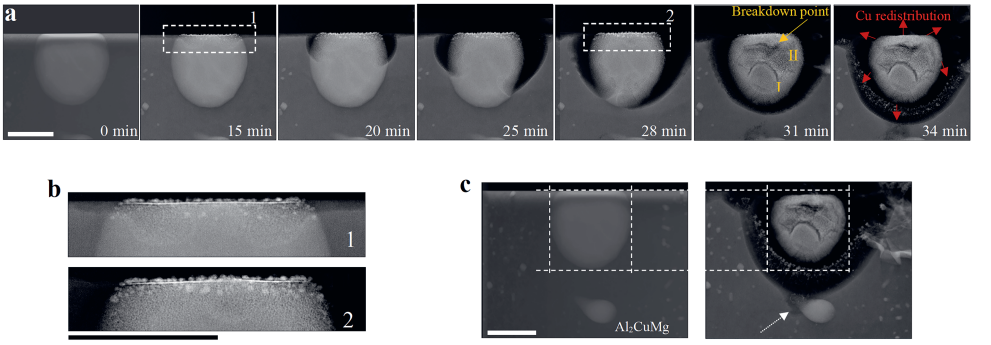


Fig. 4.4. In-situ cross-sectional observations of local corrosion by S-phase (Al_2CuMg). (a) HAADF-STEM time series of cross-sectional dealloying-driven evolutions in a sandwiched Al_2CuMg particle (Movie S3; Probe current in vacuum 1.409 nA, Convergence angle 13.7 mrad, Camera length 185 mm, Magnification 28500X). The yellow arrow indicates the breakdown location. The red arrows indicate the copper dissolution from the top and the periphery of the corroded particle. (b) Digitally-magnified view of the rectangular region shown in the STEM images taken at 15 min (No.1) and 28 min (No. 2). (c) Comparison of the particle size before and after 37 min of exposure. The white arrow indicates the involvement of a deep Al_2CuMg in corrosion propagation at an advanced stage. The specimen thickness is 350 nm including the TEOS layers. The electrolyte is 0.01 M NaCl (pH 6.5). The scale bar is 500 nm.

Fig. 4.5a and b show top-view SEM, cross-sectional STEM/EDS and selected areas electron diffraction (SAED) patterns on the bulk-corroded samples exposed ex-situ to 0.01 M NaCl for 15 min and 6 h, respectively. The SEM image in Fig. 4.5a depicts a narrow trench around the particle which has a

smooth surface due to a fine corrosion-attack morphology. The cross-sectional HAADF-STEM image of the corresponding particle shows that it is corroded partly and corrosion has penetrated deeper at the particle/matrix interface (in agreement with the in-situ observations). The EDS analysis shows that the corroded region which is uniformly nanoporous in morphology has almost been depleted in magnesium (1.3 at%) but still contains 11 at% aluminium, indicating the occurrence of dealloying. In addition, a narrow layer of nano-scale particles on the top of the corroding intermetallic particle (Region II) is clearly distinguishable from the rest (Region I). Using SAED analysis, we characterised Region II as elemental nano-scale copper particles whereas Cu and Cu_2O coexist in Region I. Comparatively, the surface of the particle exposed for 6 h is quite rough, associated with appearance of numerous clusters of deposited nano-scale Cu-rich particles around and in the trench (Fig. 4.5b). The cross-sectional STEM image shows that the particle is fully corroded and disconnected from the matrix. Variations in pores size are observed all over the remnant, probably referring to different stages of corrosion within the particle. In addition, there are the signs of breakdown on the top of the particle (indicated by the yellow arrow) where the layer of copper nanoparticles is missing. We identified the undercut particle as a Cu_2O nanoporous remnant which is covered by $Al(OH)_3$. The SAED pattern collected from the cluster (circled in yellow) shows spots matching elemental copper. With this compositional insight, we draw your attention back to Fig. 4.4a where the nano-scale copper particles on the top of the particle, increasing in size and number, dissolve away after the particle undercut event (t=29 min).

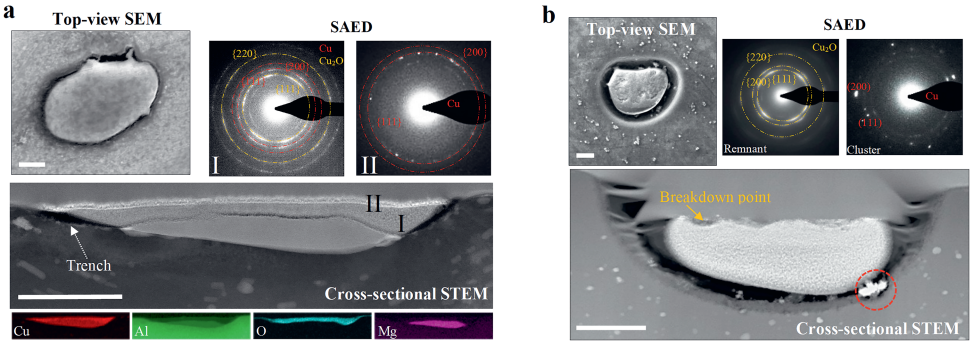


Fig. 4.5. Post-mortem analysis of corroded Al_2CuMg particles exposed to 0.01 M NaCl. (a) Top-view SEM, cross-sectional STEM/EDS and SAED analysis of an Al_2CuMg particle immersed in 0.01 M NaCl for 15 min. The SEAD patterns show characteristic rings and spots for Cu and Cu_2O; the close lattice parameters are not indexed. (b) Top-view SEM, cross-sectional STEM and SAED analysis of an Al_2CuMg particle immersed in 0.01 M NaCl for 6 h. Note that the matrix and the particle are not at the same level where the clusters nestled in the trench are identified as nano-scale elemental copper particles. This undercut particle is a nano-porous Cu_2O remnant covered by $Al(OH)_3$. The cross-sections are fabricated out of the corresponding corroded particles with FIB. The scale bar is 1 µm.

4.3.2. Local corrosion by Al_2Cu (θ-phase). Fig. 4.6a shows top-view sequences of an Al_2Cu particle in 0.01 M NaCl. The HAADF-STEM image is taken at 0 min in the absence of the electrolyte. After 37 min, a few nanoparticles (bright spots) appear at the edge and on the top of the corroding particle; there is no sign of matrix corrosion (trenching) up to this point. We observe that the nanoparticles are growing in size, and this is associated with a slight corrosion attack to the particle, itself, in particular to the edge region (t= 57 min). A comparison of the electron intensity along the dashed lines (the blue and red line) clearly discloses the matrix trenching and also the corrosion attack to the particle (Fig. 4.6b). At this stage, additional information via quasi in-situ STEM/EDS confirms selective aluminium dissolution from the particle itself (θ-phase dealloying), resulting in the trenching of the closest matrix to the dealloyed region (Fig. S4.7 and S4.9). As corrosion progresses until 81 min, a globular corrosion morphology (~20 nm scale) becomes more apparent on the particle, however, it turns into a banding morphology (~10 nm spacing) after 111 min. The transition from the globular to the band-like morphology can be seen in the digitally-magnified views in Fig. 4.6c. After 111 min, the alloy matrix has significantly been dissolved which is also associated with corrosion of nanosized dispersoids ($Al_{20}Mn_3Cu_2$), leaving several bright spots behind (Fig. 4.6c). This behaviour continues until the whole particle is about to get disconnected (t= 122 min); numerous nanoparticles are accumulated on the particle at this stage. During the next 18 min, the corrosion proceeds further with the matrix trenching and slight particle corrosion. Besides, we observe no considerable change in the particle size where fewer nanoparticles are formed at the edge of the trenched matrix (Movie S4), compared to S-phase.

Fig. 4.6d shows cross-sectional in-situ observations of θ-phase-induced local corrosion, taking place to the sandwiched specimen. Comparing the HAADF-STEM image taken at t= 0 min and 60 min reveals the corrosion initiation at several locations in the Al_2Cu particle itself; the dark region within the particle shows a fine nanoporous morphology. The snapshot taken after 60 min reveals how corrosion has propagated into the depth; the white arrows point to two bright nanoparticles accumulated on top of the particle. In spite of a higher corrosion potential of θ-phase than the alloy matrix, it seems that its self-corrosion precedes the dissolution of the matrix (trenching) which is covered by an isolating passive layer. After 100 min, corrosion has penetrated deeper, probably due to structural defect variations at the right side of the particle while the alloy matrix is slightly dissolved on the top. Looking at the STEM images of the particle taken after 105min, we see that the initially-corroded region within the particle has a finer nanoporous morphology (Region I) than the later-corroded part (Region II) where the matrix is significantly corroded. From this point, it takes about 1 min for the particle to be undercut and extensively corroded (t= 106 min). Note that similar to S-phase, the latest-corroded part of the particle is coarsest in morphology (Region III). At 110 min, we see the breakdown event right on top of the particle; associated with the appearance of redeposited nanoparticles, in particular, at the bottom of the trench (Movie S5) which is less in number as compared to S-phase.

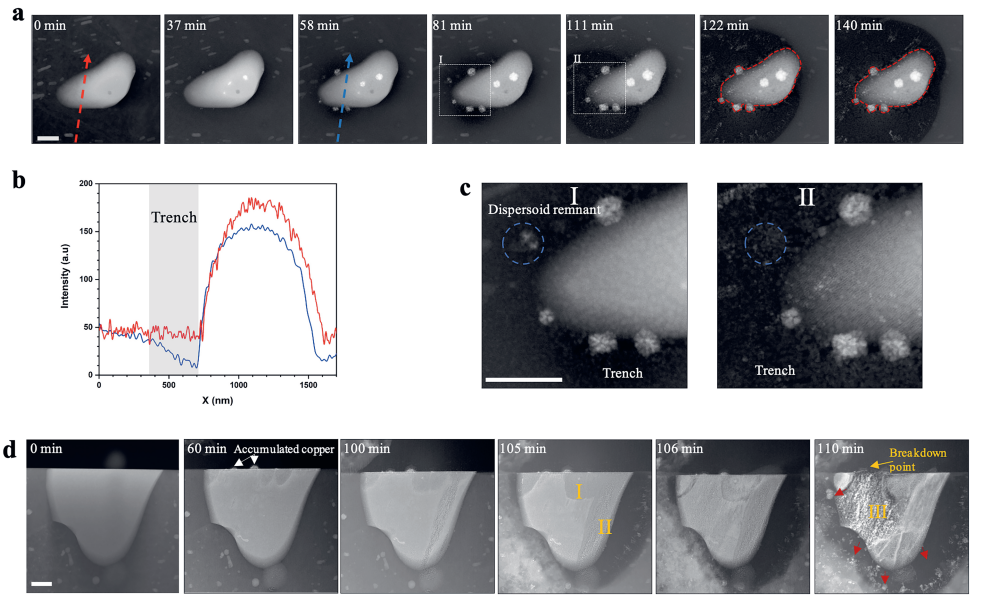


Fig. 4.6. In-situ top-view and cross-sectional-view observations of local corrosion by θ-phase (Al_2Cu). (a) HAADF-STEM time series of top-view dealloying-driven evolutions within an Al_2Cu particle and its adjacent alloy matrix (Movie S4; it is made of 52 snapshots taken at different stages of an exposure for 149 min at the camera length of 75 mm). The red dashed-lines indicate the particle area before and after the detachment. The lamella is approximately 200 nm thick, masked with 25-nm-thick TEOS layer on one side. (b) Electron intensity along the red and blue arrows in Fig. 4.6a, proving the trenching occurrence which follows the dealloying attack to the particle. (c) Digitally-magnified HAADF-STEM images of Region I and II in Fig. 4.6a, showing the transition from the globular to river-like dealloying morphology. The circled-in-blue region shows a dispersoid particle undergoing dealloying and then disappearing. (d) Cross-sectional dealloying-driven evolutions in a sandwiched Al_2Cu particle, captured by HAADF-STEM (Movie S5; Probe current in vacuum 1.409 nA, Convergence angle 13.7 mrad, Camera length 75 mm, Magnification 20000X). The total specimen thickness including TEOS layers is 350 nm. The white arrows point to the surface-diffused accumulation of copper. The yellow arrow points the breakdown location on the top of the particle. The red arrows indicate the copper dissolution merely from the periphery of the dealloyed particle at the trench bottom. The electrolyte is 0.01 M NaCl, pH 6.5. The scale bar is 500 nm.

Post-mortem analysis of the samples related to θ-phase-induced local corrosion are shown in Fig. 4.7. Cross-sectional STEM image of an Al_2Cu particle exposed for 15 min (Fig. 4.7a) reveals formation of the nanoporous layer all over the top of the particle; the depth penetration of the layer is location-dependent. A closer look at this particle is shown in the inset; additional STEM/EDS reveals the selective dissolution of aluminium (dealloying) associated with accumulation of copper nanoparticles at the particle/matrix interface. Fig. 4.7b shows a high resolution TEM image taken from the nanoporous region of a dealloyed Al_2Cu particle (Fig. S4.9a), revealing co-existing nano-sized Cu and Cu_2O nanoparticles. Further investigations are carried out on a representative Al_2Cu particle corroded for 6 h, as shown in Fig. 4.7c. The top-view SEM image reveals a trench around the particle which has a

wide opening tapered down into the depth. In addition to the layer of copper nanoparticles on the top, the cross-section shows a gradient nano-porous morphology where pore size increases towards the depth. The composition line scan reconstructed from the rectangular region in the STEM image clearly reveals selective dissolution of aluminium: its amount slightly rises with the distance from the top. This phenomenon is consistent with diffusion of selectively dissolved aluminium to the top before leaving the particle. Fig. 4.7d shows an Al_2Cu particle exposed for 19 h. The SEM image reveals that the particle surface and its adjacent matrix are corroded severely. The further analysis on the corresponding lifted-out cross-section confirms formation of an undercut Cu_2O remnant covered with aluminium hydroxide where a few clusters of nano-scale copper particles are nestled in the trench; additional evidence can be found in Fig. S4.9.

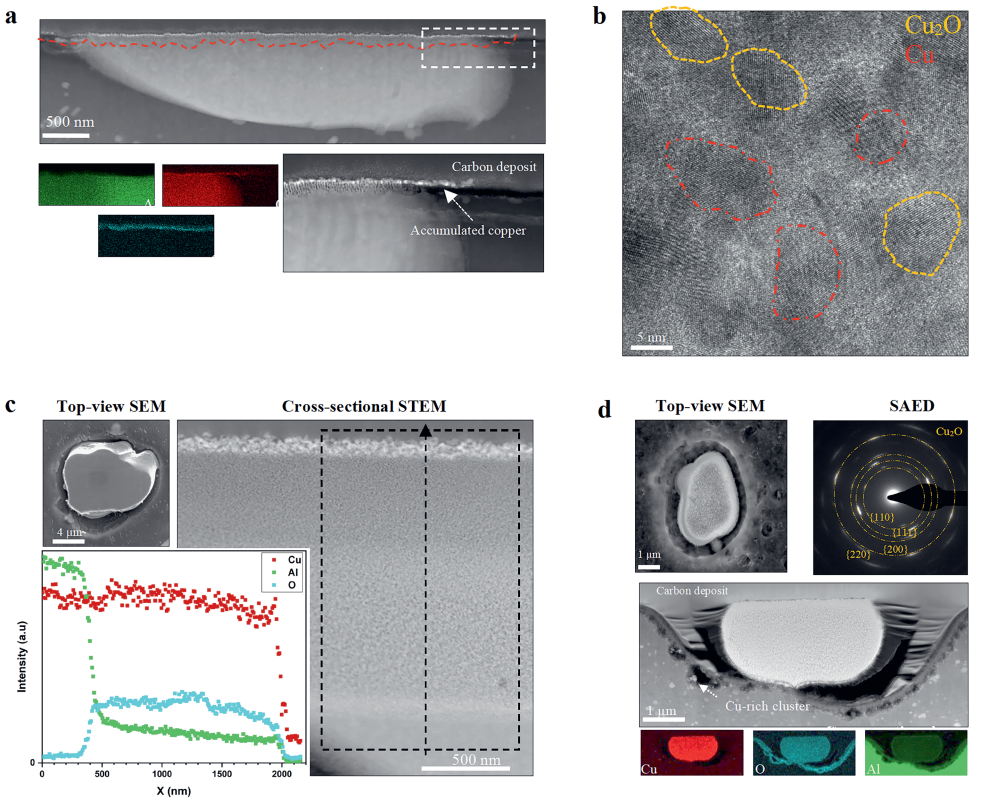


Fig. 4.7. Analysis of post-corroded Al_2Cu particles (θ-phase). (a) Cross-sectional HAADF-STEM image of an Al_2Cu particle exposed to 0.01 M NaCl for 15 min, showing several locations attacked by dealloying. The inset is the magnified view of the rectangular region analysed by STEM/EDS; the white arrow points the accumulated copper at the edge. (b) HRTEM image taken from the dealloyed region of an Al_2Cu particle corroded for 15 min, revealing coexisting Cu and Cu_2O nanoparticles (identified from the lattice plane spacings). (c) Top-view SEM, cross-sectional STEM/EDS analysis of an Al_2Cu particle immersed in 0.01 M NaCl for 6 h. The SEM image shows the smooth surface of the particle surrounded by a trench with a wide opening. The graph is the elemental profile reconstructed from the rectangular region in the cross-sectional STEM image, showing selective dissolution of aluminium. (d) Top-view SEM, cross-sectional STEM/EDS and SAED analysis of an Al_2Cu particle immersed in 0.01 M NaCl for 19 h. The remnant is characterised as a nano-porous Cu_2O particle covered by aluminium hydroxides.

4.3.3. The role of copper-rich regions in local corrosion. Up to this point, both in-situ liquid phase and analytical post-mortem TEM examinations unanimously narrate that the IMPs-induced local corrosion initiation is a consequence of a preceding dealloying attack occurring to both S-phase and the θ-phase compounds. This form of corrosion results in the formation of copper-rich regions within IMPs that are electrochemically nobler than the un-corroded regions and the adjacent alloy matrix, leading to nano-galvanic interactions between these nano-scale heterogeneities. Here, we prove that the nanoscopic copper-rich region can function as strong cathodic sites, supporting ORR reactions that leads to highly

local alkaline solution chemistry. Besides, as long as the alloy matrix is covered by the aluminium oxide passive layer which is isolating in nature, it would be protected and cannot support any electrochemical reactions. However, if the alloy matrix undergoes local breakdown due to chloride attack, solid-solution copper does also surface diffusion to around nanoscopic corrosion pits, hence acting as nano-cathodic sites as well. This has been fulfilled by analysis of the S-phase/θ-phase composite particles [60] exposed to a solution of 0.003 M $Ce(NO_3)_3$ + 0.01 M NaCl. According to E-pH diagram of cerium [61], $Ce(OH)_3$ can precipitate in solution pH approximately above 10 via a chemical reaction, it can therefore be a pH marker.

Fig. 4.8a shows STEM/EDS analysis of an Al_2CuMg/Al_2Cu composite particle exposed to 0.003 M $Ce(NO_3)_3$ + 0.01 M NaCl for 70 min. As can be seen, cerium has deposited discretely around the rims of the pits formed on the Al_2CuMg particle, neither on θ-phase nor the alloy matrix. In fact, an alkaline environment is required for triggering Ce deposition, this phenomenon proposes a nano galvanic coupling establishment between Cu-rich regions on the Al_2CuMg particle (cathodic sites) and inside the pits (anodic sites). Since cathodic reactions produce OH^-, we can claim that the surface-diffused copper on the corroded region of S-phase support the cathodic reaction like oxygen reduction reaction (ORR), leading to cerium deposition. Further evidence is shown in Fig. 4.8b, where the cross-sectional STEM/EDS analysis of an Al_2CuMg/Al_2Cu composite particle clearly reveals the precipitation of cerium hydroxide over the Al_2CuMg particle. The results herein prove that dissimilar intermetallic particles do not establish cooperative corrosion at least at early stages of corrosion owing to their different electrochemical behaviour. There is no nobility inversion and IMPs are in fact simultaneous anodic and cathodic sites since the beginning of exposure that can also form nanogalvanic coupling with the closest corroding alloy matrix.

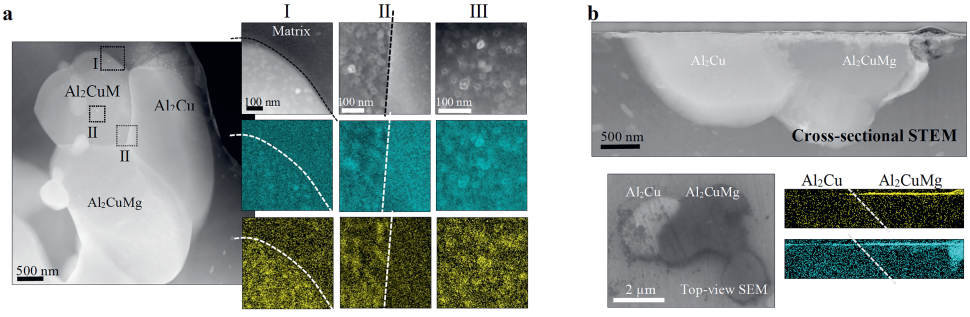


Fig. 4.8. Analysis of S-phase/θ-phase composite particles in 0.003 M $Ce(NO_3)_3$ + 0.01 M NaCl. (a) HAADF-STEM/EDS analysis of an Al_2CuMg/Al_2Cu composite particle on an argon ion-milled disk at different regions. The disk is exposed to 0.01 M NaCl+0.003 $Ce(NO_3)_3$ for 70 min (blue: O and Yellow: Ce). (b) Cross sectional STEM/EDS images of an Al_2CuMg/Al_2Cu particle exposed to 0.01 M NaCl+0.003 $Ce(NO_3)_3$ for 90 min; revealing a thin layer of cerium oxide deposited on the Al_2CuMg not on the Al_2Cu. The inset is top-view SEM image of the mixed particle before milling (blue: O and Yellow: Ce).

Furthermore, Fig. 4.9 shows how a cluster of nano-scale Cu-rich particles can drive the matrix corrosion through a consecutive deposition/dissolution process. As can be seen, the cluster establishes nano-galvanic coupling with the adjacent matrix, leading to the local matrix corrosion. This phenomenon can gradually trench around the cluster until the electrical disconnection occurs. Then, the nano-scale Cu-rich particles can acquire its free corrosion potential at which copper dissolves. Upon the release of copper into the electrolyte, it reappears as smaller nano-scale particles at the edge of the matrix where thermodynamically copper redeposition is favoured, followed by further corrosion of the alloy matrix (Movie S6).

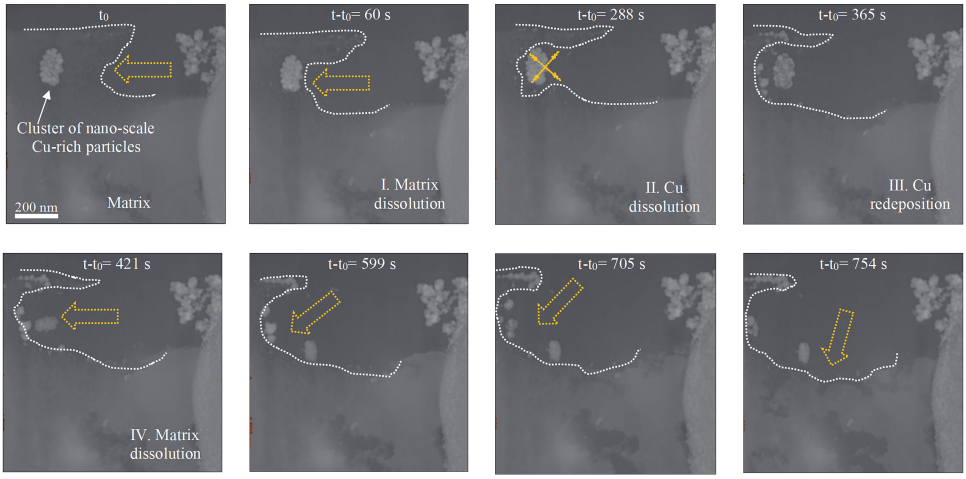


Fig. 4.9. The role of clusters of nano-scale Cu-rich particles in corrosion propagation. Time-resolved HAADF-STEM images, showing how a cluster leads to local dissolution of the matrix. (Movie S6; Probe current in vacuum 1.409 nA, Convergence angle 13.7 mrad, Camera length 185 mm, Magnification 28500X). The sample is approx. 200 nm thick and is sandwiched between two layers of TEOS.

4.4. Dealloying-driven local corrosion mechanism by Al_2CuMg and Al_2Cu

Here, in-situ direct nanoscopic top-/cross-sectional-view observations along with detailed supplementary information allow us to provide a comprehensive mechanism explaining local degradation phenomena related to precipitates hardening phases of Al_2CuMg and Al_2Cu and also controversial Cu redistribution. Local corrosion is here divided into three distinct stages including surface initiation, in-depth propagation, and particle undercut and Cu release. Fig. 4.10 schematically depicts different stages of local corrosion induced by S-phase and θ-phase in AAs where the probable electrochemical reactions occurring around the IMPs are shown in detail. It also shows the local solution chemistry and compositions at different locations of S-phase and θ-phase (this form of representation is inspired by Snyder et al. [12]).

4.4.1. Surface initiation. Local corrosion initiates by dealloying attack to IMPs but stabilizes (continuous corrosion) through nanogalvanic interactions between copper-rich regions and the IMPs. This condition gradually gives rise to a local solution chemistry in which the passive layer covering the nearby alloy matrix cannot survive, leading to its local dissolution. For S-phase, the surface initiation process happens rather shortly after exposure as magnesium is highly soluble in the studied solution, although hydrolysis of aluminium ions occurs simultaneously and can passivate some active locations. Copper does surface diffusion and appears in rims around the pits (Fig. 4.3b), subsequently rearranging in a nanoporous morphology (Fig. 4.3a). Although, copper cannot thermodynamically dissolve at this stage, it can be released via dissolution of physically-detached Cu particles. In the case of θ-phase, $Al(OH)_3$ formation inhibits corrosion at initial dissolution sites and consequently a sluggish initiation process provides copper with sufficient time to accumulate as nanoparticles on the surface in particular at the edges (Fig. 4.6a). Afterwards on both S-phase and θ-phase, nanogalvanic interactions are established between anodic zones and the copper-rich cathodic sites supporting OH^--producing reactions. Since $Al(OH)_3$ is merely stable at pH 4-9, the aluminium oxide passive layer of the nearest alloy matrix destabilizes due to local chemistry provoked by electrochemical reactions, resulting in the trench initiation (Fig. 4.2a and Fig. 4.6a).

4.4.2. In-depth propagation. During the depth propagation, cathodic reactions like oxygen reduction reactions (ORR) take place on the upper parts of the corroding IMPs while the intact part of the particle and the adjacent matrix undergo anodic dissolution. For S-phase, owing to a rapid dealloying propagation and trenching (anodic process), the rate of cathodic reactions is also rather high (to maintain overall charge neutrality), resulting in an extremely basic local chemistry atop a corroding S-phase. On the other hand, the massive exit of the corrosion products due to fast dealloying leads to the detachment of some copper-rich segments from the upper part which is highly porous (Fig. S4.8a). Then, the detached copper segments obtain their free-corrosion potential and endure anodic dissolution. However, the consequent copper ions become redeposited either mostly onto the same corroding particle (Fig. 4.4a) since the top part shows cathodic activity or on the Cu-rich regions on the alloy matrix undergoing active local dissolution (Fig. 4.2a at 16 min). Under hydrodynamic conditions, the copper ions can be carried away by the flowing electrolyte and re-plate on distant active sites like the local cathodes on the matrix. The depth propagation happens significantly slower to θ-phase and consequently a moderate basic local chemistry is built up atop a corroding particle. That explains findings of other researches in which S-phase, in cerium-inhibited solutions, is found with a thick layer of the cerium hydroxide [62] triggered by local alkalinity while θ-phase is only slightly/partly covered [63]. Additionally, due to hydrolysis of metal ions, the pore and trench environments would experience a pH gradient with lower acidity towards the top of IMPs [12]. In the region with moderate pH, aluminium hydroxide gel is stable and physically covers of the sections involved in dealloying. This mechanism is valid for both S-phase and θ-phase, but takes longer for the latter. On the other hand, the sluggish evolutions give produced

H^+ ions more time to diffuse away; thus, the trench and pore environment within the corroding Al_2Cu particles are less acidic as compared to those for the S-phase. During the progress of dealloying, the corroding IMPs enrich in copper and acquire higher corrosion potential, leading to formation of a coarser nanoporous morphology than the earlier-dealloyed regions. Note that the corrosion potential of the whole specimen is insufficiently high for direct copper corrosion before the particle undercut; however, Cu_2O nanoparticles can form as a result of physical or electrical isolation of some copper segments, enduring oxidation during the dealloying course (Fig. 4.4a, Fig. 4.5a and Fig. 4.7b).

4.4.3. Particle undercut and Cu release. As soon as the trenching undercuts the whole corroding particle, its corrosion potential rapidly goes up whereby direct dissolution of copper can occur. This event is also associated with a breakdown in the corroding IMPs due to massive dissolution and egress of the corrosion products. At this stage, the difference in behaviour of S-phase and θ-phase is the amount of copper ions they can release into the solution. Since a corroding θ-phase particle is largely covered with aluminium hydroxide gel, it gradually transforms into a Cu_2O remnant after the undercut; mostly the bottom part of θ-phase particles contributes to copper release. In contrast, S-phase contributes to redistribution of copper to the largest extent as the upper part and the periphery of the undercut particles liberate copper, followed by re-plating at aluminium hydroxide-free parts of the matrix surface. As other sources of redistributed copper, corroded nanometric copper-containing particles like dispersoids (Fig. 4.6c) and also the alloy matrix which holds approx. 0.5 wt.% Cu in solid solution (Fig. 4.3a) can be enumerated. Furthermore, the deposited nano-scale copper particles can establish local nanogalvanic coupling with the matrix and promote further local corrosion. As evidenced (see Fig. 4.9), they show an iterative process of redeposition/dissolution through which the clusters of Cu-rich particles speed up the aluminium dissolution until they get detached from the matrix. Then, the free-standing particles undergo anodic dissolution themselves, followed by redepositing back on the matrix and continue to further corrode the alloy matrix. Note that the local corrosion from the initiation to particle undercut occur to S-phase in a shorter time-scale, thus early copper ions liberated from the undercut S-phase can also be redeposited on the neighbouring θ-phase and other active intermetallic compounds.

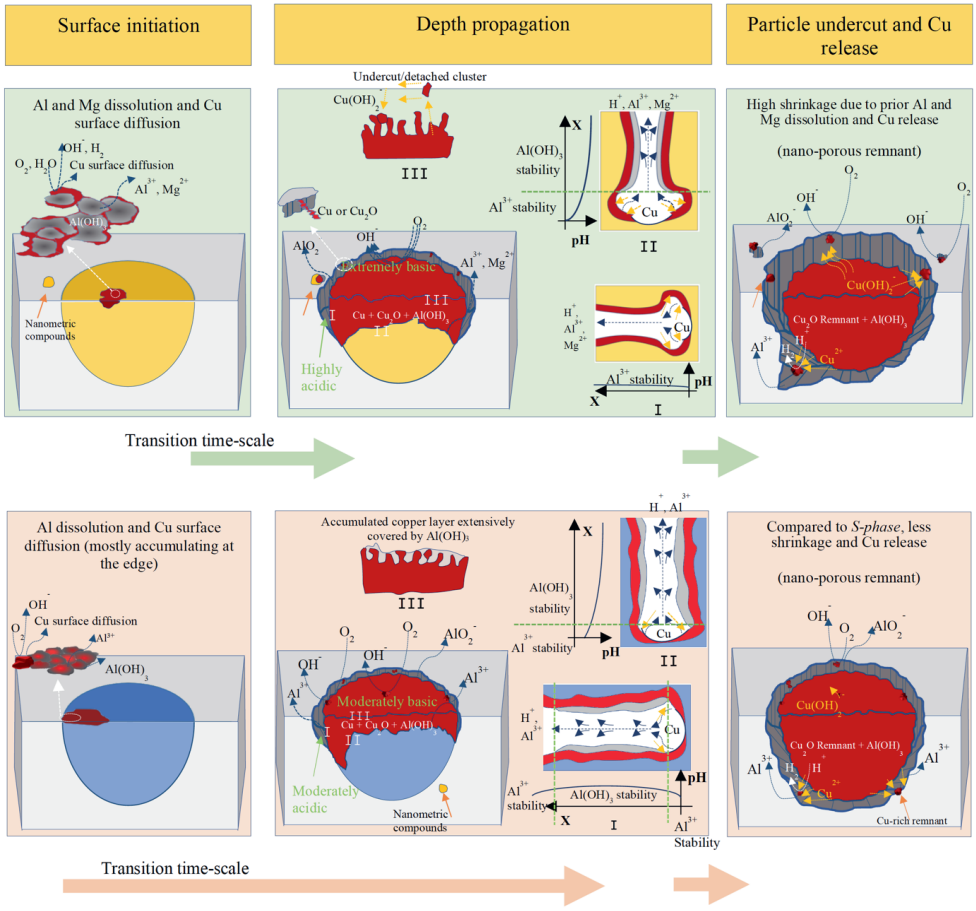


Fig. 4.10. Dealloying-induced IMPs-induced local corrosion mechanism. 3D schematic view of localized corrosion initiation induced by individual S-phase (boxed in green) and θ-phase (boxed in pink) particles embedded in the alloy matrix. The mechanism by which the corrosion initiates at the surface and propagates into the depth is shown. The probable corrosion reactions occurring around IMPs are depicted in detail. In addition, local solution chemistry and compositions at different locations on S-phase and θ-phase are shown.

4.5. Conclusions

In-situ top- and cross-sectional-view liquid phase STEM directly evidenced different stages of corrosion from surface initiation to in-depth propagation where different time-scales were observed for S-phase and θ-phase. We stress the pivotal role of dealloying attack to IMPs as the precursor of local degradations in AAs. IMPs are in fact simultaneous anodic and cathodic sites as from the beginning of exposure. Nanogalvanic interactions between the heterogeneities within the corroding IMPs themselves, and later with the closest neighbouring alloy matrix stabilise the local corrosion. S-phase is more problematic in terms of corrosion as it induces local degradation in a relatively short exposure

time and largely contributes to copper redistribution, compared to that for θ-phase. The current findings can fully explain controversial forms of IMPs-induced local corrosion in AAs like pitting and intergranular corrosion, and the copper redistribution process. Besides, they constitute a basis for reliable predictive corrosion modelling and simulation and can be used to develop smart corrosion inhibition strategies for AAs. Furthermore, the experimental package can be applied to studies in relation with corrosion of other complicated systems like stainless steels and also fabrication of advanced nanoporous materials like sensors and catalysts.

References

[1] N.E. Prasad, R.J. Wanhill, Aerospace materials and material technologies, Springer, 2017.
[2] J. Chen, E. Costan, M. Van Huis, Q. Xu, H. Zandbergen, Atomic pillar-based nanoprecipitates strengthen AlMgSi alloys, Science, 312 (2006) 416-419.
[3] A. Guinier, Structure of age-hardened aluminium-copper alloys, Nature, 142 (1938) 569-570.
[4] C. Liu, S.K. Malladi, Q. Xu, J. Chen, F.D. Tichelaar, X. Zhuge, H.W. Zandbergen, In-situ STEM imaging of growth and phase change of individual CuAl X precipitates in Al alloy, Scientific reports, 7 (2017) 1-8.
[5] S.K. Malladi, Q. Xu, M.A. van Huis, F.D. Tichelaar, K.J. Batenburg, E. Yücelen, B. Dubiel, A. Czyrska-Filemonowicz, H.W. Zandbergen, Real-time atomic scale imaging of nanostructural evolution in aluminum alloys, Nano letters, 14 (2014) 384-389.
[6] G. Preston, Structure of age-hardened aluminium-copper alloys, Nature, 142 (1938) 570-570.
[7] A.E. Hughes, N. Birbilis, J.M. Mol, S.J. Garcia, X. Zhou, G.E. Thompson, High strength Al-alloys: microstructure, corrosion and principles of protection, Recent Trends in Processing and Degradation of Aluminium Alloys, 1 (2011).
[8] P.V. Liddicoat, X.-Z. Liao, Y. Zhao, Y. Zhu, M.Y. Murashkin, E.J. Lavernia, R.Z. Valiev, S.P. Ringer, Nanostructural hierarchy increases the strength of aluminium alloys, Nature communications, 1 (2010) 1-7.
[9] G. Frankel, 2015 WR Whitney Award Lecture: The Effects of Microstructure and Composition on Al Alloy Corrosion, Corrosion, 71 (2015) 1308-1320.
[10] Z.C. Petrović, Catastrophes caused by corrosion, Vojnotehnički glasnik, 64 (2016) 1048-1064.
[11] J. Erlebacher, M.J. Aziz, A. Karma, N. Dimitrov, K. Sieradzki, Evolution of nanoporosity in dealloying, Nature, 410 (2001) 450-453.
[12] J. Snyder, K. Livi, J. Erlebacher, Dealloying silver/gold alloys in neutral silver nitrate solution: porosity evolution, surface composition, and surface oxides, Journal of the Electrochemical Society, 155 (2008) C464-C473.
[13] N. Dimitrov, J. Mann, M. Vukmirovic, K. Sieradzki, Dealloying of Al2CuMg in alkaline media, Journal of The Electrochemical Society, 147 (2000) 3283.
[14] S. Lebouil, J. Tardelli, E. Rocca, P. Volovitch, K. Ogle, Dealloying of Al_2Cu, Al_7Cu_2Fe, and Al_2CuMg intermetallic phases to form nanoparticulate copper films, Materials and Corrosion, 65 (2014) 416-424.
[15] J. Snyder, P. Asanithi, A.B. Dalton, J. Erlebacher, Stabilized nanoporous metals by dealloying ternary alloy precursors, Advanced Materials, 20 (2008) 4883-4886.
[16] Q. Chen, K. Sieradzki, Mechanisms and morphology evolution in dealloying, Journal of The Electrochemical Society, 160 (2013) C226-C231.
[17] A. Boag, A. Hughes, A. Glenn, T. Muster, D. McCulloch, Corrosion of AA2024-T3 Part I: Localised corrosion of isolated IM particles, Corrosion Science, 53 (2011) 17-26.
[18] R. Buchheit, A compilation of corrosion potentials reported for intermetallic phases in aluminum alloys, Journal of the Electrochemical Society, 142 (1995) 3994.
[19] C. Örnek, C. Leygraf, J. Pan, Real-Time Corrosion Monitoring of Aluminum Alloy Using Scanning Kelvin Probe Force Microscopy, Journal of The Electrochemical Society, 167 (2020) 081502.
[20] N. Birbilis, R. Buchheit, Investigation and discussion of characteristics for intermetallic phases common to aluminum alloys as a function of solution pH, Journal of the Electrochemical Society, 155 (2008) C117.
[21] N. Birbilis, R.G. Buchheit, Electrochemical characteristics of intermetallic phases in aluminum alloys: an experimental survey and discussion, Journal of the Electrochemical Society, 152 (2005) B140.
[22] Y. Zhu, G. Frankel, Effect of major intermetallic particles on localized corrosion of AA2060-T8, Corrosion, 75 (2019) 29-41.
[23] Y. Zhu, K. Sun, G. Frankel, Intermetallic phases in aluminum alloys and their roles in localized corrosion, Journal of The Electrochemical Society, 165 (2018) C807-C820.
[24] Y. Zhu, K. Sun, J. Garves, L.G. Bland, J. Locke, J. Allison, G. Frankel, Micro-and nano-scale intermetallic phases in AA2070-T8 and their corrosion behavior, Electrochimica Acta, 319 (2019) 634-648.

[25] A. Boag, R. Taylor, T. Muster, N. Goodman, D. McCulloch, C. Ryan, B. Rout, D. Jamieson, A. Hughes, Stable pit formation on AA2024-T3 in a NaCl environment, Corrosion Science, 52 (2010) 90-103.
[26] G. Frankel, Pitting corrosion of metals: a review of the critical factors, Journal of the Electrochemical Society, 145 (1998) 2186.
[27] A.E. Hughes, R. Parvizi, M. Forsyth, Microstructure and corrosion of AA2024, Corrosion Reviews, 33 (2015) 1-30.
[28] R. Buchheit, M. Martinez, L. Montes, Evidence for Cu ion formation by dissolution and dealloying the Al_2CuMg intermetallic compound in rotating ring-disk collection experiments, Journal of The Electrochemical Society, 147 (2000) 119-124.
[29] N. Dimitrov, J. Mann, K. Sieradzki, Copper redistribution during corrosion of aluminum alloys, Journal of the Electrochemical Society, 146 (1999) 98.
[30] N. Wint, Z. Barrett, G. Williams, H. McMurray, The Study of AA2024 De-Alloying Using Luminol Electrogenerated Chemiluminescence Imaging, Journal of The Electrochemical Society, 166 (2019) C3417.
[31] F. Renner, A. Stierle, H. Dosch, D. Kolb, T.-L. Lee, J. Zegenhagen, Initial corrosion observed on the atomic scale, Nature, 439 (2006) 707-710.
[32] P.J. Denissen, A.M. Homborg, S.J. Garcia, Interpreting electrochemical noise and monitoring local corrosion by means of highly resolved spatiotemporal real-time optics, Journal of The Electrochemical Society, 166 (2019) C3275.
[33] L. Lacroix, L. Ressier, C. Blanc, G. Mankowski, Combination of AFM, SKPFM, and SIMS to study the corrosion behavior of S-phase particles in AA2024-T351, Journal of the Electrochemical Society, 155 (2008) C131-C137.
[34] R. Parvizi, A.E. Hughes, M.Y. Tan, R.K. Marceau, M. Forsyth, P. Cizek, A.M. Glenn, Probing corrosion initiation at interfacial nanostructures of AA2024-T3, Corrosion Science, 116 (2017) 98-109.
[35] O. Schneider, G. Ilevbare, J. Scully, R. Kelly, In situ confocal laser scanning microscopy of AA 2024-T3 corrosion metrology II. Trench formation around particles, Journal of The Electrochemical Society, 151 (2004) B465-B472.
[36] J. Xiao, S. Chaudhuri, Predictive modeling of localized corrosion: an application to aluminum alloys, Electrochimica Acta, 56 (2011) 5630-5641.
[37] L. Yin, Y. Jin, C. Leygraf, N. Birbilis, J. Pan, Numerical Simulation of Micro-Galvanic Corrosion in Al Alloys: Effect of Geometric Factors, Journal of the Electrochemical Society, 164 (2017) C75-C84.
[38] T.H. da Silva, E.B. Nelson, I. Williamson, C.M. Efaw, E. Sapper, M.F. Hurley, L. Li, First-principles surface interaction studies of aluminum-copper and aluminum-copper-magnesium secondary phases in aluminum alloys, Applied Surface Science, 439 (2018) 910-918.
[39] N. De Jonge, F.M. Ross, Electron microscopy of specimens in liquid, Nature nanotechnology, 6 (2011) 695.
[40] F.M. Ross, Opportunities and challenges in liquid cell electron microscopy, Science, 350 (2015).
[41] P. Abellan, T. Moser, I.T. Lucas, J. Grate, J. Evans, N. Browning, The formation of cerium (iii) hydroxide nanoparticles by a radiation mediated increase in local pH, RSC advances, 7 (2017) 3831-3837.
[42] T. Woehl, P. Abellan, Defining the radiation chemistry during liquid cell electron microscopy to enable visualization of nanomaterial growth and degradation dynamics, Journal of microscopy, 265 (2017) 135-147.
[43] T.J. Woehl, K.L. Jungjohann, J.E. Evans, I. Arslan, W.D. Ristenpart, N.D. Browning, Experimental procedures to mitigate electron beam induced artifacts during in situ fluid imaging of nanomaterials, Ultramicroscopy, 127 (2013) 53-63.
[44] N.M. Schneider, Electron Beam Effects in Liquid Cell TEM and STEM, in: F.M. Ross (Ed.) Liquid Cell Electron Microscopy, Cambridge University Press, Cambridge, 2016, pp. 140-163.
[45] S.W. Chee, M.G. Burke, Applications of Liquid Cell TEM in Corrosion Science, in: F.M. Ross (Ed.) Liquid Cell Electron Microscopy, Cambridge University Press, Cambridge, 2016, pp. 258-275.
[46] A. Kosari, H. Zandbergen, F. Tichelaar, P. Visser, H. Terryn, A. Mol, Application of In Situ Liquid Cell Transmission Electron Microscopy in Corrosion Studies: A Critical Review of Challenges and Achievements, Corrosion, 76 (2020) 4-17.

[47] S.W. Chee, D.J. Duquette, F.M. Ross, R. Hull, Metastable structures in Al thin films prior to the onset of corrosion pitting as observed using liquid cell transmission electron microscopy, Microsc. Microanal, 20 (2014) 462-468.
[48] S.W. Chee, J.-H. Park, A. Pinkowitz, B. Engler, F.M. Ross, D. Duquette, R. Hull, Liquid Cell TEM of Al Thin Film Corrosion under Potentiostatic Polarization, Microscopy and Microanalysis, 21 (2015) 973-974.
[49] S.W. Chee, S.H. Pratt, K. Hattar, D. Duquette, F.M. Ross, R. Hull, Studying localized corrosion using liquid cell transmission electron microscopy, Chemical Communications, 51 (2015) 168-171.
[50] J.W. Key, S. Zhu, C.M. Rouleau, R.R. Unocic, Y. Xie, J. Kacher, Investigating local oxidation processes in Fe thin films in a water vapor environment by in situ liquid cell TEM, Ultramicroscopy, 209 (2020) 112842.
[51] X.L. Zhong, S. Schilling, N.J. Zaluzec, M.G. Burke, Sample preparation methodologies for in situ liquid and gaseous cell analytical transmission electron microscopy of electropolished specimens, Microscopy and Microanalysis, 22 (2016) 1350-1359.
[52] S.C. Hayden, C. Chisholm, R.O. Grudt, J.A. Aguiar, W.M. Mook, P.G. Kotula, T.S. Pilyugina, D.C. Bufford, K. Hattar, T.J. Kucharski, Localized corrosion of low-carbon steel at the nanoscale, npj Materials Degradation, 3 (2019) 1-9.
[53] R. Buchheit, R. Grant, P. Hlava, B. McKenzie, G. Zender, Local dissolution phenomena associated with S phase (Al_2CuMg) particles in aluminum alloy 2024-T3, Journal of the electrochemical society, 144 (1997) 2621.
[54] T. Hashimoto, X. Zhang, X. Zhou, P. Skeldon, S. Haigh, G. Thompson, Investigation of dealloying of S phase (Al_2CuMg) in AA 2024-T3 aluminium alloy using high resolution 2D and 3D electron imaging, Corrosion Science, 103 (2016) 157-164.
[55] M. Vukmirovic, N. Dimitrov, K. Sieradzki, Dealloying and corrosion of Al alloy 2024 T 3, Journal of The Electrochemical Society, 149 (2002) B428-B439.
[56] J. Wang, B. Zhang, Y. Zhou, X. Ma, Multiple twins of a decagonal approximant embedded in S-Al_2CuMg phase resulting in pitting initiation of a 2024Al alloy, Acta Materialia, 82 (2015) 22-31.
[57] X. Zhang, T. Hashimoto, J. Lindsay, X. Zhou, Investigation of the de-alloying behaviour of θ-phase (Al_2Cu) in AA2024-T351 aluminium alloy, Corrosion Science, 108 (2016) 85-93.
[58] N. de Jonge, Theory of the spatial resolution of (scanning) transmission electron microscopy in liquid water or ice layers, Ultramicroscopy, 187 (2018) 113-125.
[59] S. Keskin, P. Kunnas, N. de Jonge, Liquid-phase electron microscopy with controllable liquid thickness, Nano letters, 19 (2019) 4608-4613.
[60] A. Boag, A. Hughes, N. Wilson, A. Torpy, C. MacRae, A. Glenn, T. Muster, How complex is the microstructure of AA2024-T3?, Corrosion Science, 51 (2009) 1565-1568.
[61] P. Yu, S.A. Hayes, T.J. O'Keefe, M.J. O'Keefe, J.O. Stoffer, The phase stability of cerium species in aqueous systems: II. The systems. Equilibrium considerations and pourbaix diagram calculations, Journal of the Electrochemical Society, 153 (2005) C74.
[62] L. Paussa, F. Andreatta, D. De Felicis, E. Bemporad, L. Fedrizzi, Investigation of AA2024-T3 surfaces modified by cerium compounds: a localized approach, Corrosion science, 78 (2014) 215-222.
[63] K.A. Yasakau, M.L. Zheludkevich, S.V. Lamaka, M.G. Ferreira, Mechanism of corrosion inhibition of AA2024 by rare-earth compounds, The Journal of Physical Chemistry B, 110 (2006) 5515-5528.

Supplementary Materials for Chapter 4

S4.1. Effect of the electron beam and sample artifacts

S4.1.1. Electron beam effect. The delivered energy as a result of inelastic electron scattering, albeit slightly heats the liquid cell, can convert water molecules into various radical species including hydrated electrons eh^-, hydrogen radicals $H^\bullet$, hydroxyl radicals $OH^\bullet$, H_2O_2 and H^+ [6, 7]. Given the radiolysis in the irradiated region, the solution chemistry experiences the changes that might modify the electrochemical processes. To lessen this issue, an effective way is to use a fluid flow that provides fresh electrolyte [2]. However, this can itself disturb the local solution chemistry established by the electrochemical processes. In our system, there is a gentle real flow (a few µL/min) that can somehow wash the radiolysis products away. Nevertheless, we, in this part, discuss the potential effect of the electron beam in order to better analyse the obtained results.

We conducted the experiments in STEM illumination mode through which point excitation takes place while scanning the focused electron probe over the liquid cell at each scan point [8]. It has been reported that local radical concentrations in STEM mode are highly dependent on the pixel dwell time, magnification and accelerating voltage [8]. Here, the in-situ liquid phase experiments are performed at the accelerating voltage of 300 keV that produces less radicals due to lower electron stopping power in water [1]. They are furthermore carried out at rather low magnifications (either 20000X or 28500X) and a low pixel dwell time (i.e., 0.2 µs for movies and 2 µs for taking images at critical moments). However, the main concern is here raised by using relatively high probe currents measured in vacuum; i.e., 1.409 nA. In fact, we resorted to such high currents in order to acquire a desirable signal-to-noise ratio (SNR) as we have used rather thick specimens to better represent the real corrosion [4]. Thus, we here discuss the effect of the plausible radicals to evaluate how they can disturb the current results. To do so, the E-pH diagrams of the present elements in the system are highly beneficial as they show the thermodynamically stable species as a function of potential and solution pH. Fig. S4.1 shows E-pH diagrams of copper, aluminium and magnesium in 0.01 M NaCl solution at $[M^{n+}]$ 10^{-6} M.

As reported by Woehl and Abellan [1], the electron beam cannot generate either net reducing or net oxidising conditions in 0.01 M NaCl; the radicals also interact with one another. The hydrated electrons eh^-, hydrogen radicals $H^\bullet$ can reduce the oxidised species. Considering the probable range of AA2024 corrosion potential in 0.01 M NaCl (highlighted-in-blue region), Al^{3+}, Mg^{2+} and $Al(OH)_4^-$ are the reducible corrosion products that can be formed in different solution pH [9]. However, they, if reduced to elemental state, immediately and spontaneously dissolve out owing to an electrochemical instability in the current solution. That is why we have not observed any beam-induced deposition in our results. In addition, at prolonged exposure when copper is released from the detached sub-micron clusters, Cu ions can also be reduced by eh^- and $H^\bullet$. However, we just observe nano-scale copper particles being

redeposited at the edge of the trench where the isolating passive layer is removed and the potential is sufficiently low for copper re-plating. This indicates that at the used illuminating condition, the number of reducing eh^- and $H^\bullet$ does not meet the threshold value that can trigger ion-beam deposition of the current species [8]. In addition, the detached free-standing Cu nanoparticles during corrosion of S-phase readily undergo anodic dissolution, further implying a non-reducing solution chemistry under illumination.

The oxidising agents of $OH^\bullet$, H_2O_2 are of particular importance as they can anodically polarize the specimen and speed up the kinetics of corrosion. Although it has been reported that H_2O_2 (6 g/litre) insignificantly increase the corrosion potential of S-phase and θ-phase [10], its effect on the specimen corrosion potential should be discussed. The radical concentrations rise with prolonged irradiation time. But the enrichment of the corroding IMPs in copper is the main cause of the increase in corrosion potential, changing the dealloying morphology which is potential-dependent [11, 12]. On the other hand, the in-situ observations show that the major copper liberation does not happen as long as the particle is still attached to the matrix. This implies that the oxidising radicals might increase the corrosion potential but surely not above the redox potential of Cu/Cu^+. In addition, other oxidising species like $Cl^\cdot$, $Cl_2^{\cdot-}$ and $HClO^\cdot$, that can form complexes with noble metals like silver and gold [1], but they cannot influence the current systems as $CuCl_2^-$ that are highly soluble can also be present in the chloride containing solutions. Since the dealloying time-scale of θ-phase is longer than that of S-phase, we fully avoided continuous capturing for top-view observations (Fig. 4.6a), just taking snapshots. For cross-sectional observations of θ-phase (Fig. 4.6d), we started to capture when we observed a clear sign of the corrosion initiation attack.

The main concern in this work was related to the possible effect of the electron beam on the solution pH. It has theoretically been estimated that acidic solutions are less affected by the electron beam whereas neutral and alkaline solutions might acidify in the presence of the electron beam [7]. We can discuss this matter by considering different local corrosion sites. Abellan et al. [13] have recently calculated the pH evolution of water as a consequence of continuous STEM imaging; an extremely high dosage (i.e., 10^9 Gy/s) cannot drop an initial near neutral pH lower than 4. In such condition, $Al(OH)_3$ that play a crucial role in the passivation of corrosion can still be stable. On the other hand, the pH in the confined regions like the trenches and pores is greatly acidic due to the hydrolysis of hydrated cations [14], not being affected by the electron beam. It should be noted that Cl^- is reported to be $OH^\bullet$ and $H^\bullet$ scavenger in acidic solutions [1]. Thus, the solution pH in these regions would be less affected by the electron beam. However, there are regions like the top part of the intermetallic particles which support cathodic reactions that establish alkalinity. Thus, the production rate of OH^- by the electrochemical reactions and H^+ by the electron beam can greatly change the balance. In the case of S-phase, the anodic dissolution of the corroding particle and alloy matrix goes relatively fast and hence more OH^- would be produced by the balancing cathodic reactions, as compared to θ-phase in the same

time-scale. Thus, to mitigate this effect, continuous exposure of the solution to the electron beam was avoided and the critical early stages of θ-phase dealloying was observed merely by taking snapshots.

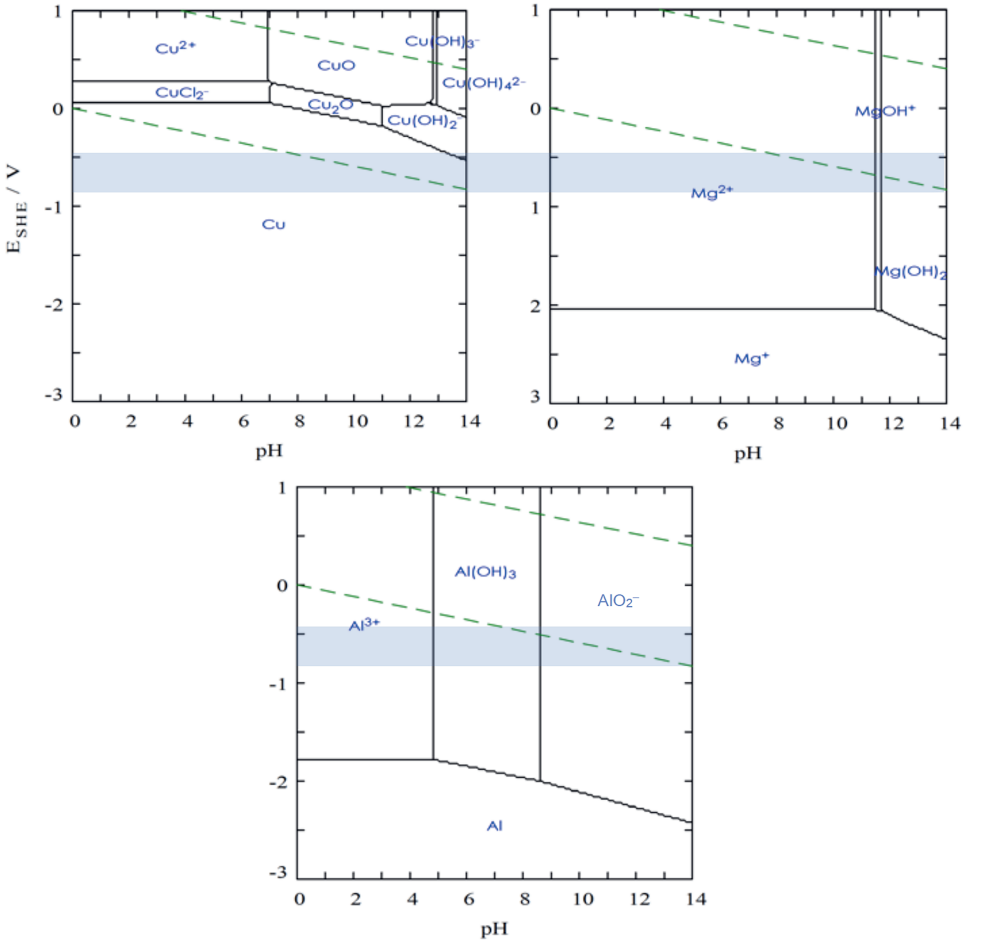


Fig. S4.1. E-pH diagrams. Simplified Eh-pH diagram of Cu, Mg, Al and Ga in 0.01 M NaCl solution at 25 °C. Note that the diagrams are plotted at 1 μM of [Cu^{2+}], [Mg^{2+}] and [Al^{3+}]. Medusa-Hydra software was used to make the diagrams.

S4.2. Sample artifacts effect. In this work, we have used a Ga ion FIB to prepare the specimens for in-situ liquid phase STEM studies. In spite of careful considerations during the preparation and sample transfer, Ga implantation into the specimen is plausible. Reportedly, Ga can reach approx. 5-10 nm from the top surface of the specimen and might accumulate particularly at grain boundaries and particle/matrix interfaces [15, 16]. This phenomenon can surely change the chemistry of the alloy and since Ga is reported to increase anodic electrochemical activity of aluminium [17], it may influence our

results as well in terms of initiation kinetics of corrosion. However, our EDS analysis on the prepared lamellae has revealed 0.1-0.5 at% Ga of target regions. Regarding the E-pH diagram, we can expect that the implanted Ga dissolves away at the initial stages of corrosion [18]. Accumulated at the particle/matric interface, gallium would be highly soluble in acidic and basic solutions. There is also the possibility of Ga_2O_3 as a deposit which probably shows cathodic activity to the alloy matrix; however, its role would be negligible due to a huge amount of copper which is significantly more noble than gallium.

S4.2. In-situ liquid phase corrosion, more evidence obtained with STEM

S4.2.1. S-phase. Here we present more evidence for the critical findings in this work. Fig. S4.2 shows top-view HAADF-STEM images of a pre-dealloyed Al_2CuMg particle that induce the matrix trenching with time. There is no mask applied on this specimen and it interacts with the electrolyte on both sides. As can be seen, the corroded particle starts to trench the matrix until the disconnection happens ($t\text{-}t_0$ = 5 min). Then the cluster of copper particles appears gradually at the edge of the trench which is electrochemically active. These observations prove that the copper-retribution process occurs right after the particle detachment whereby the remnant can adopt its free corrosion potential at which copper can thermodynamically dissolve.

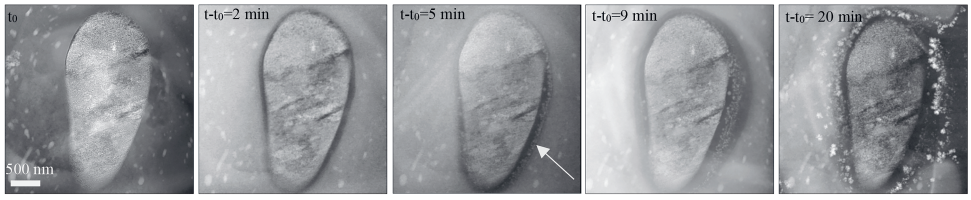


Fig. S4.2. Trenching and copper redistribution induced by a dealloyed S-phase. Time-resolved top-view HAADF-STEM observations of an Al_2CuMg particle exposed to 0.01 M NaCl solution at 300 keV. Notice that the particle has already undergone de-alloying at time t_0. Clusters of re-distributed nano-scale copper particles are indicated by white arrow. The lamella is approximately 250 nm thick and the electrolyte is fully stagnant.

***S4.2.2.* θ-phase.** Due to having a high amount of copper, Al_2Cu particles are reported to have a higher corrosion potential than the alloy matrix, showing a cathodic activity that induces the trenching form of corrosion to the adjacent matrix [19]. However, what we found out herein is the opposite. Unlike the traditional explanation, the corrosion initiates via a preceding dealloying attack to both anodic and cathodic intermetallic particles. Fig. S4.3 shows the initial stages of the dealloying attack to an Al_2Cu particle. As can be seen, the process starts by corroding the particle, not the matrix, meaning that the selective aluminium corrosion happens earlier than the passive layer breakdown. The dealloying morphology shows up in a globular appearance due to simultaneous copper surface diffusion and

selective aluminium dissolution. With prolonged time, we clearly see copper accumulation in the form of clusters of nano-scale particles over the intermetallic particle. This later leads to gradual trenching of the matrix through nanogalvanic establishment.

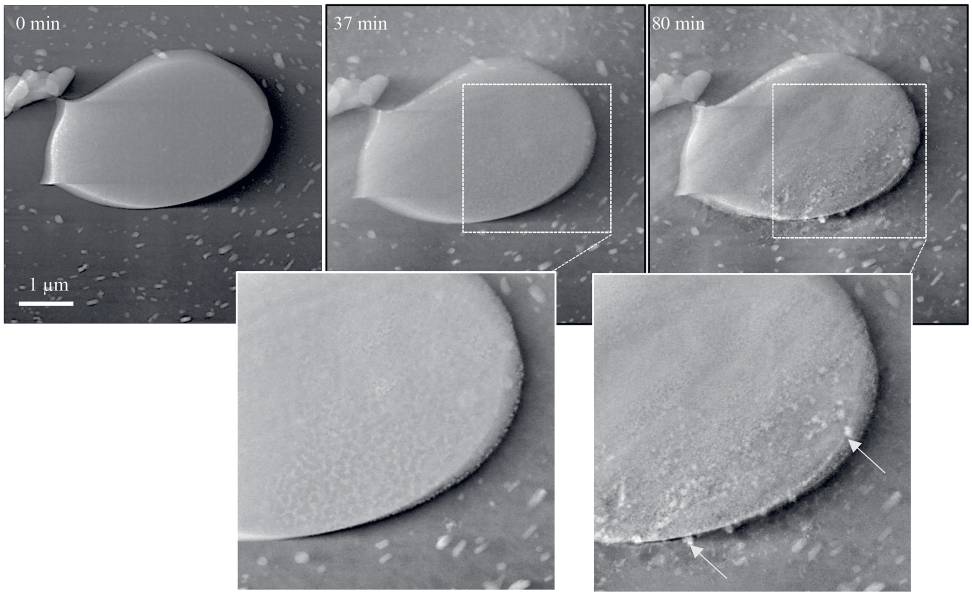


Fig. S4.3. Early stages of θ-phase corrosion. Top-view HAADF-STEM observations of a 250-nm-thick Al_2Cu particle exposed to 0.01 M NaCl solution at 300 keV. The insets are the magnified images of the rectangular region after 37 and 80 min. The white arrows indicate the nano-scale copper particles formed on/at the edge of the intermetallic particle. Note that the specimen is bare to the solution on both sides.

S4.3. Quasi in-situ TEM examinations on argon ion-milled thin specimens

Regarding the potential impact of the electron beam and sample artifacts and also to acquire detailed compositional information, we have carried out quasi in-situ examinations in parallel to support the findings through in-situ observations. To do so, argon ion-milled thin disks were used where sample artifacts are minimized. Quasi-in-situ HAADF-STEM examinations are comparable with top-view liquid phase observations and here they are in full agreement with the related findings. Since, there are no Ga artifacts and also the electron-beam effect is absent, we can claim that the electron beam insignificantly influences the in-situ results.

S4.3.1. S-Phase. Fig. S4.4a shows HAADF-STEM images of an Al_2CuMg particle before and after 20-min exposure to distilled water. Fig. S4.4b shows STEM/EDS investigations of the pits formed on the particle, indicating that the dealloying happens to S-phase even in the absence of chloride ions owing to its electrochemical instability. As can be seen, the selective dissolution of aluminium and magnesium have occurred while copper radially diffuses towards the rim of the pits [20]. It should be noted that the

HAADF-STEM image is darker in contrast inside the pits due to removal of mass by dissolution. Fig. S4.4c shows STEM/EDS analysis at the particle/matrix interface (rectangular region). As is evident, there is a row of pits at the particle/matrix interface (note the O map). Besides, a few pits are seen on the matrix; the region is circled in white.

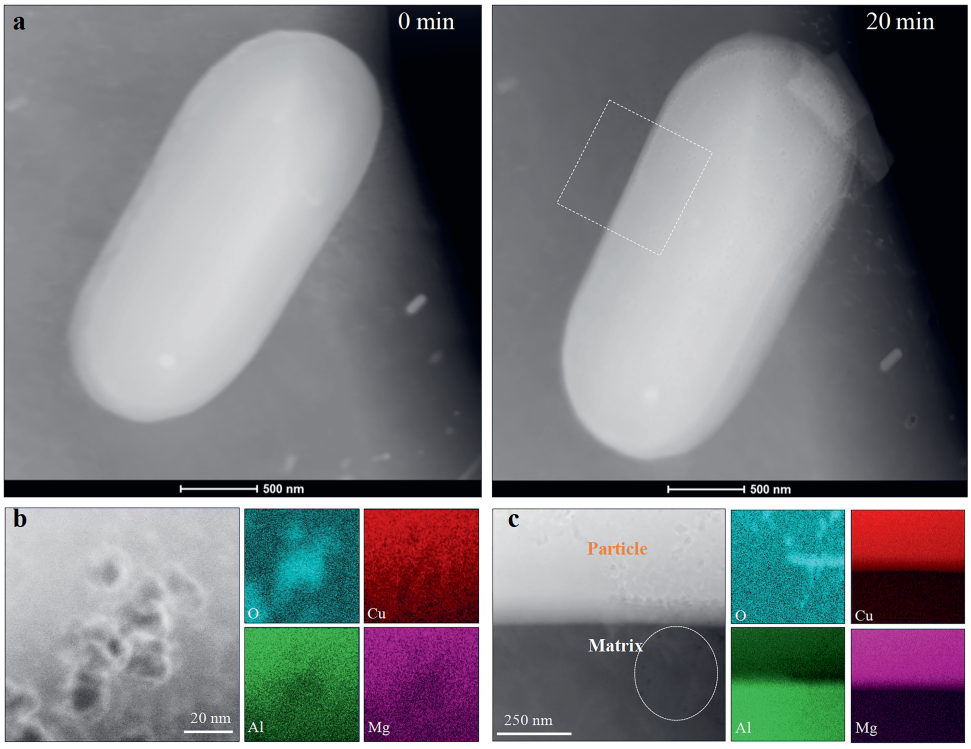


Fig. S4.4. Quasi in-situ TEM analysis of S-phase in distilled water. (a) HAADF-STEM images of an Al_2CuMg particle in distilled water. (b) STEM/EDS analysis of the pits formed on the particle after 20 min. (c) STEM/EDS analysis of the rectangular region at the particle/matrix interface. The specimen is an argon ion-milled 3-mm disk.

Fig. S4.5a shows time-resolved HAADF-STEM/EDS observations of an Al_2CuMg particle composed of three grains exposed to 0.01 M NaCl. As expected, the particle becomes depleted from magnesium and aluminium with time; it is almost empty of magnesium (0.2 at%) and contains approx. 6.3 at% after 30 min. Note that the particle is still connected to the alloy matrix and the copper redistribution process has not occurred. Fig. S4.5b demonstrates zoomed-in STEM images of the middle part of the particle (Region I), where the triple junction is located, at the same exposure times as Fig. S4.5a. As can be seen, there are several pits formed over the different grains and also at the grain boundaries and triple junction. The pits which are a consequence of selective dissolution (dealloying), spread over the particle

with time until we see a nano-porous structure appearing after 30 min. Notice that the grains and grain boundaries are not distinguishable any longer owing to atomic rearrangement of copper during the dealloying process.

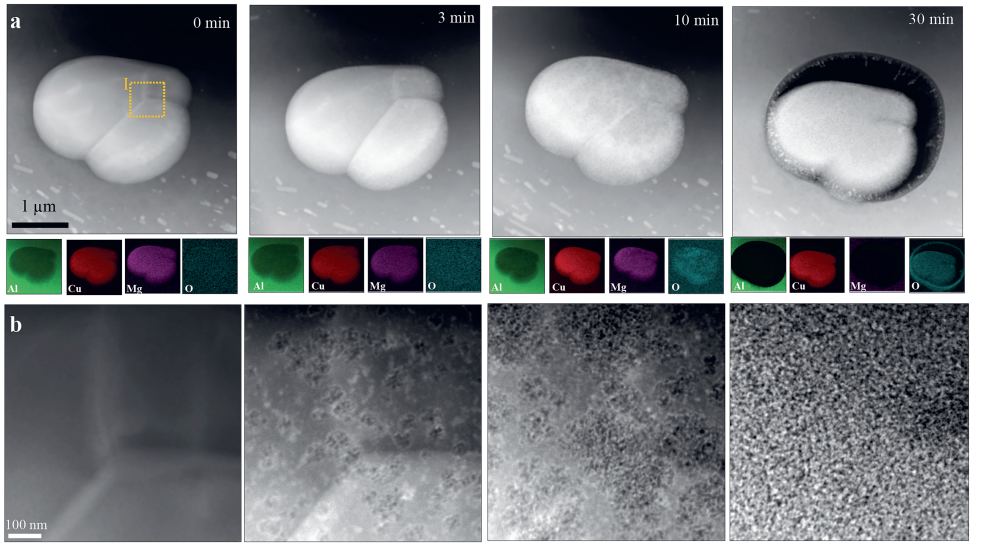


Fig. S4.5. Quasi in-situ TEM analysis of S-phase in 0.01 M NaCl. (a) Time-resolved STEM images and corresponding EDS maps at different exposure time. (b) Magnified STEM images of the central part of the particle (Region I) at the same exposure times. The specimen is an argon ion-milled 3-mm disk.

S4.3.2. **θ-phase.** Fig. S4.6a shows time-resolved HAADF-STEM images along with elemental aluminium maps of an Al_2Cu particle at different exposure times. Going through the sequence, we observe that the particle itself evolves morphologically and compositionally with time as a result of the dealloying attack. After 45 min, we observe several regions at the particle/matrix interface in which corrosion has taken place (Region I). The magnified STEM image at this stage (Fig. S4.6b) reveals wider expansion of corrosion in the particle rather than the matrix. With prolonged exposure, we clearly see the build-up of a trench around the particle. Note that the matrix trenching initiates around the corroded region on the particle after 45 min. The EDS map reveals how the corrosion depletes the particle from aluminium. After 150 min, the particle still contains approx. 5 at% aluminium. Fig. S4.6b, c and d show the transition from a globular dealloying morphology to a completely nano-porous microstructure.

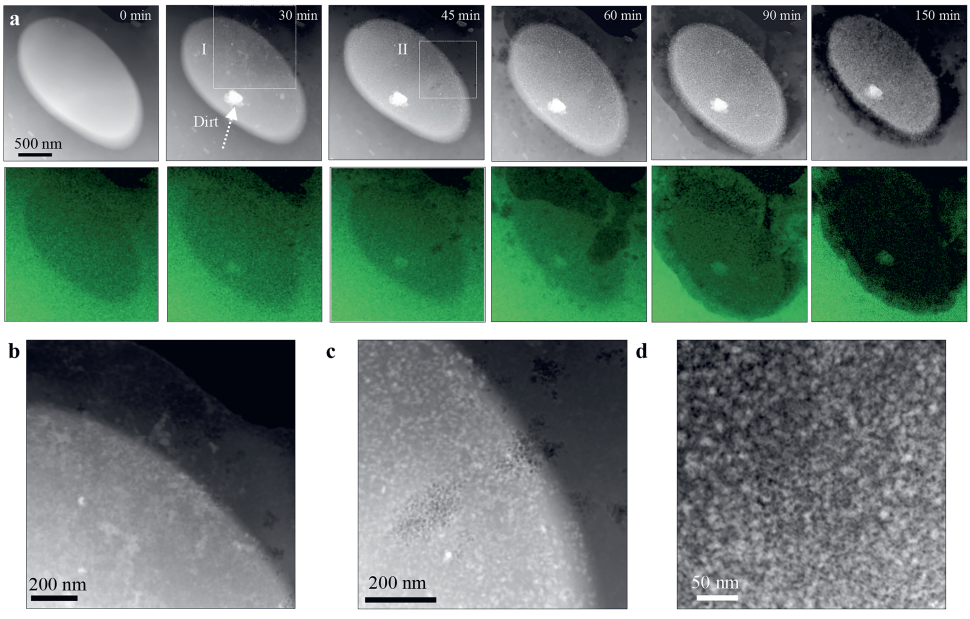


Fig. S4.6. Quasi in-situ TEM analysis of θ-phase in 0.01 M NaCl. (a) Time-resolved STEM images and corresponding aluminium map at different exposure time. (b) Magnified STEM image taken from the particle/matrix interface after 30 min (Region I). (c) Magnified STEM image taken from the particle/matrix interface after 45 min (Region II). (d) Magnified STEM image of the particle after 150 min, showing the established nano-porous structure. The specimen is an argon ion-milled 3-mm disk.

S4.4. Ex-situ TEM examinations on FIB-made cross-sections

To further evaluate the in-situ observations, we immerse the bulk AA2024-T3 samples to 0.01 M NaCl solution for different exposure times. The surface morphology of the corroded regions at the intermetallic sites was examined with SEM. Then thin cross-sections were fabricated out of particles of interest with FIB and lift-out procedure. The ex-situ examinations are compared with cross-sectional-view in-situ HAADF-STEM.

S4.4.1. S-Phase. Fig. S4.7a shows an Al_2CuMg particle exposed to 0.01 M NaCl for 15 min. The SEM image shows that a narrow trench around the particle while no nano-scale copper particles observed. Cross-sectional STEM image reveals that the corroding particle is partially-dealloyed. The inset is the magnified STEM image of the dealloyed part of the particle. As indicated by the red dashed line, there is a high porosity rim on the top of the particle. In-situ observations revealed that the copper ligament of this porous rim get detached due to egress of the corrosion products and then undergo corrosion followed by redeposition on the top of the same particle. This phenomenon leads to the establishment of a layer of nano-scale copper particles on the top of the corroding intermetallic particle with prolonged immersion time. Fig. S4.7b confirms this fact as we see a copper-rich layer on the top of the corroded particle right before the disconnection from the matrix. Note that both Al_2CuMg particles investigated

here are exposed for the same exposure time, however corrosion has occurred in lager extent to the particle with smaller size.

Fig. S4.7c shows an Al_2CuMg particle exposed for 6 h to 0.01 M NaCl. The top-view SEM clearly reveals a deep trench where the clusters of sub-micron Cu-rich particles are nestled in the matrix and within the trench. The white arrow shows the locations at which the breakdown has happened after the particle detachment form the matrix; compare the particle surface with that of the partially-dealloyed particle in Fig. S4.7a. We could record this moment at which the breakdown happens with in-situ liquid phase STEM observations. The SEM image when the stage is tilted at 52 degree reveals that the corroded particle and the matrix are not at the same level.

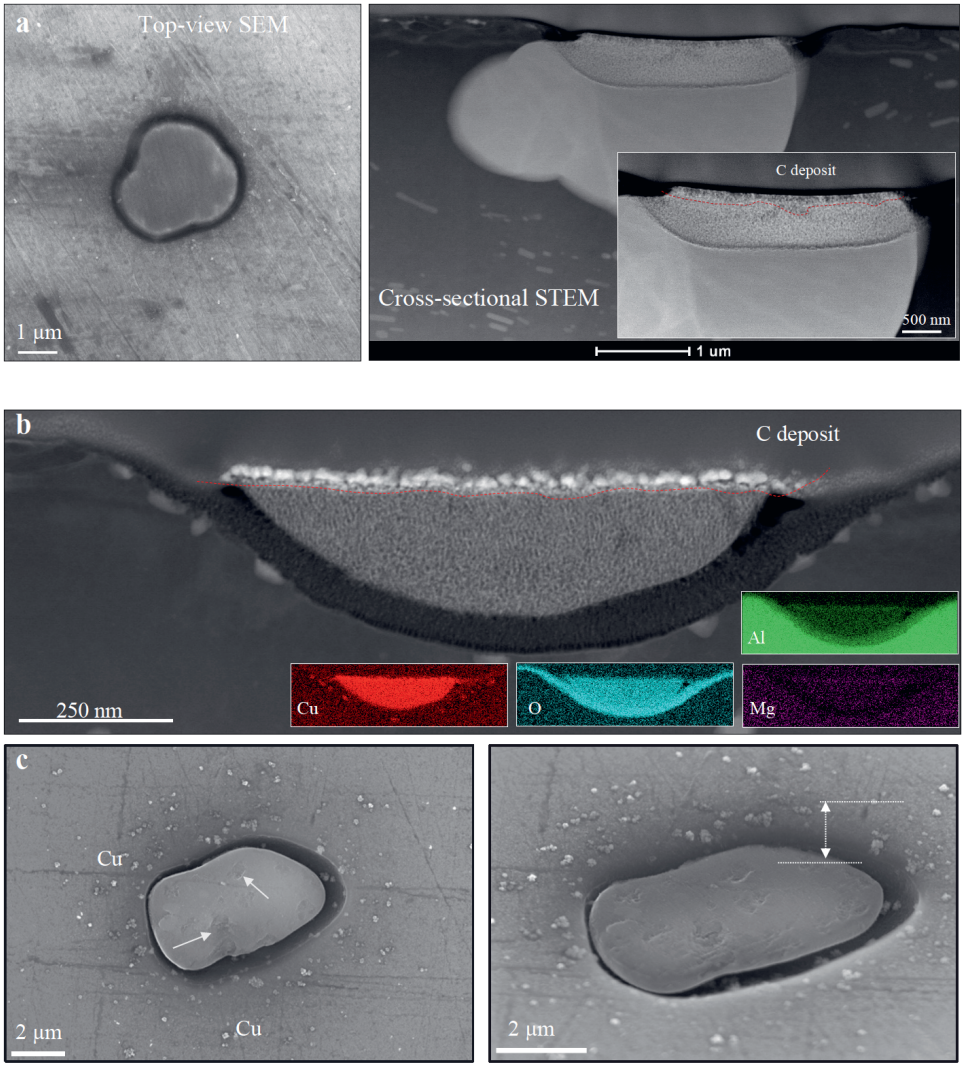


Fig. S4.7. Ex-situ analysis of S-phase in 0.01 M NaCl. (a) Top-view SEM and cross-sectional STEM analysis of an Al_2CuMg particle immersed in 0.01 M NaCl for 15 min. (b) STEM/EDS analysis of the cross-section of an Al_2CuMg particle immersed in 0.01 M NaCl for 15 min. (c) (left) Top-view SEM morphology of an Al_2CuMg particle exposed to 0.01 M NaCl for 6 h. (right) SEM image of the same particle when the stage is 52-degree tilted.

S4.4.2. θ-phase. Fig. S4.8a shows top-view SEM and cross-sectional STEM images of an Al_2Cu particle exposed to 0.01 M NaCl for 15 min. As can been seen, a narrow trench has formed around the particle which is half-dealloyed, itself. The inset is the magnified STEM image of the dealloyed part of the particle. Fig. S4.8b shows another Al_2Cu particle exposed for the same exposure time.

Comparatively, this particle is dealloyed deeper in the middle while the shallow trenches are seen on the sides (note the magnified image). The EDS map reveals the corroded part is depleted from aluminium while the no copper intensity change is observed over the corroded and intact part. Fig. S4.8c shows an Al_2Cu particle exposed for 19 h to 0.01 M NaCl. The top-view SEM clearly shows a deep trench where no copper particles observed in the proximity of the intermetallic particle. The upper inset shows the magnified SEM image of the rectangular region on the particle, showing a rough surface morphology; compare this surface with that of the partially-dealloyed particle in Fig. S4.8a. The cross-sectional SEM image of the particle reveals that expectedly the particle is fully dealloyed where a cluster of Cu-rich particles indicated by the white arrow (verified by SEM/EDS analysis) is deposited at the bottom of the trench; note that the stage is tilted at 52 degree. In-situ STEM observations revealed that such copper clusters are released from the particle after the disconnection.

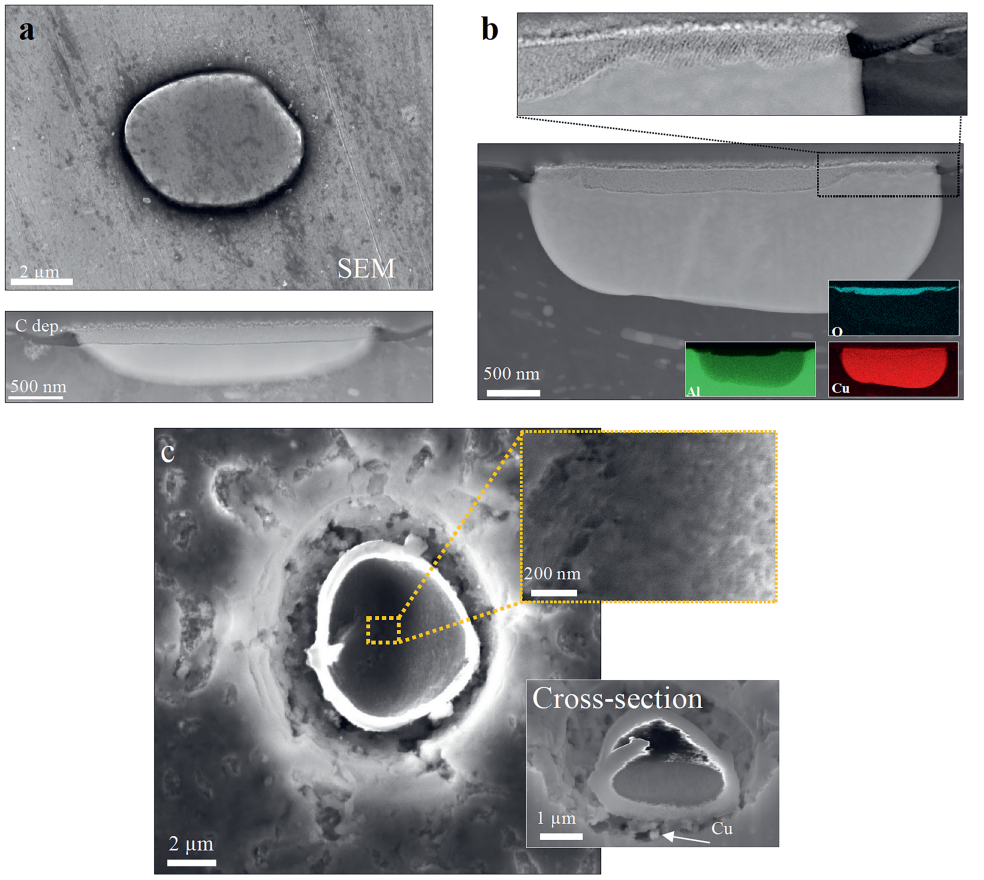


Fig. S4.8. Ex-situ analysis of θ-phase in 0.01 M NaCl. (a) Top-view SEM and cross-sectional STEM analysis of an Al_2Cu particle immersed in 0.01 M NaCl for 15 min. (b) STEM/EDS analysis of the cross-section out of an Al_2Cu particle immersed in 0.01 M NaCl for 15 min. (c) Top-view SEM image of an Al_2Cu particle exposed to 0.01 M NaCl for 19 h. The upper inset is the magnified SEM image of the rectangular region on the particle. Cross-sectional SEM image of the same particle, revealing a cluster of nano-scale Cu-rich particles deposited at the bottom of the trench. FIB milling was used to cut through the corroded particle.

S4.4.3. Clusters of nano-scale Cu-rich particles. Fig. S4.9 shows a circular pit formed on the alloy matrix; it has the diameter of 8 µm. An intermetallic particle was likely located here but the remnant has fallen out of the trench. The magnified inset reveals the presence of Cu-rich clusters at the bottom of the pit (verified by SEM/EDS analysis), corroding the adjacent matrix. This is exactly what we observe in Fig. 4.9 and Movie S6.

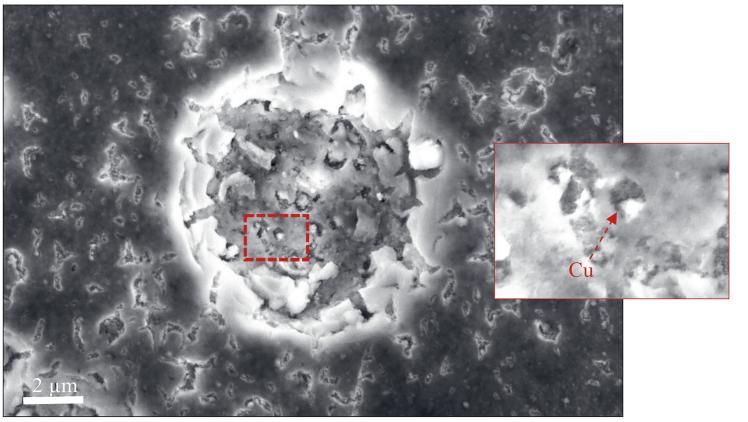


Fig. S4.9. The role of clusters of Cu-rich particles in corrosion propagation. Top-view SEM of a pit formed on AA2024-T3 surface in 0.01 M NaCl after 19 h. The inset is the magnified SEM image of the rectangular region at the bottom of the pit.

Supplementary References

[1] T. Woehl, P. Abellan, Defining the radiation chemistry during liquid cell electron microscopy to enable visualization of nanomaterial growth and degradation dynamics, Journal of microscopy, 265 (2017) 135-147.
[2] T.J. Woehl, K.L. Jungjohann, J.E. Evans, I. Arslan, W.D. Ristenpart, N.D. Browning, Experimental procedures to mitigate electron beam induced artifacts during in situ fluid imaging of nanomaterials, Ultramicroscopy, 127 (2013) 53-63.
[3] S. Keskin, P. Kunnas, N. de Jonge, Liquid-Phase Electron Microscopy with Controllable Liquid Thickness, Nano Letters, (2019).
[4] N. de Jonge, Theory of the spatial resolution of (scanning) transmission electron microscopy in liquid water or ice layers, Ultramicroscopy, 187 (2018) 113-125.
[5] N. De Jonge, F.M. Ross, Electron microscopy of specimens in liquid, Nature nanotechnology, 6 (2011) 695.
[6] N.M. Schneider, Electron Beam Effects in Liquid Cell TEM and STEM, in: F.M. Ross (Ed.) Liquid Cell Electron Microscopy, Cambridge University Press, Cambridge, 2016, pp. 140-163.
[7] N.M. Schneider, M.M. Norton, B.J. Mendel, J.M. Grogan, F.M. Ross, H.H. Bau, Electron–water interactions and implications for liquid cell electron microscopy, The Journal of Physical Chemistry C, 118 (2014) 22373-22382.
[8] T.J. Woehl, J.E. Evans, I. Arslan, W.D. Ristenpart, N.D. Browning, Direct in situ determination of the mechanisms controlling nanoparticle nucleation and growth, ACS nano, 6 (2012) 8599-8610.
[9] A.E. Hughes, R. Parvizi, M. Forsyth, Microstructure and corrosion of AA2024, Corrosion Reviews, 33 (2015) 1-30.
[10] R. Buchheit, A compilation of corrosion potentials reported for intermetallic phases in aluminum alloys, Journal of the Electrochemical Society, 142 (1995) 3994-3996.
[11] N. Dimitrov, J. Mann, M. Vukmirovic, K. Sieradzki, Dealloying of Al_2CuMg in alkaline media, Journal of The Electrochemical Society, 147 (2000) 3283.
[12] K. Wagner, S. Brankovic, N. Dimitrov, K. Sieradzki, Dealloying below the critical potential, Journal of the Electrochemical Society, 144 (1997) 3545.
[13] P. Abellan, T. Moser, I.T. Lucas, J. Grate, J. Evans, N. Browning, The formation of cerium (iii) hydroxide nanoparticles by a radiation mediated increase in local pH, RSC advances, 7 (2017) 3831-3837.
[14] G. Frankel, Pitting corrosion of metals a review of the critical factors, Journal of the Electrochemical Society, 145 (1998) 2186-2198.
[15] J. Mayer, L.A. Giannuzzi, T. Kamino, J. Michael, TEM sample preparation and FIB-induced damage, MRS bulletin, 32 (2007) 400-407.
[16] K.A. Unocic, M.J. Mills, G. Daehn, Effect of gallium focused ion beam milling on preparation of aluminium thin foils, Journal of microscopy, 240 (2010) 227-238.
[17] E. Senel, K. Nisancioglu, Effect of small concentrations of gallium and lead on anodic activation of aluminium in chloride solution, Corrosion Science, 131 (2018) 330-339.
[18] G.G. Perrault, Thermodynamics of gallium arsenide electrodeposition, Journal of The Electrochemical Society, 136 (1989) 2845-2849.
[19] X. Zhang, T. Hashimoto, J. Lindsay, X. Zhou, Investigation of the de-alloying behaviour of θ-phase (Al_2Cu) in AA2024-T351 aluminium alloy, Corrosion Science, 108 (2016) 85-93.
[20] J. Erlebacher, M.J. Aziz, A. Karma, N. Dimitrov, K. Sieradzki, Evolution of nanoporosity in dealloying, Nature, 410 (2001) 450.

CHAPTER 5

QUASI IN-SITU AND EX-SITU OBSERVATIONS OF LOCAL CORROSION INDUCED BY INTERMETALLIC CONSTITUENT PARTICLES AND DISPERSOIDS[1]

Nanoscopic characterisation of heterogeneous intermetallic particles (IMPs) which microstructurally and compositionally evolve during local corrosion is crucial in unravelling the mechanisms and sequence of initial and local corrosion events. In this chapter, we study site-specific initiation events focused on microscopic constituent intermetallic compounds and nanoscopic dispersoids in AA2024-T3 at the nanoscale using a combination of quasi in-situ and ex-situ analytical TEM approaches. Our findings show a dealloying-driven local corrosion initiation at the studied IMPs that have been considered as cathodic phases traditionally. Besides, local degradation which is a result of galvanic interactions between dealloyed regions of IMPs and their adjacent alloy matrix is largely governed by the intrinsic electrochemical instability of intermetallic compounds.

Keywords: Aerospace aluminium alloys; Quasi in-situ TEM; Cross-sectional ex-situ TEM; FIB/SEM analysis; Dealloying; Pitting corrosion

[1] **A. Kosari**, F. Tichelaar, P. Visser, H. Zandbergen, H. Terryn, A. Mol, Dealloying-driven local corrosion by intermetallic constituent particles and dispersoids in aerospace aluminium alloys, Corrosion Science, 177 (2020) 108947.

5.1. Introduction

Microstructurally complex aluminium alloys (AAs) constitute a structural material class with an essential high-strength-to-weight ratio, desirable for aerospace applications [1]. However, aerospace AAs are undesirably prone to different types of electrochemical degradation as a direct consequence of microstructural heterogeneities [2-10]. Given the pivotal importance of engineering safety in aerospace structures, detailed understanding must be acquired to describe microstructurally detrimental corrosion descriptors in deterministic terms where the literature still lacks a comprehensive mechanism [11].

Corrosion in aerospace AAs is inherently site-specific, commonly initiating in the form of localised attack at individual IMP locations [9, 12-15] where the surrounding alloy surface is covered by a protective aluminium (hydr)oxide passive layer [16, 17]. Intermetallic compounds are in fact precipitates, constituent phases and dispersoids with diverse chemical composition in a wide range of dimensions from the nano- to microscale. Precipitates like Al_2CuMg and Al_2Cu emerge in response to age hardening processes and greatly contribute to the mechanical strength enhancement in aerospace AAs [18, 19]. Comparatively, constituent phases are formed during solidification at high temperatures and normally not affected by subsequent heat treatments, having a minor contribution to mechanical properties [20, 21]. In addition, they are relatively large (>1 μm), irregularly-shaped and rather diverse in chemical composition, containing different amounts of Al, Cu, Fe, Mn and Si and characteristically crystallising in a variety of atomic structures [22]. Dispersoids like $Al_{20}Mn_3Cu_2$ are formed purposefully in the melt for grain refinement, commonly having a submicron size and being nodular-shaped [23].

For many years, electrochemical and physicochemical studies of intermetallic compounds have brought the researchers to the conclusion that local corrosion in AAs is mainly a consequence of microgalvanic interactions of IMPs with one another or mainly with the alloy matrix in their vicinity [24, 25]. Given that electrochemical reactivity is linked to chemical composition [26-29], IMPs acquire different corrosion potential than the alloy matrix when exposed to aqueous solutions [30-33]. Constituent IMPs (i.e., Al_7Cu_2Fe, $Al_{20}Mn_3Cu_2$ and $Al_{76}Cu_6Fe_7Mn_5Si_6$) are generally reported as potential cathodic phases that support cathodic reactions like oxygen reduction reaction (ORR) upon exposure, owing to a higher corrosion potential (Volta potential) than that of the alloy matrix [5, 34-36]. This process will establish a locally basic solution chemistry in which the aluminium (hydr)oxide passive layer is undermined gradually. Such electrolyte conditions can give rise to local dissolution of the surrounding matrix commonly in the form of a circumferential trench around the IMP. This form of local dissolution, known as trenching, is reportedly governed by the intrinsic cathodic activity of the cathodic compounds [9, 37]. This is in contrast to the process for anodic particles that endure self-corrosion and would be pitting locations themselves, as the surrounding matrix drives anodic dissolution of the phases of relevance (i.e., $MgZn_2$ [38] and Mg_2Si [39, 40]).

However, recent studies with experimental techniques granting a high spatial resolution have provided new insights into incongruent behaviour of cathodic phases and seemingly similar to anodic phases, they show to undergo self-corrosion at very early stages of the exposure to aqueous environments. For

instance, Zhang et al. [41] and Wang et al. [42], who used ex-situ transmission electron microscopy (TEM) to study corrosion of Al-Cu-Mg alloys, have reported the preferential dissolution of Al and Mn from $Al_{20}Cu_2Mn_3$ particles at very early stages of exposure, triggered by structural planar defects like twin boundaries. Al_2Cu particles have also been reported to show a tendency for selective aluminium dissolution (dealloying) and found partially dealloyed when embedded in the alloy matrix [43]. Recently Frankel and co-workers [44] were able to probe the early stages of IMPs-induced local corrosion, using a combined scanning electron microscopy/scanning Kelvin probe force microscopy (SEM/SKPFM) approach. In line with their prior works [45, 46], they indicated that preferential dissolution of the active element aluminium in Al_7Cu_2Fe(Mn) takes place at a faster rate than the matrix dissolution. Such observations challenge the traditional microgalvanic coupling concept based on difference in corrosion potential [32] (or Volta potential [47]) of IMPs with respect to the alloy matrix. However, in spite of the recent findings, the literature still lacks a thorough mechanistic description of how local corrosion initiates and propagates around dispersoids and constituent phases at different stages of degradation. Thus, time-resolved nanoscopic information which is crucial for reliable and accurate corrosion modelling and simulations to predict the service lifetime of AA structures are yet to be achieved [36, 48].

In this work, we continue the endeavour towards deterministic characterisation of time-resolved local corrosion focused on macroscopic constituent intermetallic compounds and nanoscopic dispersoids conventionally categorised as cathodic phases in aerospace AA2024-T3. A challenge in this regard is to provide nanoscopic observations and analysis of microstructurally and compositionally evolutions during different stages of local corrosion at the same location. To this aim, quasi in-situ TEM is a potentially powerful approach and has been widely used in recent studies of corrosion [40, 49-52]. As a drawback, quasi in-situ TEM has to be conducted on electron-transparent thin specimens which can merely represent very initial stages of corrosion [53]. Therefore, in this study we combine it with cross-sectional ex-situ TEM experiments and also supplementary focused ion beam/scanning electron microscopy (FIB/SEM) morphological investigations to explore local degradation phenomena in AAs from surface initiation to in-depth propagation.

5.2. Material and Methods

5.2.1. Top-view quasi in-situ TEM. This part of the experiments was carried out by intermittently observing an identical location on argon ion-milled thin specimens exposed to 0.01 M NaCl solution outside the electron microscope. After each exposure event, the specimens were rinsed off with distilled water for a few seconds. Then, water on the specimens was immediately absorbed by delicate-task wipes and dried under a lamp. The specimens were subjected to plasma-cleaning for 5 min right before re-inserting into the TEM column. A Tecnai F20ST/STEM 200 keV was employed to perform typical high-angle annular dark field/scanning TEM (HAADF/STEM) imaging, energy dispersive spectroscopy (EDS) elemental mapping and also high resolution TEM imaging. Note that HAADF-

STEM images are highly sensitive to variations in the effective atomic numbers (Z-contrast and local thickness) in the studied regions [54]. For energy dispersive spectroscopy (EDS) elemental mapping, an Oxford Instruments X-Max^N 100TLE windowless detector was used.

5.2.2. Cross-sectional ex-situ TEM. AA2024-T3 sheets were hand-ground down to 1200 emery paper in water, followed by polishing using 0.5 and 0.05 µm alumina slurry in a non-aqueous solution on a soft cloth. The samples were immersed in quiescent 0.01 M NaCl solution for different exposure times, followed by rinsing with distilled water. Subsequently, the surface corrosion-attack morphology of the samples was examined with SEM. Afterward, thin cross-sections of specific corroded particles were fabricated with a Thermo Fisher Helios G4 FIB and positioned on copper half grids for later TEM examinations using a dedicated lift-out procedure [55]. To protect the corroded surfaces while gallium ion-milling, a 200-nm-thick layer of carbon was deposited initially with a 2-keV electron beam, followed by ion-beam deposition until reaching a carbon thickness of approx. 1 µm. Although quasi in-situ top-view observations are highly useful to probe the early-stage initiation events, the cross-sectional investigations reveal the local corrosion propagation deeper into the sample.

5.2.3. FIB/SEM investigations. FIB/SEM serial cross-sectioning was performed on corroded IMPs in a polished sample exposed to 0.01 M NaCl for 19 h. The top-view and cross-sectional SEM morphological studies were carried out at 5 keV collecting emitted secondary electrons (SE) in ultra-high-resolution mode. FIB sectioning was conducted in a blind-mode; the ion beam was used merely for cross-sectional milling. This allows us to skip doing Pt or C deposition for protection of the top surface from ion-beam damage.

5.3. Results and Discussion

5.3.1. Isolated constituent $Al_{76}Cu_6Fe_7Mn_5Si_6$. Fig. 5.1a shows a time-resolved morphological evolution of local corrosion induced by an $Al_{76}Cu_6Fe_7Mn_5Si_6$ particle; this is the approximate composition determined with STEM/EDS. After 30 min, HAADF-STEM shows no apparent corrosion attack neither to the particle nor to the surrounding matrix. However, the magnified view of the rectangular region (Region I), shown in Fig. 5.1b, reveals some contrast variations indicating that nanoscopic local breakdown has taken place. As can be seen, numerous nano-sized pits which are darker in appearance due to material removal are formed over the particle, demonstrating corrosion initiation in the form of nano-pitting. We also observe pitted zones over the alloy matrix merely closest to the corroded regions of the particle, indicated by the white arrows. With prolonged exposure to 0.01 M NaCl (t= 60 min), the contrast variations simultaneously spread over the particle mostly (bordered by the red dashed line) but also over the matrix. After 120 min of exposure, corrosion has clearly attacked the top right corner of the particle and its adjacent matrix which is covered with bright cloud-like corrosion products verified as aluminium (hydr)oxide (see Fig. S5.1). Besides, the HAADF-STEM image taken at 150 min reveals the appearance of some bright regions on different parts of the particle,

indicated by the red arrows. The EDS analysis indicates these to be copper nanoclusters termed as copper residual. At this stage, a part of the surrounding matrix showed up in the darkest contrast due to partial dissolution (Region II). As shown in the magnified STEM/EDS image (Fig. 5.1c), the particle and its closest matrix have undergone local corrosion. Given the EDS results, selective dissolution of aluminium, manganese and to a minor extent iron and silicon from the particle is evident, coming along with copper aggregation in a globular morphology. Closest to the dealloyed zones, the alloy matrix is fully dissolved. Prolonged exposure up to 270 min causes further local degradation of both the particle and the surrounding alloy matrix. At this stage, the STEM image taken from Region III (Fig. 5.1d) shows partial dissolution of the matrix where copper-rich zones were formed already over the particle. Note that the trenching emerges merely around the dealloyed regions of the corroding particle, implying highly-local galvanic interactions.

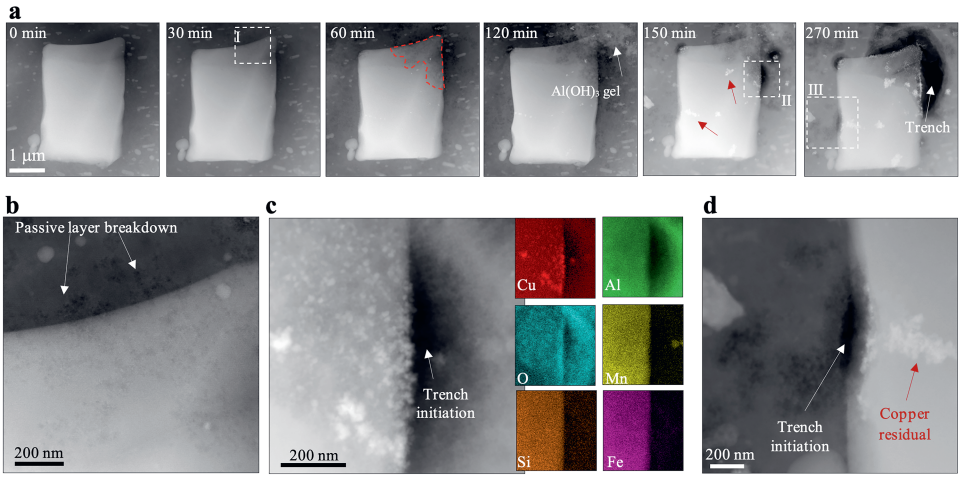


Fig. 5.1. Quasi in-situ STEM/EDS analysis of local corrosion induced by $Al_{76}Cu_6Fe_7Mn_5Si_6$ phase. (a) Time-resolved HAADF-STEM images of an $Al_{76}Cu_6Fe_7Mn_5Si_6$ particle undergoing dealloying form of local corrosion. The red arrows point to the copper residual. (b) Magnified-view HAADF-STEM image of the rectangular region (Region I) after 30 min. (c) STEM/EDS analysis of Region II at the particle/matrix interface after 150 min, revealing the aggregated region of copper due to dealloying. (d) Magnified HAADF-STEM image of Region III after 270 min. The specimen is an argon ion-milled 3-mm disk intermittently exposed to 0.01 M NaCl.

Fig. 5.2a and b show top-view SEM and cross-sectional STEM/EDS analysis of two $Al_{76}Cu_6Fe_7Mn_5Si_6$ particles at the surface of polished bulk samples immersed in 0.01 M NaCl for 6 h and 19 h, respectively. The SEM image of the particle exposed for 6 h depicts a shallow trench which is a bit darker in contrast as compared to the uncorroded matrix. The particle surface is rather smooth but numerous bright spots are distinguishable on the particle itself; it is consistent with the globular morphology shown in Fig. 5.1c. The corresponding HAADF-STEM image taken from the particle cross-section shows a bright

layer at the top of the particle; it is more pronounced in the magnified view of the rectangular region at the particle/matrix interface. As can be seen in the EDS line scan reconstructed from the indicated rectangular region in the STEM image, the top layer clearly demonstrates selective dissolution of elemental components except copper. Aluminium is the element that has dissolved severely.

Fig. 5.2b shows an $Al_{76}Cu_6Fe_7Mn_5Si_6$ particle exposed for 19 h. From the SEM image, the particle surface is quite rough in morphology, compared to the particle in Fig. 5.2a. Moreover, corrosion has fully trenched the adjacent alloy matrix, albeit that the trench has a wider opening at the left side. The cross-sectional STEM/EDS analysis shows that this particle is partially dealloyed; the corroded part is rich in copper and iron but depleted in aluminium and manganese and to a lesser extent silicon. A copper-rich layer is also seen at the upper part of the particle (see the inset corresponding to the rectangular region). Note that the matrix corrosion has propagated deeper where the particle has been more dealloyed, suggesting enhanced galvanic interactions between the copper-rich region and closely-located alloy matrix.

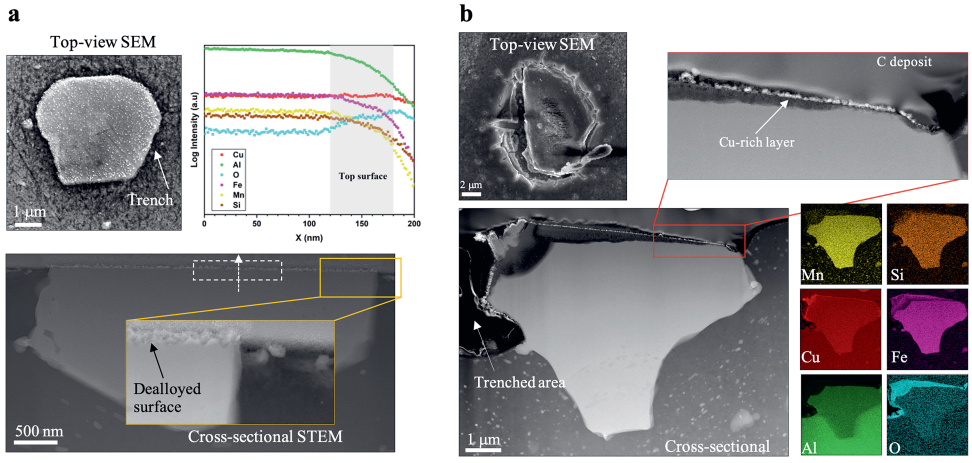


Fig. 5.2. Ex-situ SEM and TEM analysis of local corrosion induced by $Al_{76}Cu_6Fe_7Mn_5Si_6$ phase. (a) Top-view SEM and cross-sectional STEM analysis of an $Al_{76}Cu_6Fe_7Mn_5Si_6$ particle immersed in 0.01 M NaCl for 6 h. The inset is the magnified view of the orange rectangular region. The graph shows the elemental scan lines reconstructed from the rectangular region in the STEM image, revealing the top surface dealloyed. (b) Top-view SEM and cross-sectional STEM/EDS analysis of an $Al_{76}Cu_6Fe_7Mn_5Si_6$ particle immersed in 0.01 M NaCl for 19 h. The inset is the magnified view of the red rectangular region, showing the copper-rich layer on the top. The SEM images are taken using the reflected secondary electrons. The cross-sections are fabricated out of the analysed particles with FIB.

Fig. 5.3 shows the serial FIB sectioning on an $Al_{76}Cu_6Fe_7Mn_5Si_6$ particle corroded for 19 h. The top-view SEM image reveals a continuous trench around the IMP with a tight opening (Fig. 5.3a). Fig. 5.3b shows the SEM image of the same IMP when the stage is tilted at 52°. The serial FIB sections, shown

in Fig. 5.3c, were performed along with the white dashed lines. The cross-sectional SEM images reveal the dealloyed part of the particle brighter than the intact part, owing to huge removal of aluminium which is a light element. As can been seen, the top surface of the whole particle is dealloyed, although dealloying has penetrated deeper into some regions of the IMP (mind the white dashed curves).

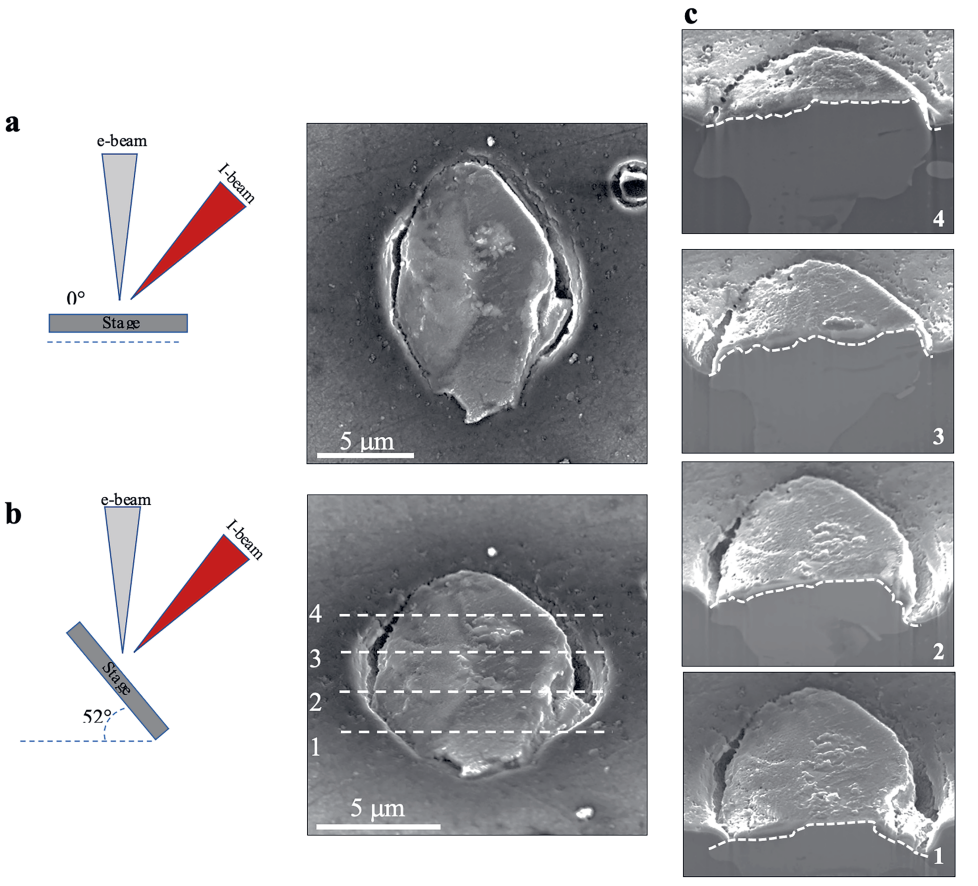


Fig. 5.3. FIB/SEM analysis of local corrosion induced by $Al_{76}Cu_6Fe_7Mn_5Si_6$ phase. (a) Top-view SEM image of an $Al_{76}Cu_6Fe_7Mn_5Si_6$ particle immersed in 0.01 M NaCl for 19 h. (b) SEM image of the same IMP when the stage is tilted at 52°. (c) SEM images of the FIB serial sections along the lines shown in Fig. 5.3b. The white dashed curves separate the dealloyed region from the intact part of the particle.

5.3.2. Isolated constituent $Al_7Cu_2Fe(Mn)$. The top-view STEM/EDS results of local corrosion induced by a particle of this group are shown in Fig. 5.4. According to the oxygen map, we see that corrosion initially attacks the particle to a greater extent than the matrix. Comparing the EDS elemental maps before and after 30-min exposure reveals that corrosion has partially depleted the particle from aluminium and manganese, implying a dealloying form of attack. At this stage, a globular morphology is seen for the largely-dealloyed region where the alloy matrix has been partially dissolved. The inset

shows the magnified view of this zone in Fig. 5.4. This phenomenon is in line with our observations for $Al_{76}Cu_6Fe_7Mn_5Si_6$. After 45 min, the globular morphology becomes more evident on the particle whilst the surrounding matrix has been fully trenched, as imaged with HAADF-STEM. The EDS maps have revealed that at this stage of exposure, the particle is almost depleted from aluminium. Manganese and to a minor extent iron are also dissolved while copper shows no clear change in intensity during the course of exposure. Compared to $Al_{76}Cu_6Fe_7Mn_5Si_6$, the local degradation takes place over a shorter time-scale for $Al_7Cu_2Fe(Mn)$ since it has a higher Cu content which can drive the dealloying process and galvanic interactions more effectively. More evidence can be found in Fig. S5.2.

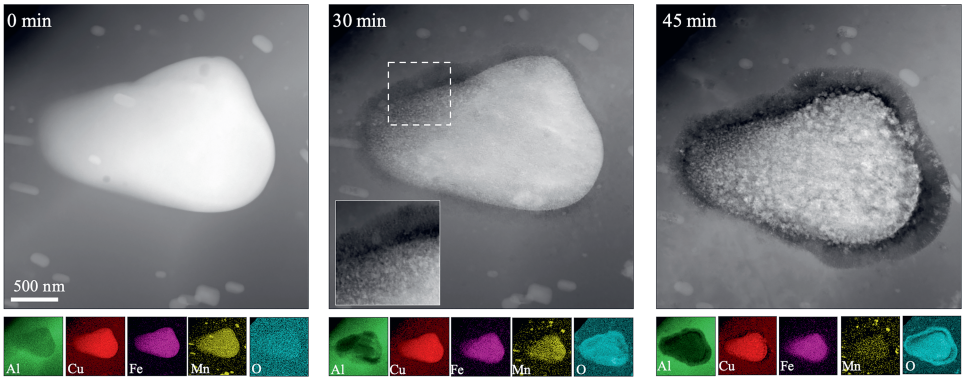


Fig. 5.4. Quasi in-situ STEM/EDS analysis of local corrosion induced by $Al_7Cu_2Fe(Mn)$ phase. HAADF-STEM images and corresponding EDS maps at different exposure times, revealing the dissolution of Al and Mn, and to a minor extent Fe from the particle. Due to Cu and Fe aggregation, the particle shows a globular morphology with time. The inset at 30 min is a closer look at the white rectangular region, revealing the dealloyed region of the particle. The specimen is an argon ion-milled 3-mm disk exposed repeatedly to 0.01 M NaCl.

Several $Al_7Cu_2Fe(Mn)$ particles on the post-corroded samples are cross-sectionally observed to get insights into how exactly this phase induces local corrosion to the surrounding alloy matrix. Fig. 5.5a shows the STEM image of an $Al_7Cu_2Fe(Mn)$ particle exposed for 15 min. According to the contrast variations, dealloying has penetrated deeper at the particle/matrix interface, associated with matrix trenching. The EDS line scan reconstructed from the indicated rectangular region in the STEM image clearly demonstrates selective dissolution of aluminium, manganese and to a minor extent iron. Besides, the upper part of the particle which appears as a bright layer in the HAADF-STEM image is enriched in copper and iron. Fig. 5.5b shows the STEM/EDS analysis of an $Al_7Cu_2Fe(Mn)$ particle at the attacked/intact interface in the sample that is immersed in 0.01 M NaCl for 6 h (Fig. S5.3). The estimated compositions of Region I and II reveals that the particle has undergone preferential dissolution of aluminium, manganese and even slightly iron. Dealloying has propagated into depth and

left behind bright stringers. In the high-resolution EDS map, these stringers are identified as copper-rich regions that are formed by surface diffusion of copper during the dealloying process [56]. Fig. 5.5c shows an $Al_7Cu_2Fe(Mn)$ particle fully dealloyed and undercut from its adjacent matrix. The particle surface is quite rough in morphology (SEM image) and the corresponding cross-section reveals a coarse globular morphology. In addition, the induced local corrosion has trenched all around the particle, leading to an undercut remnant (Fig. 5.5c) which still contains 7.0 At% Al, 5.4 At% Fe, 42.9 At% O and Cu as balance.

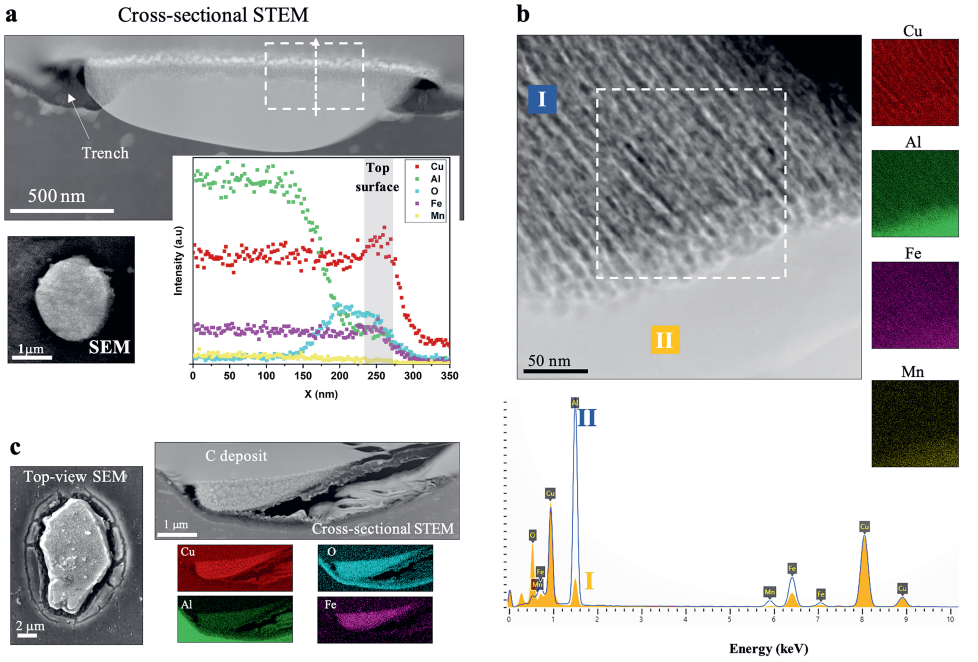


Fig. 5.5. Ex-situ analytical TEM analysis of local corrosion induced by $Al_7Cu_2Fe(Mn)$ phase. (a) Top-view SEM and cross-sectional STEM image of an $Al_7Cu_2Fe(Mn)$ particle immersed in 0.01 M NaCl for 15 min. The graph shows the elemental scan lines reconstructed from the rectangular region in the image, revealing preferential dissolution of aluminium and manganese and formation of a Cu-, Fe-rich layer on the top. (b) Magnified cross-sectional STEM/EDS analysis of a dealloyed $Al_7Cu_2Fe(Mn)$ particle exposed to 0.01 M NaCl for 6 h. The STEM image of this particle at low magnification is shown in Fig. S5.3. The spectra compare the chemical composition of the corroded (I) and intact (II) regions. (c) Top-view SEM and cross-sectional STEM/EDS analysis of an undercut $Al_7Cu_2Fe(Mn)$ particle immersed in 0.01 M NaCl for 6 h.

Fig. 5.6a and b show the SEM image of a large $Al_7Cu_2Fe(Mn)$ particle when the stage is at 0 and 52 tilt, respectively. The sample is exposed previously for 19 h in 0.01 M NaCl. The SEM images show a deep continuous trench with a wide opening around the IMP. The serial FIB sections are presented in Fig. 5.6c. The FIB section along line#1 shows the particle thoroughly dealloyed where the bottom of

the particle is obviously disconnected from the alloy matrix. The FIB sections along line#2 and line#3 reveal that this IMP has not been undercut yet, although the dealloyed front has penetrated quite deep into the particle. The FIB cross-section along line#4 has mainly endured dealloying and a tiny region is still intact. This indicates that the IMPs become deeper dealloyed close to the trenched area.

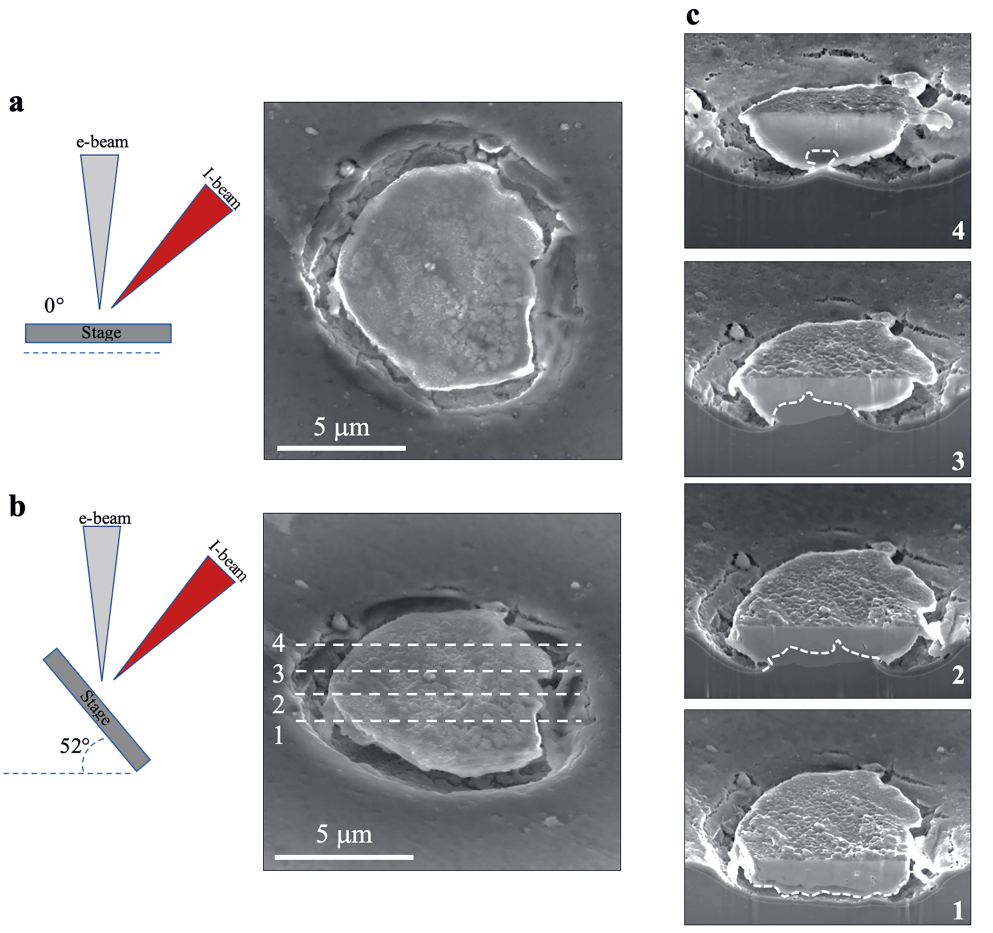


Fig. 5.6. FIB/SEM analysis of local corrosion induced by $Al_7Cu_2Fe(Mn)$ phase. (a) Top-view SEM image of an $Al_7Cu_2Fe(Mn)$ particle immersed in 0.01 M NaCl for 19 h. (b) SEM image of the same IMP when the stage is tilted at 52°. (c) SEM images of the FIB serial sections along the lines shown in Fig. 5.6b. The white dashed curves separate the dealloyed region from the intact part of the particle.

5.3.3. Dispersoids $Al_{20}Mn_3Cu_2$. Fig. 5.7a shows time-resolved HAADF-STEM images of a dispersoid undergoing local dissolution and later inducing alloy matrix trenching. The particle initially undergoes a local breakdown in the form of a nano-pit (t= 30 min). With prolonged exposure, a bright spot (verified as a copper-rich nanoparticle) appears around the pitted part of the particle (t= 60 min). After 120 min, corrosion extends over the alloy matrix closest to the locally-dissolved part of the particle. Exposed for

30 more min, a bright remnant is observed where its adjacent alloy matrix is fully dissolved in the form of a trench. To get detailed insight into compositional evolution of this phase, a specimen was exposed to distilled water for 20 min. STEM/EDS analysis of a dispersoid, shown in Fig. 5.7b, indicates that the particle has been dealloyed due to selective aluminium and manganese dissolution. Fig. 5.7c clearly shows the presence of individual nano-pits caused by dealloying over an isolated dispersoid. Although twin boundaries are reported as local dissolution sites of dispersoids [41, 42], the high-resolution TEM image (inset) reveals that local dissolution has taken place for this particle in the absence of any planar defects. This phenomenon implies that $Al_{20}Mn_3Cu_2$ dispersoids like other studied phases herein have a lower electrochemical stability and readily undergo local breakdown (pitting) themselves and preferential dealloying of active elements, as compared to the alloy matrix.

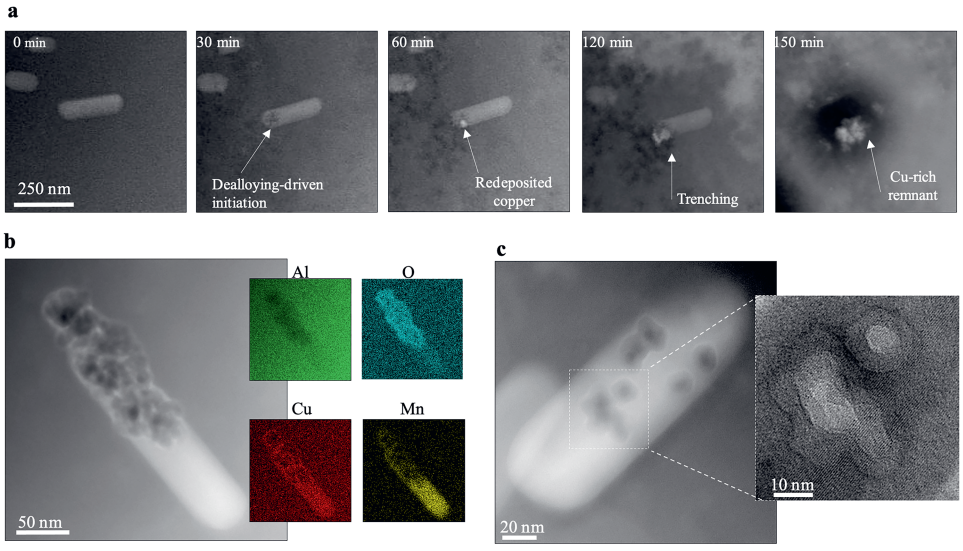


Fig. 5.7. Local corrosion induced by nanoscopic dispersoid $Al_{20}Mn_3Cu_2$. (a) HAADF-STEM images of an a dispersoid particle at different stages of corrosion. (b) STEM/EDS analysis a locally-dissolved dispersoid particle after a 20-min exposure to distilled water. (c) HAADF-STEM image of a dispersoid particle exposed for 20 min in distilled water, revealing dealloying at the particle itself. The inset is high resolution TEM image taken from the rectangular region.

5.3.4. Composite $Al_7Cu_2Fe(Mn)/Al_{76}Cu_6Fe_7Mn_5Si_6$. The study of composite IMPs is highly insightful to study the mechanisms through which different compositional domains can comparatively induce local corrosion in AAs [3]. Fig. 5.8a shows STEM/EDS results for a composite particle on an argon ion-milled sample after 320 min exposure to 0.01 M NaCl. The EDS analysis (i.e., Al and O map) shows that the domain with a higher copper amount, $Al_7Cu_2Fe(Mn)$, has undergone selective dissolution of aluminium. Besides, its adjacent alloy matrix is locally dissolved; this part of the alloy matrix, indicated by the white arrow, appears darker in contrast. Although the $Al_7Cu_2Fe(Mn)$ acquires a higher

corrosion potential (higher galvanic driving force to trigger anodic dissolution of the alloy matrix) than the $Al_{76}Cu_6Fe_7Mn_5Si_6$, it is remarkable that aluminium has also etched away from $Al_7Cu_2Fe(Mn)$ compositional domain. This phenomenon can be better explored through cross-sectional analysis of composite particles.

In Fig. 5.8b, we see a SEM image (the inset) revealing a constituent particle with a discontinuously-trenched matrix, indicated by the white arrow. Our cross-sectional TEM evaluation reveals that this is in fact an $Al_7Cu_2Fe(Mn)/Al_{76}Cu_6Fe_7Mn_5Si_6$ composite particle. As denoted by the red dashed lines in the SEM image, the $Al_7Cu_2Fe(Mn)$ domain acts like a narrow ribbon separating the large $Al_{76}Cu_6Fe_7Mn_5Si_6$ part from the alloy matrix. The trench has propagated deeper around the larger $Al_7Cu_2Fe(Mn)$ domain (left side in the STEM image). Furthermore, the inset, the zoomed-in STEM image of the white rectangular region, shows that the $Al_7Cu_2Fe(Mn)$ and $Al_{76}Cu_6Fe_7Mn_5Si_6$ are not at the same surface level. Interestingly, the dealloying attack (preferential Al and Mn dissolution) has deeply penetrated into the $Al_7Cu_2Fe(Mn)$ phase but not into the $Al_{76}Cu_6Fe_7Mn_5Si_6$ domain which has just undergone surface etching. It seems that the $Al_7Cu_2Fe(Mn)$ phase has a low electrochemical stability, whereby it endures faster dealloying than the $Al_{76}Cu_6Fe_7Mn_5Si_6$ domain. This phenomenon is more pronounced in Fig. 5.9, showing FIB/SEM analysis of a composite $Al_7Cu_2Fe(Mn)/Al_{76}Cu_6Fe_7Mn_5Si_6$ particle immersed in 0.01 M NaCl for 19 h. As evident, the alloy matrix adjacent to the $Al_7Cu_2Fe(Mn)$ domain has been trenched widely and deeply whereas it has narrowly dissolved around the $Al_{76}Cu_6Fe_7Mn_5Si_6$ domain. The cross-sectional SEM image along the dashed line shown in Fig. 5.9b reveals a deep penetration of dealloying into the $Al_7Cu_2Fe(Mn)$ domain. Mind the inset which is a closer look at the orange rectangular region in Fig. 5.9c. More evidence of the local corrosion induced by a composite particle is presented in Fig. S5.5.

The current observations suggest that IMPs undergo dealloying as a consequence of their electrochemical instability. However, the kinetics of local degradation in the alloy matrix is governed by the electrochemical reactivity of IMPs which changes during dealloying attack. On the other hand, it seems that the galvanic interactions take place quite locally and at the nanoscale between active zones of a corroding IMP and the closest alloy matrix. This phenomenon is directly attributed to the presence of the isolating corrosion products, in particular aluminium (hydr)oxide, that cannot support electrochemical reactions and physically cover electrochemically active locations [16]. Here, dedicated nanoscopic morphological and compositional observations imply that the early stages of local corrosion in AAs are more complicated than the relatively simple microgalvanic interactions between cathodic IMPs and their surrounding alloy matrix considered to date [31, 32, 34]. Dealloying attack is indeed the precursor of corrosion initiation whilst intrinsic electrochemical instability is a parameter that greatly drive the kinetics of local degradation. This is particularly noticeable for composite $Al_7Cu_2Fe(Mn)/Al_{76}Cu_6Fe_7Mn_5Si_6$ IMPs in which $Al_7Cu_2Fe(Mn)$ domain undergoes dealloying far down from the surface while it is just a surface etching for $Al_{76}Cu_6Fe_7Mn_5Si_6$. In addition, discontinuous trenching merely close to the dealloyed parts of IMPs indicate the highly localised corrosion through

nanogalvanic interactions. In fact, as long as the alloy matrix is covered with the isolating aluminium (hydr)oxide layer, it would be well protected. However, the local solution chemistry induced by dealloying of the corroding IMPs can weaken it, leading to local breakdown of the passive layer near the dealloyed region. The faster the dealloying through the intrinsic electrochemical instability of the IMPs happens, the earlier the adjacent alloy matrix dissolution takes place.

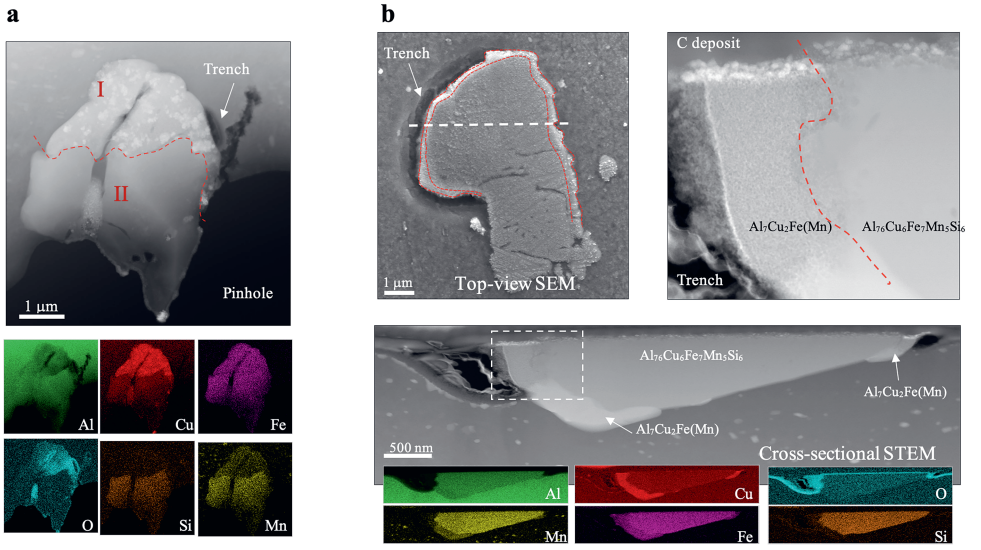


Fig. 5.8. Local corrosion induced by composite $Al_7Cu_2Fe(Mn)/Al_{76}Cu_6Fe_7Mn_5Si_6$ particles. (a) Top-view STEM/EDS analysis of a composite particle on an argon ion-milled specimen exposed to 0.01 M NaCl for 320 min. Region I is identified as $Al_7Cu_2Fe(Mn)$ which is distinguished by the red dashed line from $Al_7Cu_6Fe_7Mn_5Si_6$ domain (Region II). (b) Top-view SEM and cross-sectional STEM/EDS analysis of a composite particle on a bulk sample immersed in 0.01 M NaCl for 6 h. The cross-section is lifted out along the white dashed line. The inset shows the zoomed-in STEM image of the white rectangular region, indicating the deep penetration of dealloying into the $Al_7Cu_2Fe(Mn)$ domain.

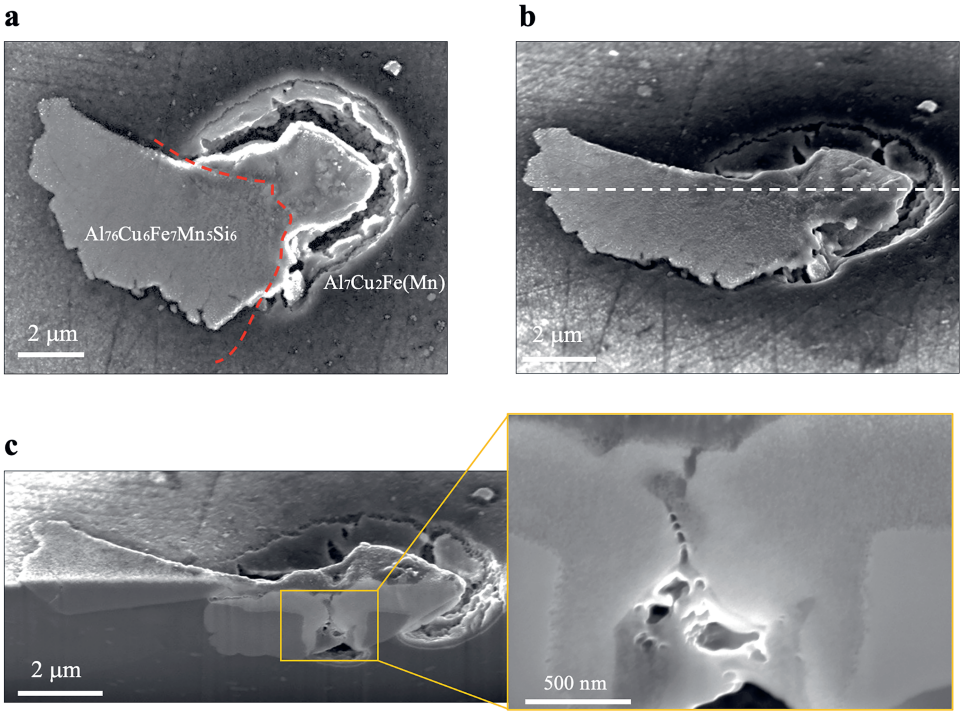


Fig. 5.9. FIB/SEM analysis of local corrosion induced by a composite $Al_7Cu_2Fe(Mn)/Al_{76}Cu_6Fe_7Mn_5Si_6$ particle. (a) Top-view SEM image of a composite $Al_7Cu_2Fe(Mn)/Al_{76}Cu_6Fe_7Mn_5Si_6$ particle immersed in 0.01 M NaCl for 19 h. (b) SEM image of the same composite IMP when the stage is tilted at 52°. (c) Cross-sectional SEM image along the dashed line shown in Fig. 5.9b. The inset is a closer look at the orange rectangular region, revealing a deep penetration of dealloying into the $Al_7Cu_2Fe(Mn)$ domain where the alloy matrix is trenched far down from the surface.

5.4. Overall local corrosion mechanism by intermetallic constituent phases and dispersoids

Our current findings in relation to early-stage surface corrosion initiation through to moderate depth propagation allow us to propose a more detailed mechanism explaining local degradation events linked to nano- and microscopic intermetallic compounds. In fact, the local corrosion can be broken down into several stages including dealloying-driven initiation, trench initiation, depth propagation and particle undercutting as depicted schematically in Fig. 5.10. Besides, the type and location of electrochemical reactions taking place at and around cathodic intermetallic compounds are proposed in further detail.

5.4.1. Dealloying-driven initiation. Local corrosion initiates in the form of nano-pitting as a consequence of dealloying of IMPs which are electrochemically unstable in aqueous electrolytes and undergo preferential dissolution of their active elemental constituents [29]. At this stage, aluminium and manganese largely, and iron slightly get corroded while the dissolution of copper is not thermodynamically favoured and gets redistributed through surface diffusion, leading to aggregated

regions of copper and iron. The Cu- and Fe-rich regions can establish nano-galvanic coupling to drive anodic dissolution of the rest of the particle as they acquire a higher corrosion potential and can accommodate ORR efficiently. The enhanced nobility causes a greater driving force for local breakdown within the adjacent alloy matrix which is covered by an aluminium (hydr)oxide passive layer. Note that the aluminium (hydr)oxide is isolating in nature and cannot support electrochemical reactions [17].

5.4.2. Trench initiation. With prolonged exposure time, the local dissolution rates in the particle and alloy matrix increase. This phenomenon gradually leads to an enhanced alkaline local chemistry in which the passive layer gets undermined [11] and subsequently the underlying metal would undergo uniform dissolution. Therefore, local corrosion occurs by discontinuous trenching within the alloy matrix at the matrix/particle interface closest to the dealloyed region. The electrochemical instability of intermetallic compounds largely governs the kinetics of degradation at this stage. As a token of this root cause of kinetic variations across different IMPs, the difference between Al_7Cu_2Fe(Mn) and $Al_{76}Cu_6Fe_7Mn_5Si_6$ is typical at this stage; dealloying penetrates rather fast into Al_7Cu_2Fe(Mn) phase as a consequence of selective dissolution of manganese and aluminium, and iron to a minor extent. To preserve the charge balance, the top part of the corroding particle has to accommodate the cathodic reactions at a high rate that produces a highly basic local chemistry in which the nearest alloy matrix starts to locally dissolve.

5.4.3. Depth propagation. Given the importance of IMP chemical composition, progressive dealloying controls the electrochemical reactivity of IMPs as Cu- and Fe-rich locations on a corroding IMP are highly noble that can actively support cathodic reactions and drive anodic dissolution of the adjacent alloy matrix. In contrast, silicon can largely hinder the electrochemical reactivity since during its oxidation, it turns into SiO_2 which is semiconducting but stable in a wide range of pH [57]. Manganese is highly soluble in neutral and anodic solution and hence etched away in the beginning of exposure [57]. Aluminium is electrochemically active in nature; however, its (hydr)oxide form is stable at pH 4-9 [57]. At early stages of corrosion, the corroded region can be passivated by the formation of an aluminium (hydr)oxide layer (see Fig. 5.1a at 120 min). However, it cannot withstand the established galvanic interaction and the consequent aggressive local solution chemistry, hence would chemically dissolve (Fig. 5.1a). In fact, the presence of aluminium (hydr)oxide, which is isolating, can physically cover the electrochemically active sites and leads to galvanic interactions within nanometric distances only, in particular at very early stages of corrosion. Note that Cu may also undergo oxidation inside the corroding IMPs, turning into Cu_2O during the depth propagation step of local corrosion. This phenomenon can occur as a consequence of physical or electrical isolation of some copper segments [58]. All the constituent compounds are of higher electrochemical stability than active phase like Al_2CuMg [29, 58]. Thus, local degradation induced by the latter takes place over a relatively shorter time-scale; associated with the release of copper ions that can get redeposited on the top of nearby corroding constituent IMPs [28, 59-64], as the SEM inset shows in Fig. 5.10. Besides, in a work using

liquid-phase TEM, we have evidenced that corroded S-phase particles largely release copper ions to the solution upon the particle undercutting process which can be redeposited on the active sites of the alloy surface like other corroding IMPs [58]. This phenomenon can greatly contribute to the enhanced cathodic activity of the IMPs, leading to nano-galvanic coupling within the corroding IMPs and with the closest alloy matrix. Thus, the local dissolution of the matrix gradually trenches all around the particle and corrosion simultaneously propagates into the matrix and corroding IMP. The more reactive the corroding intermetallic compound is, the deeper corrosion propagates into it.

5.4.4. Particle undercutting. The local dissolution continues to dissolve the alloy matrix until undercutting the particle. At this point, the corroding IMPs can acquire higher corrosion potentials and end up as a fully dealloyed remnant. Afterwards, some copper can be released from the particle as the corrosion potential of the undercut IMP would be high enough for copper dissolution [29]. The remnant might later fall out and leave behind a corrosion pit. The whole mechanism is the same for sub-micron dispersoids, albeit occurring over a shorter time- and smaller length-scales shown in Fig. 5.10 as well.

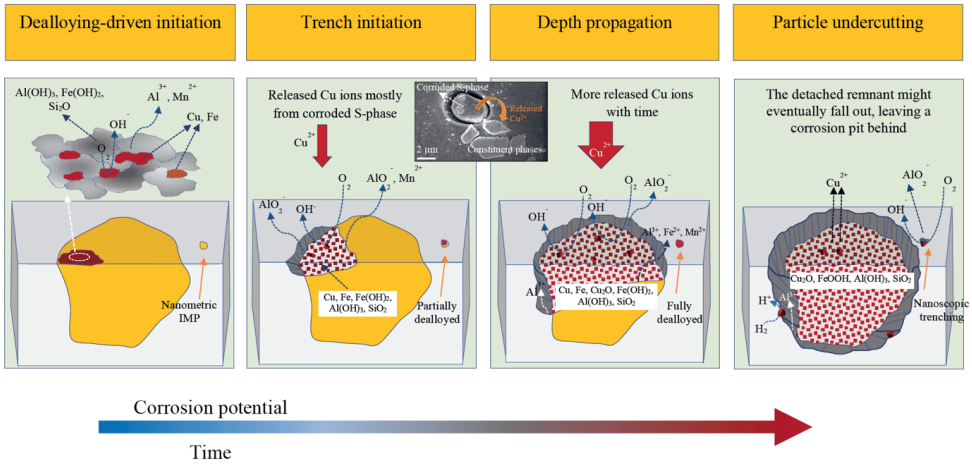


Fig. 5.10. Dealloying-driven local corrosion mechanism. 3D schematic view of localised corrosion initiation induced by cathodic dispersoids and constituent phases. The probable corrosion reactions occurring around IMPs are depicted in detail. As schematically shown, corrosion initiates at the surface of the particle itself and then simultaneously propagates in the depth and trenches at the closest alloy matrix through nanogalvanic interactions. The inset is a top-view SEM image taken from a post-corroded sample, showing released copper from a dealloyed Al_2CuMg (S-phase) and redeposited on other IMPs and the alloy matrix around.

5.5. Conclusions

Time-resolved top-view nanoscopic observations along with complementary cross-sectional post-mortem investigations confirm that cathodic phases evolve microstructurally and compositionally during local corrosion. Local corrosion basically initiates at cathodic intermetallic compounds in the

form of dealloying attack (mainly selective dissolution of Al and Mn) as they are electrochemically unstable themselves. Trenching initiates closest to the dealloyed region as a consequence of the local solution chemistry being established initially due to nanogalvanic interactions within a corroding IMP. Besides, the galvanic interactions between dealloyed regions of IMPs and the adjacent alloy matrix stabilise local degradations. The intrinsic electrochemical stability of intermetallic compounds is proposed as the main controlling factor driving the kinetics of local degradation rather than the numerously reported corrosion potential (surface Volta potential) difference between the cathodic particle and the surrounding matrix. This is based on direct nanoscopic observations of composite $Al_7Cu_2Fe(Mn)/Al_{76}Cu_6Fe_7Mn_5Si_6$ IMPs where the noble domain ($Al_7Cu_2Fe(Mn)$) shows dealloying far down from the surface, causing deep discontinuous trenching of the alloy matrix in the closest vicinity at a faster rate than that adjacent to the adjacent $Al_{76}Cu_6Fe_7Mn_5Si_6$ domain. Although the presence of noble elements like Cu and Fe greatly contributes to electrochemical reactivity of intermetallic compounds, it is largely hindered by other elements like Al and Si due to the formation of isolating or semi-conductive corrosion products that are unable of supporting electrochemical reactions. Besides, the redeposited copper sourced from corroding particles, such as Al_2CuMg, can accelerate the kinetics of the IMPs dealloying and local alloy matrix degradation. The nanoscopic dispersoids $Al_{20}Mn_3Cu_2$ undergo similar degradation stages but over a shorter time- and length-scale.

References

[1] P. Rambabu, N. Eswara Prasad, V.V. Kutumbarao, R.J.H. Wanhill, Aluminium Alloys for Aerospace Applications, in: N.E. Prasad, R.J.H. Wanhill (Eds.) Aerospace Materials and Material Technologies : Volume 1: Aerospace Materials, Springer Singapore, Singapore, 2017, pp. 29-52.
[2] G. Frankel, 2015 WR Whitney Award Lecture: The Effects of Microstructure and Composition on Al Alloy Corrosion, Corrosion, 71 (2015) 1308-1320.
[3] A. Boag, A. Hughes, N. Wilson, A. Torpy, C. MacRae, A. Glenn, T. Muster, How complex is the microstructure of AA2024-T3?, Corrosion Science, 51 (2009) 1565-1568.
[4] J. Scully, D. Peebles, A. Romig, D. Frear, C. Hills, Metallurgical factors influencing the corrosion of aluminum, Al-Cu, and Al-Si alloy thin films in dilute hydrofluoric solution, Metallurgical Transactions A, 23 (1992) 2641-2655.
[5] A.E. Hughes, R. Parvizi, M. Forsyth, Microstructure and corrosion of AA2024, Corrosion Reviews, 33 (2015) 1-30.
[6] Z. Wang, P. Chen, H. Li, B. Fang, R. Song, Z. Zheng, The intergranular corrosion susceptibility of 2024 Al alloy during re–ageing after solution treating and cold–rolling, Corrosion Science, 114 (2017) 156-168.
[7] M.-L. de Bonfils-Lahovary, L. Laffont, C. Blanc, Characterization of intergranular corrosion defects in a 2024 T351 aluminium alloy, Corrosion Science, 119 (2017) 60-67.
[8] M.O. Speidel, Stress corrosion cracking of aluminum alloys, Metallurgical Transactions A, 6 (1975) 631.
[9] A. Boag, A. Hughes, A. Glenn, T. Muster, D. McCulloch, Corrosion of AA2024-T3 Part I: Localised corrosion of isolated IM particles, Corrosion Science, 53 (2011) 17-26.
[10] J. De Wit, Local potential measurements with the SKPFM on aluminium alloys, Electrochimica Acta, 49 (2004) 2841-2850.
[11] A.E. Hughes, N. Birbilis, J.M. Mol, S.J. Garcia, X. Zhou, G.E. Thompson, High strength Al-alloys: microstructure, corrosion and principles of protection, Recent Trends in Processing and Degradation of Aluminium Alloys, 1 (2011).
[12] A. Boag, R. Taylor, T. Muster, N. Goodman, D. McCulloch, C. Ryan, B. Rout, D. Jamieson, A. Hughes, Stable pit formation on AA2024-T3 in a NaCl environment, Corrosion Science, 52 (2010) 90-103.
[13] G. Ilevbare, O. Schneider, R. Kelly, J. Scully, In situ confocal laser scanning microscopy of AA 2024-T3 corrosion metrology I. Localized corrosion of particles, Journal of The Electrochemical Society, 151 (2004) B453-B464.
[14] J. Li, J. Dang, A summary of corrosion properties of Al-rich solid solution and secondary phase particles in Al alloys, Metals, 7 (2017) 84.
[15] R. Parvizi, M.Y. Tan, A.E. Hughes, Recent Insights into Corrosion Initiation at the Nanoscale, in: Fundamentals of Aluminium Metallurgy, Elsevier, 2018, pp. 525-551.
[16] N. Wint, Z. Barrett, G. Williams, H. McMurray, The Study of AA2024 De-Alloying Using Luminol Electrogenerated Chemiluminescence Imaging, Journal of The Electrochemical Society, 166 (2019) C3417-C3430.
[17] Z. Szklarska-Smialowska, Pitting corrosion of aluminum, Corrosion science, 41 (1999) 1743-1767.
[18] C. Liu, S.K. Malladi, Q. Xu, J. Chen, F.D. Tichelaar, X. Zhuge, H.W. Zandbergen, In-situ STEM imaging of growth and phase change of individual CuAl X precipitates in Al alloy, Scientific reports, 7 (2017) 1-8.
[19] S.K. Malladi, Q. Xu, M.A. van Huis, F.D. Tichelaar, K.J. Batenburg, E. Yücelen, B. Dubiel, A. Czyrska-Filemonowicz, H.W. Zandbergen, Real-time atomic scale imaging of nanostructural evolution in aluminum alloys, Nano letters, 14 (2014) 384-389.
[20] A.E. Hughes, A. Glenn, N. Wilson, A. Moffatt, A.J. Morton, R.G. Buchheit, A consistent description of intermetallic particle composition: An analysis of ten batches of AA2024-T3, Surface and interface analysis, 45 (2013) 1558-1563.
[21] R.P. Wei, C.-M. Liao, M. Gao, A transmission electron microscopy study of constituent-particle-induced corrosion in 7075-T6 and 2024-T3 aluminum alloys, Metallurgical and Materials Transactions A, 29 (1998) 1153-1160.

[22] N. Birbilis, Y. Zhu, S. Kairy, M. Glenn, J.-F. Nie, A. Morton, Y. Gonzalez-Garcia, H. Terryn, J. Mol, A. Hughes, A closer look at constituent induced localised corrosion in Al-Cu-Mg alloys, Corrosion Science, 113 (2016) 160-171.
[23] L. Del Castillo, E. Lavernia, Microstructure and mechanical behavior of spray-deposited Al-Cu-Mg (-Ag-Mn) alloys, Metallurgical and materials transactions A, 31 (2000) 2287-2298.
[24] A. Hughes, A. Boag, A. Glenn, D. McCulloch, T. Muster, C. Ryan, C. Luo, X. Zhou, G. Thompson, Corrosion of AA2024-T3 Part II: Co-operative corrosion, Corrosion Science, 53 (2011) 27-39.
[25] N. Birbilis, T.H. Muster, R.G. Buchheit, Corrosion of Aluminum Alloys, in: P. Marcus (Ed.) Corrosion mechanisms in theory and practice, CRC press, 2011.
[26] V. Guillaumin, P. Schmutz, G. Frankel, Characterization of corrosion interfaces by the scanning Kelvin probe force microscopy technique, Journal of the Electrochemical Society, 148 (2001) B163-B173.
[27] P. Schmutz, G. Frankel, Characterization of AA2024-T3 by scanning Kelvin probe force microscopy, Journal of the Electrochemical Society, 145 (1998) 2285-2295.
[28] L. Lacroix, L. Ressier, C. Blanc, G. Mankowski, Combination of AFM, SKPFM, and SIMS to study the corrosion behavior of S-phase particles in AA2024-T351, Journal of the Electrochemical Society, 155 (2008) C131-C137.
[29] S. Lebouil, J. Tardelli, E. Rocca, P. Volovitch, K. Ogle, Dealloying of Al_2Cu, Al_7Cu_2Fe, and Al_2CuMg intermetallic phases to form nanoparticulate copper films, Materials and Corrosion, 65 (2014) 416-424.
[30] R. Buchheit, A compilation of corrosion potentials reported for intermetallic phases in aluminum alloys, Journal of the Electrochemical Society, 142 (1995) 3994.
[31] N. Birbilis, R. Buchheit, Investigation and discussion of characteristics for intermetallic phases common to aluminum alloys as a function of solution pH, Journal of The Electrochemical Society, 155 (2008) C117-C126.
[32] N. Birbilis, R.G. Buchheit, Electrochemical characteristics of intermetallic phases in aluminum alloys an experimental survey and discussion, Journal of The Electrochemical Society, 152 (2005) B140-B151.
[33] K.D. Ralston, T.L. Young, R.G. Buchheit, Electrochemical evaluation of constituent intermetallics in aluminum alloy 2024-T3 exposed to aqueous vanadate inhibitors, Journal of the electrochemical society, 156 (2009) C135-C146.
[34] N. Birbilis, M.K. Cavanaugh, R.G. Buchheit, Electrochemical behavior and localized corrosion associated with Al_7Cu_2Fe particles in aluminum alloy 7075-T651, Corrosion Science, 48 (2006) 4202-4215.
[35] B. Mazurkiewicz, A. Piotrowski, The electrochemical behaviour of the Al_2Cu intermetallic compound, Corrosion Science, 23 (1983) 697-707.
[36] L. Yin, Y. Jin, C. Leygraf, N. Birbilis, J. Pan, Numerical Simulation of Micro-Galvanic Corrosion in Al Alloys: Effect of Geometric Factors, Journal of the Electrochemical Society, 164 (2017) C75-C84.
[37] O. Schneider, G. Ilevbare, J. Scully, R. Kelly, In situ confocal laser scanning microscopy of AA 2024-T3 corrosion metrology II. Trench formation around particles, Journal of The Electrochemical Society, 151 (2004) B465-B472.
[38] J. Wloka, S. Virtanen, Detection of nanoscale η-$MgZn_2$ phase dissolution from an Al-Zn-Mg-Cu alloy by electrochemical microtransients, Surface and Interface Analysis: An International Journal devoted to the development and application of techniques for the analysis of surfaces, interfaces and thin films, 40 (2008) 1219-1225.
[39] A. Laurino, E. Andrieu, J.-P. Harouard, J. Lacaze, M.-C. Lafont, G. Odemer, C. Blanc, Corrosion behavior of 6101 aluminum alloy strands for automotive wires, Journal of The Electrochemical Society, 160 (2013) C569-C575.
[40] S.K. Kairy, N. Birbilis, Clarifying the Role of Mg_2Si and Si in Localized Corrosion of Aluminum Alloys by Quasi In Situ Transmission Electron Microscopy, Corrosion, 76 (2020) 464-475.
[41] B. Zhang, J. Wang, B. Wu, E. Oguzie, K. Luo, X. Ma, Direct observation of atomic-scale origins of local dissolution in Al-Cu-Mg alloys, Scientific reports, 6 (2016) 39525.
[42] J. Wang, B. Zhang, Y. Zhou, X. Ma, Multiple twins of a decagonal approximant embedded in S-Al2CuMg phase resulting in pitting initiation of a 2024Al alloy, Acta Materialia, 82 (2015) 22-31.

[43] X. Zhang, T. Hashimoto, J. Lindsay, X. Zhou, Investigation of the de-alloying behaviour of θ-phase (Al_2Cu) in AA2024-T351 aluminium alloy, Corrosion Science, 108 (2016) 85-93.
[44] Y. Zhu, K. Sun, J. Garves, L.G. Bland, J. Locke, J. Allison, G. Frankel, Micro-and nano-scale intermetallic phases in AA2070-T8 and their corrosion behavior, Electrochimica Acta, 319 (2019) 634-648.
[45] Y. Zhu, G. Frankel, Effect of major intermetallic particles on localized corrosion of AA2060-T8, Corrosion, 75 (2019) 29-41.
[46] Y. Zhu, K. Sun, G. Frankel, Intermetallic phases in aluminum alloys and their roles in localized corrosion, Journal of The Electrochemical Society, 165 (2018) C807-C820.
[47] C. Örnek, C. Leygraf, J. Pan, Real-Time Corrosion Monitoring of Aluminum Alloy Using Scanning Kelvin Probe Force Microscopy, Journal of The Electrochemical Society, 167 (2020) 081502.
[48] L. Yin, Y. Jin, C. Leygraf, J. Pan, A FEM model for investigation of micro-galvanic corrosion of Al alloys and effects of deposition of corrosion products, Electrochimica Acta, 192 (2016) 310-318.
[49] S. Malladi, F. Tichelaar, Q. Xu, M. Wu, H. Terryn, J. Mol, F. Hannour, H. Zandbergen, Quasi in situ analytical TEM to investigate electrochemically induced microstructural changes in alloys: AA2024-T3 as an example, Corrosion science, 69 (2013) 221-225.
[50] B. Zhang, J. Wang, B. Wu, Y. Zhou, X. Ma, Quasi-in-situ ex-polarized TEM observation on dissolution of MnS inclusions and metastable pitting of austenitic stainless steel, Corrosion Science, 100 (2015) 295-305.
[51] Y. Zhang, P. Gore, W. Rong, Y. Wu, Y. Yan, R. Zhang, L. Peng, J.-F. Nie, N. Birbilis, Quasi-in-situ STEM-EDS insight into the role of Ag in the corrosion behaviour of Mg-Gd-Zr alloys, Corrosion Science, 136 (2018) 106-118.
[52] Y. Zhu, J.D. Poplawsky, S. Li, R.R. Unocic, L.G. Bland, C.D. Taylor, J.S.W. Locke, E.A. Marquis, G.S. Frankel, Localized corrosion at nm-scale hardening precipitates in Al-Cu-Li alloys, Acta Materialia, (2020) 204-213.
[53] A. Kosari, H. Zandbergen, F. Tichelaar, P. Visser, H. Terryn, A. Mol, Application of In Situ Liquid Cell Transmission Electron Microscopy in Corrosion Studies: A Critical Review of Challenges and Achievements, Corrosion, 76 (2020) 4-17.
[54] D.B. Williams, C.B. Carter, The transmission electron microscope, in: Transmission electron microscopy, Springer, 1996, pp. 3-17.
[55] J. Mayer, L.A. Giannuzzi, T. Kamino, J. Michael, TEM sample preparation and FIB-induced damage, MRS bulletin, 32 (2007) 400-407.
[56] J. Erlebacher, M.J. Aziz, A. Karma, N. Dimitrov, K. Sieradzki, Evolution of nanoporosity in dealloying, Nature, 410 (2001) 450-453.
[57] M. Pourbaix, Atlas of Electrochemical Equilibria in Aqueous Solutions, National Association of Corrosion Engineers, Houston, TX, 2nd English edn, (1974) 384-392.
[58] A. Kosari, H. Zandbergen, F. Tichelaar, P. Visser, H. Terryn, J.M.C. Mol, In-situ nanoscopic observations of dealloying-driven local corrosion from surface initiation to in-depth propagation, Corrosion Science, (2020) In press.
[59] R. Buchheit, M. Martinez, L. Montes, Evidence for Cu ion formation by dissolution and dealloying the Al_2CuMg intermetallic compound in rotating ring-disk collection experiments, Journal of The Electrochemical Society, 147 (2000) 119-124.
[60] N. Dimitrov, J. Mann, K. Sieradzki, Copper redistribution during corrosion of aluminum alloys, Journal of the Electrochemical Society, 146 (1999) 98.
[61] M. Vukmirovic, N. Dimitrov, K. Sieradzki, Dealloying and corrosion of Al alloy 2024 T 3, Journal of The Electrochemical Society, 149 (2002) B428-B439.
[62] T. Hashimoto, X. Zhang, X. Zhou, P. Skeldon, S. Haigh, G. Thompson, Investigation of dealloying of S phase (Al_2CuMg) in AA 2024-T3 aluminium alloy using high resolution 2D and 3D electron imaging, Corrosion Science, 103 (2016) 157-164.
[63] R. Buchheit, R. Grant, P. Hlava, B. McKenzie, G. Zender, Local dissolution phenomena associated with S phase (Al_2CuMg) particles in aluminum alloy 2024-T3, Journal of the electrochemical society, 144 (1997) 2621.
[64] L. Lacroix, L. Ressier, C. Blanc, G. Mankowski, Statistical study of the corrosion behavior of Al_2CuMg intermetallics in AA2024-T351 by SKPFM, Journal of the Electrochemical Society, 155 (2008) C8-C15.

Supplementary Materials for Chapter 5

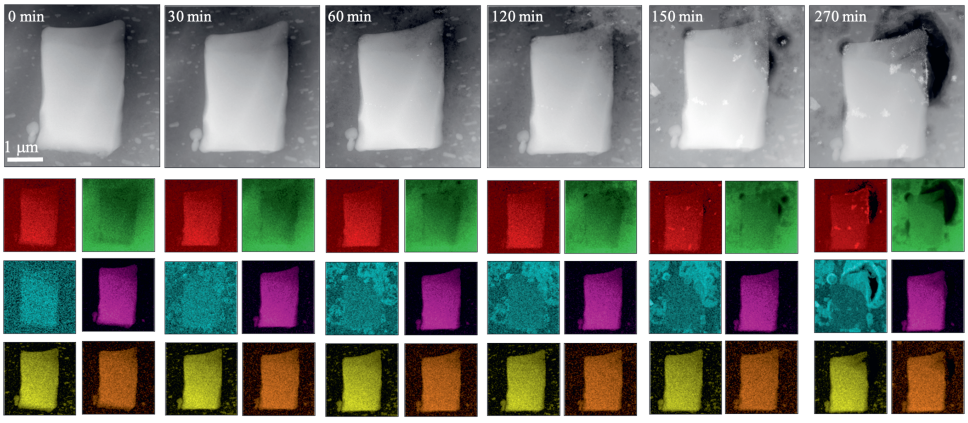


Fig. S5.1. Quasi in-situ STEM/EDS analysis of local corrosion induced by $Al_{76}Cu_6Fe_7Mn_5Si_6$ phase. The STEM images are shown as Fig. 5.1a in the main body of the paper. Here, the time-resolved EDS maps are presented. Cu (red), Al (green), O (blue), Fe (purple), Mn (yellow) and Si (orange).

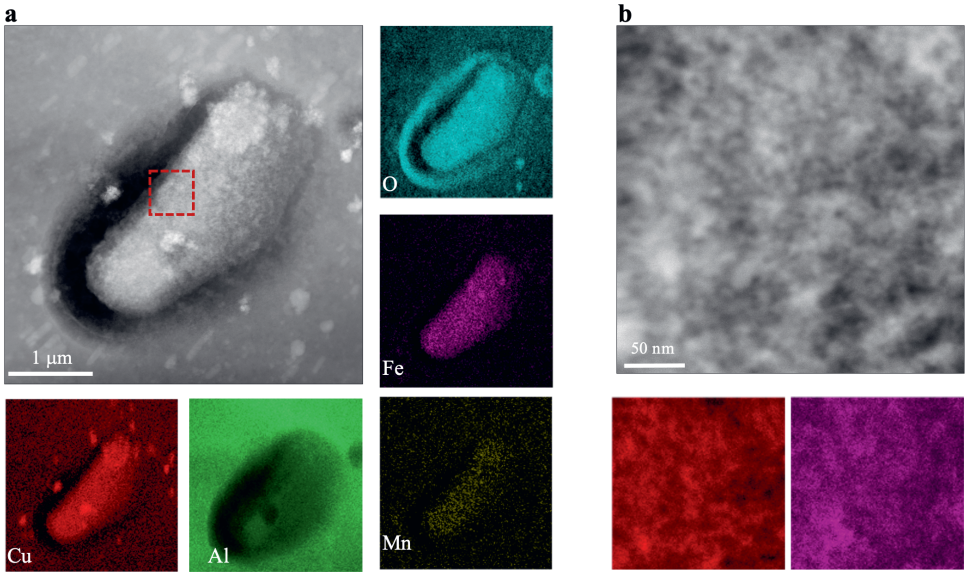


Fig. S5.2. (a) Ex-situ STEM/EDS analysis of local corrosion induced by an $Al_7Cu_2Fe(Mn)$ particle on an argon ion-milled sample exposed to 0.01 M NaCl for 320 min. (b) Magnified STEM images along with Cu (red) and Fe (purple) maps of the rectangular region in Fig. S5.2a.

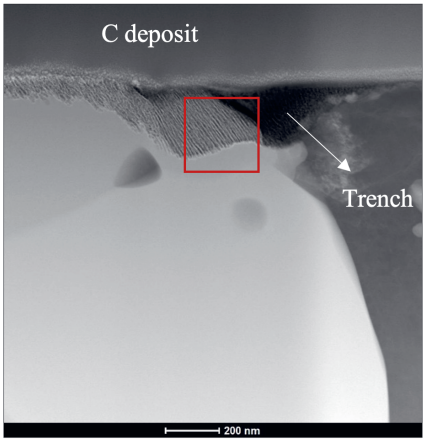


Fig. S5.3. HAADF-STEM image of an $Al_7Cu_2Fe(Mn)$ particle exposed to 0.01 M NaCl for 6 h and undergone dealloying in the upper part. The detailed analysis of the region indicated by the red rectangle is shown in the main body of the paper as Fig. 5.5b.

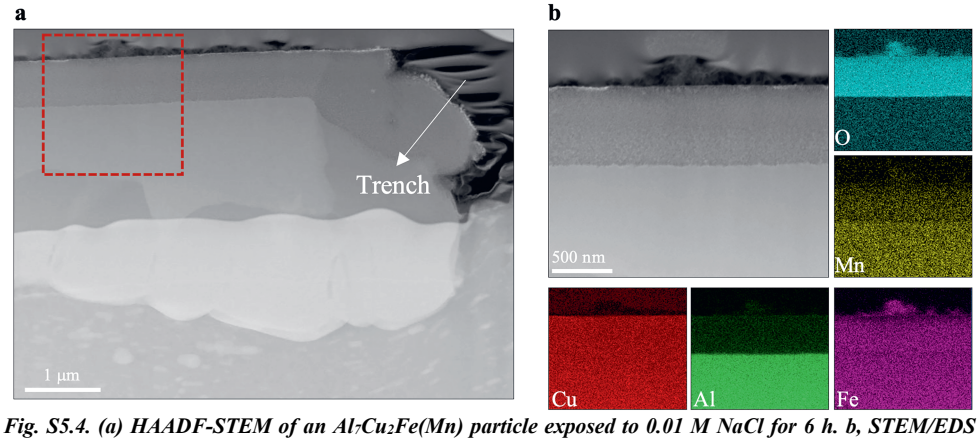


Fig. S5.4. (a) HAADF-STEM of an $Al_7Cu_2Fe(Mn)$ particle exposed to 0.01 M NaCl for 6 h. b, STEM/EDS analysis of the rectangular region in Fig. S5.4a, revealing dealloying of the particle and also accumulation of iron hydroxide and aluminium hydroxide on the top part.

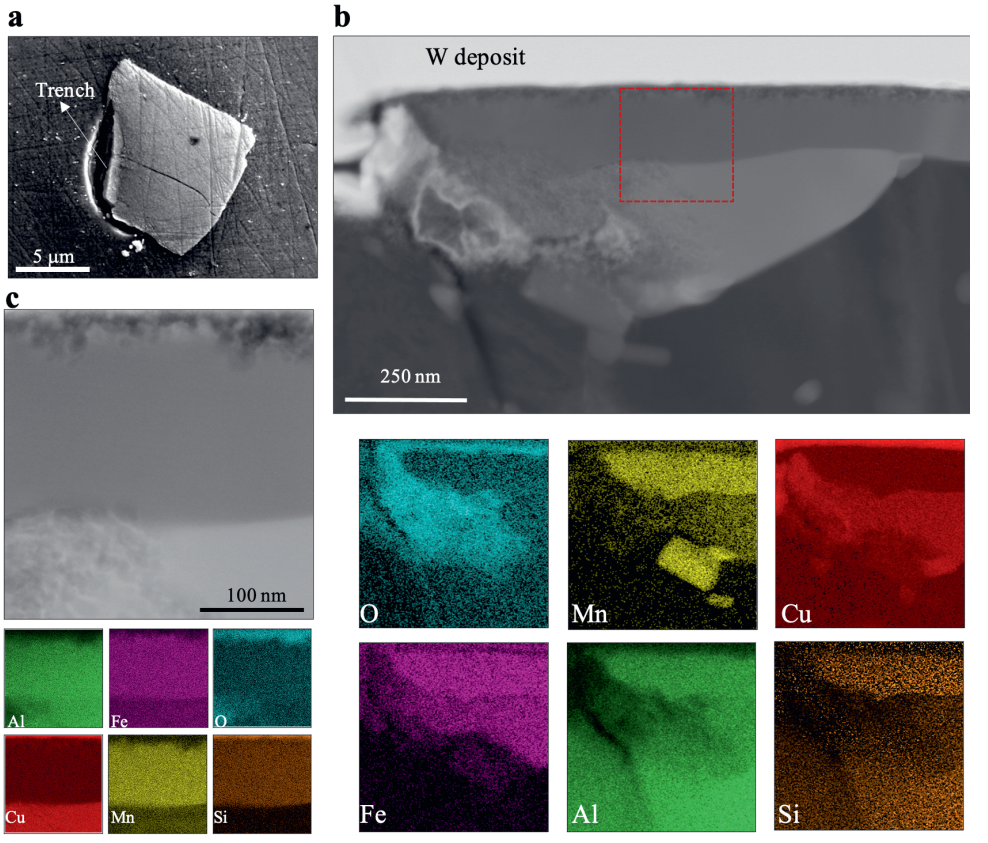


Fig. S5.5. (a) SEM image of a composite particle of $Al_7Cu_2Fe(Mn)/Al_{76}Cu_6Fe_7Mn_5Si_6$ immersed in 0.01 M NaCl for 6 h, showing a discontinuous trench indicated by the white arrow. (b) Cross-sectional STEM/EDS analysis of the particle, revealing the deep propagation of dealloying into $Al_7Cu_2Fe(Mn)$ domain. (c) The magnified STEM/EDS analysis of the red rectangular region in Fig. S5.5b, indicating selective dissolution of Al and Mn from the upper part of the $Al_{76}Cu_6Fe_7Mn_5Si_6$ domain.

CHAPTER 6

CROSS-SECTIONAL ANALYTICAL TEM CHARACTERISATION OF THE CONVERSION LAYER FORMED ON AA2024-T3 BY A LITHIUM-LEACHING COATING[1]

This chapter focuses on the cross-sectional characterisation of the protective conversion layer formed on AA2024-T3 by lithium-leaching from a polyurethane coating in a corrosive environment. The layer shows a multi-layered arrangement comprising nanoscopic local phases. Transmission electron microscopy (TEM) and complementary high-resolution secondary ion mass spectroscopy (SIMS) were employed to observe the cross-sections of the entire layer formed at different locations of a 1-mm-wide scribe, in terms of morphology, structure and chemical composition. The conversion layer was comprised of two ubiquitous sublayers; a thin dense layer (i.e., 150 nm) adjacent the alloy substrate and a porous layer. The former represents an amorphous lithium-containing pseudoboehmite phase, Li-pseudoboehmite, whereas the latter is composed of amorphous and crystalline products; an outer columnar layer merely seen on the peripheral region is also crystalline. Through a sandwich structure and the $d_{(003)}$ basal spacing, the crystalline phases were identified as Li-Al layered double hydroxide. Although lithium was found uniformly spread within different regions, the local phases with no/low concentration of lithium were revealed with energy filtered TEM and confirmed with SIMS analysis.

Keywords: Leachable lithium carbonate; Layered double hydroxide; AA2024-T3; High Resolution TEM; Energy Filtered TEM; SIMS

[1] **A. Kosari**, P. Visser, F. Tichelaar, S. Eswara, J-N. Audinot, T. Wirtz, H. Zandbergen, H. Terryn, J.M.C. Mol, Cross-sectional characterization of the conversion layer formed on AA2024-T3 by a lithium-leaching coating, Applied Surface Science, 512 (2020) 145665.

6.1. Introduction

A high strength-to-weight ratio is a key characteristic that has made aluminium alloy (AA) 2024-T3 attractive for aerospace applications. However, its high susceptibility to localised corrosion because of a heterogeneous microstructure is a downside of this alloy [1-3]. For many decades, hexavalent chromium-containing compounds have been applied reliably for conversion surface treatments and active protective coating pigmentation [4-6]. However, international health and safety legislation is imposing restrictions on their utilisation, demanding the development of new corrosion inhibitive systems with reduced ecological footprints. This requires researchers either to establish new corrosion mitigation strategies or introduce new inhibitor compounds, providing equal or better active protection as compared to the existing chromated systems [7, 8].

In the early 1990s, lithium salts dissolved in alkaline solutions were reported to stabilise aluminium hydroxide through lithium intercalation, showing a corrosion inhibitive character for aluminium and its alloys [9-11]. In 1996, Drewien et al. proposed an alkaline lithium carbonate-lithium hydroxide bath, which favoured the hydrotalcite formation over aluminium hydroxides, as a promising alternative to chromate conversion coatings [12]. Later, Visser and Hayes patented the use of lithium-salts as a leachable corrosion inhibitor when incorporated in organic coatings to provide active corrosion protection [13]. Visser and his co-workers demonstrated that a protective layer was generated from these lithium-leaching coatings. Thereafter, the studies were focused on the characterisation, formation mechanism and corrosion protection properties of the conversion layer formed in artificially-damaged areas from lithium-leaching model coatings using chemical and electrochemical characterisation techniques [14-16].

In an earlier work, Visser et al. reported that leaching of lithium-salts from the coating matrix can establish an alkaline environment (pH 9-10) within the defect area, facilitating the formation of a conversion layer on AA2024-T3 [17]. In fact, gradual leaching can induce a ranging local electrolyte chemistry in the scribe, resulting in the formation of different conversion layer morphologies with exposure time. Furthermore, the crystallographic orientation of grains at the surface of the underlying metal alloy microstructure plays a role as well [17]. In terms of composition, the results suggested formation of an Li-Al layered double hydroxide (LDH) structure over an aluminium hydroxide gel [17]. The layer, albeit morphologically diverse, is capable to protect the aluminium substrate in aggressive environments like neutral salt spray (NSS) conditions [16]. The morphology of the conversion layer shows a multi-layered structure composed of two ubiquitous layers; a dense layer adjacent to the alloy substrate and a porous layer. A columnar outer layer is also observed in the peripheral region of the scribe as a consequence of higher local pH and lithium concentration [14]. Electrochemical impedance spectroscopy studies revealed that the inner dense layer is the main contributor to the overall corrosion protection provided by the conversion layer while the porous and columnar layers contribute only to a minor extent [18].

Although previous studies have shown that lithium plays a determinative role in the layer formation, the full characterisation of the layer has been challenging as lithium is hard to detect within such conversion layers. Lithium has very low characteristic X-ray energy and this causes limitations to detect it even with windowless energy dispersive spectroscopy (EDS) detectors on TEM. Auger electron spectroscopy (AES) can detect lithium; however, it cannot be used for the current system as the lithium peak overlaps with the binding energy of aluminium oxide. X-ray photoelectron spectroscopy (XPS) analysis is restricted by a low sensitivity (about 1%wt detection limit) towards lithium and additionally a low lateral resolution to differentiate the dissimilar phases of a surface area. Visser et al. have used XPS, detecting 4.5-4.8 at.% lithium just at the surface of the conversion layer, that was associated with Li-Al LDH [17]. However, lithium might be present also in the inner parts of the layer either below the XPS detection threshold or removed while sputtering the top part, hence remaining undetected. Recently, Marcoen et al. employed time-of-flight secondary ion mass spectrometry (ToF-SIMS) to follow the generation of the protective conversion layer within a 1-mm-wide scribe as a function of Li-leaching time in a corrosive environment [19]. They reported that initially a hydrated aluminium oxide surface layer with a little incorporated lithium is formed upon exposure, which laterally grows as a result of further Li-leaching. Subsequently, a columnar deposit, with likely an LDH structure, can nucleate when the lithium concentration surpasses a certain threshold in the coating defect. Nevertheless, all the time-resolved information is collected from the near-top surfaces which provide no cross-sectional chemical insights into the mature layer. In spite of the mobile character of lithium to the electron beam [20, 21], energy filtered transmission electron microscopy (EF-TEM) technique can be used to map lithium at a high resolution. Following that analysis approach, Liu et al. [14] detected lithium in different parts of the conversion layer with EF-TEM. However, owing to the difficulties preparing the TEM specimens out of different locations in the deep scribe, the cross-sections of the entire layer were not studied to observe the lithium distribution. In addition, high resolution TEM (HR-TEM) examinations to structurally characterise the local phases were not conclusive, likely caused by the destructive influence of the used electron beam on the structure. That is why the lithium conversion layer which spatially comprises many sub-micron local phases has not completely been described in terms of composition and structure, yet. This information is of great importance to fully elucidate the formation mechanism of the conversion layer within the scribe.

This work is aimed to fully characterise the protective layer on a morphological, structural and chemical level. Therefore, TEM is utilised to study the protective conversion layer generated from lithium-leaching coatings as this technique allows to produce chemical and structural images at nanometric and atomic level. The analytical TEM investigations including HR-TEM imaging, selected area electron diffraction (SAED) patterns, EF-TEM and EDS analysis are carried out on the cross-sections of the entire layer obtained by a dedicated focused ion beam (FIB) sample preparation procedure. Complementarily, cross-sectional elemental maps of the layer are acquired through high-resolution

SIMS. The findings obtained in this study reveals spatial distribution of lithium within different nanoscopic parts where the local phases are structurally characterised as well.

6.2. Materials and methods

The coating was formulated as a white opaque primer using the compounds listed in Table 1 [22]. Polyurethane was used as the polymer matrix as its chemistry shows no interaction with discrete particulate ingredients in the primer preventing interference with the leachability of the lithium carbonate corrosion inhibitor [23]. The lithium-salt loaded coatings have a total pigment volume concentration (PVC) of 30 vol%, comprising 15 vol% inorganic pigments and fillers and 15 vol% lithium carbonate, respectively. The same procedure as reported already elsewhere was used for the coating preparation [14]. AA2024-T3 sheets, provided by Arconic, with a thickness of 0.8 mm were used as the substrate. The substrate was pre-treated by a tartaric sulfuric acid (TSA) anodising process using a potential of 15 V for 25 min at 43°C, leading to an anodic film of 3-3.5 μm, according to aerospace application requirements (AIPI 02-01-003). Coatings were applied with a high-volume low pressure (HVLP) spray gun followed by a 1-h flash-off at 23 °C and curing at 80 °C for 16 h. The dry coating thickness was 20 to 25 μm. The coated panels, with dimensions of 7 cm×7 cm, were damaged intentionally (St. Andrews cross) with a carbide steel milling blade, creating 1-mm-wide scribes penetrating 100–150 μm into the metal. Prior to placing the panels in the salt spray chamber, their backs and sides were masked with a polyester tape. The panels were exposed to a 5% (w/w) NaCl neutral salt spray (NSS) environment (ASTM-B117) for 168 h. After the exposure, the samples were rinsed with flowing deionised water for 2 min in order to quench the process and remove any chloride residues.

For TEM investigations, the thin cross-sections of the entire layer were fabricated successfully from the regions of interest by means of a Thermo Fisher Helios G4 FIB and lift-out procedure. Prior to gallium ion milling, top-view appearances of the conversion layer were first examined using 2-keV secondary-electron scanning electron microscopy (SE-SEM) observations. To protect the conversion layer from gallium damage, a layer of carbon was initially deposited with the electron beam, followed by Pt deposition with the Ga ion beam (see Fig. S6.1). A Tecnai F20ST/STEM 200 kV was used for typical bright-field TEM imaging and scanning transmission electron microscopy/energy dispersive spectroscopy (STEM/EDS) elemental mapping. A Titan cubed Cs-corrected 300 kV, equipped with a direct electron (DE-16) camera, was employed for conducting high resolution TEM (HR-TEM) imaging at a low dose rate, i.e., 19 e/Å^{2}s. To map lithium within the conversion layer, the Li K-edge was energy-filtered by inserting 6-eV slits before and after the corresponding edge (EF-TEM jump-ratio approach) at either 80 or 300 keV. The identical procedure was used to filter the Al $L_{2,3}$-edge with an onset at ΔE=73 eV. To do so, the same electron dose rate as HR-TEM was used but the exposure time increased up to 60 s for acquiring sufficient counts.

High-resolution secondary ion mass spectroscopy (SIMS) imaging was performed in a helium ion microscope (HIM) (Zeiss, Peabody, MA, USA) coupled with a mass spectrometer [24-26]. To avoid

edge effects during the SIMS analysis, the cross-section samples were embedded in Wood alloy. The SIMS images were acquired using 20 keV Ne^+ primary ion with a probe current of 3 pA, leading to a probe size in the range 20–40 nm. The raster size was from 5x5 μm^2 to 10x10 μm^2 with a matrix of 512x512 $pixels^2$. The sample stage was biased to +500 V to allow the detection of positive secondary ions. The parallel detection capability of the SIMS spectrometer enables the detection of several masses simultaneously; the secondary ions detected were $^7Li^+$, $^{24}Mg^+$ and $^{27}Al^+$.

6.3. Results and Discussion

In general, the layer can be recognised by two predominant top-view morphologies; as shown in Fig. 6.1. The layer formed in the peripheral area (Region I) appears with a petal-like top view whereas the middle region (Region II) appearance shows globular features. A mixed morphology is observed normally while passing from the peripheral to the middle region (see Fig. S6.2). In fact, the conversion layers are cross-sectionally different in morphology, including various local phases that are yet to be fully identified.

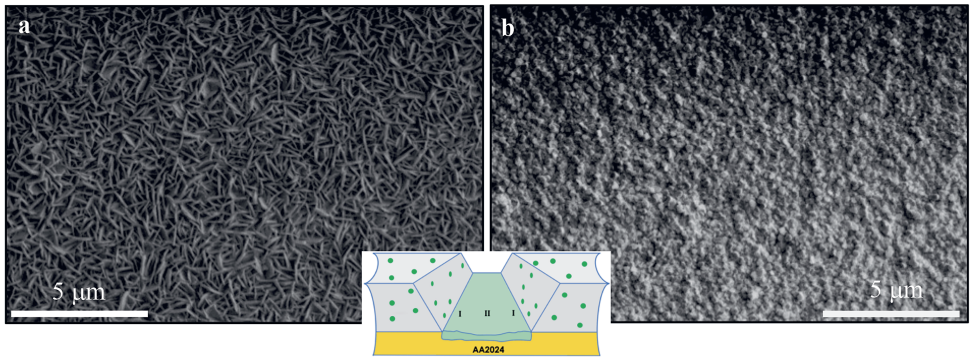


Fig. 6.1. Top-view SEM images of the conversion layer formed at the different regions of the scribe; (a) the peripheral part as Region I and (b) the middle part as Region II are denoted schematically in the inset.

6.3.1. Cross-sectional characterisation of the layer formed in the peripheral region. A typical cross-sectional morphology of the layer formed at the peripheral region of the scribed area is revealed by TEM micrography, as shown in Fig. 6.2a. The thickness of the layer is approx. 1 µm. It should be noted that the outer region of the scribe is the area where a higher alkalinity and lithium concentration is probable due to the leaching process from the coating [19]. The cross-section reveals a multi-layered morphology which is comprised of three distinct sublayers; a 150-nm-thick dense layer with roundish porosities on the substrate, a 700-nm-thick columnar layer on the top and a thin porous layer in between. HR-TEM observations of the columnar part of the layer reveal a local sandwich structure [27], directly referring to a layered double hydroxide (LDH) structure which can be characterised through the $d_{(003)}$

basal spacing of its hexagonal structure (see Fig. 6.2b) [28-30]. The $d_{(003)}$ basal spacing corresponds to the stacking sequence symmetry; however, this spacing is highly dependent on the type of intercalated anions [31]. In Fig. 6.2b, in areas with lattice spacing, numerous crystal imperfections are observed (circled in Fig. 6.2b), leading to varied values of the d spacing (i.e., 7.4-8.2 Å). In order to extract further structural information, attempts were made to record magnified images in a low dose condition, but the layer was rapidly evolving due to removal of interlayer water with the electron beam (see Fig. S6.3). The observed lattice spacing corresponds well to the $d_{(003)}$ spacing in hydrotalcite (i.e., 7.62 Å) reported by Drewien et al. [12] and Hou et al. [36]. However, the chloride intercalation is also feasible as it can reportedly give rise to a slight increase in the d spacing (i.e., 7.8 Å) [36]. For the current system, the formation of $LiAl_2$-CO_3 LDH (i.e., $[LiAl_2(OH)_6](CO_3)_{0.5}\cdot nH_2O$) is most plausible. It has been reported that CO_3^{2-} and H_2O co-exist in the interlayer spacing (anionic part) whereas Al^{3+}, Li^{+} and OH^{-} are present in the (003) plane [29, 32-37]. However, chloride might also be accommodated in the anionic interlayer spacing and thus $[LiAl_2(OH)_6]Cl\cdot nH_2O$ or $[Li_{0.99}Al_{2.01}(OH)_6](CO_3)_{0.44}Cl_{0.01}\cdot nH_2O$ can be established [36]; as depicted in the inset in Fig. 6.2b. Please note that the coated panels were exposed to NSS environment and a minor amount of chloride (~1.3 At%) is detected within the layer with EDS analysis (see Fig. S6.6). In addition, lithium in the LDH sheets might partially be replaced with magnesium that exists in the conversion layer (~1.2 At%); this might cause a rise in the d spacing as well [36]. To avoid any confusion, they are all defined as Li-Al LDH in this work.

A closer look at the porous layer shows that the porous structure is comprised of amorphous and crystalline products (Fig. 6.2c). Measuring the d spacing indicates the presence of Li-Al LDH at some parts of the porous layer, but in a dissimilar morphology than the columnar layer. In addition, the $d_{(003)}$ spacing can also be recognised in the local Fast Fourier Transform (FFT) of different parts in the image. The dense layer represents an amorphous structure, revealing no interference spots in the FFT of the image (see Fig. 6.2d). However, care should be taken not to turn the amorphous layer into a nano-crystalline one by exposure to a high-dose electron beam, as shown in Fig. S6.4.

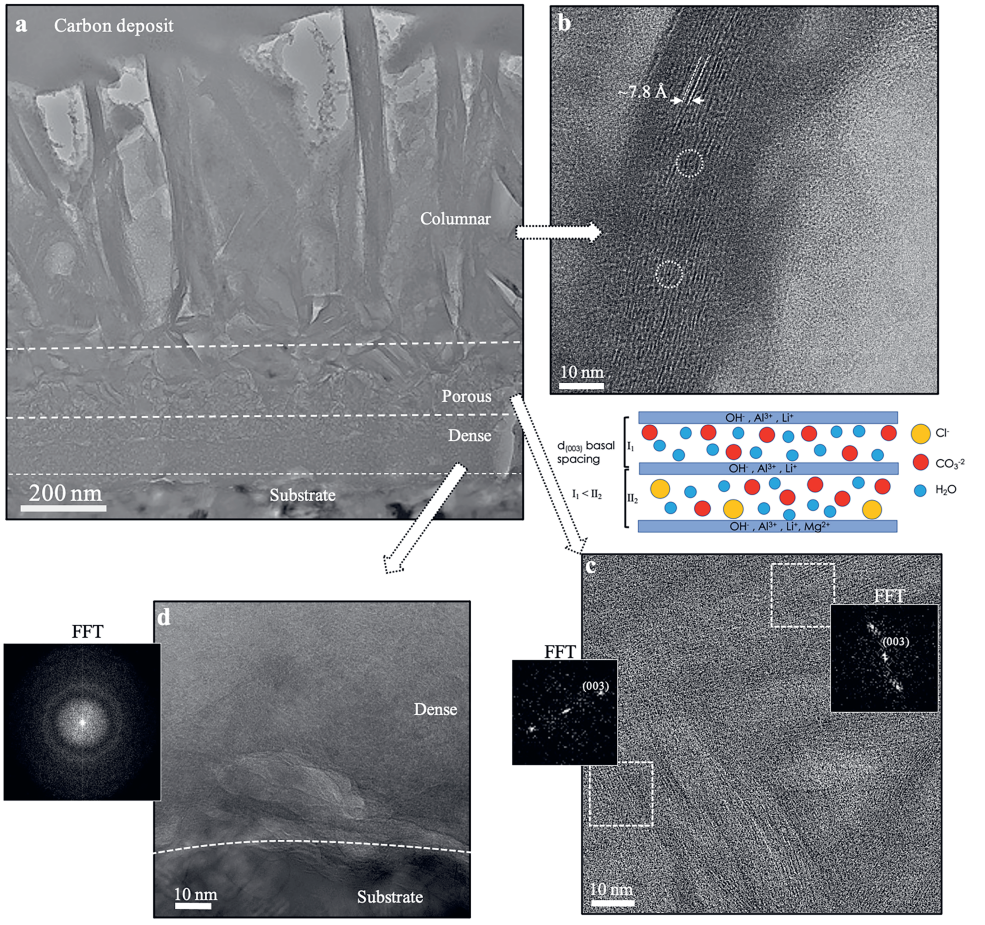


Fig. 6.2. (a) Cross-sectional TEM micrograph of the conversion layer formed in the peripheral region which is composed of three distinct sublayers. (b) HR-TEM image of an individual column, revealing the sandwich structure of the local phases. According to the d spacing, the structure represents Li-Al LDH; the circled regions are locations with crystal imperfections. The inset schematically shows a layered double hydroxide structure. (c) A closer look at the porous layer, revealing formation of Li-Al LDH but in a different morphology than columnar layer. The FFTs of the squared regions show interference spots corresponding to the (003) plane. (d) A zoomed-in image of the dense layer; the FFT pattern of the dense layer implies an amorphous structure.

To map lithium, electron energy loss spectroscopy (EELS) spectra were initially collected from the layers formed in the peripheral and middle region; Li K-edge clearly shows up as illustrated in Fig. S6.5. Energy filtered TEM (EF-TEM) was used to map lithium and aluminium; other elements including Mg, Cl, C and O are also detected within the layer with EDS analysis and presented in Fig. S6.6. Due to the presence of an extended Plasmon peak, jump-ratio EF-TEM imaging in which the intended element is mapped through dividing the Li K-edge filtered image by the pre-edge filtered

image was performed instead of normal elemental mapping with two pre-edge slits [26]. In addition, STEM/EELS mapping was also not feasible, because of perforation of the layer by the electron beam while collecting the spectrum at the required dwell time. The EF-TEM results are shown in Fig. 6.3. Comparing the Li and Al maps in Fig. 6.3a, lithium is uniformly distributed throughout the conversion layer, in particular within the dense layer. However, the local aluminium hydroxides with no/low concentration of lithium are also revealed in the top part of the layer, indicated by the yellow arrows in Fig. 6.3a. A closer elemental analysis of the porous layer/columnar layer interface discloses that lithium is present rather homogeneously over the different local phases, mostly matching to aluminium (see Fig. 6.3b). A map taken from a part of an individual column clearly reveals the presence of lithium in the form of layers while no Al and Li signals come from the interlayer spacing. As reported, there are no cations in the anionic part as aluminium and lithium are accommodated in the LDH sheets (i.e., (003) plane), see the inset in Fig. 6.2b.

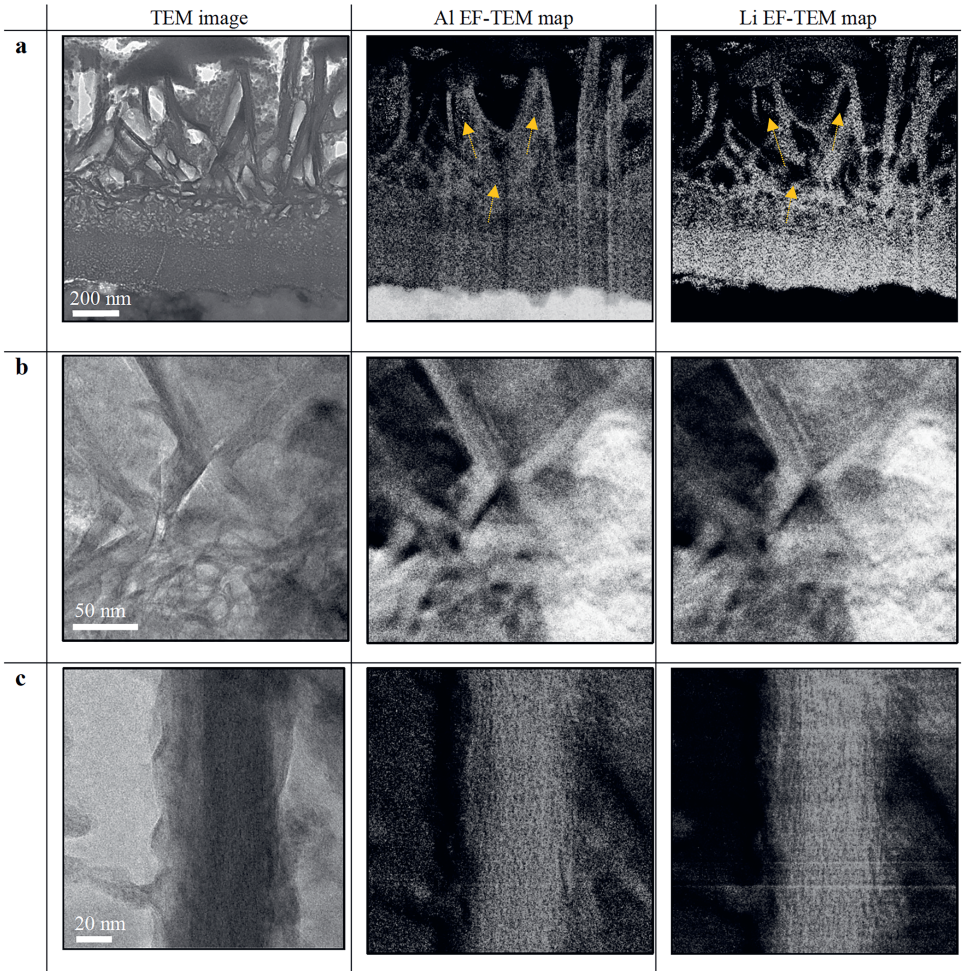


Fig. 6.3. Bright field TEM images and the corresponding EF-TEM maps of aluminium and lithium obtained at 300 keV; (a) the entire layer formed in the peripheral region; the yellow arrows indicate lithium-free region, (b) at columnar layer/porous layer interface and (c) an individual column in the top layer. Li K-edge and Al $L_{2,3}$-edge were filtered by putting 6-eV slits before and after the corresponding edges (jump-ratio technique), respectively.

6.3.2. Cross-sectional characterisation of the layer formed in the middle region. Fig. 6.4 shows structural TEM analysis of the conversion layer established in the middle region of the scribe. Compared to the peripheral region, the middle-region layer comprises an inner barrier layer with a heterogeneous morphology and a significantly thicker porous layer (ca. 400 nm) where the columnar part is missing (see Fig. 6.4a). It should be noted that the conversion layer formed in the middle area (approx. 500 nm) is thinner than that formed in the peripheral region of the scribe. HR-TEM imaging of the porous part of the conversion layer evidences the crystalline local phases within this sublayer, shown in Fig. 6.4b.

Although a smaller d spacing has been measured (i.e., 7.2 Å), but it still implies the presence of Li-Al LDH. In addition, the appearance of the spots in the selected area electron diffraction (SAED) pattern shows that the porous layer is composed of co-existing crystalline and amorphous phases. Verified by the collected SAED pattern, the dense layer is structurally amorphous, as observed for the peripheral region, where roundish 5-20 nm porosities are also seen (see Fig. 6.4c). The porosity size increases with the distance from the substrate; the porosities in the porous layer are irregular in shape.

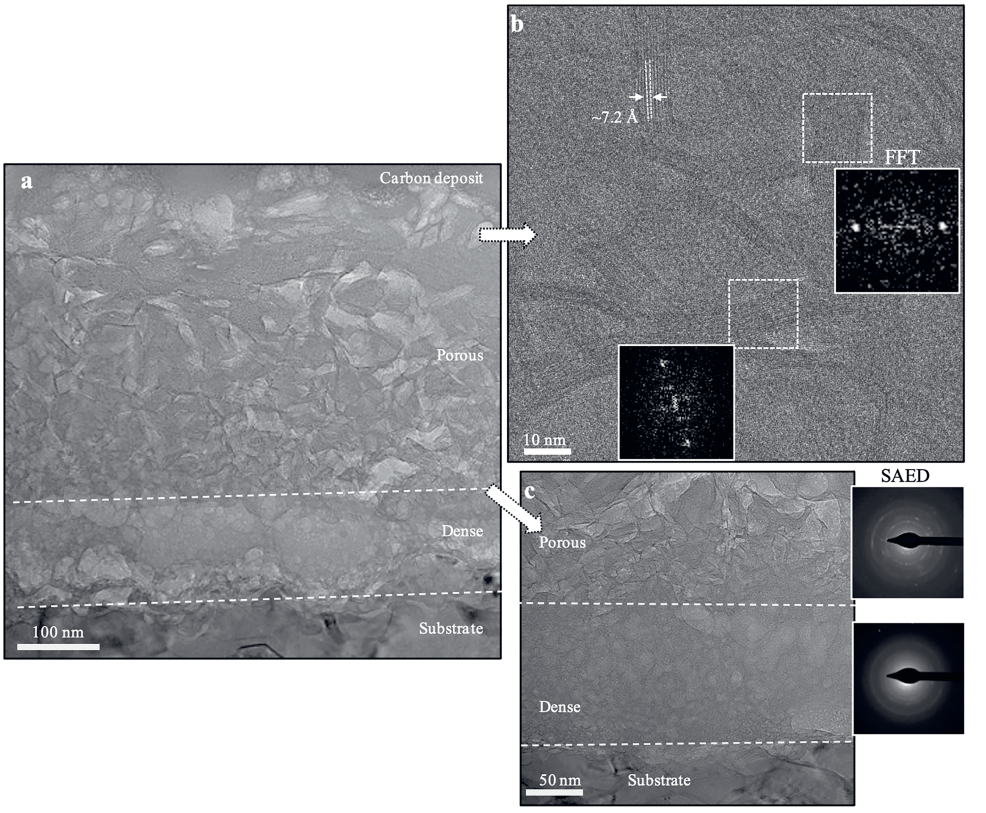


Fig. 6.4. (a) Cross-sectional TEM micrograph of the conversion layer formed in the middle region, comprising a dense and porous layer. (b) HR-TEM image and local FFTs of the porous layer, revealing local phases with Li-Al LDH characteristic. (c) A closer look at the dense and porous layer; nano-porosities are evident within the dense layer. SAED pattern reveals that the dense layer is amorphous whereas the porous layer is composed of amorphous and crystalline local phases.

EF-TEM was used to see the distribution of lithium in the layer of the middle region. As shown in Fig. 6.5a, lithium is spread uniformly within the dense and porous layer similar to the peripheral region. Recently in a work, Visser et al. detected lithium throughout the 1-mm scribe, albeit at lower concentrations in the middle region [38]. However, the local lithium-poor products can hardly be

distinguished in the EF-TEM lithium and aluminium maps which are the projection of the whole thickness. Moreover, EF-TEM maps are mainly intensity-based images with moderate detection limit and therefore inadequate to map elements present at low concentration. Thus, a high-sensitivity surface analysis is beneficial to discriminate between the regions in the protective layer with high and low lithium concentration. For this reason, high resolution SIMS analysis was performed on a cross-section of the protective layer in the middle region. Because of possible artefacts that may arise near the peripheral areas (e.g., uneven electric field for secondary ion extraction), the SIMS analysis was limited to the middle region of the scribe. An overlay of $^{27}Al^{+}$ and $^{7}Li^{+}$ SIMS images is presented in Fig. 6.5b, revealing a higher lithium signal in the inner part of the conversion layer. The presence of lithium is detected rather intensely and uniformly in the inner part of the layer whereas partly observed in the top part. Fig. 6.5c shows the line profiles along the yellow arrow in Fig. 6.5b. As can be seen, Al and Li concentrations decrease towards the top part where the layer has a higher level of porosity. In addition, a maximum Li/Al ratio of ~0.05 is estimated within the dense amorphous layer close to the substrate (note the right-side y-axis of Fig. 6.5c). This shows that the amorphous inner layer products contain lithium, as qualitatively observed in the EF-TEM maps. On the other hand, the presence of the products with less lithium can be an indication of lithium concentration variation at different stages at which various local phases can exist.

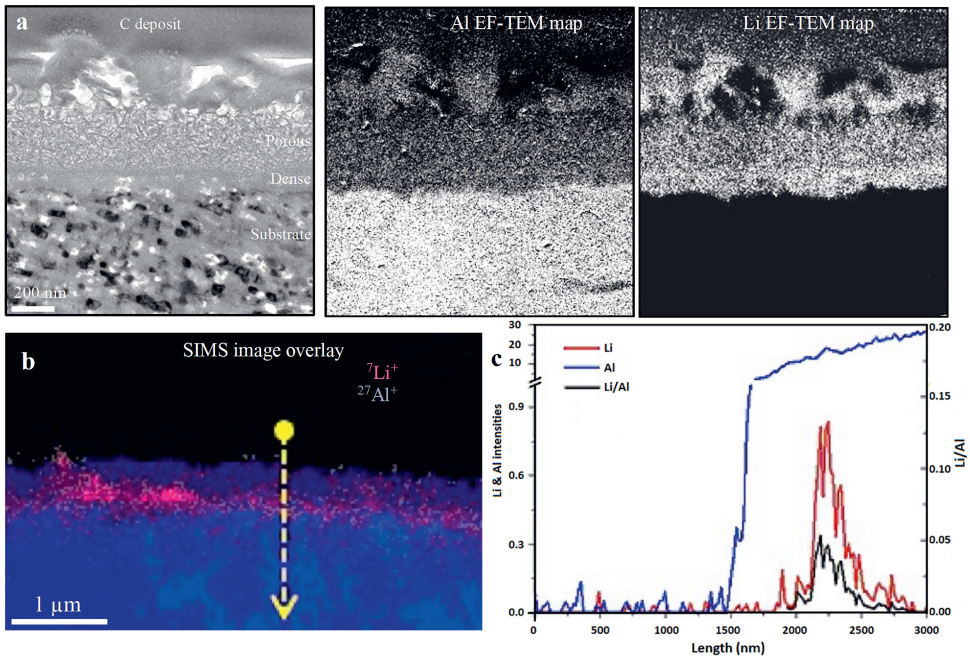


Fig. 6.5. (a) Bright field TEM images and the corresponding EF-TEM maps of aluminium and lithium obtained at 80 keV. (b) SIMS elemental distribution of Li and Al in the middle region. (c) Line elemental and Li/Al ratio profiles along the indicated arrow.

6.4. Overall cross-sectional and lateral conversion layer formation mechanism

The leaching of lithium carbonate occurs upon exposure of the coated and scribed panels to NSS, establishing a lateral concentration gradient of lithium and pH within the scribe (see Fig. 6.6) [14, 17]. Presumably, the Li concentration and pH are also diverse in the direction perpendicular to the surface which can result in the formation of a multi-layered morphology and chemistry of the conversion layer at different locations of the scribe [38, 39]. To establish a Li-Al conversion layer, lithium becomes available through the corrosion inhibitor leaching while aluminium is provided by the direct dissolution of the substrate. Scanning ion-selective electrode technique (SIET) measurements by Visser et al. [17] showed that the pH within the scribe rapidly goes up to 9.5 after 5 min of the exposure and stabilises at approx. 9.7; such alkalinity is high enough to trigger active dissolution of the substrate as the aluminium oxide passive layer would be undermined and soluble AlO_2^- would be stable. The lithium then starts to intercalate, resulting in the formation of stable corrosion products like Li-Al LDH. Through this simultaneous dissolution/precipitation process, the formation of the conversion layer may occur in the alkaline environment. For instance, the peripheral layer (Region I) appears in a columnar morphology as this region endures higher pH at which Li-Al LDH is merely stable [38]. Comparatively, in the middle part (Region II) a lower dissolution/precipitation ratio is expected as a result of a lower

alkalinity, leading to the formation of a less porous layer that contains lithium free aluminium hydroxides.

As schematically shown in Fig. 6.6, closest to the substrate, a ubiquitous dense layer in which roundish nano-porosities are evident is formed. Visser et al. proved that this layer is the main contributor of the corrosion protection [18]. Considering all structural and chemical characterisations into account, the amorphous dense inner layer can be Li-pseudoboehmite in agreement with what Visser et al. identified previously using the reference samples [17]. Pseudoboehmite is known as an aluminium compound with the chemical composition AlO(OH); however, it is finely crystalline boehmite that contains a high amount of water [40]. The porous middle layer is quite diverse in chemical composition and morphology and characterised as a mixed layer of co-existing lithium free/containing amorphous and Li-Al LDH crystalline products. The porous outer layer formed in the middle part is twice thicker than that in the peripheral region. Considering the chemical composition of the layer, the lithium-free phase is mainly aluminium hydroxide whereas the amorphous Li-containing part can be Li-pseudoboehmite. The presence of lithium-free products can be an indication of local pH and Li concentration variation in which various corrosion products can remain stable. Establishment of a columnar morphology is directly ascribed to the solution chemistry experienced by the peripheral regions. According to the chemical composition of the layer, $[LiAl_2(OH)_6](CO_3)_{0.5}\cdot nH_2O$) is considered to be the most prominent product in the columnar layer, intercalation of Cl^- in the anionic interlayer spacing can also lead to the formation of $[LiAl_2(OH)_6]Cl\cdot nH_2O$ or $[Li_{0.99}Al_{2.01}(OH)_6](CO_3)_{0.44}Cl_{0.01}\cdot nH_2O$ which have both a layered double hydroxide character.

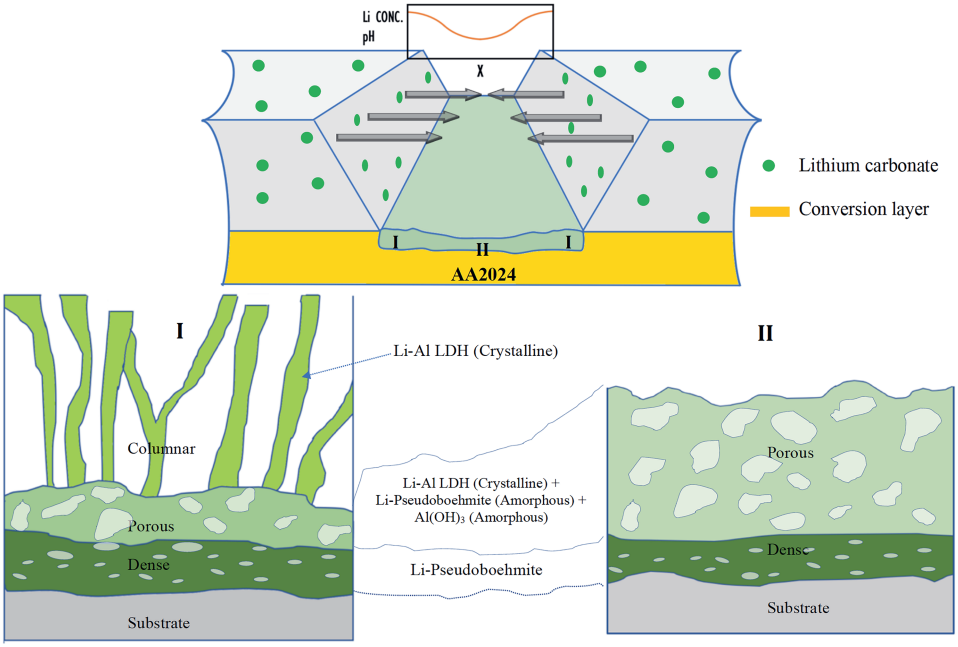


Fig. 6.6. Schematic representation of the lithium carbonate leaching from the coating, resulting in a lateral pH and Li concentration within the scribe. The scribe can be divided into peripheral (Region I) and middle (Region II) parts which experience different solution chemistry during the NSS exposure. The cross-sectional morphology of the formed layers is location-dependent and different local phases can be distinguished at the peripheral and middle region respectively.

6.5. Conclusions

In this study, the conversion layer generated on AA2024-T3 from a Li-leaching coating was fully characterised. This was achieved through successful analytical TEM and SIMS studies over the cross-sections of the entire layer formed at different locations of the scribe. It was shown that the conversion layer, regardless of the location in the scribe, is composed of an inner dense layer and a porous layer. The peripheral region which experiences higher pH and lithium concentrations during the exposure to a corrosive environment comprises an additional outer columnar layer. Lithium was found uniformly spread over the different sublayers, although the local phases with no/low concentration of lithium were also detected. The dense layer, approx. 100-150 nm thick, was specified as amorphous Li-incorporated aluminium hydroxides with a high amount of trapped water (named Li-pseudoboehmite). It was shown that the columnar morphology is composed of single-crystal pillars of Li-Al LDH. This is a product of CO_3^{2-}, H_2O and even Cl^- intercalation between the $d_{(003)}$ planes which contains Al^{3+}, Li^+ and OH^-, leading to a sandwich structure. Crystal imperfections were also observed within the structure. The porous layer, shown to be thicker in the middle region, consists of co-existing amorphous and crystalline compounds. The crystalline products are Li-Al LDH while the amorphous products may comprise different

concentration of lithium. Crystallisation of the amorphous dense layer and removal of interlayer water from the Li-Al LDH structure were observed under the electron beam but could competently be avoided through a low-dose imaging.

References

[1] A. Boag, R. Taylor, T. Muster, N. Goodman, D. McCulloch, C. Ryan, B. Rout, D. Jamieson, A. Hughes, Stable pit formation on AA2024-T3 in a NaCl environment, Corrosion Science, 52 (2010) 90-103.
[2] A.E. Hughes, R. Parvizi, M. Forsyth, Microstructure and corrosion of AA2024, Corrosion Reviews, 33 (2015) 1-30.
[3] N. Birbilis, Y. Zhu, S. Kairy, M. Glenn, J.-F. Nie, A. Morton, Y. Gonzalez-Garcia, H. Terryn, J. Mol, A. Hughes, A closer look at constituent induced localised corrosion in Al-Cu-Mg alloys, Corrosion Science, 113 (2016) 160-171.
[4] M. Kendig, R. Buchheit, Corrosion inhibition of aluminium and aluminium alloys by soluble chromates, chromate coatings, and chromate-free coatings, Corrosion, 59 (2003) 379-400.
[5] M. Kendig, S. Jeanjaquet, R. Addison, J. Waldrop, Role of hexavalent chromium in the inhibition of corrosion of aluminium alloys, Surface and Coatings Technology, 140 (2001) 58-66.
[6] L. Xia, E. Akiyama, G. Frankel, R. McCreery, Storage and release of soluble hexavalent chromium from chromate conversion coatings equilibrium aspects of Cr VI concentration, Journal of The Electrochemical Society, 147 (2000) 2556-2562.
[7] A.E. Hughes, I.S. Cole, T.H. Muster, R.J. Varley, Designing green, self-healing coatings for metal protection, Npg Asia Materials, 2 (2010) 143-151.
[8] O. Gharbi, S. Thomas, C. Smith, N. Birbilis, Chromate replacement: what does the future hold?, npj Materials Degradation, 2 (2018) 1-8.
[9] J. Fernandes, M. Ferreira, Effect of carbonate and lithium ions on the corrosion performance of pure aluminium, Electrochimica acta, 37 (1992) 2659-2661.
[10] C. Rangel, M. Travassos, The passivation of aluminium in lithium carbonate/bicarbonate solutions, Corrosion science, 33 (1992) 327-343.
[11] R.G. Buchheit, M. Bode, G. Stoner, Corrosion-resistant, chromate-free talc coatings for aluminium, Corrosion, 50 (1994) 205-214.
[12] C. Drewien, M. Eatough, D. Tallant, C. Hills, R. Buchheit, Lithium-aluminium-carbonate-hydroxide hydrate coatings on aluminium alloys: Composition, structure, and processing bath chemistry, Journal of materials research, 11 (1996) 1507-1513.
[13] P. Visser, S.A. Hayes, WO2010112605-A1, (2010).
[14] Y. Liu, P. Visser, X. Zhou, S.B. Lyon, T. Hashimoto, M. Curioni, A. Gholinia, G.E. Thompson, G. Smyth, S.R. Gibbon, Protective film formation on AA2024-T3 Aluminium Alloy by leaching of lithium carbonate from an organic coating, Journal of The Electrochemical Society, 163 (2016) C45-C53.
[15] P. Visser, Y. Liu, H. Terryn, J. Mol, Lithium salts as leachable corrosion inhibitors and potential replacement for hexavalent chromium in organic coatings for the protection of aluminium alloys, Journal of Coatings Technology and Research, 13 (2016) 557-566.
[16] P. Visser, Y. Liu, X. Zhou, T. Hashimoto, G.E. Thompson, S.B. Lyon, L.G. van der Ven, A.J. Mol, H.A. Terryn, The corrosion protection of AA2024-T3 aluminium alloy by leaching of lithium-containing salts from organic coatings, Faraday discussions, 180 (2015) 511-526.
[17] P. Visser, A. Lutz, J. Mol, H. Terryn, Study of the formation of a protective layer in a defect from lithium-leaching organic coatings, Progress in Organic Coatings, 99 (2016) 80-90.
[18] P. Visser, M. Meeusen, Y. Gonzalez-Garcia, H. Terryn, J.M. Mol, Electrochemical evaluation of corrosion inhibiting layers formed in a defect from lithium-leaching organic coatings, Journal of The Electrochemical Society, 164 (2017) C396-C406.
[19] K. Marcoen, P. Visser, G. Trindade, M.-L. Abel, J. Watts, J. Mol, H. Terryn, T. Hauffman, Compositional study of a corrosion protective layer formed by leachable lithium salts in a coating defect on AA2024-T3 aluminium alloys, Progress in Organic Coatings, 119 (2018) 65-75.
[20] S. Basak, J. Jansen, Y. Kabiri, H.W. Zandbergen, Towards optimization of experimental parameters for studying Li-O2 battery discharge products in TEM using in situ EELS, Ultramicroscopy, 188 (2018) 52-58.
[21] S. Muto, K. Tatsumi, Detection of local chemical states of lithium and their spatial mapping by scanning transmission electron microscopy, electron energy-loss spectroscopy and hyperspectral image analysis, Microscopy, 66 (2016) 39-49.

[22] J.S. Laird, A.E. Hughes, C.G. Ryan, P. Visser, H. Terryn, J. Mol, Particle induced gamma and X-ray emission spectroscopies of lithium based alloy coatings, Nuclear Instruments and Methods in Physics Research Section B: Beam Interactions with Materials and Atoms, 404 (2017) 167-172.
[23] P. Visser, H. Terryn, J.M.C. Mol, Aerospace Coatings, in: A.E. Hughes, J.M.C. Mol, M.L. Zheludkevich, R.G. Buchheit (Eds.) Active Protective Coatings: New-Generation Coatings for Metals, Springer Netherlands, Dordrecht, 2016, pp. 315-372.
[24] D. Dowsett, T. Wirtz, Co-registered in situ secondary electron and mass spectral imaging on the helium ion microscope demonstrated using lithium titanate and magnesium oxide nanoparticles, Analytical chemistry, 89 (2017) 8957-8965.
[25] P. Gratia, I. Zimmermann, P. Schouwink, J.-H. Yum, J.-N. Audinot, K. Sivula, T. Wirtz, M.K. Nazeeruddin, The many faces of mixed ion perovskites: unraveling and understanding the crystallization process, ACS Energy Letters, 2 (2017) 2686-2693.
[26] T. Wirtz, O. De Castro, J.-N. Audinot, P. Philipp, Imaging and Analytics on the Helium Ion Microscope, Annual Review of Analytical Chemistry, 12 (2019) 523-543.
[27] L. Li, R. Ma, Y. Ebina, K. Fukuda, K. Takada, T. Sasaki, Layer-by-layer assembly and spontaneous flocculation of oppositely charged oxide and hydroxide nanosheets into inorganic sandwich layered materials, Journal of the American Chemical Society, 129 (2007) 8000-8007.
[28] S. Nagendran, G. Periyasamy, P.V. Kamath, Structure models for the hydrated and dehydrated nitrate-intercalated layered double hydroxide of Li and Al, Dalton Transactions, 45 (2016) 18324-18332.
[29] J. Thiel, C. Chiang, K.R. Poeppelmeier, Structure of lithium aluminium hydroxide dihydrate ($LiAl_2$ (OH) 7.2 H_2O), Chemistry of Materials, 5 (1993) 297-304.
[30] J.L. Gunjakar, T.W. Kim, H.N. Kim, I.Y. Kim, S.-J. Hwang, Mesoporous layer-by-layer ordered nanohybrids of layered double hydroxide and layered metal oxide: highly active visible light photocatalysts with improved chemical stability, Journal of the American Chemical Society, 133 (2011) 14998-15007.
[31] I.C. Chisem, W. Jones, Ion-exchange properties of lithium aluminium layered double hydroxides, Journal of Materials Chemistry, 4 (1994) 1737-1744.
[32] M. Yasaei, M. Khakbiz, E. Ghasemi, A. Zamanian, Synthesis and characterization of ZnAl-NO_3 (-CO_3) layered double hydroxide: A novel structure for intercalation and release of simvastatin, Applied Surface Science, 467 (2019) 782-791.
[33] S.P. Newman, W. Jones, Synthesis, characterization and applications of layered double hydroxides containing organic guests, New journal of chemistry, 22 (1998) 105-115.
[34] M.-C. Lin, F.-T. Chang, J.-Y. Uan, Synthesis of Li–Al-carbonate layered double hydroxide in a metal salt-free system, Journal of materials chemistry, 20 (2010) 6524-6530.
[35] V. Rives, Layered double hydroxides: present and future, Nova Publishers, 2001.
[36] X. Hou, D.L. Bish, S.-L. Wang, C.T. Johnston, R.J. Kirkpatrick, Hydration, expansion, structure, and dynamics of layered double hydroxides, American Mineralogist, 88 (2003) 167-179.
[37] G. Choi, H. Piao, Z.A. Alothman, A. Vinu, C.-O. Yun, J.-H. Choy, Anionic clay as the drug delivery vehicle: tumor targeting function of layered double hydroxide-methotrexate nanohybrid in C33A orthotopic cervical cancer model, International journal of nanomedicine, 11 (2016) 337-348.
[38] P. Visser, K. Marcoen, G. Trindade, M. Abel, J. Watts, T. Hauffman, J. Mol, H. Terryn, The chemical throwing power of lithium-based inhibitors from organic coatings on AA2024-T3, Corrosion Science, 150 (2019) 194-206.
[39] P. Visser, Y. Gonzalez-Garcia, J.M. Mol, H. Terryn, Mechanism of passive layer formation on AA2024-T3 from alkaline lithium carbonate solutions in the presence of sodium chloride, Journal of The Electrochemical Society, 165 (2018) C60-C70.
[40] B. Baker, R. Pearson, Water content of pseudoboehmite: A new model for its structure, Journal of Catalysis, 33 (1974) 265-278.

Supplementary Materials for Chapter 6

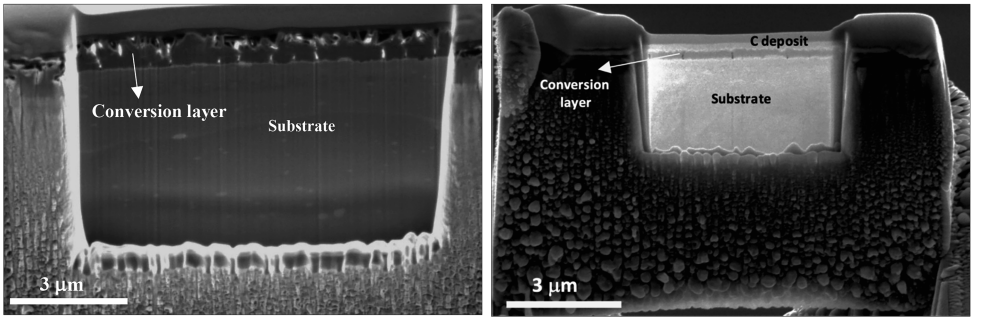


Fig. S6.1. SEM images of the cross-sections of the entire layer taken out of (left) the peripheral region and (right) the middle region fabricated with FIB.

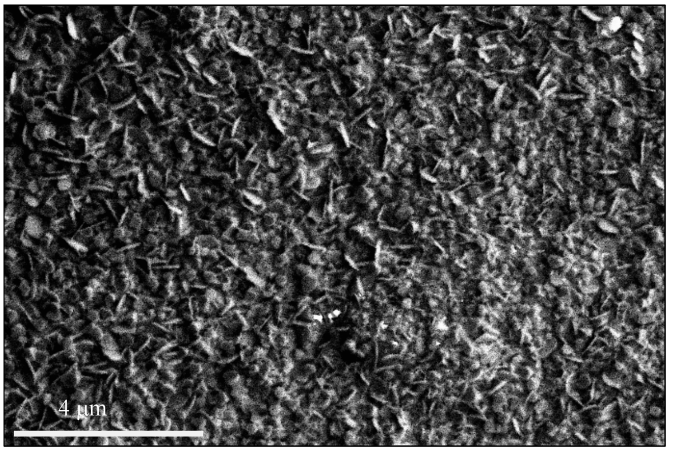


Fig. S6.2. Top-view SEM images of the conversion layer on the transition region between the peripheral and middle region.

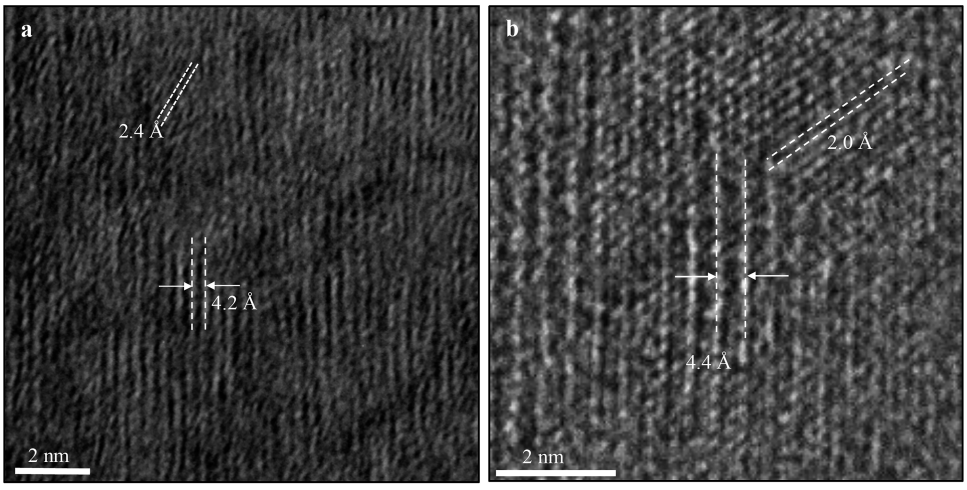


Fig. S6.3. High resolution TEM images of the crystalline columns, revealing the beam impact on the characteristic d spacing. The beam-damaged regions reveal atomic fringes; however, no distinct compound was conclusively representative. As a matter of fact, the interlayer spacing started shrinking to the values approx. 4.40 Å whilst illumination. This phenomenon can directly be attributed to elimination of interlayer water from the anion part of the LDH structure.

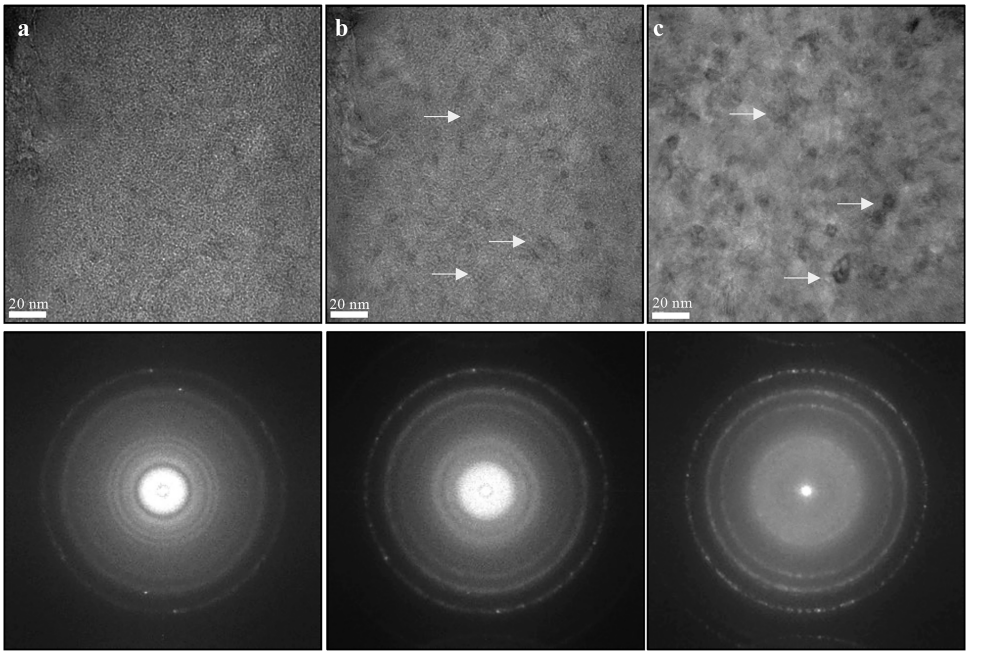


Fig. S6.4. TEM image and the corresponding FFT of the dense layer continuously exposed to a 200-kV electron beam. The image taken (a) immediately, (b) after 1 min and (c) after 10 min. The spots appearing in the FFT images reveal that the dense layer is basically amorphous but the electron beam can turn it into a nano-crystalline structure. Since the layer contains a considerable amount of water, the electron beam can give rise to its elimination, whereby nucleation of the crystalline compounds is stimulated at some thermodynamically-favoured regions.

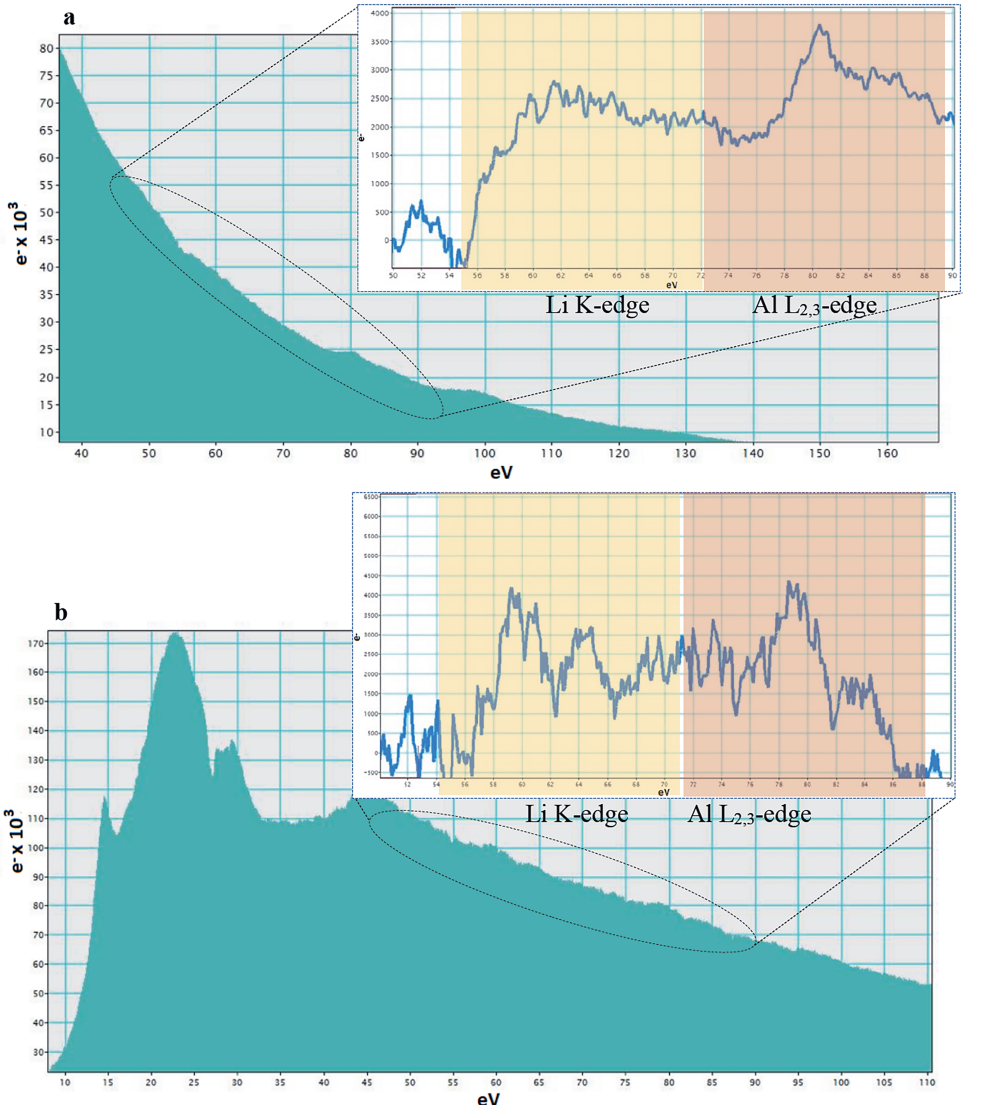


Fig. S6.5. EELS spectra collected from (a) the peripheral region at 300 keV (b) the middle region at 80 keV. Jump ration approach was used to map Li and Al through Al Li K-edge and Al $L_{2,3}$-edge, respectively. The insets are the spectra with the removed background.

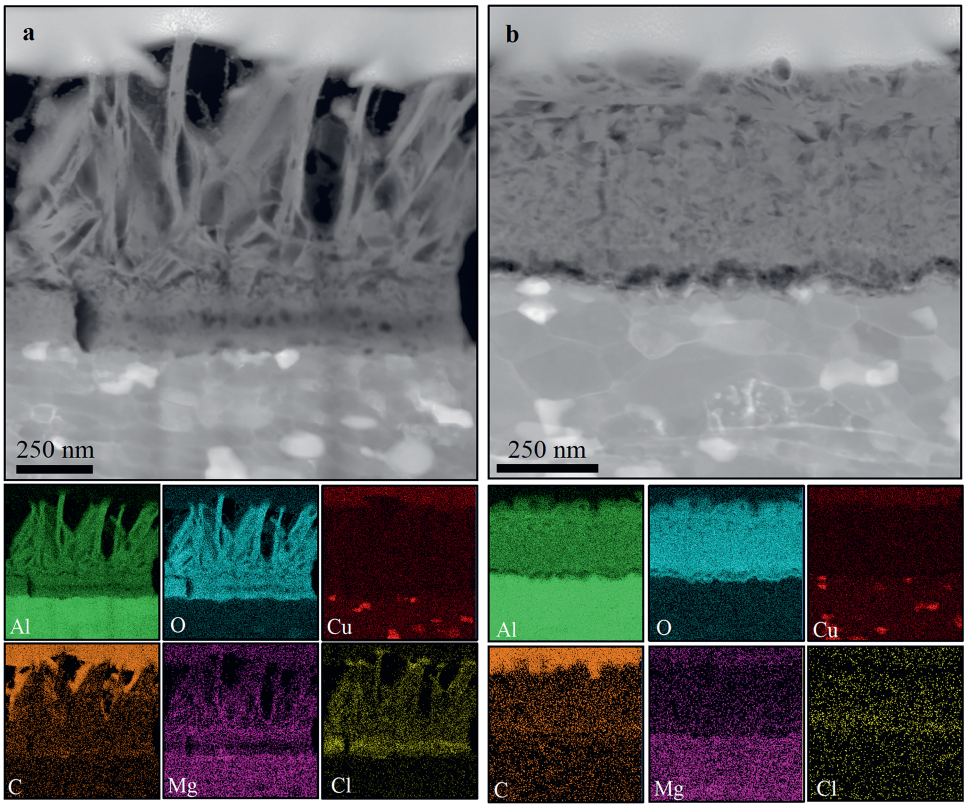


Fig. S.6.6. ADF-STEM image and the corresponding EDS elemental mapping of the conversion layer formed in (a) the peripheral region and (b) the middle region. To detect possible elements incorporated into the conversion layer, the elemental maps were obtained. As it can be seen, the specimens, taken out of the peripheral and middle region, mainly contain aluminium and oxygen; additionally, a little amount of chloride and magnesium was detected. Carbon was also found throughout the layer although the contrast in the map is dominated by the carbon overlay used to avoid damages while Ga ion-milling (sample preparation step). The presence of chloride with a higher intensity near the substrate (chloride attack) can be explained because of chloride attack of the substrate exposed to NSS. Magnesium is believed to originate from the AA2024-T3 substrate and leaching of MgO pigment, however the peripheral specimen has revealed more magnesium as it is close to the wall, receiving more leaching MgO. Further STEM/EDS examinations were carried out on different samples but the same results were acquired.

CHAPTER 7

LIQUID-PHASE TEM OBSERVATIONS OF LITHIUM-BASED CONVERSION LAYER FORMATION[1]

Lithium salts incorporated into organic coatings are released at damaged locations to establish a conversion layer in which distinct sublayers have different barrier characteristics. Thus, detailed knowledge on the sequence of formation events from the early stages of nucleation towards the final multi-layered arrangement is essential for developing and optimising lithium-leaching technology for protective coatings. In this chapter, liquid phase-transmission electron microscopy (LP-TEM) is employed to observe nanoscopic morphological evolutions in-situ during the lithium-based conversion process of AA2024-T3. Thanks to dedicated preparation of delicate sandwiched TEM specimens allowing us to explore the events cross-sectionally, we provide real-time direct mechanistic information on the conversion process from the initiation to an advanced growth stage. In parallel, we perform supplementary ex-situ SEM and TEM investigations to support and validate the LP-TEM findings. The unprecedented experimental approach developed and executed in this study provides an inspiring base for studying also other complicated surface conversion processes in-situ and at the nanoscopic scale.

Keywords: Liquid-phase TEM; Sandwiched thin specimen; Aerospace aluminium alloys; Conversion coating process, Lithium salts

[1] **A. Kosari**, F. Tichelaar, P. Visser, P. Taheri, H. Zandbergen, H. Terryn, J.M.C. Mol, Nanoscopic and in-situ cross-sectional observations of Li-based conversion coating formation using Liquid-Phase TEM, npj Materials Degradation, 5:40 (2021).

7.1. Introduction

Aerospace aluminium alloys (AAs) are highly susceptible to local corrosion attack [1], thus demanding reliable, efficient and active protection during their service life [2]. However, the highly complex microstructure of AAs, leading to enhanced mechanical properties [3], brings along complicated corrosion mechanisms that make effective inhibition challenging [4-9]. For decades, reliable active protection has been fulfilled by the application of hexavalent chromate-based conversion and organic coatings [10-13]. However, being recognised to be toxic and carcinogenic, the urgent need has risen to be replaced by non-toxic systems due to increasingly strict international health and safety legislation [14]. Thus, there has been a growing attention in the development of alternative systems that are not only eco-friendly but also provide reliable and long-lasting corrosion protection.

Up to now, several chromate-free conversion systems that are potentially worthy of consideration for industrial applications have been introduced, thanks to dedicated and extensive research [15]. Categorised according to the dominant chemistry, trivalent chromium compounds [16-18], rare earth salts [19-21], mixed zirconium/titanium systems [22, 23], lithium salts [24, 25] and transition metal oxyanion additives [26, 27] can be mentioned. Amongst these options studied, lithium salts have the merit of being potentially used as both conversion bath chemicals [28, 29] and in particular as a leaching inhibitor compound in organic coatings [30-33]. The latter application of lithium salts has been considered promising for the future of green active corrosion protection of AAs [34, 35]. In this scheme, lithium salts incorporated into organic coatings are able to leach with a long-range throwing power at damaged locations of organic coating (scribe) [32], triggering an irreversible conversion process [33]. The anionic part of lithium salts like lithium carbonate can induce an alkaline environment (pH 9-11) [36] within the scribe where severe corrosion is expected due to instability of the aluminium oxide passive layer under such conditions [37, 38]. However, lithium plays a critical role in the conversion process by stabilising the corrosion products, leading to the gradual formation of a conversion layer with a multi-layered arrangement [28, 39].

The typical morphology of a Li-based conversion layer fully grown within an artificial 1-mm-wide scribe in neutral salt spray environment includes a columnar outer layer and thin dense inner layer where a porous layer resides in between [40, 41]. The sublayers contribute to the corrosion protection of the underlying AAs substrate differently and as reported [42], the dense inner layer, which has in fact the lowest porosity, offers the best protective contribution among the different sublayers. In terms of chemical composition, the outer columnar layer is composed of mostly crystalline aluminium-lithium layered double hydroxide (LDH) while the dense inner layer contains amorphous lithium-pseudoboehmite; a mixture of both amorphous and crystalline products is found in the porous layer [40].

Up to now, a good understanding in relation to structure, morphology, and composition of the conversion layer has been acquired. However, a detailed knowledge on the sequence of formation events from the early stages of nucleation towards the final multi-layered arrangement is still missing.

This is of pivotal importance to understand the mechanism involved in the lithium-based conversion process and its further development towards a sustainable active protection technology with optimal reliability. Thus, an approach that can provide direct and real-time morphological observations of the entire conversion process at high temporal and spatial resolution is crucial.

To this aim, liquid phase-transmission electron microscopy (LP-TEM) [43-46] can be considered to observe dynamic morphological changes at AA surfaces as a consequence of interactions with a Li-based solution. However, one of the great challenges in this regard and related to the current work is that the TEM specimens (lamellae) require electron transparency and generally consist of foils of roughly 50-400 nm thickness. On the other hand, once the still relatively-thin specimens are exposed to an aggressive environment (e.g., alkaline solutions for aluminium and its alloys), they may dissolve very quickly. Therefore, without any dedicated specimen preparation, the conversion process in which the aqueous Li-based solution dissolves a part of the metal surface to form a chemically-mixed layer cannot be fulfilled. Thus, sandwiching thin specimens between inert cover layers can be a remedy in this case as the oxidation direction can be controlled to take place in the plane of the specimen rather than perpendicular to it, i.e., through-thickness. For such sandwiched specimens, the interaction initiates at the side of the thin masked lamellae where it can penetrate cross-sectionally. This approach was employed successfully for cross-sectional LP-TEM observations of intermetallic phases-induced local corrosion in AAs [47].

This study is devoted to elucidating the formation mechanism of a protective conversion coating from a Li-salt based solution in space and time. Here, we therefore employ a purposeful specimen masking procedure and also an intricate sample preparation and transfer-to-liquid-cell procedure for dedicated in-situ LP-TEM analysis. The application of liquid-phase TEM for studying sandwiched thin specimens enables to uniquely visualize the cross-sectional sequence of events with the required spatial and temporal resolution to resolve the formation mechanism from early-stage formation to the final multi-layered arrangement.

7.2. Method

***7.2.1. Liquid-phase scanning* TEM.** We employed a Thermo-Fisher Helios G4 FIB/SEM equipped with the EasyLift NanoManipulator system to prepare the TEM specimens (lamellae) and also to transfer them to the liquid cells. Relatively thick (approx. 300-400 nm) lamellae were fabricated and masked with 30-nm-thick layers of tetraethyl orthosilicate (TEOS) on both sides (Fig. 7.1a) to cross-sectionally observe the conversion layer formation. Thick specimens provide more material for the formation of the Li-based conversion layer while the resolution still remains good enough to explore nanoscopic morphological evolutions during the process. The sample transfer procedure and TEOS deposition parameters were presented in detail elsewhere [47]. To transfer the specimens to the chips, the needle was welded to the prepared specimen with a 100-nm thick TEOS layer using the electron beam (Fig. 7.1b). Interestingly, there is no need to cut off the TEOS weld and it smoothly detaches itself

upon landing the lamella on the chip and the electron transparent membrane. Note that the cut-off process using the gallium beam might result in contaminating the specimen with gallium. When positioned on the chip, the lamellae were also masked with rather thick TEOS layers on three sides, leaving the clean edge bare to interact with the electrolyte (Fig. 7.1c). Note that TEOS is electrochemically inactive and does not establish galvanic interaction with the AAs specimen. The chips were plasma cleaned for 1 min before putting the liquid cells together to remove contaminations and to make the surfaces hydrophilic, facilitating the initial flow to fill up the liquid cell with the electrolyte [48]. It should be noted that the electrolyte was stationary over the experiments in order to avoid disturbing the local solution chemistry during the conversion process by a flowing electrolyte. When loaded on a home-made liquid-cell TEM holder, the specimens were located at the entrance side of the electron probe to effectively mitigate the beam-broadening effect on the resolution in STEM mode (Fig. 7.1c) [49]. A schematic representation of the current liquid-phase STEM research approach is shown in Fig. 7.1d.

A Cs corrected Thermo-Fisher Titan 300 kV TEM was employed to perform in-situ studies. For low-dose in-situ imaging, a bright field (BF) detector was used as it further alleviates the beam-broadening effect and additionally has the benefit of an enhanced signal-to-noise ratio compared to a high angle annular dark filed (HAADF) detector [50]. To effectively lessen the electron beam impact on solution chemistry, a low beam current of 0.1 nA, measured with liquid between the membranes only (no sample), was used. Besides, a few snapshots were merely taken during an experiment of 1 hr. Note that the studied solution is moderately alkaline but may gradually turn acidic if it were continuously exposed to the electron beam, hence the interrupted but frequent imaging procedure applied [51, 52]. Snapshots at critical stages were taken at 5,000X magnification of 2048 × 2048 pixels. To further mitigate the electron effect regarding the point-excitation in STEM mode [53], the drift corrected frame integration (DCFI) function on the Thermo Fisher Velox software was used to integrate 3 acquired frames at a low dwell time of 0.2 µs. The electrolyte, 0.01 M NaCl + 0.01 M Li_2CO_3 (pH 10.6), was stagnant during the experiment. According to the literature, this solution chemistry is representative for lithium concentration and pH in a defect area of 1 mm wide when leaching takes place from the coating matrix [39].

***7.2.2. Typical SEM/TEM* analysis.** For ex-situ analysis, 2-mm-thick sheets of AA2024-T3 were polished in a 0.5 and 0.05 µm alumina slurry in a non-aqueous solution on a soft cloth, followed by cleaning with isopropanol in an ultrasonic bath. Afterwards, an area of approx. 25 cm^2 of the specimens was exposed to either 5 mL (electrolyte thickness = 2 mm) or 100 mL (electrolyte thickness = 40 mm) 0.01 M NaCl + 0.01 M Li_2CO_3 (pH 10.6) solution for 7 h. After completion of the exposure, the samples were rinsed off carefully with copious distilled water for a few seconds to avoid direct salt precipitation upon drying. Then, the surface morphology of the conversion layer formed on the alloy matrix was inspected with SEM performed at 15 keV collecting emitted secondary electrons (SE) in ultra-high-resolution mode. Besides, the thin cross-sections for TEM were fabricated out of regions of interest

with FIB and lift-out procedure for detailed morphological and compositional investigations. STEM/EDS microanalysis was performed using a Cs corrected Thermo Scientific Titan 300kV (S)TEM with the Super-X configuration consisting of 4 Si Drift Detectors (SDDs).

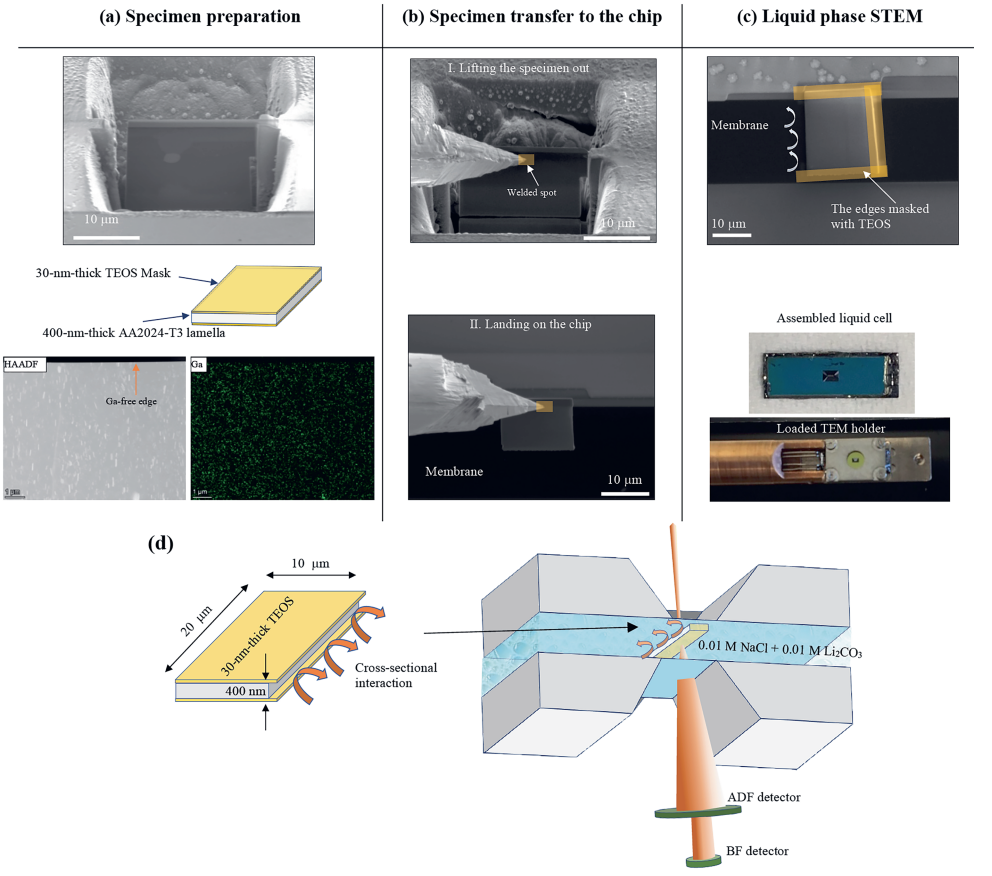


Fig. 7.1. Liquid-phase STEM study of Li-based conversion coating formation using sandwiched thin specimens. (a) The lamellae of 400-nm thick are fabricated out of AA2024-T3 sheets using a Ga ion FIB/SEM. Afterwards, the prepared specimens are sandwiched by applying two 30-nm-thick layers of TEOS to control the oxidation direction. The sandwiched thin specimens control the oxidation direction to be in the plane of the specimen allowing for cross-sectional observation of the conversion process. The STEM image and the corresponding Ga map shows a sandwiched lamella with a clean (Ga free) edge to interact with the electrolyte. (b) The sandwiched lamella is transferred carefully and precisely to the chips. (c) When positioned on the chip, three other edges of the lamella are masked with TEOS, leaving the clean edge bare only. The put-together chips are sealed with an epoxy resin glue and the tip of a home-made liquid TEM holder with a loaded liquid cell is shown. (d) The experiments are performed in scanning TEM mode using either a bright field or high angle annular dark field detector. The specimen is also located at the entrance side of the liquid cell to lessen the impact of the beam-broadening caused by the thick electrolyte.

7.3. Results

7.3.1. LP-TEM studies of the conversion layer formation. Fig. 7.2 shows snapshots taken at different stages of the conversion layer formation at the side of a sandwiched lamella. The BF-STEM image at 0 min shows that the lamella contains three grains. This BF-STEM image has been acquired in the absence of electrolyte; note that water causes multiple scattering of the electrons leading to a diminished contrast [50]. After 23 min of exposure, we see an active dissolution of the alloy matrix without any sign of conversion layer formation. Until the total exposure of 42 min, the corrosion continues to further dissolve the alloy matrix; approx. 3.48 μm of the specimen is dissolved totally up to this point. At 42 min, initial precipitation of the conversion layer in the form of tiny needles is observed, indicated by the orange arrows. Interestingly, the preliminary precipitation takes place when enhanced dissolution is seen in the dissolution front due to the locally-dissolved matrix at the grain boundary [54, 55]. As the corrosion further propagates into the sandwiched specimen, the needles increase in number and to an average length of approx. 0.8 μm (at 47 min). The inset allows a closer look at the layer after 55 min, revealing the formation of a porous layer upon further penetration of corrosion into the sandwiched specimen. The STEM image taken at 60 min reveals the conversion layer with a multi-layered arrangement. The needles, observed at the outer side of the specimen, are representative for the columnar morphology reported in prior literature [41]. The porous-like layer becomes darker in contrast as it gets closer to the alloy matrix. This can be linked to the less porous morphology of the layer formed closest to the alloy matrix and at the latest stage of the conversion process. Thus, we here consider the layer near to the alloy matrix as the dense layer as reported in prior literature [41]. It should be noted that here we merely report on the morphological evolutions; the sublayers might undergo structural and compositional modifications at different formation stages, but the current technique is unable to reveal them at the same time. As shown in Fig. 7.2b, the kinetics of the dissolution gradually slows down upon conversion layer formation at different stages. The dissolution front has penetrated approx. 1950 nm from 0 to 23 min (84 nm/min), approx. 1530 nm from 23 to 42 min (80 nm/min), approx. 300 nm from 42 to 47 min (62 nm/min) and approx. 700 nm from 47 to 60 min (53 nm/min) in depth.

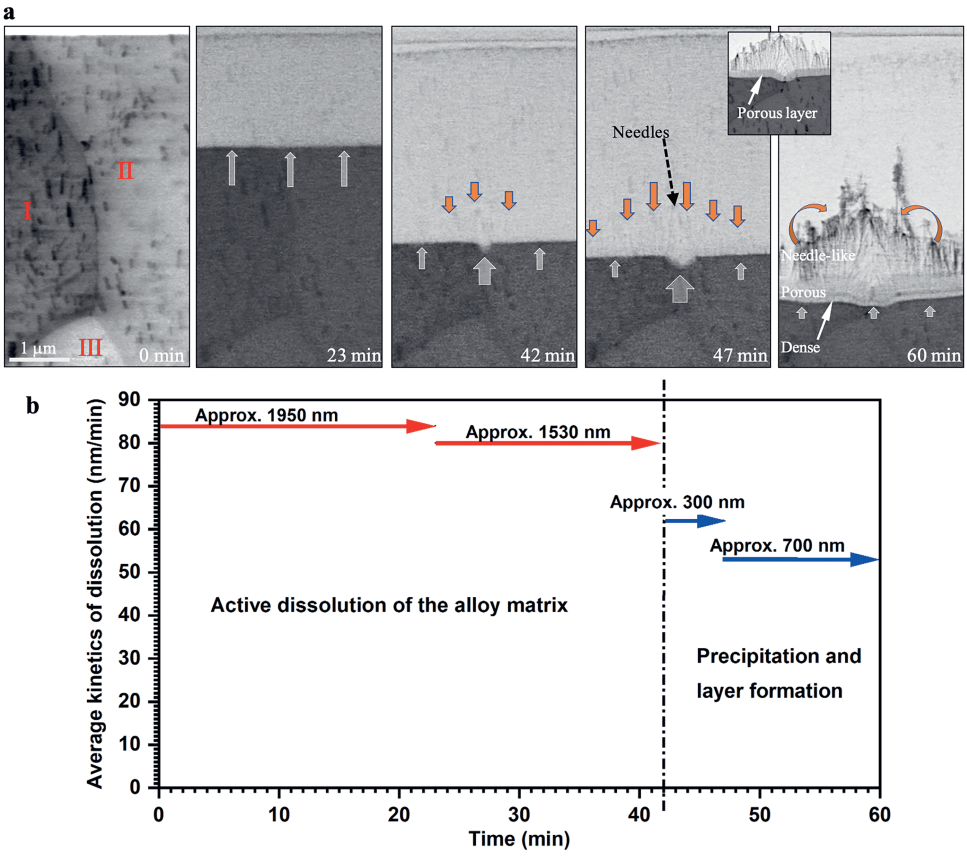


Fig. 7.2. Cross-sectional liquid-phase STEM observations of the conversion layer formation in 0.01 M NaCl + 0.01 M Li_2CO_3. (a) Time-resolved BF-STEM images of the conversion layer at different stages of the formation at the bare side of a sandwiched lamella. The image taken at 0 min is in the absence of the electrolyte, revealing three grains in the specimen. The process begins by uniformly dissolving the alloy until needles appear at the solution/alloy interface. A mature conversion layer including the columnar and porous layer is observed after 60 min. The inset is a closer look at the conversion layer taken at 55 min. The white and orange arrows indicate the dissolution and precipitation process, respectively. The specimen is approx. 400-nm thin excluding the TEOS layers. (b) The graph presents the average kinetics of the alloy matrix dissolution at different stages of the conversion process.

Fig. 7.3 show the further investigations of the very early stages of the conversion layer formation on a sandwiched specimen. At the beginning of exposure, the HAADF-STEM shows the appearance of some dents at the edge of the specimen, indicated by the white arrows (t = 5 min). However, the entire surface gets involved in the dissolution process and the alloy matrix starts to dissolve relatively uniformly (t = 25 min). Interestingly, the dissolution front (the substrate/layer interface) reveals an undulating pattern that shows temporary local anodes while penetrating into depth. Besides, the nanoscopic intermetallic particles (IMPs are revealed as the bright spots in the HAADF-STEM image) which are distributed over

the alloy matrix also undergo corrosion, either fully disappearing or leaving behind bright remnants as indicated by the red arrows.

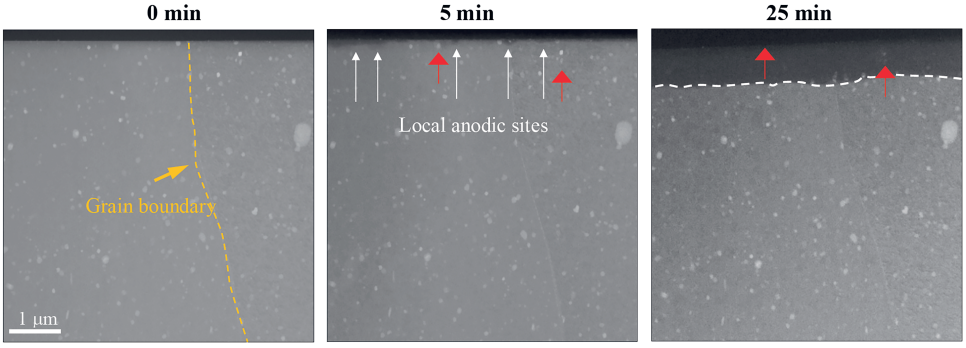


Fig. 7.3. LP-TEM observations of initial stages of the conversion layer formation in 0.01 M NaCl + 0.01 M Li_2CO_3. Time-resolved HAADF-STEM images of a sandwiched specimen, showing initial local anodes and then the subsequent uniform dissolution. The white arrows indicate initial local dissolution sites. The red arrows point to the nanoscopic copper-rich IMP as the potential cathodic sites. The specimen is approx. 300-nm thin excluding the TEOS layers.

Fig. 7.4 shows the HAADF-STEM images of a sandwiched specimen including three grains being involved in the conversion layer formation. Having been exposed for 30 min, we clearly see the formation of the needles while the porous layer is still absent. Note that the images are taken in the absence of the electrolyte. This is consistent with the real-time LP-TEM observations shown in Fig. 7.2, revealing the needle-like structure as the preceding morphology. As can been seen, grain I shows a higher electrochemical activity and dissolved to a greater extent, as compared to grain II. This phenomenon can be linked to specific atomic planes that dissolve in a faster rate; this phenomenon has been observed by Visser et al. for bulk samples as well [36]. The dissolution along the grain boundaries is accelerated as shown by the red arrows; more evidence can be found in Supplementary Data. It should be noted that the formation of the needles is a dynamic process including simultaneous dissolution of the specimen and establishments of single columns.

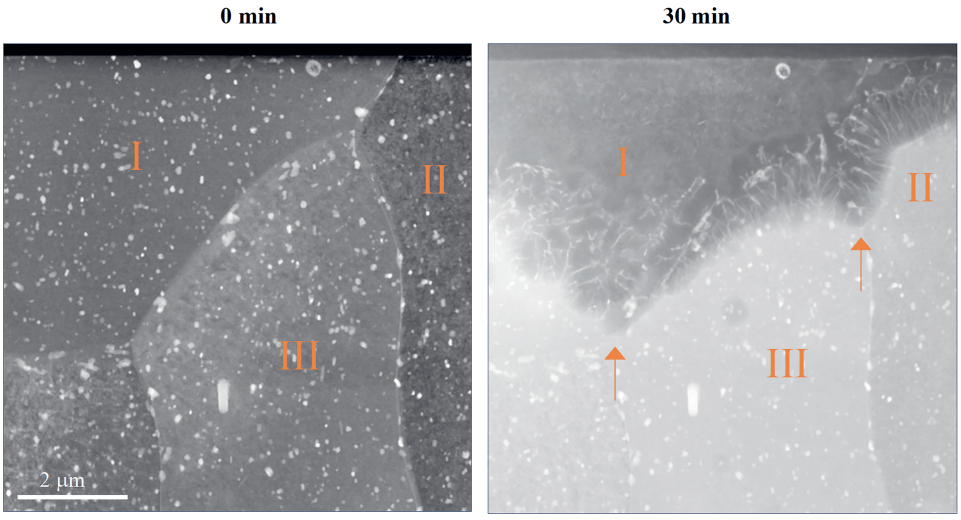


Fig. 7.4. LP-TEM observations of initial stages of the conversion layer formation in 0.01 M NaCl + 0.01 M Li_2CO_3. HAADF-STEM images of a sandwiched lamella before and after 30 min exposure, revealing different electrochemical activity of grain boundaries (orange arrows) and also grains. The images are taken in the absence of the electrolyte. The specimen is approx. 350-nm-thin excluding the TEOS layers.

Fig. 7.5 shows the post-mortem HAADF-STEM/EDS analysis of the conversion layer formed on a sandwiched lamella exposed to 0.01 M NaCl + 0.01 M Li_2CO_3 for 1 h. The HAADF-STEM image reveals three distinct sublayers, verifying that the sandwiched specimens are representative for the conversion layer formation studies. As is shown, aluminium is the main elemental contributor of the layer and it has been detected everywhere within the conversion layer. The presence of oxygen is a clear indication of the conversion layer formation where copper-rich regions originating from the corrosion of nanoscopic Cu-rich IMPs are distinguishable [47]. Unfortunately, the relatively high thickness of the sandwiched specimen including the Si_xN_y membrane and mask layers hindered energy electron loss spectroscopy (EELS) studies to map lithium.

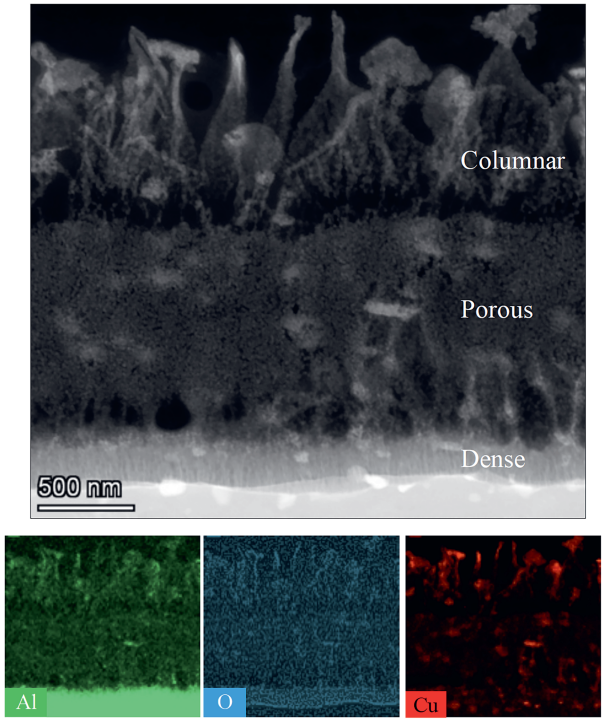


Fig. 7.5. Post-mortem analysis of the conversion layer formed on a sandwiched specimen in 0.01 M NaCl + 0.01 M Li_2CO_3. HAADF-STEM/EDS analysis of the preformed conversion layer, showing a multi-layered arrangement. Furthermore, Al, O and Cu are identified as main elements incorporated into the layer. Cu-rich regions are the corroded nanometric intermetallic particles. Note that lithium cannot be detected via EDS technique.

7.3.2. Analysis of the conversion layer on bulk samples. In order to support and validate the LP-TEM results, we conducted a similar surface conversion treatment on polished AA2024-T3 bulk samples. Fig. 7.6a shows the corrosion-attack morphology of a sample of approx. 25 cm^2 exposed to 100 mL (electrolyte thickness = 40 mm) of the studied solution for 7 h. It shows that the formation of the conversion layer is delayed if the sample is exposed to a large amount of 0.01 M NaCl + 0.01 M Li_2CO_3 solution. As evident, the corrosion-attack morphology is rather rough due to severe corrosion. Furthermore, the corresponding SEM image reveals no conversion layer formed on this sample. In contrast, we see the formation of the conversion layer within the same period if an identical sample is exposed to 5 mL of the solution (electrolyte thickness = 2 mm). In Fig. 7.6b, the alloy surface is still shiny and the SEM image obviously shows the typical petal top-view morphology of the conversion layer [41].

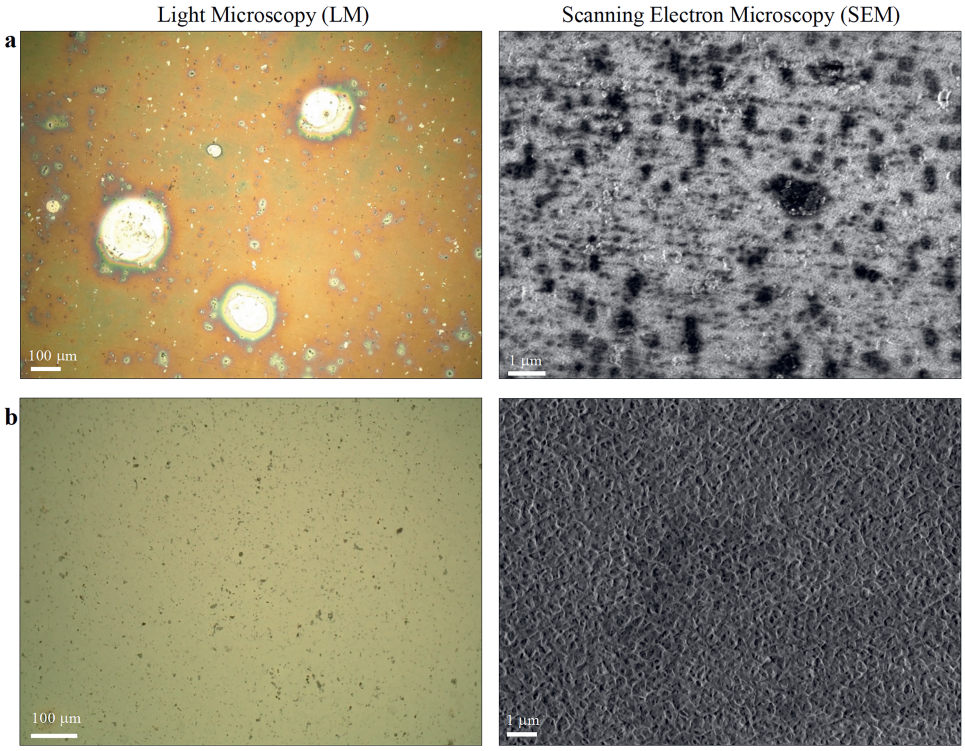


Fig. 7.6. Surface morphology of the AAs sample exposed to different amount of 0.01 M NaCl + 0.01 M Li_2CO_3 solution for 7 h. LM and SEM images of the conversion layer formed at the batch condition of the solution volume/exposed surface area ratio of (a) 4 mL/cm² and (b) 0.2 mL/cm².

Fig. 7.7 shows the cross-sectional STEM/EDS analysis of the conversion layer corresponding to Fig. 7.6b. Morphologically, the layer is composed of a columnar outer layer of 50-100 nm thick and an underlying porous layer of the same thickness. Comparatively, the conversion layers generated from leaching of lithium carbonate within the scribe in salt spray environment are rather thicker as they are exposed to different electrolyte conditions and for a longer period (i.e., 168 h). As expected, the layer mainly contains aluminium and oxygen, implying the formation of a conversion layer. Interestingly, some bright spots are observed in the HAADF-STEM image corresponding to the elemental copper map; note the white arrows. The incorporation of lithium in the conversion layer has already been demonstrated elsewhere [39, 40]. In a prior work, we demonstrated that lithium can be found in both amorphous and crystalline compounds within the conversion layer [40].

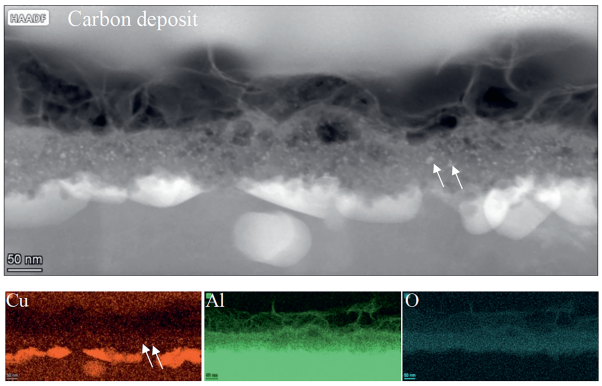


Fig. 7.7. Post-mortem analysis of the conversion layer formed on the bulk alloy. Cross-sectional STEM/EDS analysis of the conversion layer. The white arrows point to the copper-rich regions in the conversion layer; see the Cu map. The lamella was fabricated with the lift-out FIB procedure out of the sample exposed to 5 mL of 0.01 M NaCl + 0.01 M Li_2CO_3 solution for 7 h.

7.4. Discussion

Here, the direct LP-TEM observations along with the complementary analysis provide us with a comprehensive insight into the mechanisms of the Li-based conversion process on AAs at high temporal and spatial resolution. Fig. 7.8 schematically shows different stages of the conversion layer formation in the sandwiched thin specimen corresponding to the bulk system. The graph schematically shows the change of the $Al(OH)_4^-$ concentration and the dissolution kinetics while the conversion layer evolves morphologically.

Given the instability of an aluminium oxide passive layer in the alkaline environment (here pH 10.6) [56], the active dissolution of the alloy matrix initiates at some regions of the matrix upon passivity loss. It preferably takes place at the grain boundaries or nanoscopic IMPs which have higher electrochemical activity [47, 55]. The active dissolution of the alloy matrix leads to a higher concentration of $Al(OH)_4^-$ at the alloy matrix/solution interface. For the sandwiched thin specimen, the mass transfer of $Al(OH)_4^-$ ions from the interface outwards takes place through the confined region between the layers of TEOS. Since, $Al(OH)_4^-$ is the only soluble species in the studied alkaline environment, this phenomenon causes a retarding impact on the kinetics of aluminium dissolution with time, in particular when the dissolution front penetrates further into the depth, lengthening the diffusion path. Nevertheless, the dissolution of the alloy matrix continues until the needles appear as the first precipitates upon supersaturation.

In fact, the conversion layer appears in the form of the needles as a part of the surface undergoing active dissolution while the precipitation happens in its close vicinity. As the conversion process proceeds, the $Al(OH)_4^-$ concentration at different locations of the alloy matrix/solution interface reaches supersaturation, leading to a higher rate of precipitation; the needles grow taller and increase in number. In fact, the substrate is the only source for supplying the main constituent element of the conversion

layer being aluminium. According to Drewien et al, supersaturation of solution by $Al(OH)_4^-$ is critical for triggering the precipitation of stable and protective Li-incorporated corrosion products[28]. In the presence of lithium, the supersaturation state may require lower concentrations of $Al(OH)_4^-$ as compared to the supersaturated condition in pure water. Under the experimental conditions of LP-TEM, the supersaturation can actually be fulfilled at the expense of the substrate dissolution until reaching a critical concentration of $Al(OH)_4^-$. This can explain why the conversion layer formation is delayed if a larger amount of the lithium-containing solution is used as observed for the post-exposure ex-situ microscopic analysis. Therefore, the higher solution volume needs excess dissolution of the substrate to become saturated (Fig. 7.6).

From this stage onwards, the conversion layer shows a porous morphology due to a supersaturated state and slower dissolution rate of the alloy matrix (higher precipitation/dissolution rate). However, the dissolution front still moves along until the formation of a sublayer which is less porous (dense-like layer), effectively slowing down the process. This phenomenon can also hinder the diffusion of dissolved ions outwards and accommodates local $Al(OH)_4^-$ supersaturation in which the next sublayer consequently shows up in a less porous morphology. Since the dense layer can act well as a protective barrier, it effectively hinders further dissolution until the conversion layer process comes to a halt. Besides, it is reasonable to assume that the pH gradually drops with distance from the surface which can also thermodynamically favour the passivation of the alloy surface. However, the dissolution front can penetrate into depth as long as the local pH is above 8 [56].

Given the prior investigations by Visser et al. [39] and the current observations with LP-TEM, we can correlate all the stages of the conversion process in the sandwiched thin specimens to those taking place in the bulk samples from a mechanistic point of view. As schematically shown in Fig. 7.8, initial stages of active dissolution are identical in both the thin and bulk system. For the sandwiched thin specimens, the required local supersaturation can however happen over shorter periods, although the sandwiched thin specimens experience a considerably larger solution amount to the exposed surface area within the liquid cell. That is caused by the confinement between two layers of TEOS which allows the thin specimens to preserve their local solution chemistry at the matrix/solution interface. Besides, in the bulk system, the dissolution front penetrates into the alloy matrix and consequently the columns further grow in 3-dimensional space and get entangled with time, as compared to 2-dimensionally grown needles in the sandwiched thin specimens. This phenomenon can effectively slow down the dissolution rate and lengthen the conversion process. As directly observed with LP-TEM, the dense layer forms at the latest stages of the conversion process when the kinetics of dissolution/precipitation ratio is low; this is the case for the bulk state as well. Given the enhanced barrier properties of the dense layer, the samples exposed longer to a lithium containing solution can thus reveal superior corrosion performance in line with prior work reported by Visser et al. [39]. In fact, they can acquire a thicker dense layer during a longer period of exposure.

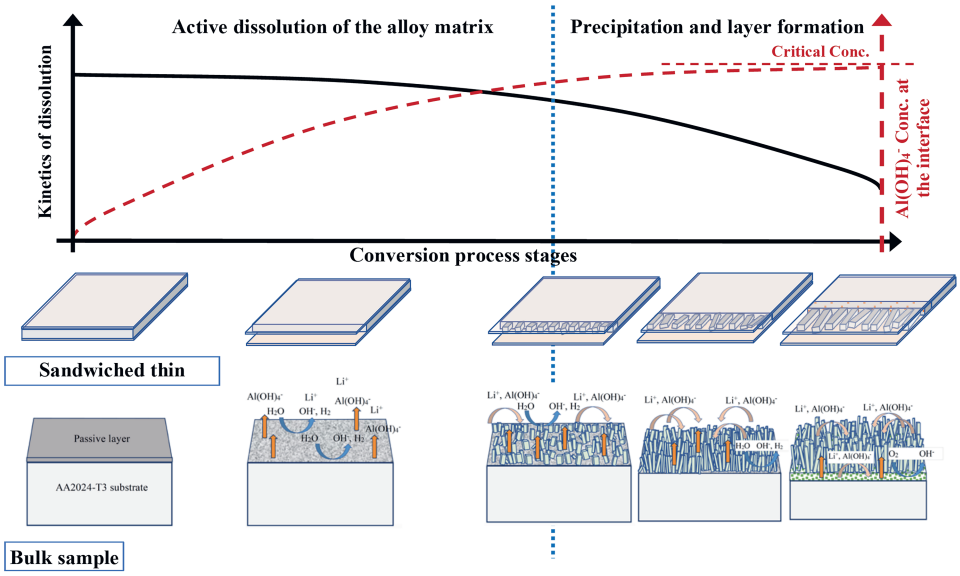


Fig. 7.8. Morphological stages of the lithium-based conversion layer formation. The graph schematically shows the change of the $Al(OH)_4^-$ concentration and the dissolution kinetics while the conversion layer morphologically evolves. The pictures schematically show different stages of the conversion layer formation in the sandwiched thin specimen corresponding to the bulk system.

7.5. Conclusions

LP-TEM using the sandwiched specimens allows to study degradation and deposition processes at AA surfaces in-situ in aggressive environments at high temporal and spatial resolution. Here, we employed that to observe, for the first time, morphological evolutions during the Li-based conversion process including different stages of the layer formation on aerospace aluminium alloys. In LP-TEM, the experimental conditions are rather different, in terms of the specimen size and solution volume from bulk systems traditionally studied, resulting in a shorter period of the conversion process. However, the sandwiched specimen can still be considered representative for morphological evolutions during different stages of the conversion process. Thanks to the sandwiched thin specimens, the solution is confined between two layers of TEOS, enhancing local supersaturation.

In this study, the supersaturation by $Al(OH)_4^-$ of the solution is found to be key to establishing the conversion layer and is formed at the expense of the dissolution of the alloy substrate. The direct nanoscopic evidence revealed that the sublayer with a columnar morphology forms initially, precipitating upon supersaturation at local active anodes sites like grain boundaries firstly. It continues to grow after which the further growth appears in a porous morphology and is completed by the formation of a thin dense layer closest to the substrate. The establishment and growth of the conversion layer can lead to a higher precipitation/dissolution ratio with time, subsequently causing the formation

of sublayers with less porous characteristics. The approach and the findings of the current study can be applied to study and explain layer formation mechanisms of other complicated conversion systems.

References

[1] A.E. Hughes, N. Birbilis, J.M. Mol, S.J. Garcia, X. Zhou, G.E. Thompson, High strength Al-alloys: microstructure, corrosion and principles of protection, in: Z. Ahmad (Ed.) Recent Trends in Processing and Degradation of Aluminium Alloys, 2011, pp. 223-262.
[2] P. Visser, H. Terryn, J.M. Mol, Aerospace coatings, in: A.E. Hughes, J.M.C. Mol, M.L. Zheludkevich, R.G. Buchheit (Eds.) Active Protective Coatings, Springer, 2016, pp. 315-372.
[3] P.V. Liddicoat, X.-Z. Liao, Y. Zhao, Y. Zhu, M.Y. Murashkin, E.J. Lavernia, R.Z. Valiev, S.P. Ringer, Nanostructural hierarchy increases the strength of aluminium alloys, Nature communications, 1 (2010) 1-7.
[4] A. Boag, A. Hughes, A. Glenn, T. Muster, D. McCulloch, Corrosion of AA2024-T3 Part I: Localised corrosion of isolated IM particles, Corrosion Science, 53 (2011) 17-26.
[5] A. Kosari, F. Tichelaar, P. Visser, H. Zandbergen, H. Terryn, J. Mol, Dealloying-driven local corrosion by intermetallic constituent particles and dispersoids in aerospace aluminium alloys, Corrosion Science, 177 (2020) 108947.
[6] C. Örnek, C. Leygraf, J. Pan, Real-Time Corrosion Monitoring of Aluminum Alloy Using Scanning Kelvin Probe Force Microscopy, Journal of The Electrochemical Society, 167 (2020) 081502.
[7] R. Parvizi, A.E. Hughes, M.Y. Tan, R.K. Marceau, M. Forsyth, P. Cizek, A.M. Glenn, Probing corrosion initiation at interfacial nanostructures of AA2024-T3, Corrosion Science, 116 (2017) 98-109.
[8] R. Buchheit, M. Martinez, L. Montes, Evidence for Cu ion formation by dissolution and dealloying the Al2CuMg intermetallic compound in rotating ring-disk collection experiments, Journal of the Electrochemical Society, 147 (2000) 119.
[9] G. Frankel, 2015 WR Whitney Award Lecture: The Effects of Microstructure and Composition on Al Alloy Corrosion, Corrosion, 71 (2015) 1308-1320.
[10] P. Campestrini, H. Terryn, J. Vereecken, J. De Wit, Chromate conversion coating on aluminum alloys: III. Corrosion protection, Journal of the Electrochemical Society, 151 (2004) B370.
[11] M. Kendig, R. Buchheit, Corrosion inhibition of aluminum and aluminum alloys by soluble chromates, chromate coatings, and chromate-free coatings, Corrosion, 59 (2003) 379-400.
[12] G. Ilevbare, J. Scully, J. Yuan, R. Kelly, Inhibition of pitting corrosion on aluminum alloy 2024-T3: effect of soluble chromate additions vs chromate conversion coating, Corrosion, 56 (2000) 227-242.
[13] A. Hughes, R. Taylor, B. Hinton, Chromate conversion coatings on 2024 Al alloy, Surface and Interface Analysis: An International Journal devoted to the development and application of techniques for the analysis of surfaces, interfaces and thin films, 25 (1997) 223-234.
[14] R. Saha, R. Nandi, B. Saha, Sources and toxicity of hexavalent chromium, Journal of Coordination Chemistry, 64 (2011) 1782-1806.
[15] M. Becker, Chromate-free chemical conversion coatings for aluminum alloys, Corrosion Reviews, 37 (2019) 321-342.
[16] L. Li, G.M. Swain, Effects of aging temperature and time on the corrosion protection provided by trivalent chromium process coatings on AA2024-T3, ACS applied materials & interfaces, 5 (2013) 7923-7930.
[17] Y. Guo, G.S. Frankel, Characterization of trivalent chromium process coating on AA2024-T3, Surface and Coatings Technology, 206 (2012) 3895-3902.
[18] X. Verdalet-Guardiola, R. Saillard, B. Fori, S. Duluard, C. Blanc, Comparative analysis of the anticorrosive properties of trivalent chromium conversion coatings formed on 2024-T3 and 2024-T351 aluminium alloys, Corrosion Science, 167 (2020) 108508.
[19] M. Forsyth, T. Markley, D. Ho, G.B. Deacon, P. Junk, B. Hinton, A. Hughes, Inhibition of corrosion on AA2024-T3 by new environmentally friendly rare earth organophosphate compounds, Corrosion, 64 (2008) 191-197.
[20] J. Li, B. Hurley, R. Buchheit, Microelectrochemical characterization of the effect of rare earth inhibitors on the localized corrosion of AA2024-T3, Journal of The Electrochemical Society, 162 (2015) C563.
[21] P.J. Denissen, V. Shkirskiy, P. Volovitch, S.J. Garcia, Corrosion Inhibition at Scribed Locations in Coated AA2024-T3 by Cerium-and DMTD-Loaded Natural Silica Microparticles under Continuous Immersion and Wet/Dry Cyclic Exposure, ACS applied materials & interfaces, 12 (2020) 23417-23431.

[22] P. Santa Coloma, U. Izagirre, Y. Belaustegi, J. Jorcin, F. Cano, N. Lapeña, Chromium-free conversion coatings based on inorganic salts (Zr/Ti/Mn/Mo) for aluminum alloys used in aircraft applications, Applied Surface Science, 345 (2015) 24-35.
[23] A. Sarfraz, R. Posner, M.M. Lange, K. Lill, A. Erbe, Role of intermetallics and copper in the deposition of ZrO2 conversion coatings on AA6014, Journal of the Electrochemical Society, 161 (2014) C509.
[24] P. Visser, Y. Liu, X. Zhou, T. Hashimoto, G.E. Thompson, S.B. Lyon, L.G. van der Ven, A.J. Mol, H.A. Terryn, The corrosion protection of AA2024-T3 aluminium alloy by leaching of lithium-containing salts from organic coatings, Faraday discussions, 180 (2015) 511-526.
[25] P. Visser, H. Terryn, J.M. Mol, Active corrosion protection of various aluminium alloys by lithium-leaching coatings, Surface and Interface Analysis, 51 (2019) 1276-1287.
[26] S.B. Madden, J.R. Scully, Inhibition of AA2024-T351 corrosion using permanganate, Journal of the Electrochemical Society, 161 (2014) C162.
[27] A. Hughes, J. Gorman, T. Harvey, A. Galassi, G. McAdam, Development of permanganate-based coatings on aluminum alloy 2024-T3, Corrosion, 62 (2006) 773-780.
[28] C. Drewien, M. Eatough, D. Tallant, C. Hills, R. Buchheit, Lithium-aluminum-carbonate-hydroxide hydrate coatings on aluminum alloys: Composition, structure, and processing bath chemistry, Journal of materials research, 11 (1996) 1507-1513.
[29] R.G. Buchheit, M. Bode, G. Stoner, Corrosion-resistant, chromate-free talc coatings for aluminum, Corrosion, 50 (1994) 205-214.
[30] J.S. Laird, P. Visser, S. Ranade, A. Hughes, H. Terryn, J. Mol, Li leaching from Lithium Carbonate-primer: An emerging perspective of transport pathway development, Progress in Organic Coatings, 134 (2019) 103-118.
[31] K. Marcoen, P. Visser, G. Trindade, M.-L. Abel, J. Watts, J. Mol, H. Terryn, T. Hauffman, Compositional study of a corrosion protective layer formed by leachable lithium salts in a coating defect on AA2024-T3 aluminium alloys, Progress in Organic Coatings, 119 (2018) 65-75.
[32] P. Visser, K. Marcoen, G. Trindade, M. Abel, J. Watts, T. Hauffman, J. Mol, H. Terryn, The chemical throwing power of lithium-based inhibitors from organic coatings on AA2024-T3, Corrosion Science, 150 (2019) 194-206.
[33] P. Visser, H. Terryn, J.M. Mol, On the importance of irreversibility of corrosion inhibitors for active coating protection of AA2024-T3, Corrosion Science, 140 (2018) 272-285.
[34] P. Visser, S. Hayes, Low-temperature-curable coating composition useful as anticorrosive primer coating for non-ferrous metal substrates, particularly aluminum or aluminum alloy, comprises film-forming resin, curing agent, and lithium salt, in, WO2010112605-A1, 2010.
[35] O. Gharbi, S. Thomas, C. Smith, N. Birbilis, Chromate replacement: what does the future hold?, npj Materials Degradation, 2 (2018) 1-8.
[36] P. Visser, A. Lutz, J. Mol, H. Terryn, Study of the formation of a protective layer in a defect from lithium-leaching organic coatings, Progress in Organic Coatings, 99 (2016) 80-90.
[37] M. Tabrizi, S. Lyon, G. Thompson, J. Ferguson, The long-term corrosion of aluminium in alkaline media, Corrosion science, 32 (1991) 733-742.
[38] G. Burstein, R. Cinderey, Evolution of the corrosion potential of repassivating aluminium surfaces, Corrosion science, 33 (1992) 475-492.
[39] P. Visser, Y. Gonzalez-Garcia, J.M. Mol, H. Terryn, Mechanism of passive layer formation on AA2024-T3 from alkaline lithium carbonate solutions in the presence of sodium chloride, Journal of The Electrochemical Society, 165 (2018) C60.
[40] A. Kosari, P. Visser, F. Tichelaar, S. Eswara, J. Audinot, T. Wirtz, H. Zandbergen, H. Terryn, J. Mol, Cross-sectional characterization of the conversion layer formed on AA2024-T3 by a lithium-leaching coating, Applied Surface Science, 512 (2020) 145665.
[41] Y. Liu, P. Visser, X. Zhou, S.B. Lyon, T. Hashimoto, M. Curioni, A. Gholinia, G.E. Thompson, G. Smyth, S.R. Gibbon, Protective film formation on AA2024-T3 aluminum alloy by leaching of lithium carbonate from an organic coating, Journal of The Electrochemical Society, 163 (2015) C45.
[42] P. Visser, M. Meeusen, Y. Gonzalez-Garcia, H. Terryn, J.M. Mol, Electrochemical evaluation of corrosion inhibiting layers formed in a defect from lithium-leaching organic coatings, Journal of The Electrochemical Society, 164 (2017) C396.

[43] S.W. Chee, M.G. Burke, 12 Applications of Liquid Cell TEM in Corrosion Science, Liquid Cell Electron Microscopy, (2016) 258.
[44] A. Kosari, H. Zandbergen, F. Tichelaar, P. Visser, H. Terryn, A. Mol, Application of In Situ Liquid Cell Transmission Electron Microscopy in Corrosion Studies: A Critical Review of Challenges and Achievements, Corrosion, 76 (2020) 4-17.
[45] F.M. Ross, Opportunities and challenges in liquid cell electron microscopy, Science, 350 (2015).
[46] S.C. Hayden, C. Chisholm, R.O. Grudt, J.A. Aguiar, W.M. Mook, P.G. Kotula, T.S. Pilyugina, D.C. Bufford, K. Hattar, T.J. Kucharski, Localized corrosion of low-carbon steel at the nanoscale, npj Materials Degradation, 3 (2019) 1-9.
[47] A. Kosari, H. Zandbergen, F. Tichelaar, P. Visser, P. Taheri, H. Terryn, J. Mol, In-situ nanoscopic observations of dealloying-driven local corrosion from surface initiation to in-depth propagation, Corrosion Science, 177 (2020) 108912.
[48] T.J. Woehl, K.L. Jungjohann, J.E. Evans, I. Arslan, W.D. Ristenpart, N.D. Browning, Experimental procedures to mitigate electron beam induced artifacts during in situ fluid imaging of nanomaterials, Ultramicroscopy, 127 (2013) 53-63.
[49] N. De Jonge, F.M. Ross, Electron microscopy of specimens in liquid, Nature nanotechnology, 6 (2011) 695-704.
[50] N. de Jonge, Theory of the spatial resolution of (scanning) transmission electron microscopy in liquid water or ice layers, Ultramicroscopy, 187 (2018) 113-125.
[51] N.M. Schneider, Electron beam effects in liquid cell TEM and STEM, liquid cell electron microscopy, (2016) 140-163.
[52] N.M. Schneider, M.M. Norton, B.J. Mendel, J.M. Grogan, F.M. Ross, H.H. Bau, Electron–water interactions and implications for liquid cell electron microscopy, The Journal of Physical Chemistry C, 118 (2014) 22373-22382.
[53] T. Woehl, P. Abellan, Defining the radiation chemistry during liquid cell electron microscopy to enable visualization of nanomaterial growth and degradation dynamics, Journal of microscopy, 265 (2017) 135-147.
[54] Z. Wang, P. Chen, H. Li, B. Fang, R. Song, Z. Zheng, The intergranular corrosion susceptibility of 2024 Al alloy during re–ageing after solution treating and cold–rolling, Corrosion Science, 114 (2017) 156-168.
[55] M.-L. de Bonfils-Lahovary, L. Laffont, C. Blanc, Characterization of intergranular corrosion defects in a 2024 T351 aluminium alloy, Corrosion Science, 119 (2017) 60-67.
[56] M. Pourbaix, Atlas of electrochemical equilibria in aqueous solution, NACE, 307 (1974).

Supplementary Materials for Chapter 7

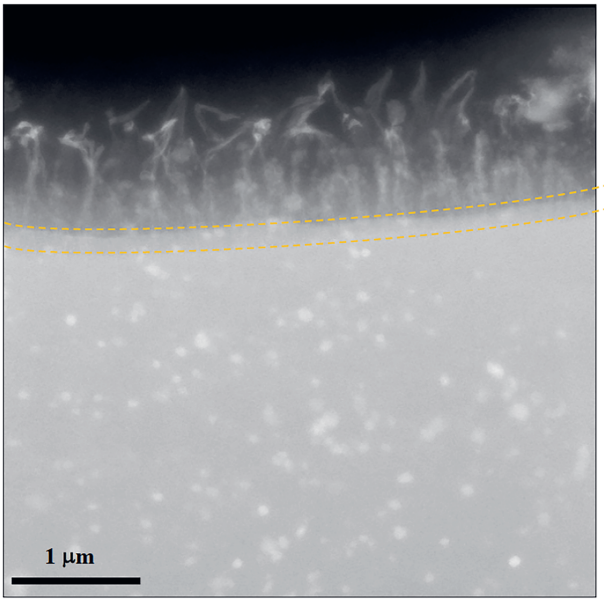


Fig. S7.1. HAADF-STEM image of the conversion layer formed on the sandwiched specimen after 30-min exposure to 0.01 M NaCl + 0.01 M Li_2CO_3, revealing the columnar layer as the initially-appearing morphology of the layer. The dashed yellow lines show the dissolution front. The specimen was loaded on a chip and exposed to the electrolyte outside the microscope. The formation process was frozen after 30 min by immediately drying the chip by towelling with a specific paper.

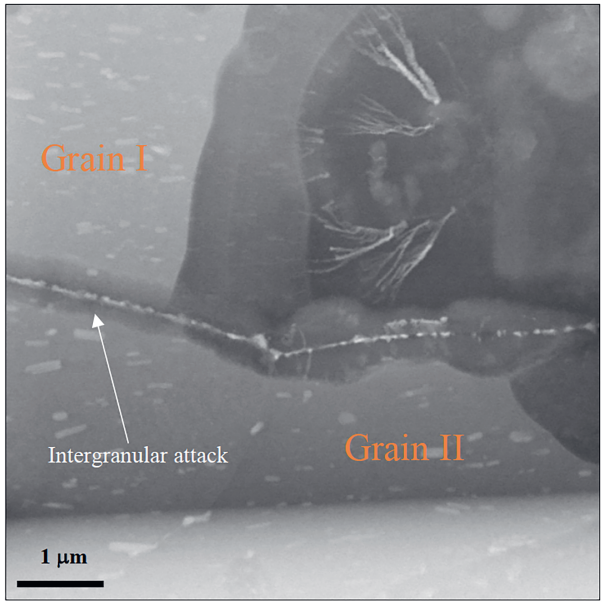


Fig. S7.2. HAADF-STEM image of the sandwiched specimen exposed to 0.01 M NaCl + 0.01 M Li_2CO_3. Grain I and the grain boundary show higher electrochemical activity in the solution. The formation of the columnar and dense layer merely on Grain I is an indication of local supersaturation around the grain due to extensive dissolution.

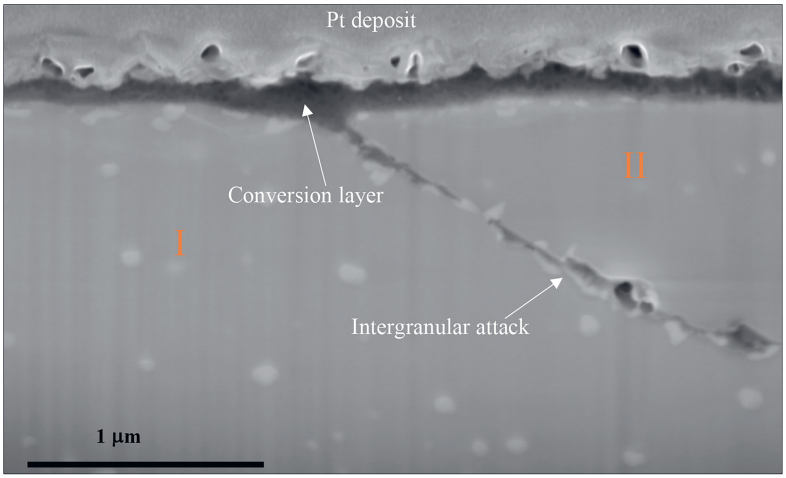


Fig. S7.3. FIB/SEM morphological analysis of the layer formed over the alloy matrix, showing the intergranular attack of a specific grain. The 25 cm^2 area of the sample is exposed to 5 mL of 0.01 M NaCl + 0.01 M Li_2CO_3 solution for 7 h.

CHAPTER 8

FIB/SEM, TEM AND ELECTROCHEMICAL STUDIES OF LITHIUM-BASED CONVERSION LAYER AT THE ALLOY MATRIX AND INTERMETALLIC PARTICLES[1]

In this chapter, we study local lithium-based conversion layer formation at the alloy matrix and intermetallic particles (IMPs) in AA2024-T3 through top- and cross-sectional-view morphological observations along with open circuit potential measurements in the condition mimicking coating defects. The results reveal the critical role of lithium during five stages of conversion process in which the alloy matrix and IMPs evolve morphologically, compositionally, and electrochemically. Passive layer and alloy matrix dissolution leading to surface Cu-enrichment and S-phase dealloying occur at early stages of exposure. Formation and growth of a columnar layer precede the dense layer establishment which leads to passivation. Dealloying of Al_2CuMg can assist the conversion process by providing local supersaturation.

Keywords: AA2024-T3; Intermetallic particles; Dealloying; Lithium carbonate; Conversion coating; Passivation; TEM; FIB/SEM

[1] **A. Kosari**, F. Tichelaar, P. Visser, H. Zandbergen, H. Terryn, J.M.C. Mol, Laterally-resolved formation mechanism of a lithium-based conversion layer at the matrix and intermetallic particles in aerospace aluminium alloys, Corrosion Science, 190 (2021) 109651.

8.1. Introduction

In recent years, lithium salts have drawn high attention as hexavalent chromium-free corrosion inhibitors due to a passivating character for a variety of aluminium alloys (AAs) [1-5]. However, the preliminary investigations go back to 1987 when Gui and Devine observed an unexpected passivity while anodically polarising AA6061-T6 in an alkaline lithium carbonate solution [6]. In 1994, Buchheit et al. generated protective hydrotalcite conversion coatings by immersing AAs in an alkaline lithium carbonate solution followed by heat treatment at a relatively low temperature in air [7]. Later, Drewien et al. confirmed the formation of Li-Al layered double hydroxide (Li-Al LDH) on AA1100 through a conversion layer process in a lithium carbonate-lithium hydroxide solution (pH 11-12) [8]. Another major breakthrough was established many years later in 2010 when Visser and Hayes showed that lithium salts can be incorporated into organic coatings to provide active corrosion protection [9]. In this scheme, incorporated lithium salts [10, 11] are released with a long-range throwing power at damaged coating locations [12], establishing an alkaline environment of approximately pH 10 [13]. In the presence of lithium, this is associated with the formation of an irreversible conversion layer at the coating defect that can effectively and reliably protect the AA substrate [14]. Thereafter, the studies were dedicated to characterising the generated layer in artificial scribes subjected to neutral salt spray (NSS) exposure [15, 16].

Up to now, detailed structural and compositional studies have revealed a uniform distribution of lithium throughout the conversion layer which appears in a multi-layered arrangement depending on the location in the scribe [17]. In general, there is a columnar outer layer identified as Li-Al LDH and a dense inner layer which represents an amorphous lithium-containing pseudoboehmite phase [17]. Besides, a porous layer in which both amorphous and crystalline compounds co-exist resides in between [17]. Extensive electrochemical evaluations have shown that the conversion layer can well protect AAs substrate; the inner dense layer shows the highest barrier properties compared to other two sublayers [18].

Regarding the formation mechanism, the studies have indicated that the lithium-based conversion layer goes through several morphological and compositional stages from initiation to completion. In one of their works, Visser et al. set up an electrochemical cell representing the aqueous conditions of a scribe area exposed to lithium carbonate-sodium chloride solution [19]. Combined with compositional and morphological investigations, they proposed three consecutive stages of oxide thinning, anodic dissolution and hydroxide film formation, and growth. In fact, the final stage occurs through a competitive film formation and dissolution process, leading to transformation of the outer aluminium hydroxide layer into a Li-Al LDH. However, the studies have so far been dedicated to exploring the mechanism and the different stages of the conversion layer formation on the alloy matrix more than at and around intermetallic particles (IMPs).

Intermetallic phases in aerospace AAs significantly contribute to their mechanical properties, but they bring along a deteriorated corrosion resistance due to their higher electrochemical activity compared to

the alloy matrix [20-24]. Therefore, local corrosion evidently takes place at IMPs locations [25-28]. Given the local, heterogeneous and enhanced electrochemical activity induced by IMPs in AAs, it is therefore particularly crucial in corrosion inhibition strategies to consider and optimise the protection at and around IMPs. So, the current work focused on gaining detailed understanding of the conversion layer formation at and around different types of intermetallic compounds in AA2024-T3. We endeavour to find a correlation between the substrate's overall electrochemical response and the local morphological evolutions at different stages of exposure. To this end, we record the open circuit potential (OCP) of AA2024-T3 exposed to a lithium carbonate–sodium chloride solution for 7 h. In parallel, top-view and cross-sectional morphological observations are conducted by means of focused ion beam/scanning electron microscopy (FIB/SEM) analysis to provide further insights into different stages of the conversion layer formation related to intermetallic phases in particular. Moreover, X-ray diffraction (XRD) analysis are performed to confirm the role of lithium in the conversion process.

8.2. Materials and methods

AA2024-T3 sheets were SiC ground to #1200 and then polished on a soft cloth in alumina slurries of 0.5 and 0.05 μm in a non-aqueous solution. The samples were placed in an electrochemical cell setup providing an exposed area of 3.14 cm^2. The cell was filled with 1.23 mL of 0.01 M NaCl + 0.01 M Li_2CO_3 solution (pH 10.6), providing a relatively thin-film electrolyte condition (approx. 4-mm thick) representative for the scribe area. According to Visser et al. [13, 19], such a solution composition is fairly representative for lithium concentration and pH in a defect area of 1 mm wide upon lithium carbonate leaching from the coating. In this estimation, different parameters including the coating thickness [10], lithium carbonate loading [9], volume of defect area and the lithium depletion depth [12] in the coating were considered. The open circuit potential (OCP) of the samples exposed to the aerated solution were recorded versus an Ag/AgCl saturated reference electrode for the duration of 7 h. Prior investigations have shown that the conversion process can proceed to an advanced stage of formation within this period of exposure [19]. From the typical OCP evolution behaviour, different exposure times were chosen at which subsequent exposure tests were stopped for detailed microscopic investigations of the conversion layer formed at those times. In addition, we have exposed AA2024-T3 samples to a lithium-free 0.01 M NaCl + 0.01 M Na_2CO_3 solution (pH 10.6) and in an identical condition in terms of the electrolyte thickness (approx. 4 mm) in order to understand lithium impact on the layer formation and OCP evolutions.

Prior to preparation for microscopic analysis, samples were rinsed with flowing distilled water in order to quench the conversion layer formation process. FIB/SEM cross-sectioning was carried out over different areas of the exposed samples by means of a Thermo-Fisher Helios G4 FIB/SEM microscope. The top-view and cross-sectional SEM morphological studies were performed at 15 keV collecting emitted secondary electrons (SE) in ultra-high-resolution mode. The chemical composition of

individual IMPs was estimated using energy dispersive spectroscopy (EDS - not shown here). FIB sectioning was conducted in a blind-mode, whereby the ion beam was used only for milling. It allows us to omit providing a Pt or C overlay process for protection of the top surface from Ga ion-beam damage. Besides, the thin TEM cross-sections were fabricated out of regions of interest with FIB and lift-out procedure [29] for detailed structural and composition investigations. STEM/EDS microanalysis was performed using a Cs corrected Thermo Scientific Titan 300kV (S)TEM with the Super-X configuration consisting of 4 Si Drift Detectors (SDDs).

X-Ray diffraction (XRD) measurements were carried out with a Bruker D8 Discover diffractometer and Eiger-2 500k 2D-detector. The samples exposed to 0.01 M NaCl + 0.01 M Li_2CO_3 for 2 and 7 h were radiated by Cu-Kα X-ray continuously from 10° to 25° (2θ) at a step size of 0.040 °/2θ and a counting time of 1s per step. Then, the acquired data were analysed by means of Bruker software DiffracSuite.EVA vs 5.2.

8.3. Results and discussion

8.3.1. OCP evolution during the conversion layer formation. Fig. 8.1 shows the OCP behaviour of the AA2024-T3 sample exposed to 0.01 M NaCl + 0.01 M Li_2CO_3 over time. According to the OCP evolutions, we can identify five distinct stages of the conversion layer formation. Stage I shows up as a sharp initial drop from -1150 mV to a minimum of -1420 mV during the first 60 s. Immediately after, the system experiences the first increase in the OCP values, reaching a plateau of -1220 mV at 800 s. Stage III appears as the second rise in the OCP towards a plateau of -1000 mV after more than 1 h. The stage IV is associated with the third rise in the OCP values gradually reaching -600 mV at 4 h. From this point onwards, the system reveals a nearly stabilised behaviour (Stage V) where the OCP slightly changes to -400 mV after a total exposure of 7 h.

It should be noted that OCP represents an electrochemical situation in which the total anodic and cathodic currents are equal. Thus, any modification related to anodic/cathodic reactivities as a consequence of the gradual morphological and compositional evolutions on the surface can cause an impact on the electrochemical response of the system, here OCP values [30]. Therefore, we study the different phases including the alloy matrix and intermetallic compounds to see how they individually contribute to the OCP values during the conversion process. Given the OCP evolution with time, the samples were therefore taken at the certain exposure times of the formation. The time intervals include 60 s (Late Stage I), 200 s (Early Stage I), (late Stage I) 800 s, (Stage III) 2800 s, 2 h (Stage IV) and 7 h (Stage V), representing distinct times of exposure emerging in the OCP graph.

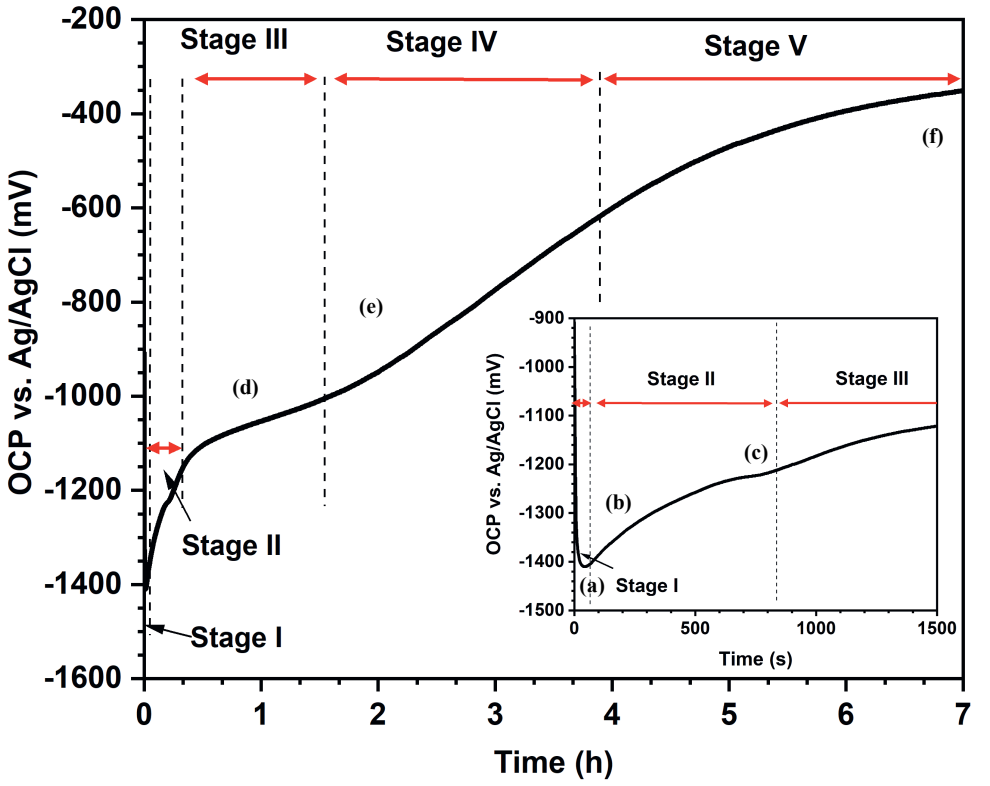


Fig. 8.1. Open circuit potential (OCP) evolution of AA2024-T3 exposed to 0.01 M NaCl + 0.01 M Li_2CO_3 (pH 10.6). Five stages can be considered for the conversion layer formation. Based on that, we have picked exposure times of (a) 60 s, (b) 200 s, (c) 800 s, (d) 2800 s, (e) 2 h and (f) 7 h to study the morphological evolutions of the conversion layer with time.

8.3.2. Morphological characterisation of the conversion layer on the alloy matrix at different exposure times. Fig. 8.2 shows top-view SEM images of the AA2024-T3 surface after the specific periods of exposure to 0.01 M NaCl + 0.01 M Li_2CO_3 solution. Fig. 8.3a reveals that the polished surface has been slightly corroded during the first 60 s of the exposure. At 200 s (Fig. 8.2b), we observe a roughened morphology for the surface, indicating further corrosion of the alloy matrix. After 800 s (Fig. 8.2c), we see that the surface has started to turn into a different top-view configuration, acquiring a petal-like morphology. Prolonged exposure until 2800 results in the appearance of a clear layer on the alloy surface (Fig. 8.2d). Fig. 8.2e shows a more pronounced petal-like morphology after 2 h (Fig. 8.2e). This is a clear indication of the conversion layer formation over the alloy matrix, in particular after 7 h when the petals have considerably grown (Fig. 8.2f).

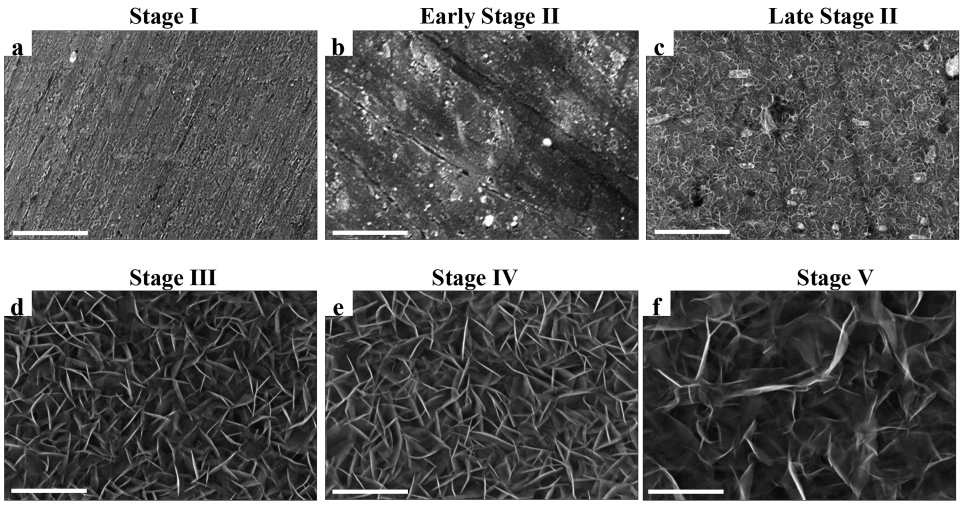


Fig. 8.2. Top-view observations of the conversion layer exposed to 0.01 M NaCl + 0.01 M Li_2CO_3. SEM images of AA2024-T3 surface at different exposure times of (a) 60 s; (b) 200 s; (c) 800 s; (d) 2800 s; (e) 2 h; (f) 7 h. The scale bar represents 1 μm.

Fig. 8.3 shows the SEM images of the FIB cross-sections when the stage is at 52° tilt. As is evident in Fig. 8.3a and b, the initial exposure to 0.01 M NaCl + 0.01 M Li_2CO_3 until 200s does not lead to conversion layer formation. This implies that the alloy matrix merely undergoes dissolution at this stage. After 800 s, we observe the formation of a very thin (hydr)oxide layer (approx. 50 nm) on the alloy surface (Fig. 8.3c). The cross-sectional SEM image at 2800 s (Fig. 8.3d) indicates the formation of a conversion layer in a columnar morphology, preceding other reported sublayers. Prolonged exposure until 2 h is associated mainly with the columnar layer thickening, although a dense-like layer has appeared at some locations, indicated by the blue arrow (Fig. 8.3e), owing to different local activities and thus local solution chemistry. However, a 7-h exposure comes along with the confirmation of a uniform dense-like layer formation close to the alloy substrate as clearly shown in Fig. 8.3f. Besides, the columnar layer has slightly grown as compared to the layer grown for 2 h. In general, the top-view and cross-sectional SEM images confirm different formation stages of the conversion layer gradually covering the entire alloy matrix. It should be stressed that here we report on the morphological evolutions at different stages while the sublayers can endure compositional and structural modifications during the conversion process also [15].

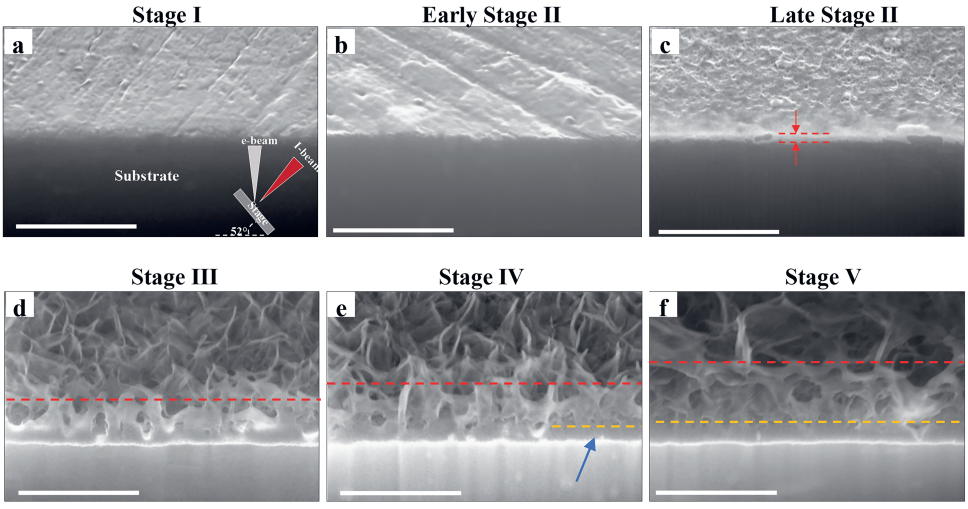


Fig. 8.3. Cross-sectional observations of the conversion layer exposed to 0.01 M NaCl + 0.01 M Li_2CO_3. SEM images of AA2024-T3 surface at different exposure times of (a) 60 s; (b) 200 s; (c) 800 s; (d) 2800 s; (e) 2 h; (f) 7 h. The sections are made using FIB milling. The red dashed lines indicate the highest location in the conversion layer at each stage. The orange dashed line separates the columnar layer from the dense-like layer. The blue arrow in Fig. 8.3e points at the location at which a dense-like layer is observed. The scale bar is 1 µm.

Characterised in the several studies, the conversion layer is mainly composed of aluminium, lithium and oxygen [15, 17, 19]. The studied solution holds lithium, however aluminium needs to be supplied through the direct anodic dissolution of the alloy matrix. Thus, the cathodic reactions (i.e., dominantly water reduction) come about in return for charge neutralisation. This phenomenon is associated with the local nucleation and growth of hydrogen bubbles at some locations (i.e., IMPs), leading to the gradual de-wetting of the regions involved. Regions which get de-wetted at later stages of exposure reveal different surface morphologies as compared to those de-wetted earlier. Since every single morphology is related to a distinct stage of the conversion process, the morphological variations owing to such a local phenomenon can be considered instructive to better understand the mechanisms behind the conversion layer formation. In this regard, Fig. 8.4a shows the SEM images of a hydrogen bubble footprint; the sample was exposed for 7 h. The inset is the optical macrograph of the alloy surface being exposed to the solution after about 7 h. As can be seen, the gradual de-wetting has resulted in a different surface morphology, representing different stages of the conversion process. A closer look at the green rectangular region is shown in Fig. 8.4b. According to the top-view morphology, the red arrow approximately denotes the transition from Stage I to Stage III. Furthermore, the yellow arrow includes Stage III to Stage V. Fig. 8.4c shows the cross-sectional SEM image corresponding to the red rectangular region. As is evident, the alloy matrix has endured dissolution before appearance of the primary conversion precipitate. As reported by Drewien et al [8], the supersaturation by $Al(OH)_4^-$ of the solution is critical for formation of the conversion layer. In fact, the alkaline solution continues to

dissolve the alloy surface until reaching the required supersaturation at the surface. Fig. 8.4d shows the SEM image of the cross-section corresponding to the yellow rectangular region. Going over the image from left to right, we observe that the dissolution front slightly penetrates into further depth while the columnar layer/solution interface increases to a higher level, implying a dissolution/precipitation process at the advanced stages of the conversion layer formation.

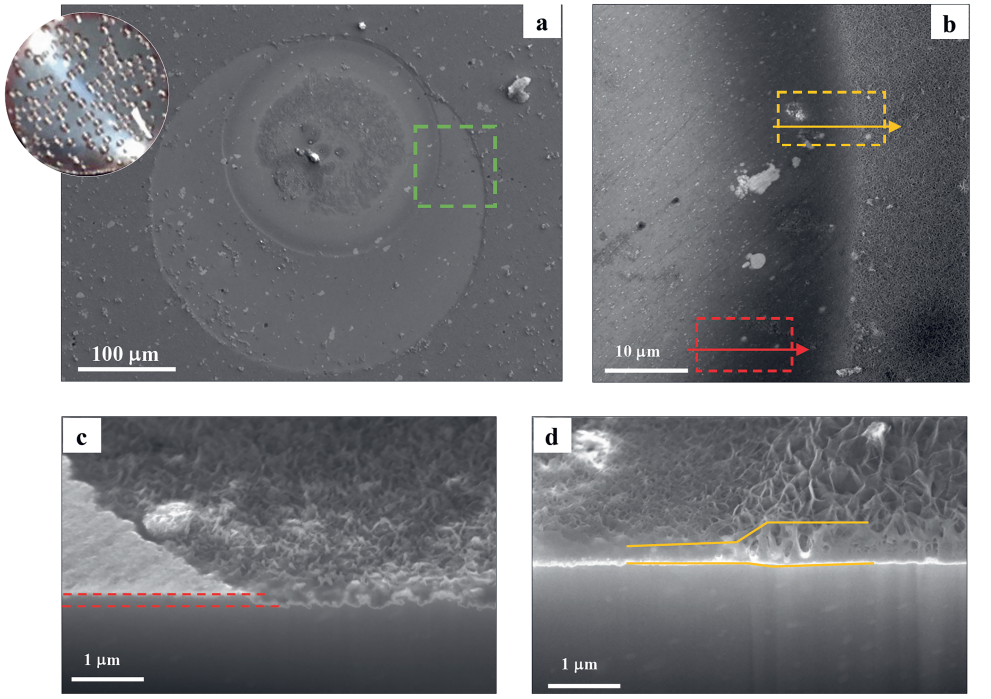


Fig. 8.4. Top-view and cross-sectional observation of the conversion layer at the bubble locations. (a) Top-view SEM image of the surface morphology around a bubble formed as a consequence of hydrogen evolution reactions. The bubbles initiate at several locations on the surface and grow with time. Thus, different stages of the layer formation can be recognised within the bubble regions. The inset shows the bubbles formed on AA2024-T3 surface after 7 h of exposure. (b) Top-view SEM image of the green rectangular regular region shown in Fig. 8.4a. (c) Cross-sectional SEM image of the region along the red dashed rectangle shown in Fig. 8.4b. (d) Cross-sectional SEM image of the region along the yellow arrow (yellow dashed rectangle) shown in Fig. 8.4b. The sections are made via FIB milling.

8.3.3. Morphological characterisation of the conversion layer on IMPs at different exposure times.

Fig. 8.5 shows morphological observations of different intermetallic phases in AA2024-T3 exposed to 0.01 M NaCl + 0.01 M Li_2CO_3 for 60 s. At this stage, we see no indication of the layer formation over all the IMPs and they look still bare. Fig. 8.5a and a_1 shows top-view and cross-sectional SEM mages of an S-phase particle. The top-view image shows a dark ribbon all around this particle. The FIB cross-

section reveals that this peripheral region has slightly been trenched at this stage. Besides, we see that the corrosion has penetrated into the particle at some locations as shown by the red arrows. We later confirm that selective dissolution of aluminium and magnesium from S-phase (i.e., dealloying) gradually occurs in the studied solution. Fig. 8.5b shows another S-phase particle showing a similar corrosion-attack morphology. Furthermore, Al_2Cu and constituent phase particles are found almost intact at this stage; see Fig. 8.5c-e. It should be mentioned that constituent phases are Al, Fe, Si, Mn and Cu-containing particles which are formed during the alloy solidification [31].

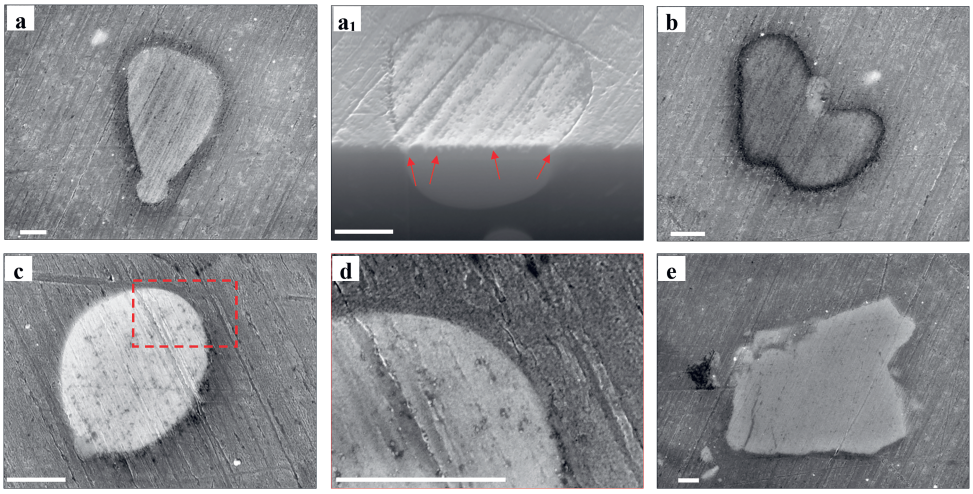


Fig. 8.5. Morphological observations of intermetallic phases in AA2024-T3 exposed to 0.01 M NaCl + 0.01 M Li_2CO_3 for 60 s. (a and a_1) Top-view and cross-sectional SEM images of an Al_2CuMg particle. The red arrows indicate the slightly-dealloyed regions in the particle. (b) Top-view SEM image of an Al_2CuMg particle; the peripheral shallow trench around the particle looks darker in contrast. (c) Top-view SEM image of an Al_2Cu particle. (d) The magnified view of the rectangular region indicated in Fig. 8.5c. (e) Top-view SEM image of a constituent-phase particle. The scale bar is 1 μm.

Fig. 8.6 shows the top-view and cross-sectional morphology of different IMPs after 200 s. It is obvious that the S-phase particles have undergone a clear change in morphology. Fig. 8.6a-a_2 reveal formation of a petal-like layer on the S-phase particle while the surrounding alloy matrix is still bare. The cross-sectional SEM image indicates further penetration of the dealloying and the alloy trenching into depth. It seems that a fast release of $Al(OH)_4^-$ ions from the Al_2CuMg particle due to dealloying provides the local supersaturation for the conversion process. This actually happens via a two-step electrochemical/chemical reaction of Al^{3+} to $Al(OH)_3$ and then to $Al(OH)_4^-$ under the alkaline conditions [32]. This has led to the formation of the petal-like layer merely over the S-phase particles and not yet on the alloy matrix. In contrast, Al_2Cu and constituent phase particles have still not been involved in the conversion process (see Fig. 8.6b-d).

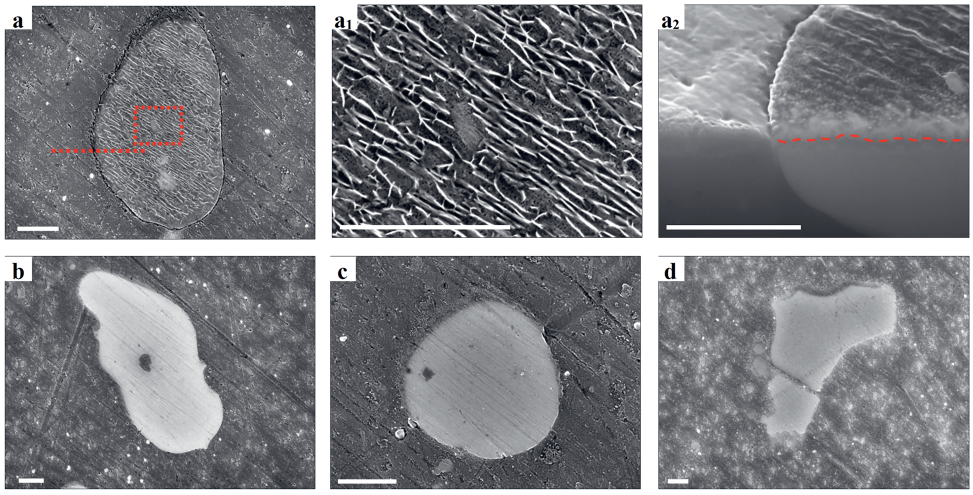
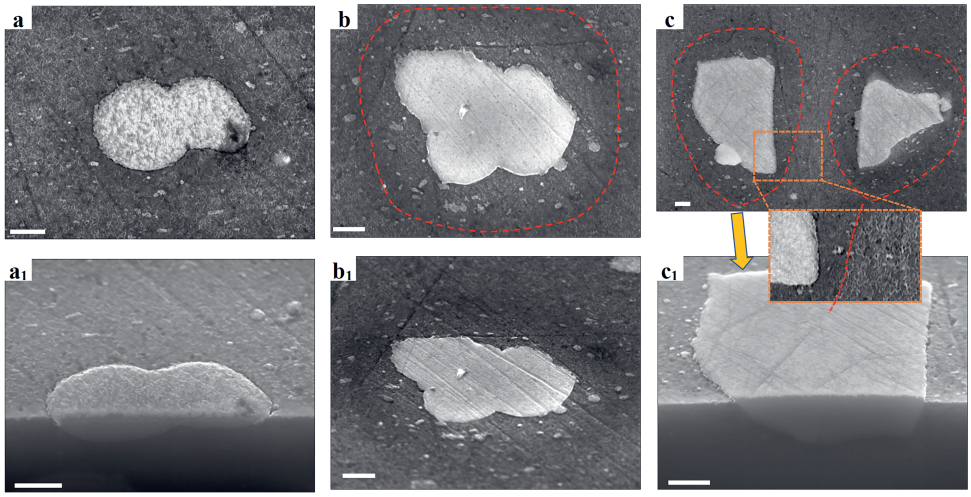


Fig. 8.6. Morphological observations of intermetallic phases in AA2024-T3 exposed to 0.01 M NaCl + 0.01 M Li_2CO_3 for 200 s. (a, a_1 and a_2) Top-view and cross-sectional SEM images of an Al_2CuMg particle. The top-view SEM image reveals the initial formation of a columnar layer on the particle. (a_1) shows the magnified view of the rectangular region indicated in Fig. 8.6a. (a_2) shows the cross-sectional SEM image along the red dashed line indicated in Fig. 8.6a, revealing the dealloyed top region in the particle. (b and c) Top-view SEM image of two Al_2Cu particles. (d) Top-view SEM image of a constituent-phase particle. The scale bar is 1 μm.

Fig. 8.7 shows top-view and cross-sectional micrographs of representative IMPs after 800 s. As can be seen in Fig. 8.7a and a_1, the conversion layer on the S-phase has insignificantly changed while the surrounding alloy matrix has acquired a similar morphology. The cross-sectional SEM image reveals that the dealloying has propagated more into depth at the peripheral regions of the particle where the alloy matrix has been trenched tightly around the particle. This behaviour has also been observed in uninhibited NaCl solutions [25]. Interestingly, Al_2Cu and constituent phase particles and their close vicinity are still uncovered; the bare regions are indicated by the red closed curves in Fig. 8.7b and c. This phenomenon is caused by the lack of $Al(OH)_4^-$ ions which are essential for the conversion layer process. In fact, these two phases are rather electrochemically stable and slightly endure dealloying, resulting in limited concentration of $Al(OH)_4^-$ ions which need to be supplied from the dissolution of the adjacent alloy matrix. This also explains why a solution locally dilute in $Al(OH)_4^-$ ions exists around Al_2Cu and constituent phase particles, causing a delay in the layer formation.



Fig, 8.7. Morphological observations of intermetallic phases in AA2024-T3 exposed to 0.01 M NaCl + 0.01 M Li_2CO_3 for 800 s. (a and a_1) Top-view and cross-sectional SEM images of an Al_2CuMg particle. A columnar layer has formed on the particle and also on the adjacent alloy matrix around it. (b and b_1) SEM images of an Al_2Cu particle; (b) stage tilt 0° and (b_1) stage tilt 52°. The columnar layer is merely observed outside the red closed curve. (c and c_1) Top-view and cross-sectional SEM image of a constituent-phase particle. As is evident in the inset, there is no columnar layer formed within the closed curves. The scale bar is 1 μm.

After 2800 s, we found all the IMPs fully covered by the conversion layer revealing a petal-like top-view morphology (Fig. 8.8). As can be seen in top-view and cross-sectional SEM images (Fig. 8.8a and a_1), the S-phase particle has further but slightly been dealloyed, in particular, at the particle/alloy matrix interface (mind the corresponding inset). The formed layer has the character of a columnar morphology from a cross-sectional point of view [17]. The conversion layer formed on both Al_2Cu (Fig. 8.8b and b_1) and constituent phase particles (Fig. 8.8c and c_1) is similar to that on the S-phase from a top- and cross-sectional view. No significant indication of dealloying and trenching is observed in these two phases. However, the top surface of the Al_2Cu and constituent phase particles has been slightly dealloyed since they are more electrochemically stable than S-phase [25, 26]. Besides their dealloying happens sluggishly in the studied solution. It means that the dissolution of their surrounding alloy matrix has provided the saturation of the local solution by $Al(OH)_4^-$ ions required for the layer formation. Given the OCP curve (Fig. 8.1), the system is actively evolving towards the positive values; this is a clear indication of passivity acquirement [32].

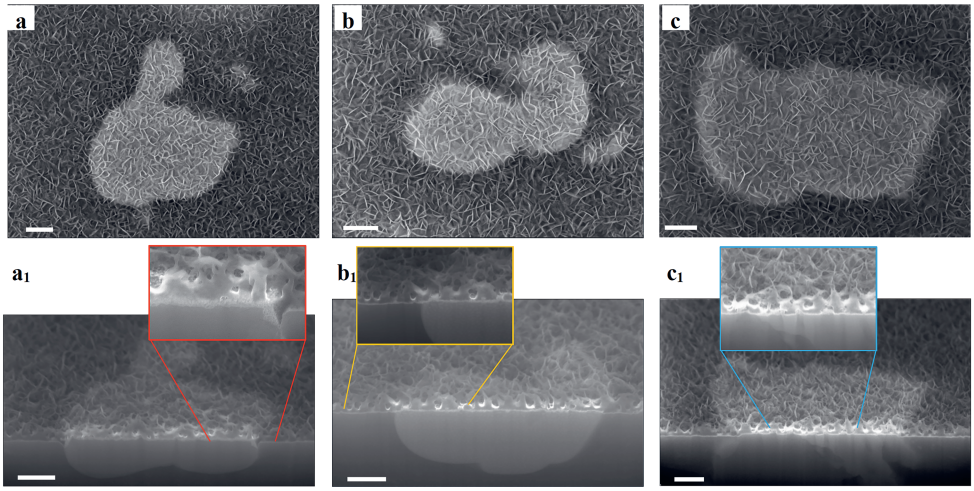


Fig. 8.8. Morphological observations of intermetallic phases in AA2024-T3 exposed to 0.01 M NaCl + 0.01 M Li_2CO_3 for 2800 s. Top-view and cross-sectional SEM images of (a and a_1) an Al_2CuMg particle, (b and b_1) an Al_2Cu particle and (c and c_1) a constituent-phase particle. The insets are the magnified views of the indicated cross-sectional regions. At this stage, the top-view images reveal the entire alloy matrix and IMPs are covered with a columnar layer. The scale bar is 1 μm.

Prolonged exposure up to 2 h has resulted in the further growth of the conversion layer. All the IMPs have insignificantly changed in terms of morphology of the lithium-based layer (Fig. 8.9). However, it is remarkable that the layer over the IMPs is still thickening. Afterwards, the AA2024 sample starts to stabilise based on the OCP values, nearly reaching a plateau of -400 mV after 7 h. At this stage, the top-view petal-like morphology has considerably coarsened (Fig. 8.10). The S-phase particle has partly dealloyed, although there is a deep penetration of dealloying at the particle/matrix interface (Fig. 8.10a and a_1). A dense-like sublayer has appeared in the conversion layer formed on the alloy matrix at this stage; however, the columnar layer is still observed over the S-phase particle. This is also the case for the other types of IMPs (i.e., Al_2Cu and constituent phase particles). The fact is that the dense-like layer forms at the latest stage of the exposure due to further but slowed-down penetration of corrosion into alloy matrix. This phenomenon that cannot take place on the IMPs is associated with the formation of a layer with less porosities. The growth of the columnar layer on the IMPs is a consequence of the direct precipitation from the saturated solution which will be discussed later.

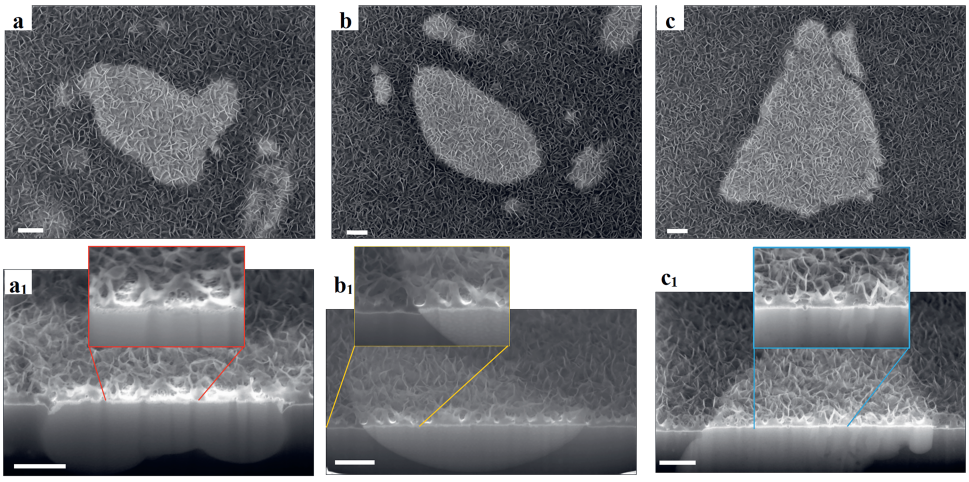


Fig. 8.9. Morphological observations of intermetallic phases in AA2024-T3 exposed to 0.01 M NaCl + 0.01 M Li_2CO_3 for 2 h. Top-view and cross-sectional SEM images of (a and a_1) an Al_2CuMg particle, (b and b_1) an Al_2Cu particle and (c and c_1) a constituent-phase particle. The insets are the magnified views of the indicated cross-sectional regions. The scale bar is 1 µm.

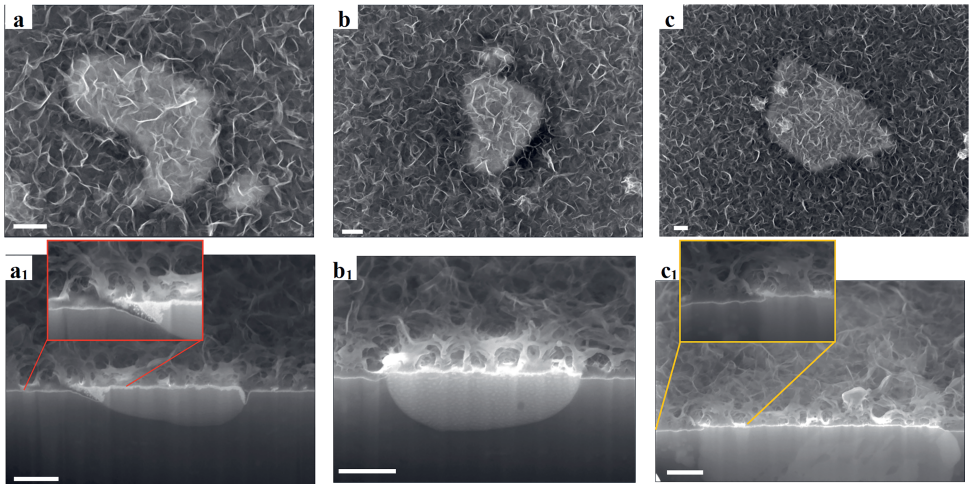


Fig. 8.10. Morphological observations of intermetallic phases in AA2024-T3 exposed to 0.01 M NaCl + 0.01 M Li_2CO_3 for 7 h. Top-view and cross-sectional SEM images of (a and a_1) an Al_2CuMg particle, (b and b_1) an Al_2Cu particle and (c and c_1) a constituent-phase particle. The insets are the magnified views of the indicated cross-sectional regions. The scale bar is 1 µm.

To explore how the dealloying can accelerate the formation of the conversion layer, we take a closer look at the S-phase particles with Scanning TEM/energy dispersive spectroscopy (STEM/EDS). The TEM cross-sections were prepared with FIB and lift-out procedure out of the S-particles exposed to the

identical solution for 7 h. Fig. 8.11 shows an S-phase particle which has been dealloyed partly. It should be mentioned that the dealloying morphology of this particle is a bit different than that of other S-phase particles in this study as it has been exposed to a different amount of 0.01 M NaCl + 0.01 M Li_2CO_3 solution (electrolyte thickness of approx. 2 mm) for 7 h which shows an effect on the morphology of the dealloying and conversion layer. S-phase is known as an intermetallic compound with a high electrochemical instability in a wide range of solution pH, generally undergoing dealloying due to preferential dissolution of aluminium and magnesium and also rearrangement of copper in a nano-porous morphology [25]. The cross-sectional STEM image shows a nano-porous dealloying morphology in the periphery of the particle; the dealloying is penetrated more into the particle from the bottom part. Besides, it is remarkable that the conversion layer on the particle and on its adjacent matrix has the same thickness. However, the dense layer is missing on the particle and it merely composes of a columnar layer. Besides, corrosion products with a similar morphology to the dense layer is formed within the trench. The corresponding EDS elemental maps (Fig. 8.11) show that the dealloyed regions of the particle are depleted from magnesium. Given that magnesium is insoluble in solutions of pH higher than 12, herein its preferential dissolution is plausible as the studied solution provides insufficient alkalinity for the stability of magnesium. Aluminium dissolution has happened to a lesser extent; however, the formation of a dense-like layer within the trench implies the role of lithium intercalation in stabilisation of aluminium-based corrosion products. As expected, copper does not endure dissolution, as long as the corroding particle is connected to the matrix, and it has rearranged in a nano-porous morphology.

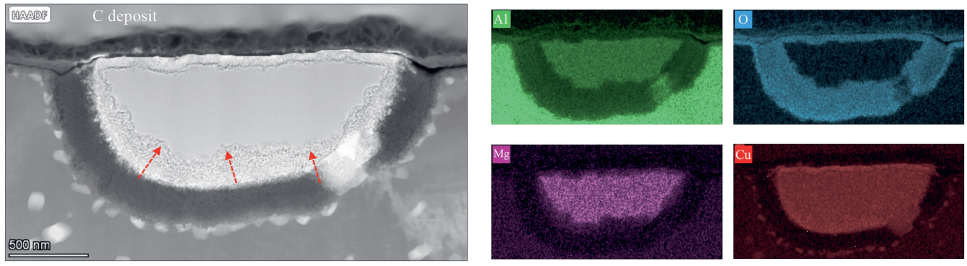


Fig. 8.11. STEM/EDS characterisation of S-phase. Cross-sectional STEM/EDS analysis of an Al_2CuMg particle exposed to 0.01 M NaCl + 0.01 M Li_2CO_3 solution for 7 h (electrolyte thickness of approx. 2 mm), revealing the selective dissolution of Al and Mg from the particle. The lamella was fabricated with the lift-out FIB procedure.

8.3.4. XRD analysis of the formed conversion layer. XRD patterns collected from the samples exposed for 2 and 7 h to are shown in Fig. 8.12. The presence of Li-Al LDH can be identified through the appearance of characteristic (003) and (006) peaks [8]. Since X-ray interactions takes place with an atom's electron cloud [33], the atomic scattering factors are relatively low for Li, C and Al which

contribute to the intensity of basal reflections in Li-Al LDH. Thus, X-rays get scattered to a minor extent only while traveling through the thin surface conversion layers which leads to emerging reflections originating from the IMPs. This is particularly problematic for Li-Al LDH identification since the strong reflections corresponding to Al_7Cu_2Fe show up at the grazing angles very close to the characteristic Li-Al LDH peaks. This is evident in Fig. 8.12 where the (002) peaks of Al_7Cu_2Fe make the basal reflections corresponding to Li-Al LDH appear as a shoulder in the XRD spectra. This is the case for both samples exposed to 0.01 M NaCl + 0.01 M Li_2CO_3 for 2 and 7 h. Thus, a pure aluminium exposed to the studied solution for 7 h was analysed with XRD to fortify and confirm the above hypothesis of Li-Al LDH formation. As can be seen, the pure aluminium sample shows a solo strong reflection related to the basal (003) plane. Thus, the formation of Li-Al LDH takes place as a direct consequence of the lithium-based conversion process according to the XRD results. Morphological investigations revealed that this can happen through the appearance of a columnar morphology after a 2800-s exposure at the latest.

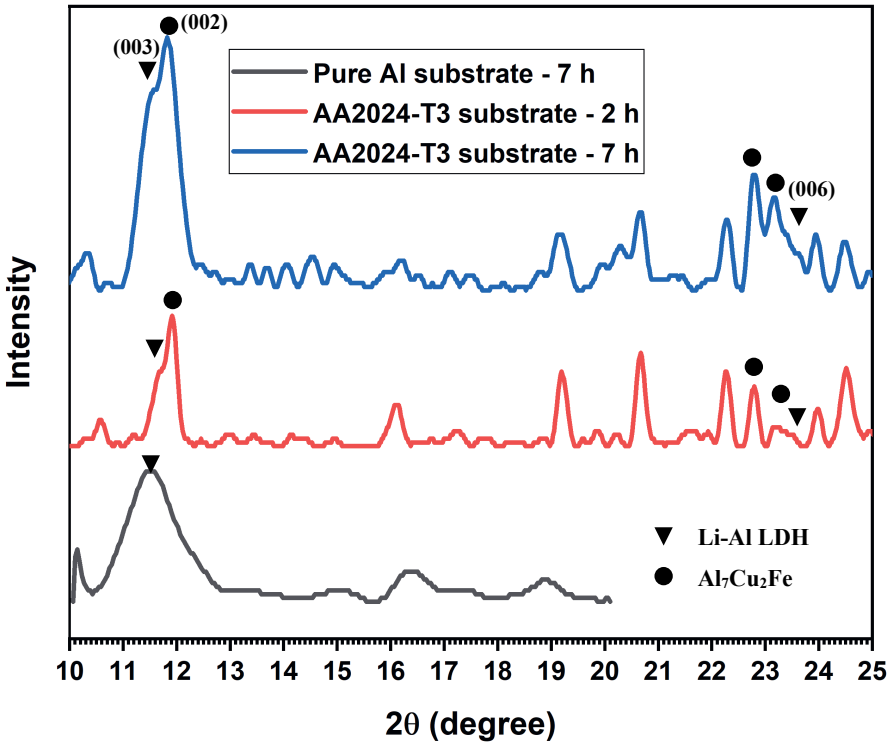


Fig. 8.12. XRD patterns of the conversion layer formed on AA2024-T3 and pure aluminium after exposure to 0.01 M NaCl + 0.01 M Li_2CO_3. The (003) and (006) peaks are characteristic for Li-Al LDH. The AA2024-T3 sample shows other reflections originating from different intermetallic compounds; some of the peaks corresponding to Al_7Cu_2Fe show up at the grazing angles very close to the characteristic Li-Al LDH peaks.

8.3.5. Exposure to a sodium carbonate solution (lithium-free). Our recent work on the cross-sectional chemical composition of the conversion layer has shown a relatively homogeneous distribution of lithium throughout the different sub-layers [17]. In order to better understand how its presence affects the layer formation, we have exposed AA2024-T3 samples to a lithium-free 0.01 M NaCl + 0.01 M Na_2CO_3 solution (pH 10.6) and in an identical condition in terms of the electrolyte thickness (approx. 4 mm). The results related to the electrochemical and morphological analysis are shown in Fig. 8.13. In Fig. 8.13a, we see the evolution of the OCP values over 5 h of exposure during which the system acquires OCP values similar to those for the lithium-containing system. As can be seen, the system shows nearly identical behaviour and values during the first 1500 s (Compare the inset here and Fig. 8.1). Afterwards, the OCP reaches a state of little change at -1200 mV until 3 h. However, the system experiences an abrupt rise in the OCPs values, reaching -400 mV in the next 2 h of exposure. Given the morphological evolutions of the alloy matrix and the different IMPs presented in Fig. 8.13b-e, we notice a clear dissimilarity of the morphology in the absence and presence of lithium. As is evident, the alloy matrix has severely been corroded, revealing a typical corrosion-attack morphology observed for aluminium in alkaline environments [34, 35]. A thin but highly porous layer of aluminium hydroxide is merely formed. S-phase particles are found in a dealloyed and trenched condition where no conversion layer has been formed. Besides, the alloy matrix has not been trenched around Al_2Cu and constituent phase particles; however, it has uniformly but deeply been dissolved during the exposure. It seems that lithium plays a crucial role in the stabilisation of the corrosion products in the studied alkaline environment, causing the conversion process to occur.

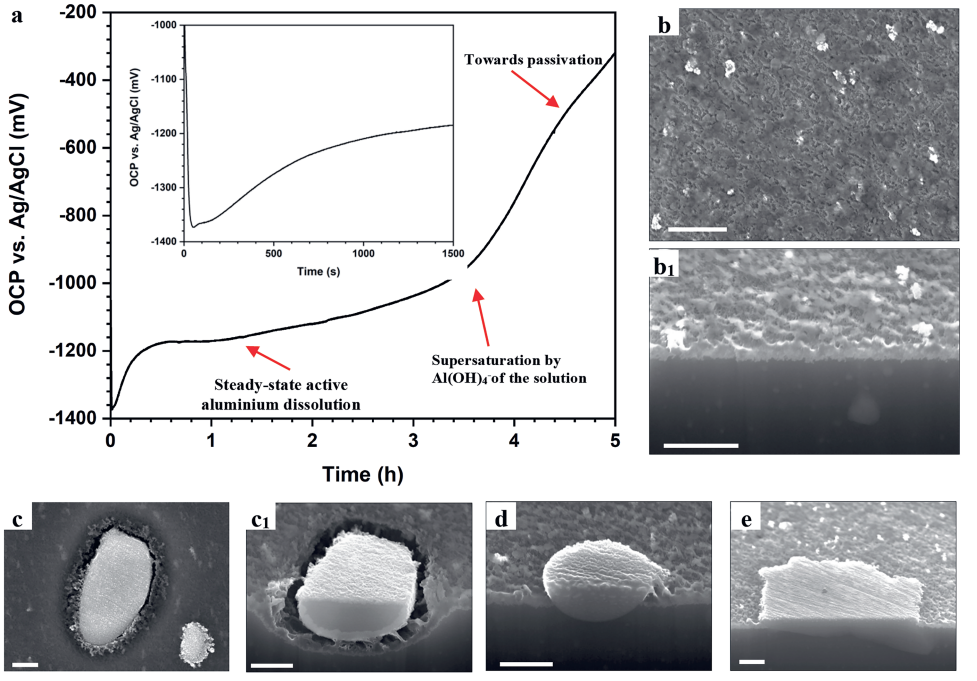


Fig. 8.13. Electrochemical and morphological evaluations of AA2024-T3 exposed to 0.01 M NaCl + 0.01 M Na_2CO_3 (lithium-free solution; pH 10.6) for 5 h. (a) OCP response of AA2024-T3 over time. The inset shows a closer look at the OCP behaviour at early stages of exposure. (b and b_1) Top-view and cross-sectional SEM images of the alloy matrix, revealing the surface to be severely corroded while a highly porous thin aluminium hydroxide layer has been formed during the exposure. (c and c_1) Top-view and cross-sectional SEM images of an Al_2CuMg particle, showing that the particle has undergone dealloying and besides the surrounding alloy matrix has been fully trenched. Cross-sectional SEM image of (d) an Al_2Cu and (e) a constituent-phase particle which have been surface-dealloyed while their adjacent matrix has been dissolved significantly (stage tilt 52°). The scale bar is 1 μm.

In the absence of lithium, the pre-existing surface aluminium oxide is just dissolved during the first 60 s, resulting in a decrease in the OCP value [32]. Subsequently, the massive dissolution of the alloy matrix comes about and this leads to a higher concentration of $Al(OH)_4^-$ at the surface. This phenomenon causes an impact on the kinetics of aluminium dissolution with time (i.e., higher anodic Tafel slope), emerging as an increase in the OCP value [34]. The mass transfer of $Al(OH)_4^-$ ions from the surface to the bulk solution reaches a steady state condition after 500 s; that is why we see a plateau in the OCP plot from 500 s to 3 h. Since, $Al(OH)_4^-$ is the only soluble species in the studied alkaline environment [36], the porous aluminium hydroxide (acting as the intermediate [32, 37]) layer becomes stable upon the supersaturation of the limited solution (i.e., 1.23 mL solution for 3.14 cm^2 area of the sample). This is associated with the abrupt increase in the OCP values since the formed layer can slow down the anodic dissolution of the alloy matrix. In addition, the gradual copper enrichment of the

surface and S-phase particles as a direct consequence of the alloy matrix dissolution and dealloying, respectively, can contribute to the OCP increase at different stages of exposure as well. In fact, Cu-rich regions can increase cathodic activity of the surface through accommodating water and oxygen reduction reactions, leading to an increase in the OCP values. In comparison, the conversion process can take place in the presence of lithium in the vicinity of the surface where the required local supersaturation is fulfilled at Stage III. We discuss the mechanism of relevance in detail in the next section.

8.4. Local formation mechanism of the conversion layer

Top-view and cross-sectional FIB/SEM observations along with the recorded OCP values can elucidate how the alloy matrix and different IMPs evolve during the conversion process in the lithium carbonate-containing solution as shown schematically in Fig. 8.14. As discussed earlier, the supersaturation of the solution by $Al(OH)_4^-$ ions of the solution is of critical stage for the initiation of the conversion process. The supersaturation is fulfilled through the direct dissolution of the substrate. If the solution can acquire the required supersaturation locally, the conversion layer can take place consequently at those locations. This phenomenon is well pronounced for S-phase particles where a fast dealloying can effectively enhance the local supersaturation and hence the local lithium-based conversion process.

8.4.1. Alloy matrix. At Stage I, the alloy matrix initially loses its passivity in the studied alkaline environment, inducing a drop in the OCP value during the first 60 s. At Stage II, the process proceeds by active dissolution of the alloy matrix; the kinetics of aluminium dissolution decreases gradually due to the accumulation of $Al(OH)_4^-$ ions, which form through the transformation of Al^{3+} to $Al(OH)_3$ and then to $Al(OH)_4^-$ under the alkaline conditions present at the surface. In addition, the surface gradually becomes enriched in copper as the alloy matrix holds 0.2-0.5 at% Cu and besides due to dealloying of the nanoscopic IMPs (i.e. S-phase and dispersoids) [38]. As discussed in Section 3.4, these two phenomena bring about a gradual increase in the OCP value. In contrast to the lithium-free solution, the conversion layer nucleates and starts growing in a columnar morphology upon reaching the required supersaturation at the surface (Stage III). At Stage (IV), the dissolution front still penetrates into the alloy matrix and consequently the columns further grow and get entangled with time. The OCP continues to increase in this period as the alloy matrix progressively acquires passivity (i.e., anodic Tafel slope increases). Although the columnar layer is not highly protective, the entangled network of the long columns can effectively slow down the dissolution rate. This causes a positive impact on the densification of the conversion layer; thus, the next sublayer which appears is a dense layer close to the substrate (Stage V). Simultaneously, the columnar layer grows through direct precipitation of the Li-containing products from the saturated solution, resulting in coarsening of the columnar morphology. At Stage V, the system experiences a nearly stabilised condition and the OCP curve plateaus due to the passivation by the lithium-based conversion layer.

8.4.2. S-phase (Al_2CuMg) particles. Al_2CuMg compound is a highly electrochemically active phase that quickly interacts with the alkaline Li-containing solution upon exposure (Stage I). At Stage II, S-phase particles release $Al(OH)^{4-}$ and Mg^{2+} in the studied solution as a direct consequence of dealloying causing the local supersaturation of the solution and copper enrichment of the corroding particles. The former triggers the formation of the columnar morphology over S-phase particles preceding that on the alloy matrix. The latter gives rise to the increase in the OCP values by increasing cathodic activities of the surface. At Stage III, the columnar layer grows and this is associated with further penetration of dealloying. Stage IV comes with further growth of the columnar layer on the particle and adjacent at the alloy matrix, although the preferential trenching of the alloy matrix takes place too. There is no difference between Stage IV and V for the S-phase particle where the further columnar layer growth, particle dealloying and alloy matrix trenching simultaneously but sluggishly occur.

8.4.3. Al_2Cu and constituent phase particles. Al_2Cu and constituent phase particles show a high electrochemical stability in the alkaline lithium-containing solution, undergoing a slight dealloying throughout the 7-h exposure. At Stage I and II, they insignificantly release $Al(OH)_4^-$ into the solution due to sluggish dealloying disabling to reach supersaturation. Thus, the alloy matrix is the only source for providing $Al(OH)_4^-$ ions as the main component of the lithium-based conversion layer. That is why the conversion layer is observed over the whole alloy matrix except the region surrounding the Al_2Cu and constituent phase particles (Stage III). Similar to S-phase particles, the only columnar layer grows through the precipitation during Stage IV and V while the alloy matrix acquires a dense-like sublayer at Stage V by further penetrating into the depth.

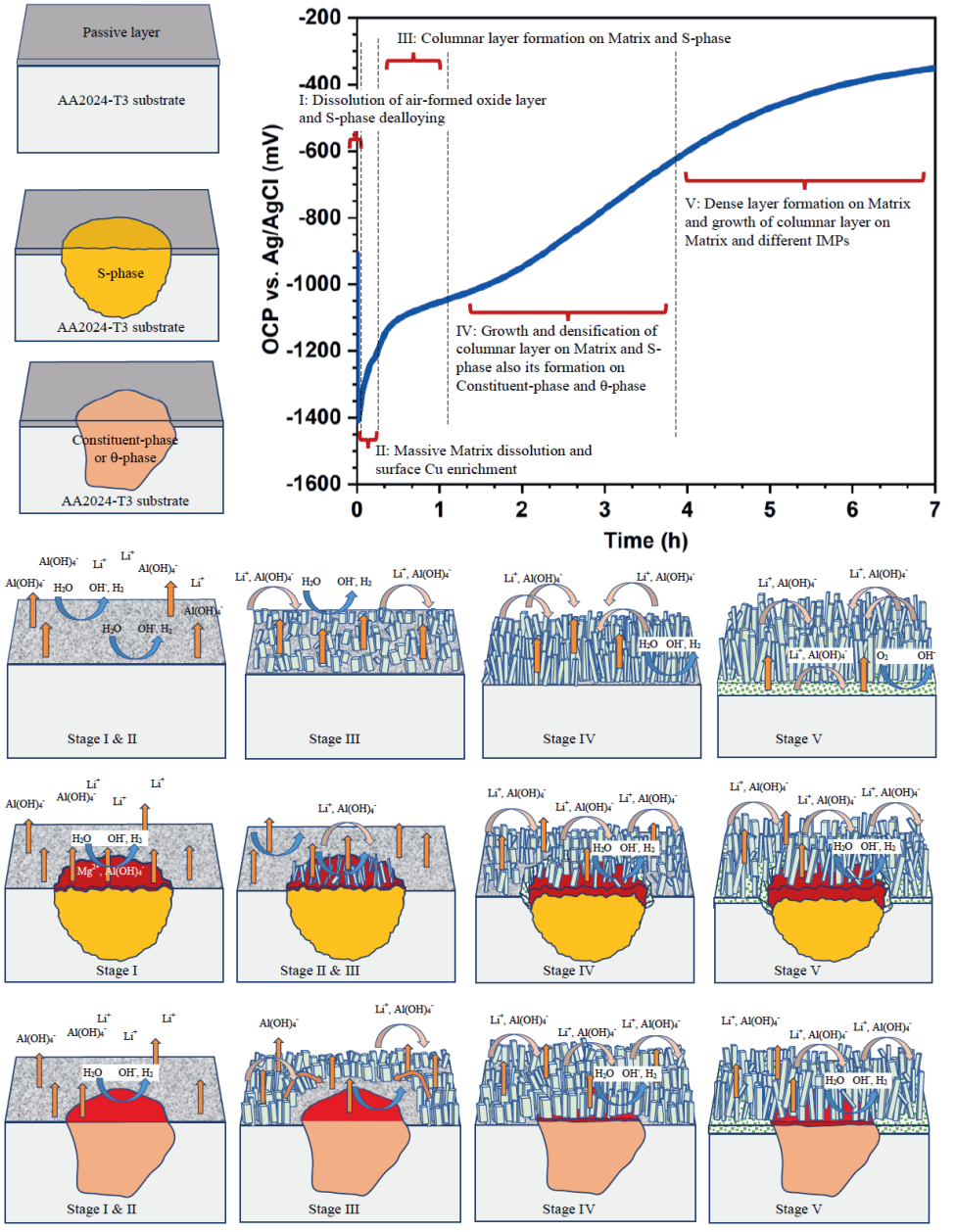


Fig. 8.14. The formation mechanism of the conversion layer on AA2024-T3. 3D schematic view of formation mechanism of the conversion layer on different regions in the alloy linked to the OCP response of the whole system. The probable corrosion and precipitation reactions taking place on the alloy matrix and also around IMPs are depicted in detail. The columnar morphology is the initial layer being formed over the matrix and it is the only layer formed over IMPs. The dense layer is established with a proceeding dissolution front into the alloy matrix or within trenches around S-phase particles. Copper-rich regions like the top-surface parts of the dealloyed IMPs or nanoscopic remnants are responsible for supporting cathodic reactions.

8.5. Conclusions

While our previous works provided a general lithium-based conversion layer formation mechanism, here we unravelled the laterally resolved formation mechanisms of the layer at the matrix and IMPs of AA2024-T3 in a condition mimicking coating defects when lithium carbonate is used as the leaching inhibitor. With sub-micron resolved top-view and cross-sectional FIB/SEM analysis along with OCP recording, we distinguished 5 stages (out of a 7-h exposure) during the conversion process in which the alloy matrix and different IMPs evolve morphologically, compositionally and electrochemically. We found that AA2024-T3 does not acquire passivation in early exposure times up to 800 s (Stage I and II). Passivity loss leads to the initial OCP drop during the first 60 s. However, active alloy matrix dissolution and surface Cu-enrichment mainly contribute to the rise in OCP values by modifying anodic and cathodic activities, respectively. Upon reaching local supersaturation at Stage III, the conversion layer appears in a columnar morphology on S-phase, alloy matrix and other intermetallic compounds in a chronological order. This is associated with a rise in OCP values due to the diminished kinetics of the anodic aluminium dissolution. Faster dealloying of S-phase can enhance the conversion process by providing relatively rapidly $Al(OH)_4^-$ ions (local supersaturation). Besides, lithium plays a critical role in stabilising the corrosion products; no conversion process occurs under the same exposure conditions but in the absence of lithium. At Stage IV (starting from approx. 1 h and lasting until 4 h), the columnar layer grows and the OCP values rise. Finally, Stage V is involved with the formation of the dense-like layer closest to the alloy matrix while IMPs are merely covered with a columnar layer. At this stage, the system acquires passivation, revealing a plateaued OCP curve owing to the electrochemical stabilisation (i.e., nearly constant anodic and cathodic behaviour). Finally, the critical role of lithium in the conversion process was revealed through complementary experiments in a sodium carbonate solution and X-ray diffraction analysis.

References

[1] P. Visser, H. Terryn, J.M.C. Mol, Active corrosion protection of various aluminium alloys by lithium-leaching coatings, Surface and Interface Analysis, 51 (2019) 1276-1287.
[2] P. Visser, Y. Liu, H. Terryn, J.M.C. Mol, Lithium salts as leachable corrosion inhibitors and potential replacement for hexavalent chromium in organic coatings for the protection of aluminum alloys, Journal of Coatings Technology and Research, 13 (2016) 557-566.
[3] O. Gharbi, S. Thomas, C. Smith, N. Birbilis, Chromate replacement: what does the future hold?, npj Materials Degradation, 2 (2018) 1-8.
[4] D. Mata, M. Serdechnova, M. Mohedano, C.L. Mendis, S.V. Lamaka, J. Tedim, T. Hack, S. Nixon, M.L. Zheludkevich, Hierarchically organized Li–Al-LDH nano-flakes: a low-temperature approach to seal porous anodic oxide on aluminum alloys, RSC advances, 7 (2017) 35357-35367.
[5] C.D. Dieleman, P.J. Denissen, S.J. Garcia, Long-term active corrosion protection of damaged Coated-AA2024-T3 by embedded electrospun inhibiting nanonetworks, Advanced Materials Interfaces, 5 (2018) 1800176.
[6] J. Gui, T.M. Devine, Influence of lithium on the corrosion of aluminum, Scr. Metall.;(United States), 21 (1987).
[7] R.G. Buchheit, M.D. Bode, G.E. Stoner, Corrosion-resistant, chromate-free talc coatings for aluminum, Corrosion, 50 (1994) 205-214.
[8] C.A. Drewien, M.O. Eatough, D.R. Tallant, C.R. Hills, R.G. Buchheit, Lithium-aluminum-carbonate-hydroxide hydrate coatings on aluminum alloys: Composition, structure, and processing bath chemistry, Journal of materials research, 11 (1996) 1507-1513.
[9] P. Visser, S.A. Hayes, Anti-corrosive coating composition, WO2010112605-A1, in, 2010.
[10] P. Visser, Y. Liu, X. Zhou, T. Hashimoto, G.E. Thompson, S.B. Lyon, L.G. van der Ven, A. Mol, H.A. Terryn, The corrosion protection of AA2024-T3 aluminium alloy by leaching of lithium-containing salts from organic coatings, Faraday discussions, 180 (2015) 511-526.
[11] Y. Liu, P. Visser, X. Zhou, S.B. Lyon, T. Hashimoto, A. Gholinia, G.E. Thompson, G. Smyth, S.R. Gibbon, D. Graham, An investigation of the corrosion inhibitive layers generated from lithium oxalate-containing organic coating on AA2024-T3 aluminium alloy, Surface and Interface Analysis, 48 (2016) 798-803.
[12] P. Visser, K. Marcoen, G.F. Trindade, M. Abel, J. Watts, T. Hauffman, J.M.C. Mol, H. Terryn, The chemical throwing power of lithium-based inhibitors from organic coatings on AA2024-T3, Corrosion Science, 150 (2019) 194-206.
[13] P. Visser, A. Lutz, J.M.C. Mol, H. Terryn, Study of the formation of a protective layer in a defect from lithium-leaching organic coatings, Progress in Organic Coatings, 99 (2016) 80-90.
[14] P. Visser, H. Terryn, J.M.C. Mol, On the importance of irreversibility of corrosion inhibitors for active coating protection of AA2024-T3, Corrosion Science, 140 (2018) 272-285.
[15] K. Marcoen, P. Visser, G.F. Trindade, M.-L. Abel, J.F. Watts, J.M.C. Mol, H. Terryn, T. Hauffman, Compositional study of a corrosion protective layer formed by leachable lithium salts in a coating defect on AA2024-T3 aluminium alloys, Progress in Organic Coatings, 119 (2018) 65-75.
[16] Y. Liu, P. Visser, X. Zhou, S.B. Lyon, T. Hashimoto, M. Curioni, A. Gholinia, G.E. Thompson, G. Smyth, S.R. Gibbon, Protective film formation on AA2024-T3 aluminum alloy by leaching of lithium carbonate from an organic coating, Journal of The Electrochemical Society, 163 (2015) C45.
[17] A. Kosari, P. Visser, F. Tichelaar, S. Eswara, J.N. Audinot, T. Wirtz, H. Zandbergen, H. Terryn, J.M.C. Mol, Cross-sectional characterization of the conversion layer formed on AA2024-T3 by a lithium-leaching coating, Applied Surface Science, 512 (2020) 145665.
[18] P. Visser, M. Meeusen, Y. Gonzalez-Garcia, H. Terryn, J.M.C. Mol, Electrochemical evaluation of corrosion inhibiting layers formed in a defect from lithium-leaching organic coatings, Journal of The Electrochemical Society, 164 (2017) C396.
[19] P. Visser, Y. Gonzalez-Garcia, J.M.C. Mol, H. Terryn, Mechanism of passive layer formation on AA2024-T3 from alkaline lithium carbonate solutions in the presence of sodium chloride, Journal of The Electrochemical Society, 165 (2018) C60.
[20] A.E. Hughes, N. Birbilis, J.M.C. Mol, S.J. Garcia, X. Zhou, G.E. Thompson, High strength Al-alloys: microstructure, corrosion and principles of protection, Recent Trends in Processing and Degradation of Aluminium Alloys, 1 (2011).

[21] A. Boag, R.J. Taylor, T.H. Muster, N. Goodman, D. McCulloch, C. Ryan, B. Rout, D. Jamieson, A.E. Hughes, Stable pit formation on AA2024-T3 in a NaCl environment, Corrosion Science, 52 (2010) 90-103.
[22] Y. Zhu, K. Sun, G.S. Frankel, Intermetallic phases in aluminum alloys and their roles in localized corrosion, Journal of The Electrochemical Society, 165 (2018) C807.
[23] G.O. Ilevbare, O. Schneider, R.G. Kelly, J.R. Scully, In situ confocal laser scanning microscopy of AA 2024-T3 corrosion metrology: I. Localized corrosion of particles, Journal of the Electrochemical Society, 151 (2004) B453.
[24] N. Birbilis, R.G. Buchheit, Electrochemical characteristics of intermetallic phases in aluminum alloys: an experimental survey and discussion, Journal of the Electrochemical Society, 152 (2005) B140.
[25] A. Kosari, H. Zandbergen, F. Tichelaar, P. Visser, P. Taheri, H. Terryn, J.M.C. Mol, In-situ nanoscopic observations of dealloying-driven local corrosion from surface initiation to in-depth propagation, Corrosion Science, 177 (2020) 108912.
[26] A. Kosari, F. Tichelaar, P. Visser, H. Zandbergen, H. Terryn, J.M.C. Mol, Dealloying-driven local corrosion by intermetallic constituent particles and dispersoids in aerospace aluminium alloys, Corrosion Science, 177 (2020) 108947.
[27] A.E. Hughes, R. Parvizi, M. Forsyth, Microstructure and corrosion of AA2024, Corrosion Reviews, 33 (2015) 1-30.
[28] R.G. Buchheit, R.P. Grant, P.F. Hlava, B. McKenzie, G.L. Zender, Local dissolution phenomena associated with S phase (Al2CuMg) particles in aluminum alloy 2024-T3, Journal of the electrochemical society, 144 (1997) 2621.
[29] J. Mayer, L.A. Giannuzzi, T. Kamino, J. Michael, TEM sample preparation and FIB-induced damage, MRS bulletin, 32 (2007) 400-407.
[30] E. McCafferty, Kinetics of corrosion, in: Introduction to Corrosion Science, Springer, 2010, pp. 119-175.
[31] N. Birbilis, Y.M. Zhu, S.K. Kairy, M.A. Glenn, J.-F. Nie, A.J. Morton, Y. Gonzalez-Garcia, H. Terryn, J.M.C. Mol, A.E. Hughes, A closer look at constituent induced localised corrosion in Al-Cu-Mg alloys, Corrosion Science, 113 (2016) 160-171.
[32] G.T. Burstein, R.J. Cinderey, Evolution of the corrosion potential of repassivating aluminium surfaces, Corrosion science, 33 (1992) 475-492.
[33] Y. Waseda, E. Matsubara, K. Shinoda, X-ray diffraction crystallography: introduction, examples and solved problems, Springer Science & Business Media, 2011.
[34] K.C. Emregül, A.A. Aksüt, The behavior of aluminum in alkaline media, Corrosion science, 42 (2000) 2051-2067.
[35] S.-I. Pyun, S.-M. Moon, Corrosion mechanism of pure aluminium in aqueous alkaline solution, Journal of Solid State Electrochemistry, 4 (2000) 267-272.
[36] M. Pourbaix, Atlas of electrochemical equilibria in aqueous solution, NACE, 307 (1974).
[37] M.R. Tabrizi, S.B. Lyon, G.E. Thompson, J.M. Ferguson, The long-term corrosion of aluminium in alkaline media, Corrosion science, 32 (1991) 733-742.
[38] N. Wint, Z.S. Barrett, G. Williams, H.N. McMurray, The study of AA2024 de-alloying using luminol electrogenerated chemiluminescence imaging, Journal of The Electrochemical Society, 166 (2019) C3417.

CHAPTER 9

QUASI IN-SITU AND EX-SITU TEM, AND ELECTROCHEMICAL INVESTIGATIONS OF LOCAL CORROSION INHIBITION BY A CERIUM-BASED INHIBITOR[1]

Cerium-based compounds have been studied for decades as non-toxic candidates for the protection of aerospace aluminium alloys (AAs) like AA2024-T3. However, the complex heterogeneous microstructure of these alloys has hindered a thorough understanding of the subsequent stages of corrosion protection provided by this class of inhibitors. Thus, this chapter is devoted to unravelling the interaction mechanisms of different intermetallic particles (IMPs) in AA2024-T3 with cerium nitrate at the nanoscopic scale. This has been fulfilled through detailed top-view and cross-sectional analytical TEM investigations along with electrochemical evaluations. In line with the findings in Chapter 4 and 5, we here report dealloying of IMPs as the main factor governing the rate of local cerium precipitation in contrast to micro-galvanic corrosion between IMPs and the surrounding matrix. Furthermore, we discuss a connection between the electrochemical response of the AA2024-T3 system and the morphological and compositional evolutions of individual IMPs including Al_2CuMg, Al_2Cu, $Al_7Cu_2Fe(Mn)$ and $Al_{76}Cu_6Fe_7Mn_5Si_6$ at different stages of a 96-h exposure.

Keywords: Aerospace aluminium alloys; Cerium salt; Quasi in-situ TEM; Cross-sectional ex-situ TEM; Dealloying; Corrosion inhibition

[1] **A. Kosari**, M. Ahmadi, F. Tichelaar, P. Visser, Y. Gonzalez-Garcia, H. Zandbergen, H. Terryn, J. M. C. Mol, Editors' Choice—Dealloying-Driven Cerium Precipitation on Intermetallic Particles in Aerospace Aluminium Alloys, Journal of The Electrochemical Society, 168 (2021) 041505.

9.1. Introduction

Aerospace aluminium alloys (AAs) are a class of structural materials that contain intermetallic compounds including precipitates, constituent particles and dispersoids ranging from nano- to micrometre scales. In AA2024-T3, Al_2CuMg and Al_2Cu are precipitates that appear in response to age hardening processes while constituent phases like $Al_7Cu_2Fe(Mn)$ and $Al_{76}Cu_6Fe_7Mn_5Si_6$ are formed during solidification, contributing, to different extents, to the mechanical strength of the alloy [1]. In terms of corrosion, intermetallic particles (IMPs) are electrochemically active locations in the alloy matrix at which local corrosion attack evidently takes place [2-7]. Therefore, the use of inhibitors that can effectively impede local electrochemical activity of IMPs is necessary to prevent local stress concentrations and eventually the loss of structural integrity of AA applications. For decades, this purpose has reliably been fulfilled via hexavalent-chromium based chemistries, in spite of their undesirable impact on health and environment [8-10]. However, due to strict international health and safety legislation, they have to be entirely replaced with non-toxic and efficient inhibitive systems in the near future [11].

Following that, cerium-based compounds have been introduced as promising non-toxic inhibitors and examined extensively to inhibit localised corrosion of AAs [12-24]. The main protective properties of this group of inhibitors are attributed to the formation of an insoluble cerium (hydr)oxide precipitate via a chemical route and as a response to the local alkalinity established by electrochemical activity of individual IMPs (microgalvanic corrosion) [25, 26]. However, the literature still lacks an agreement when it comes to explaining the detailed mechanisms in relation to the morphology and sequence of cerium (hydr)oxide precipitation on individual intermetallic compounds. For instance, according to Paussa et al. [27], local alkalisation at magnesium-rich regions of a corroding S-phase (Al_2CuMg) can trigger the cerium precipitation. However, Li et al. [28] proposed initial cerium precipitate as a consequence of electrochemical transition of S-phase from an anodic to a cathodic particle (nobility inversion), after which the precipitate continues to thicken. Aldykewicz et al. [29] merely detected cerium on Cu-rich IMPs and not on Fe/Mn-containing IMPs. In contrast, Yasakau et al. [26] found a cerium deposit on a Fe-containing particle, appearing in a nodular morphology. In addition, Campestrini et al. proposed the Cu redeposition as a critical condition to form a thick cerium oxide layer otherwise the IMPs do not function as preferential nucleation sites during the conversion process [30]. Besides, morphological and compositional evolutions of θ-phase (Al_2Cu) during the interaction with cerium-based inhibitors has not been addressed in the literature yet.

Therefore, the current work is devoted to exploring detailed interaction mechanisms of cerium nitrate, as an effective and efficient inhibitor, [31, 32] with different types of intermetallic compounds in AA2024-T3. In fact, we put efforts into correlating the conventional electrochemical response and the nanoscopic morphological and compositional evolutions related to different IMPs over an exposure up to 96 h. A challenge in this regard is the complicated electrochemical behaviour of IMPs themselves,

including their nanoscopic morphological and compositional evolution with time. Recently, we reported a dealloying-driven local corrosion initiation mechanism for both conventional anodic and cathodic intermetallic phases [33, 34]. Besides, we brought up the intrinsic electrochemical instability of intermetallic compounds as a dominant factor controlling the kinetics of local degradation [33, 34]. Here, we further address how the dealloying process and electrochemical stability can establish a local solution chemistry driving cerium precipitation over IMPs. To this aim, we initially record open circuit potential (OCP) and linear polarization resistance (LPR) of AA2024-T3 samples exposed to a cerium-containing solution along with general top-view morphological observations of the surface. Furthermore, detailed top-view and cross-sectional analytical transmission electron microscopy (TEM) on individual Al_2CuMg, Al_2Cu, $Al_7Cu_2Fe(Mn)$ and $Al_{76}Cu_6Fe_7Mn_5Si_6$ particles are carried out to provide nanoscopic insights into the inhibition mechanism at different stages of exposure and particularly related to the different intermetallic chemistries.

9.2. Experimental

9.2.1. Electrochemical evaluations. — Prior to electrochemical measurements, AA2024-T3 sheet were ground down to #1200 and then polished on a soft cloth in alumina slurries of 0.5 and 0.05 μm, respectively, in a non-aqueous solution. The freshly-polished samples of 3.14 cm^2 were exposed to 0.01 M NaCl + 0.003 M $Ce(NO_3)_3$ solution (pH = 5.2) for a period of 96 h while the OCP values were monitored continuously versus an Ag/AgCl saturated reference electrode. Besides, the superimposed LPR measurements were carried out every 15 min during the first 2 h and every 1 h for the rest of exposure with an amplitude of ±10 mV versus the OCP at a scan rate of 1 mV/s and in a conventional three-electrode set-up. The LPR values were estimated by considering the linear part (i.e., slope) of potential versus current curves around the OCP.

9.2.2. Analytical TEM studies. — Top-view quasi in-situ TEM analysis was conducted on argon ion-milled 3-mm disks intermittently exposed to 0.01 M NaCl + 0.003 M Ce(NO3)3 solution. In this part, the experiments were performed by repeatedly observing an identical location on the specimens exposed to the studied solution outside the electron microscope. After each exposure event, the specimens were rinsed off with distilled water for a few seconds. Then, water on the specimens was immediately absorbed by delicate-task wipes and the specimens were dried under a lamp, followed by plasma-cleaning right before re-inserting into the TEM column. Cross-sectional TEM investigations were carried out on the polished AA2024-T3 sheets exposed to the same solution for different exposure times of 1.5, 6, 24 and 96 h. After completion of the exposure, the samples were rinsed off with distilled water for a few seconds to avoid direct salt precipitation upon drying. The surface morphology of IMPs was examined initially with secondary electron scanning electron microscopy/energy dispersive spectroscopy (SEM/EDS) and then the thin cross-sections were fabricated out of the IMPs of interest with a Thermo-Fisher Helios G4 focused ion beam/scanning electron microscope (FIB/SEM). A Tecnai

F20ST/STEM 200 kV equipped with an Oxford Instruments X-MaxN 100TLE windowless detector and a high resolution Gatan imaging filter (GIF) were employed to perform typical (scanning)TEM imaging, EDS, electron energy loss (EEL) spectroscopy and energy-filtered TEM. To do elemental mapping on the samples, EDS and EF-TEM analysis were conducted. The latter was obtained by filtering Ce-$M_{3,4}$ and Cu-$L_{2,3}$-edge using 30-eV and 20-eV slits, respectively. The EEL-spectra of cerium were collected at an energy resolution of 0.9 eV and energy dispersion of 0.1 eV/pixel. Multiple linear least-squares (MLLS) fitting was used to fit the reference spectra of Ce(III) and Ce(IV) to the collected spectra, distinguishing the oxidation state of the cerium deposit at different exposure times [35]. Prior to the fitting process, the background signal was subtracted from the spectra using the power law model. Subsequently, to remove the possible impact of plural scattering on the fitting results, the log-ratio method using the zero-loss peak of the corresponding spectra was applied [36].

9.3. Results and discussion

9.3.1. Electrochemical and morphological of the alloy surface during exposure. — Fig. 9.1a shows the OCP and LPR values recorded for AA2024-T3 continuously exposed to the studied solution. During the first 1.5 h of exposure, we see the corrosion potential of the sample going up from -510 to -460 mV. In the same course of exposure, the LPR plot shows an increase from 45 to 85 kΩ in value, although an initial drop of 15 kΩ is distinguishable from 15 min to 30 min. Up to this point, the top-view SEM/EDS examinations (Fig. 9.1b; the corresponding EDS spectra are partly shown in Supplementary Materials) show no clear indication of cerium precipitation, although the evolving electrochemical response (i.e., OCP and LPR values) implies the occurrence of nanoscopic events that cannot be revealed here due to the limited resolution of SEM. Prolonged exposure up 6 h causes a gradual increase and decrease in the OCP and LPR values, respectively. The OCP value reaches approximately -440 mV while the LPR steeply goes down to 30 kΩ and then starts to slowly increase to 45 kΩ. At this stage, the S-phase particles reveal an obvious change in contrast associated with of cerium (hydr)oxide precipitation confirmed by EDS analysis (see Supplementary Materials) while we observe no clear alteration to the other types of IMPs.

From 6 to 24 h, the OCP and LPR values steeply increase to -330 mV and 160 kΩ. Up until 24 h, we observe more S-phase particles significantly covered with the cerium-based precipitate. Besides, θ-phase indicates a sign of interaction with the environment as the contrast has slightly changed on some of the particles. At this stage, we still cannot distinguish any change to the constituent phase particles. From this stage on, the inhibited system stabilises as both the OCP and LPR values show plateaus at around -350 mV and 300 kΩ, respectively. The SEM image shows several pits on the surface that are probably left behind by the fallen-out S-phase particles since we comparatively found a lower number of surface S-phase particles at this stage. Furthermore, the θ-phase particles look completely darker in

contrast, appearing in a nodular morphology, while most of the constituent phase particles seem bare until 96 h of exposure (mind the representative corresponding SEM images).

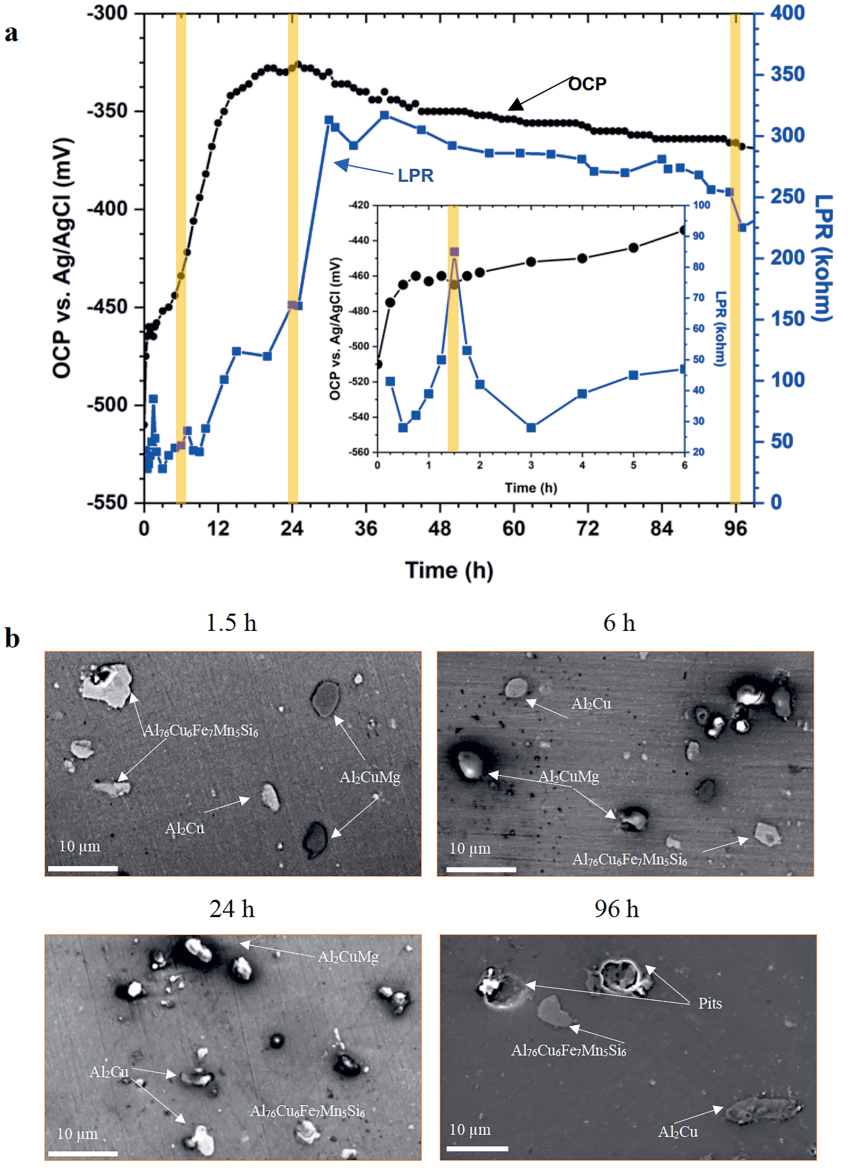


Fig. 9.1. General electrochemical and morphological analysis with time. (a) OCP (Black line with circle markers) and LPR (Blue line with rectangle markers) values recorded for the AA2024-T3 sample continuously exposed to 0.01 M NaCl + 0.003 M $Ce(NO_3)_3$ solution for 96 h. (b) Top-view SEM images of the exposed samples after different exposure times. The images are acquired by collecting the secondary electrons (SE) at an acceleration voltage of 10 kV.

9.3.2. Nanoscopic examinations of exposed isolated IMPs— Nanoscopic investigations are needed for a detailed understanding of the link between the morphological and compositional evolution to the corresponding electrochemical response of the alloy during exposure. Therefore, in this part, we perform analytical TEM measurements over individual IMPs in AA2024-T3 exposed to 0.01 M NaCl + 0.003 M $Ce(NO_3)_3$ solution for different exposure times.

S-phase (Al_2CuMg) — Fig. 9.2 shows quasi in-situ STEM/EDS analysis of an Al_2CuMg particle. A 5-min exposure slightly evolves the particle as compared to the fresh condition (not shown here). A few Cu nanoparticles appeared at the edge likely due to the dealloying of the upper thin part (mind the corresponding Cu map). At this stage, we detected no clear cerium precipitate on any region and the particle still contains considerable amounts of aluminium and magnesium. At the total exposure of 30 min, we observe nano-aggerates grown at the edge of the particle where the copper nanoparticles were formed initially. The EDS maps reveals that these are Cu-rich regions which can partly be sourced from the corroded nanometric Cu-containing IMPs that undergo dealloying and release copper in a shorter time-scale. Given the aluminium and magnesium map, we see that dealloying has occurred to this region whilst the rest of the particle is still intact. At this stage, we merely detect cerium on Cu-rich region and not on the intact part of the particle. This phenomenon suggests the Cu-rich regions as the main sites for cathodic activities, leading to the required alkalinity for the cerium precipitation. This has further been investigated by studying another S-phase particle shown in Fig. 9.2b. As can be seen, the dealloying has led to the formation of Cu-rich regions over an S-phase particle; however, cerium has just been detected around these regions as discrete islands. With prolonged exposure (i.e., towards 60 min exposure time in total), we see that the nano-aggregates have further grown, associated with dealloying of the entire particle and trenching of the adjacent alloy matrix. The EDS maps show that the particle is depleted in aluminium and magnesium, although the latter is still found in some regions where the highest alkalinity is expected (note the white arrow in the Mg map). During the next 30 min exposure (i.e., towards 90 min exposure time in total), the particle changes slightly in terms of cerium precipitation; however, some Cu-aggregates apparently attached to the matrix appear in the trench. They can actually be the redeposited copper, resulting from a process occurring right after the particle detachment from the alloy matrix [33]. Besides, the EEL-spectrum collected from the particle and fitted to the reference spectra reveals that the deposited cerium, at this stage, has the valency of three (Ce(III)). This implies that the initial cerium precipitates as a direct consequence of alkalisation by the cathodic activities, herein, Cu-rich regions.

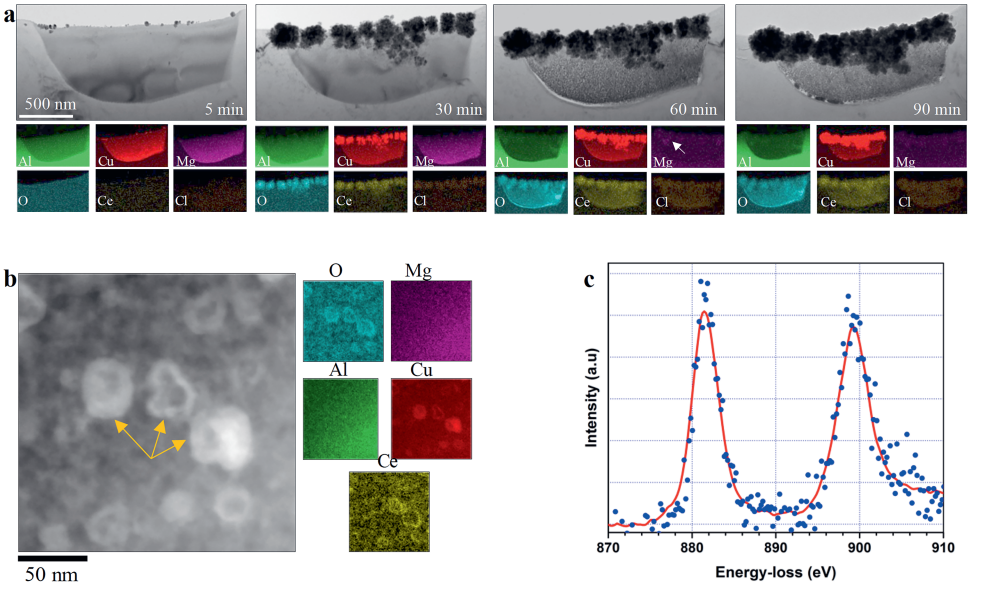


Fig. 9.2. Quasi in-situ studies of S-phase inhibition. (a) Time-resolved TEM images and the corresponding EDS maps of an Al_2CuMg particle intermittently exposed to 0.01 M NaCl + 0.003 M $Ce(NO_3)_3$. (b) High angle annular dark field (HAADF)-STEM/EDS analysis of an Al_2CuMg particles exposed to the same solution for 40 min, revealing the discretely-deposited cerium at the Cu-rich rims. (c) EEL-spectrum collected from the S-phase particle in Fig. 9.2a after 90 min; the red curve represents the MLLS fitting to the experimental dots.

Fig. 9.3 shows an Al_2CuMg particle on an AA2024-T3 sheet exposed for 1.5 h. As can be seen in the top-view SEM image, there is no clear indication of cerium precipitation at this stage while bright nanoscopic spots are observed on this particle. The cross-sectional STEM image reveals that the top part of the particle has slightly been dealloyed and this has been associated with precipitation of a narrow layer of cerium (hydr)oxide as shown in the oxygen map.

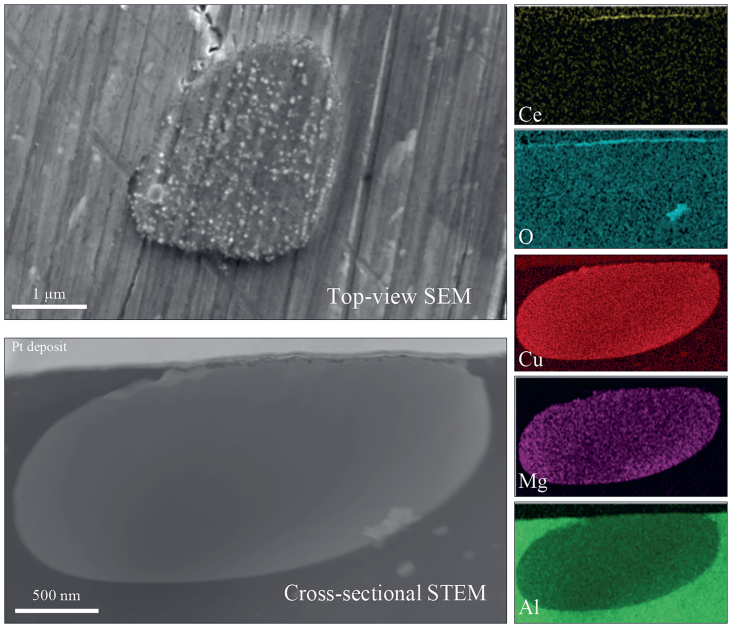


Fig. 9.3. Post-mortem analysis of exposed S-phase particles after 1.5 h. Top-view SEM and cross-sectional STEM/EDS analysis of an Al_2CuMg particle on an AA2024-T3 sheet exposed to 0.01 M NaCl + 0.003 M $Ce(NO_3)_3$. The cross-section has been prepared with FIB. Mind that there is a Pt layer deposited over the particle to protect it from Ga damage while milling.

Top-view SEM in Fig. 9.4 reveals an S-phase particle which is fully covered with a cerium-based layer after 6 h. The STEM image taken from the corresponding cross-section reveals the formation of a thick precipitate on the particle which is slightly extended to the adjacent matrix, although the cerium cap is highly porous. As can be seen, the cerium layer is also present over the adjacent alloy matrix. Interestingly, the dealloying has shallowly penetrated into the particle while there is no indication of the alloy matrix dissolution. It seems that the cerium layer is unable of inhibiting not only the initial dealloying of S-phase but also corrosion propagation into the depth of the corroding particle.

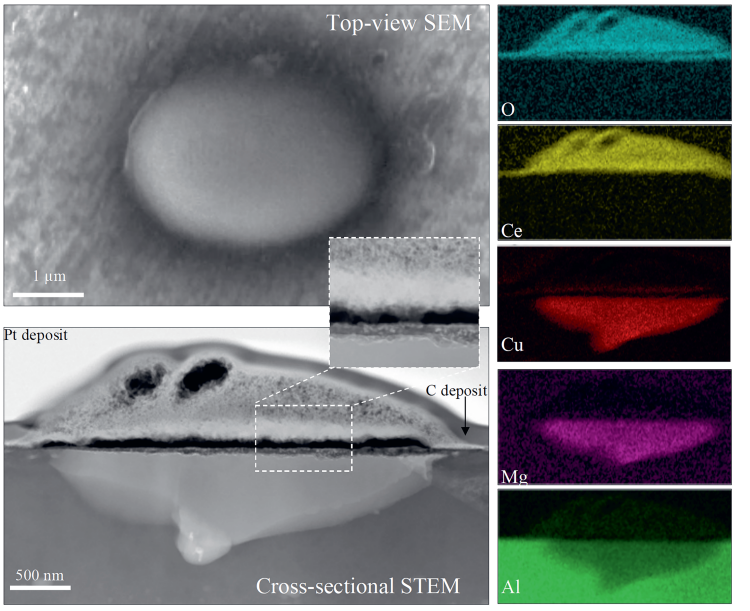


Fig. 9.4. Post-mortem analysis of exposed S-phase particles after 6 h. Top-view SEM and cross-sectional STEM/EDS analysis of an Al_2CuMg particle on an AA2024-T3 sheet exposed to 0.01 M NaCl + 0.003 M $Ce(NO_3)_3$. The inset is the magnified view of the rectangular region on the particle. The cross-section has been fabricated with FIB. Mind that there is a thin layer of carbon followed by Pt deposition on the particle to protect it from Ga damage while milling.

This phenomenon has further been evidenced in Fig. 9.5, showing an S-phase particle on the sample exposed for 6 h. The top-view SEM image shows a fully covered S-phase particle with the cerium-based precipitate. However, the SEM image when the stage is tilted at 52º reveals a gap between the cerium cap and the alloy substrate (Fig. 9.5b). This implies that at this stage, the underlying environment is not fully insulated from the bulk solution. Looking at the cross-sectional SEM image of this particle (Fig. 9.5c), we find the cerium layer quite porous and probably unable of particle protection as dealloying has penetrated relatively deep at some locations. Fig. 9.5d shows a closer look at the deep dealloyed region in this particle, indicated by the dashed rectangle. The STEM image reveals the formation of a nano-porous morphology as a consequence of dealloying. Given the corresponding elemental map, we observe the preferential dissolution of aluminium and to a larger extent magnesium from the particle, associated with the rearrangement of copper in a nanoporous morphology. In addition, we have detected chlorine as an indication of the chloride attack responsible for corrosion, here dealloying. Interestingly, the cerium has just been detected at the top of the particle and not within the dealloyed regions. Cathodic reactions taking place at the upper Cu-rich part of the particle where oxygen is readily available provide the required alkalinity for the cerium precipitation. However, the propagation of corrosion into the depth (here dealloying) causes an acidic environment, due to metal ion hydrolysis, in which cerium is stable in its soluble ionic state.

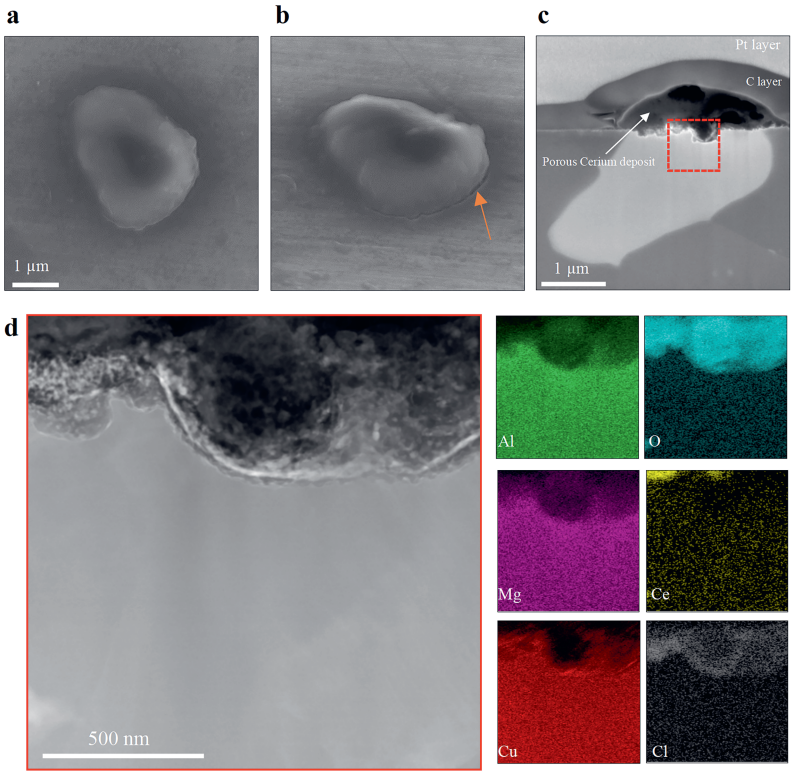


Fig. 9.5. Post-mortem analysis of exposed S-phase particles after 6 h. (a) Top-view SEM of an Al_2CuMg particle on an AA2024-T3 sheet exposed to 0.01 M NaCl + 0.003 M $Ce(NO_3)_3$. (b) SEM image of the particle when the stage is tilted at 52 º; the orange arrow indicates the gap between the alloy surface and cerium layer. (c) Cross-sectional SEM image of the same particle; the white arrow denotes the porous cerium layer. (d) STEM/EDS analysis of the rectangular region shown in Fig. 9.5c. The cross-section has been fabricated with FIB. Mind that there is a thin layer of carbon followed by Pt deposition on the particle to protect it from Ga damage while milling.

Prolonged exposure of the AA2024-T3 to 0.01 M NaCl + 0.003 M $Ce(NO_3)_3$ comes along with a change in the corrosion-attack morphology of S-phase particles. Fig. 9.6 shows top-view SEM and cross-sectional STEM/EDS analysis of an S-phase particle. The top-view image reveals the particle and its adjacent alloy matrix covered by the cerium (hydr)oxide layer (bright region) where a circumferential trench is distinguishable as a dark ring at particle/matrix interface. The cross-sectional STEM shows a rather dense cerium layer that has undergone rupture at the trench location. The remnant is fully dealloyed but not undercut, revealing a nano-porous morphology. The elemental map of the rectangular region found the particle enriched in copper but depleted in magnesium and aluminium. Besides, the Ce map clearly demonstrates the presence of a rupture where interestingly a thin layer of aluminium (hydr)oxide has emerged over the cerium cap. This phenomenon is well clear in the corresponding elemental Al and O maps.

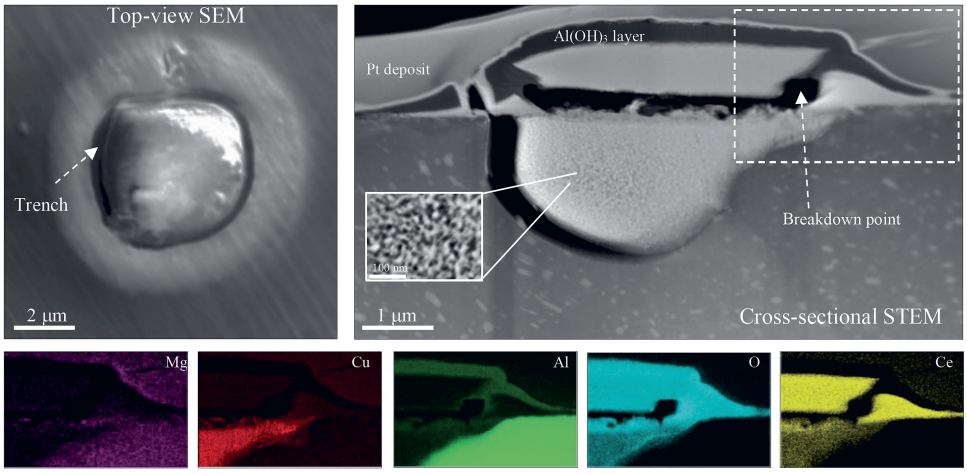


Fig. 9.6. Post-mortem analysis of exposed S-phase particles after 24 h. Top-view SEM and cross-sectional STEM/EDS analysis of an Al_2CuMg particle on an AA2024-T3 sheet exposed to 0.01 M NaCl + 0.003 M $Ce(NO_3)_3$. The inset is the magnified STEM image revealing the nanoporous morphology of the dealloyed remnant. The elemental maps correspond to the rectangular region shown in the STEM image. The cross-section has been fabricated with FIB; mind that there is a Pt layer deposited to protect the particle from Ga damage while milling.

Further investigations have been performed on another S-phase particle exposed for 24 h. The cross-sectional TEM image (Fig. 9.7a) shows a fully dealloyed particle where its surrounding matrix has been trenched too. As can be seen, it seems that a part of the cerium precipitate has been dissolved where a string of corrosion products is observed. The STEM/EDS analysis of this region is shown in Fig. 9.7b. The STEM image reveals the nano-porous morphology of the S-phase remnant where we see a cerium cap covering both the particle and its adjacent alloy matrix. The white arrow indicates the corrosion products, identified as aluminium (hydr)oxide, that are about to rupture the cerium layer. The EDS analysis reveals a thin Mg-rich layer on the top of the particle, although the particle contains almost no magnesium. It should be noted that this is just a thin FIB section of the whole particle and the rupture has happened at some regions of the cerium precipitate. That is why the cerium layer has been covered by aluminium (hydr)oxide. Fig. 9.7c shows the EEL-spectrum collected from the particle and fitted to the reference spectra. The fitting result indicates that the precipitated cerium on this particle has a Ce(IV)/Ce(III) ratio of 14%. This implies that the transformation of Ce(III) to Ce(IV) is time-dependent as reported by other researchers [23, 37, 38]. Hydrogen peroxide (H_2O_2) as an oxidising agent can be responsible for the Ce(III)-to-Ce(IV) transformation as its presence has recently been shown as a consequence of oxygen reduction [39]. Besides, the oxidation of Ce(III) can take place directly over the Cu-rich particle where the solution pH and potential can be high enough; mind the E-pH diagram for cerium [25].

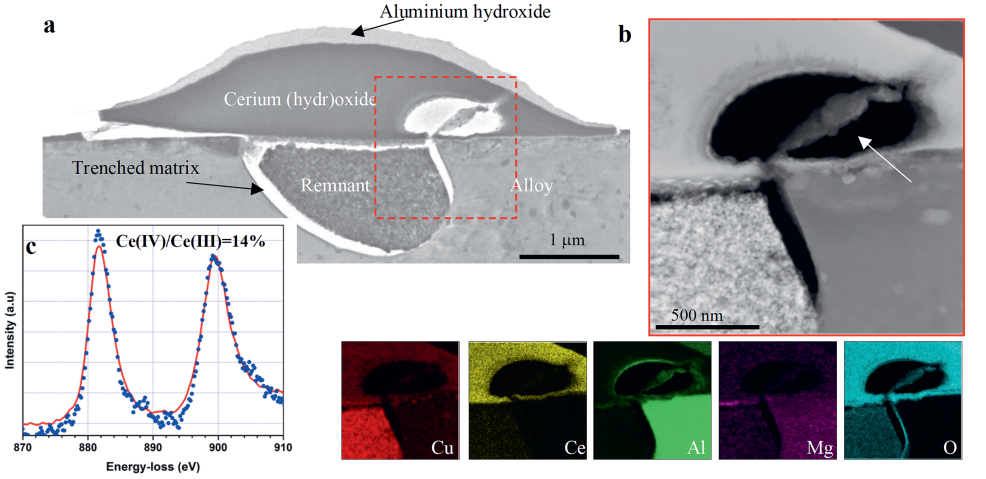


Fig. 9.7. Post-mortem analysis of exposed S-phase particles after 24 h. (a) Cross-sectional TEM image of an Al_2CuMg particle on an AA2024-T3 sheet exposed to 0.01 M NaCl + 0.003 M $Ce(NO_3)_3$. (b) STEM/EDS analysis of the rectangular region shown in Fig. 9.7a. The white arrow shows the corrosion products while leaving the trenched area. (c) EEL-spectrum collected from the particle; the red curve represents the MLLS fitting to the experimental dots. A Ce(IV)/Ce(III) ratio of 14% was estimated by the MLLS fitting of experimental dots.

Fig. 9.8 shows the FIB/SEM 3D reconstruction of an S-phase particle on an AA2024-T3 exposed for 24 h. Fig. 9.8a reveals a buried S-phase remnant and its adjacent alloy matrix covered by a thick layer of cerium (hydr)oxide layer. The location at which the breakdown has occurred is indicated from side- and bottom-view by the white and black arrows in Fig. 9.8b and c, respectively. Top-view 3D reconstruction when the cerium-based cap is removed reveals the circumferential corrosion of the alloy matrix surrounding a dealloyed S-phase remnant (Fig. 9.8d). As evident in Fig. 9.8e, the corrosion pit is left behind as a consequence of the alloy matrix trenching. This implies although the S-phase particles are mostly buried under a thick layer of cerium (hydr)oxide, dealloying and trenching corrosion take place underneath and eventually result in pitting corrosion.

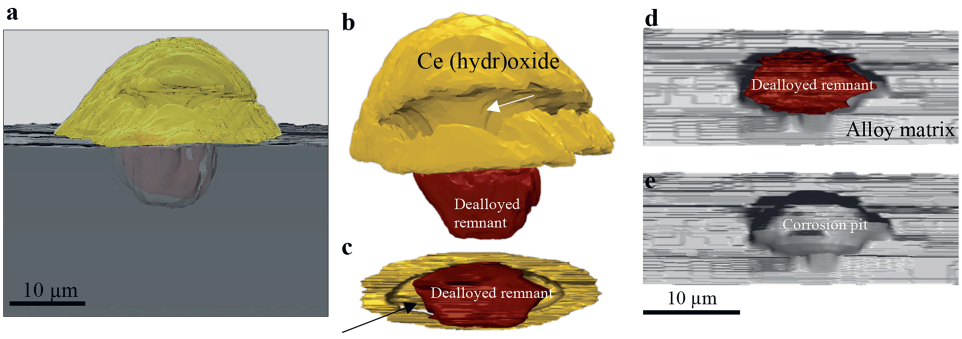


Fig. 9.8. 3D FIB/SEM reconstruction of a S-phase particle after 24 h. (a) 3D reconstruction of the full system including the dealloyed particle, cerium (hydr)oxide precipitate and adjacent alloy matrix. (b) 3D reconstruction from the side-view when the alloy matrix is removed. The white arrow shows the ruptured part of the cerium-based cap. (c) 3D reconstruction from bottom-view when the alloy matrix is removed. The black arrow shows the ruptured part of the cerium-based cap. (d) Top-view 3D reconstruction when the cerium-based cap is removed. (e) Top-view 3D reconstruction when both the cerium (hydr)oxide layer and dealloyed particle are removed, revealing the corrosion pit formed as a consequence of the alloy matrix trenching.

θ-phase (Al_2Cu). —Ex-situ analytical TEM analysis was performed on individual θ-phase particles in AA2024-T3 sheets exposed for different exposure times. Fig. 9.9 shows an Al_2Cu particle exposed to 0.01 M NaCl + 0.003 M $Ce(NO_3)_3$ for 6 h. The top-view SEM reveals several bright spots discretely on the particle; however, there is no indication of significant cerium precipitation at this stage. The STEM/EDS analysis of the corresponding cross-section along the red dashed line reveals local precipitation of cerium on this particle. In fact, we observe cerium precipitation merely and discretely at Cu-rich locations on the particle. Here, the EDS analysis identifies the hills on the particle as $Al(OH)_3$ where the copper aggregates are formed in close vicinity (mind the elemental maps). As we have recently reported, corrosion initiates at θ-phase particles as a direct consequence of dealloying, leading to selective dissolution of aluminium and accumulation of copper [33]. In fact, the Cu-rich regions are potential cathodic sites around which an alkaline local solution chemistry is expected, triggering the cerium precipitation.

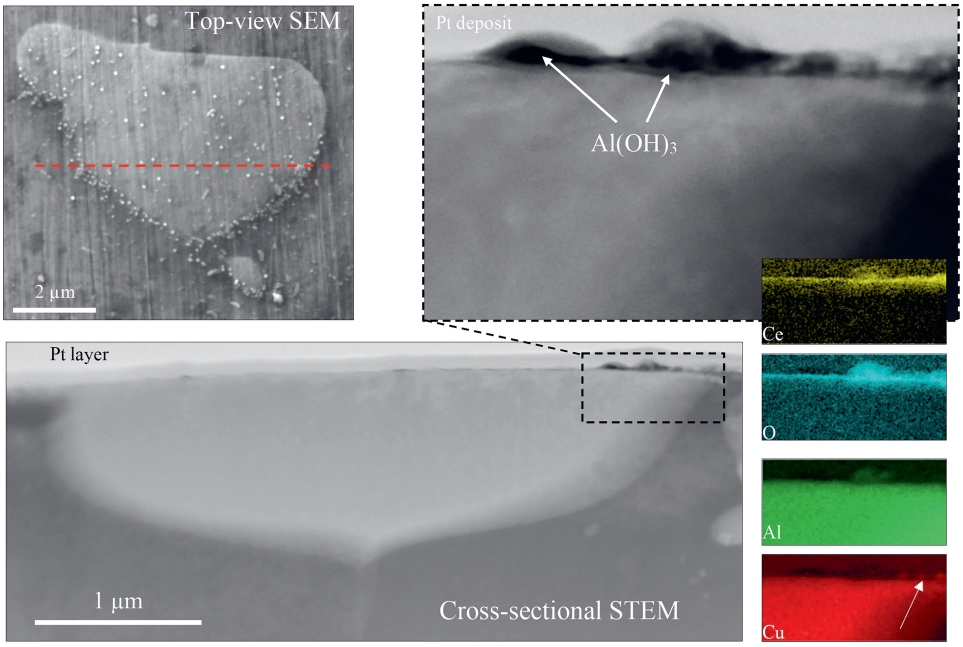


Fig. 9.9. Post-mortem analysis of exposed θ-phase particles after 6 h. Top-view SEM and cross-sectional STEM/EDS analysis of an Al_2Cu particle on an AA2024-T3 sheet exposed to 0.01 M NaCl + 0.003 M $Ce(NO_3)_3$. The elemental maps correspond to the rectangular region shown in the STEM image. The cross-section has been fabricated with FIB; mind that there is a Pt layer deposited to protect the particle from Ga damage while milling.

Prolonged exposure for 24 h comes along with a clear change in the top-view morphology of θ-phase particles. The top-view SEM image shown in Fig. 9.10 reveals a nodular layer on an Al_2Cu particle. The cross-sectional STEM/EDS analysis shows that the hills are in fact $Al(OH)_3$. A closer look at those regions reveals that they are formed merely in close vicinity of the dealloyed segments of the particle. The STEM image shows the occurrence of dealloying gradually penetrating in depth. This is well clear in the elemental maps, proving selective dissolution of aluminium and local precipitation of cerium.

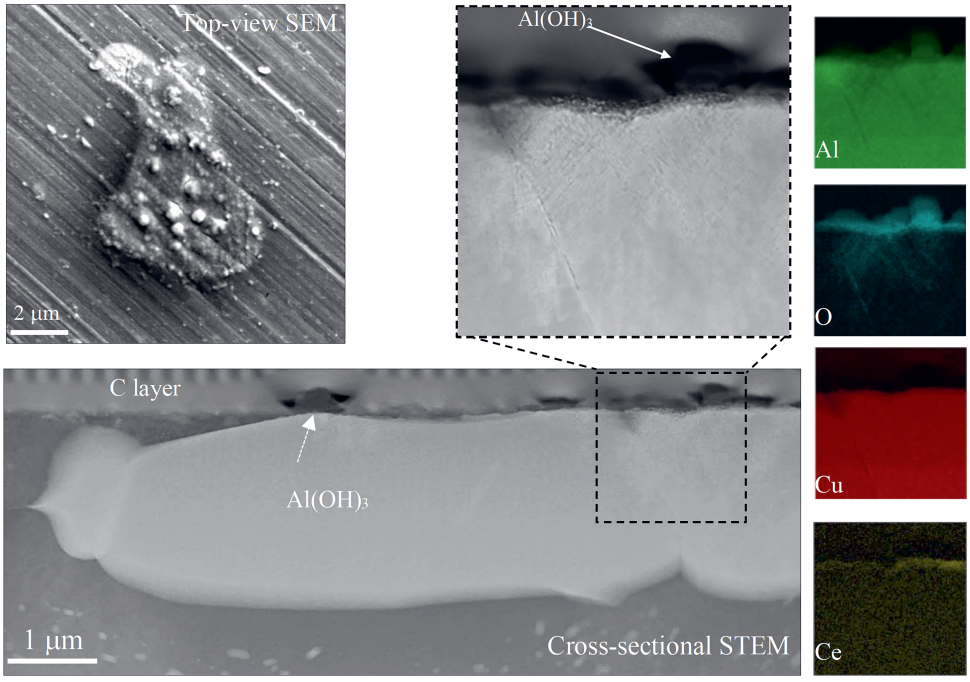


Fig. 9.10. Post-mortem analysis of exposed θ-phase particles after 24 h. Top-view SEM and cross-sectional STEM/EDS analysis of an Al_2Cu particle on an AA2024-T3 sheet exposed to 0.01 M NaCl + 0.003 M $Ce(NO_3)_3$. The elemental maps correspond to the rectangular region shown in the STEM image. The cross-section has been fabricated with FIB; mind that there is a C layer deposited to protect the particle from Ga damage while milling.

A coarse nodular morphology is observed once θ-phase particles are exposed for a longer exposure time (i.e., 96 h). In Fig. 9.11, the top-view SEM image shows a covered Al_2Cu particle surrounded by a trench with a tight opening. The cross-sectional STEM image reveals a nano-porous morphology caused by dealloying where the adjacent alloy matrix has been fully trenched. The EDS analysis shows that the particle is depleted in aluminium while a thin mixed layer of cerium (hydr)oxide and aluminium (hydr)oxide is observed on the top. The Ce(IV)/Ce(III) ratio of 8% within the deposit is estimated by MLLS fitting of the collected spectrum. Compared to S-phase, the cerium deposit is rather thin on the θ-phase particle. Like for S-phase, it seems that cerium cannot inhibit dealloying of Al_2Cu particles and dealloying eventually occurs to both phases. As we recently reported, dealloying of θ-phase takes place over a longer time of exposure as it is electrochemically more stable than S-phase [33]. Here, the faster dealloying probably leads to a higher rate of cerium precipitation. In fact, the dealloying rate seems to be accountable for establishing the required local chemistry required for cerium precipitation; this phenomenon will be discussed later.

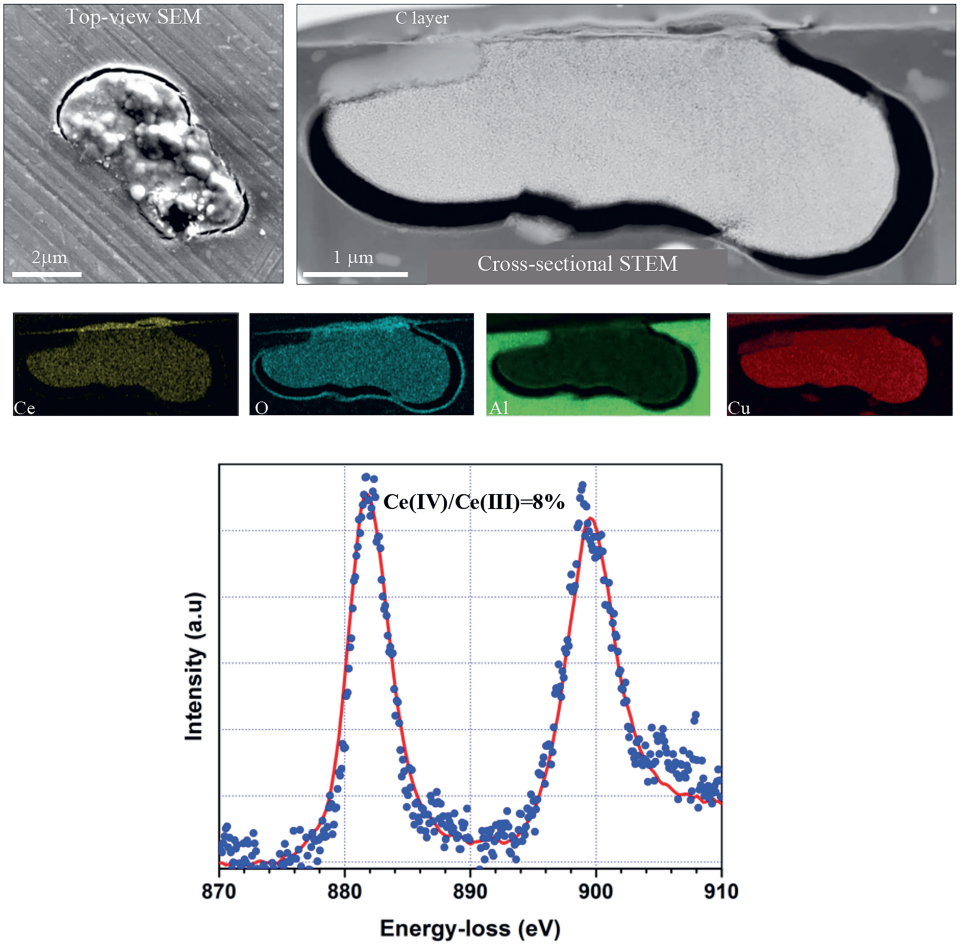


Fig. 9.11. Post-mortem analysis of exposed θ-phase particles after 96 h. Top-view SEM and cross-sectional STEM/EDS analysis of an Al_2Cu particle on an AA2024-T3 sheet exposed to 0.01 M NaCl + 0.003 M $Ce(NO_3)_3$. The graph is the EEL-spectrum collected from the particle; the red curve represents the MLLS fitting to the experimental dots. A Ce(IV)/Ce(III) ratio of 8% was estimated by the MLLS fitting of experimental dots.

Constituent phases ($Al_7Cu_2Fe(Mn)$, $Al_{76}Cu_6Fe_7Mn_5Si_6$). —We studied a variety of particles at exposure times of 1.5, 6 and 24 h and mostly no indication of cerium interaction with the constituent phases was found (see Supplementary Materials). However, our quasi in-situ investigations showed that the constituent phases might respond differently to the cerium-containing solution during the exposure. In fact, we detected cerium merely on constituent phase particles that have accommodated redeposited Cu nanoparticles. Otherwise, they show no interaction with the cerium-inhibited solutions in short periods of exposure. For instance, Fig. 9.12a shows quasi in-situ TEM/EFTEM-EELS analysis of an $Al_7Cu_2Fe(Mn)$ particle in an argon ion-milled thin specimen. After 30 min of exposure, we see the

appearance of the nanoparticles, identified as elemental copper, on this particle, leading to a slight cerium precipitation. Besides, the EELS analysis shows a Ce(IV)/Ce(III) ratio of 0 at this stage. A closer look at these Cu nanoparticles is shown in Fig. 9.12b. With prolonged exposure until 90 min, we see the nanoparticles slightly growing in size and number and this is associated with slightly more Ce(III) deposited on the particle. After total exposure of 150 min, the particle has been analysed using STEM/EDS, clearly showing the presence of the Cu nanoparticles (Fig. 9.12c). As expected, the elemental map shows some cerium deposited on the particle around Cu-rich regions. In addition, there are regions on the particle depleted in aluminium, implying the occurrence of dealloying. In a prior work [33], we have shown that the redeposited Cu nanoparticles commonly originate from the undercut S-phase particles, speeding up the dealloying of constituent phases. In should be noted the Cu redeposition takes place on some of the constituent phases even in the uninhibited solutions (see Supplementary Materials).

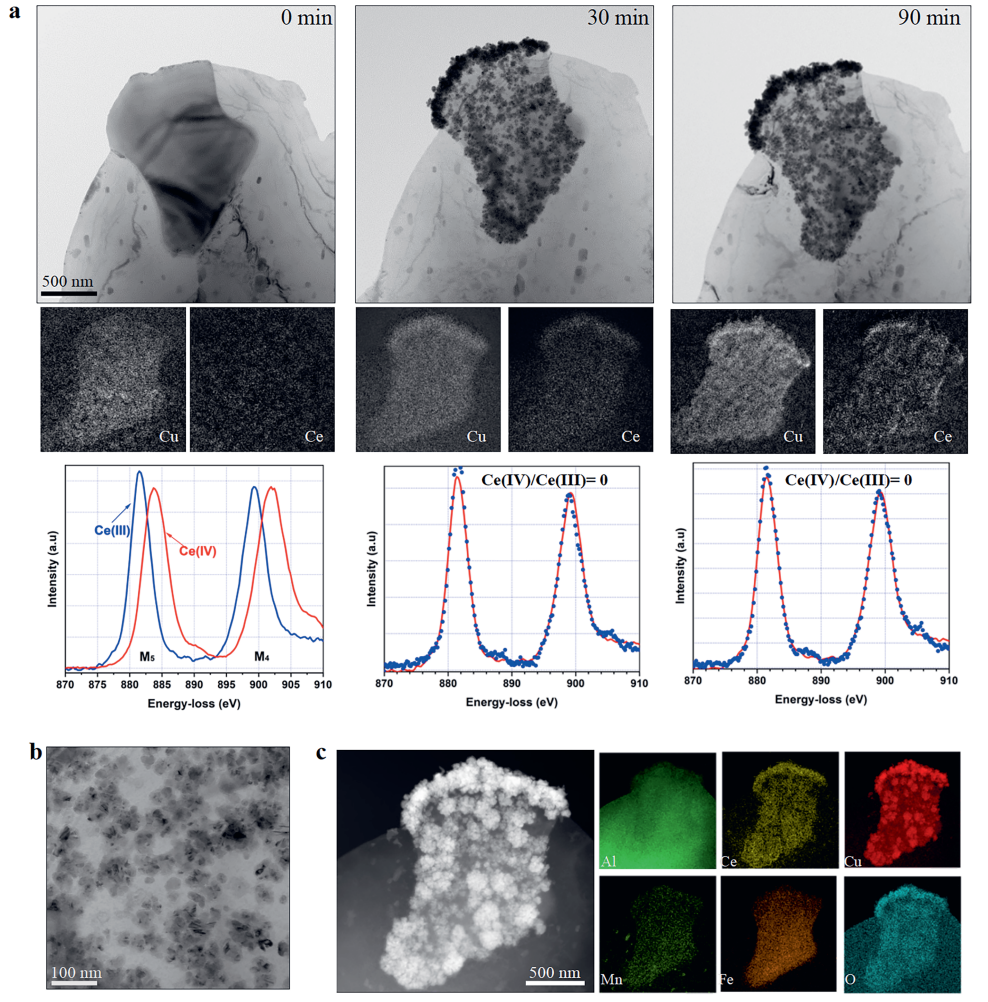


Fig. 9.12. Quasi in-situ studies of Al_7Cu_2Fe(Mn) inhibition. (a) Quasi in-situ TEM/EFTEM-EELS study of an Al_7Cu_2Fe(Mn) particle exposed to 0.01 NaCl+ 0.003 $Ce(NO_3)_3$ at different exposure times. EELS spectra were collected from the particle at each exposure time. Cerium and copper were mapped using energy-filtering the corresponding edges in the EELS spectra. The graphs at 0 min exposure are reference spectra of Ce(III) and Ce(IV). The collected spectra were MLLS fitted to the reference spectra. (b) A closer look at the particle after 30 min exposure shows the redeposited Cu nanoparticles. These particles can accelerate de-alloying of the particle so that the environment reach enough alkalinity for Ce precipitation. (c) STEM/EDS image of the particle after 150 min clearly proves the presence of cerium oxide islands around the Cu nanoparticles.

Further investigations were carried out ex-situ on a variety of particles at exposure times of 1.5, 6, 24 and 96 h. Typically, cerium does not interact with the constituent phases in short periods of exposure in the absence of the redeposited Cu nanoparticles (see Supplementary Materials). For instance, Fig. 9.13 shows an Al_7Cu_2Fe(Mn) particle exposed to 0.01 M NaCl + 0.003 M $Ce(NO_3)_3$ for 96 h. The top-

view SEM image shows regions having a brighter contrast on the particle whilst no circumferential trenching is observed. The cross-sectional STEM image reveals a few hills identified as $Al(OH)_3$ on the particle. Given the STEM/EDS analysis, we see that the particle has slightly been dealloyed on the top, causing the formation of a thin Cu-rich layer (see the Cu map). The interesting point is that cerium has been discretely deposited at the dealloyed locations.

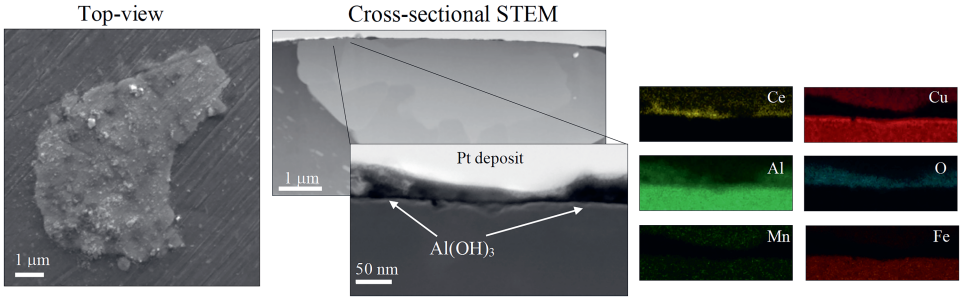


Fig. 9.13. Post-mortem analysis of exposed $Al_7Cu_2Fe(Mn)$ particles after 96 h. Top-view SEM and cross-sectional STEM/EDS analysis of an $Al_7Cu_2Fe(Mn)$ particle on an AA2024-T3 sheet exposed to 0.01 M NaCl + 0.003 M $Ce(NO_3)_3$. The elemental maps correspond to the rectangular region shown in the STEM image. The cross-section has been fabricated with FIB; mind that there is a Pt layer deposited to protect the particle from Ga damage while milling.

We have also found $Al_7Cu_2Fe(Mn)$ particles that are covered uniformly with a thin layer of cerium (hydr)oxide. Fig. 9.14 shows the top-view morphology of an $Al_7Cu_2Fe(Mn)$ particle with the bright spots all over the particle. Our analysis identified them as copper nano-particles or -clusters deposited mostly on the particle and slightly over the alloy matrix. The cerium map superimposed on the cross-sectional STEM image shows a thin uniform layer of cerium (hydr)oxide on this particle. Interestingly, cerium precipitation is observed at the Cu-rich locations on the alloy matrix as well. The magnified STEM/EDS analysis of the rectangular region clearly reveals that the top surface of the particle has slightly been dealloyed and this is associated with a uniform cerium precipitation. This is consistent with quasi in-situ TEM results, implying a role of Cu nanoparticles in enhancing cerium precipitation.

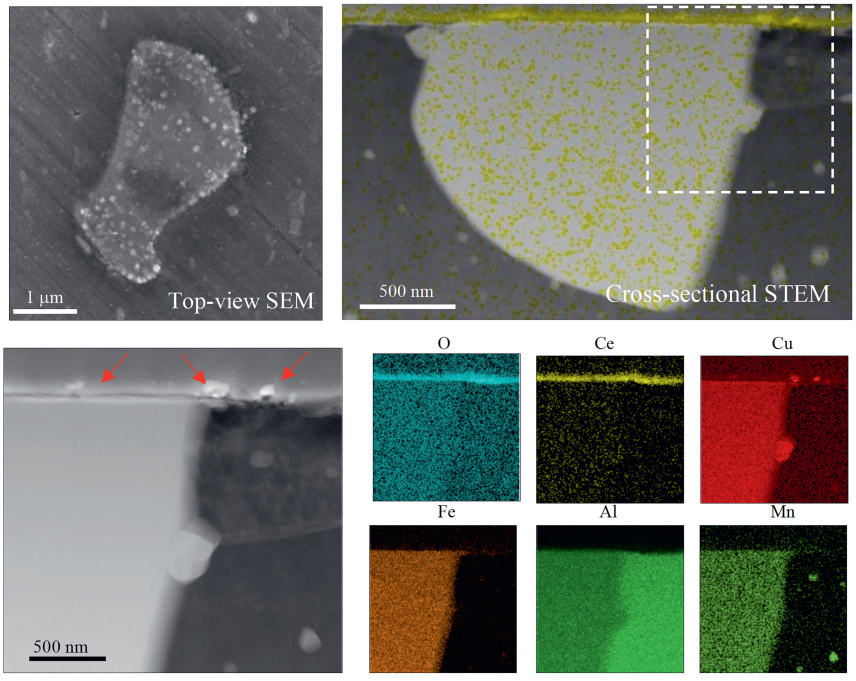


Fig. 9.14. Post-mortem analysis of exposed $Al_7Cu_2Fe(Mn)$ particles after 96 h. Top-view SEM and cross-sectional STEM/EDS analysis of an $Al_7Cu_2Fe(Mn)$ particle on an AA2024-T3 sheet exposed to 0.01 M NaCl + 0.003 M $Ce(NO_3)_3$. The cerium map is superimposed on the STEM image. The elemental maps correspond to the rectangular region shown in the STEM image. The white arrow indicate the Cu nanoparticles deposited on the $Al_7Cu_2Fe(Mn)$ particle and its adjacent matrix. These Cu nanoparticles cause an enhanced cerium deposition. The cross-section has been fabricated with FIB; mind that there is a C layer deposited to protect the particle from Ga damage while milling.

Fig. 9.15 shows an $Al_{76}Cu_6Fe_7Mn_5Si_6$ particle on a AA2024 exposed for 96 h. The SEM image reveals bright spot on the particle, although no sign of corrosion attack to its adjacent matrix. Our cross-sectional TEM evaluation reveals that this particle has not interacted with cerium-inhibited solution (Fig. 9.15b). A closer look at the particle shown in Fig. 9.15c shows that although the particle has been slightly dealloyed, no cerium peak shows up in the collected EDS spectrum. In fact, $Al_{76}Cu_6Fe_7Mn_5Si_6$ particles are stable phases that sluggishly undergo dealloying during the exposure. Thus, the rate of dealloying surely seems to have an impact on local solution chemistry which drives the cerium precipitation. This phenomenon will be discussed in the next section.

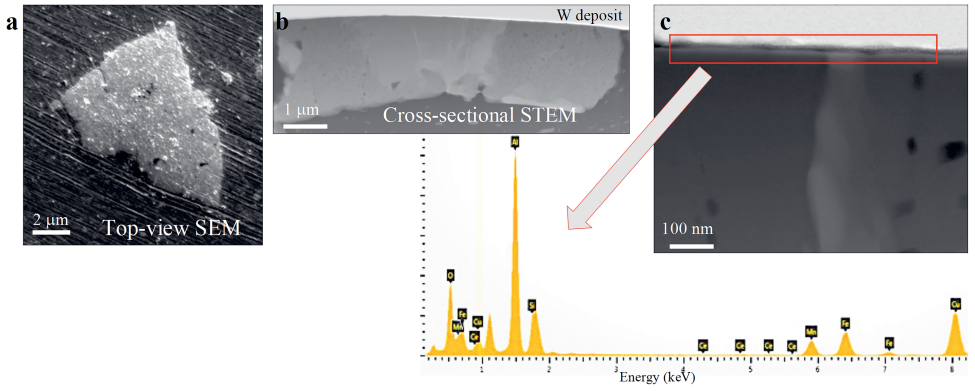


Fig. 9.15. Post-mortem analysis of exposed $Al_{76}Cu_6Fe_7Mn_5Si_6$ particles after 96 h. (a) Top-view SEM and (b) cross-sectional STEM analysis of an $Al_{76}Cu_6Fe_7Mn_5Si_6$ particle on an AA2024-T3 sheet exposed to 0.01 M NaCl + 0.003 M $Ce(NO_3)_3$. (c) The STEM image shows a closer look at the top part of the particle which has slightly been dealloyed. The EDS map collected from the rectangular region shows that no cerium has been precipitated on this particle.

9.4. Local corrosion inhibition mechanism by cerium-based inhibitors

Conventionally, microgalvanic coupling established between isolated IMPs and their surrounding matrix has been proposed as the main cause of local corrosion in aluminium alloys [40, 41]. We have recently reported that IMPs are in fact active phases that undergo initial dealloying regardless of their cathodic and anodic types while the microgalvanic coupling takes place between the dealloyed parts of an IMP and its surrounding alloy matrix at moderate stages [33, 34]. This phenomenon in turn drives local corrosion and further promotes the local solution chemistry around the IMPs. Here, we observed that dealloying is the root cause of cerium precipitation and not microgalvanic coupling. Actually, nanogalvanic coupling within the corroding IMPs induces a local solution chemistry that leads to local cerium precipitation. However, the approach used in this study is unable of determining how alkaline the solution chemistry is around different IMPs. Nevertheless, we know that cerium precipitation can only occur on IMPs when the local pH is sufficiently alkaline. For Al_2CuMg particles, the local solution chemistry is probably strongly alkaline as we observe a high rate of precipitation. Besides, if the dealloying stops at some points owing to the cerium-based layer, the local pH decreases and no further precipitation would take place which is the case for constituent phases. In addition, relatively slow but ongoing dealloying happens to Al_2Cu particles where the particles of relevance are found to be fully dealloyed but covered with a thin layer of cerium (hydr)oxide. Thus, individual intermetallic particles can experience different local solution chemistry and local corrosion potential that will surely affect the Ce(IV)/Ce(III) ratio as well. For S-phase, stronger local alkalinity and higher corrosion potential due to dealloying can lead to a higher Ce(IV)/Ce(III) ratio, compared to other intermetallic phases. Furthermore, the oxidation of Ce(III) to Ce(IV) by H_2O_2 is time-dependent; therefore for Al_2Cu and

constituent phase intermetallic particles which get involved in the cerium deposition process later, a lower Ce(IV)/Ce(III) ratio can be considered reasonable. We further discuss the impact of cerium precipitation on morphological and compositional evolutions of different individual intermetallic phases.

9.4.1. Inhibition mechanism of S-phase—Al_2CuMg particles are highly active and undergo dealloying at a relatively fast rate [33]. The initial selective dissolution of aluminium and magnesium results in the formation of copper rich regions on the S-phase particles that can support cathodic reactions through a nanogalvanic coupling. This phenomenon gradually established a very local alkalinity that is required for cerium precipitation. We have already proved that all the anodic and cathodic reaction will take place on one single particle at early stages [33]. At this stage, the cerium precipitation cannot inhibit dealloying and it progressively propagates into the depth. At moderate stages, the S-phase particle still endures dealloying while oxygen evolution as the cathodic reaction takes place on the Cu-rich top of the particle [42]. This leads to a precipitation of a thick but porous cerium cap over the particle and its adjacent alloy matrix. It should be noted the cerium (hydr)oxides may have relatively low electrical conductivity and the cathodic reaction has to happen beneath the cerium layer.

As the dealloying further penetrates into the particle, the adjacent alloy matrix also gets involved in the process and starts to dissolve circumferentially. Unlike the top part of the particle, there is an acidic environment established in depth due to metal hydrolysis. In such an environment, aluminium and magnesium are soluble species in water, releasing from the particle and its surrounding matrix. This increasingly leads to the accumulation of corrosion products underneath the cerium precipitate, causing internal pressure. Thus, this gives rise to rupture or partial dissolution of the cerium deposit since cerium (hydr)oxides are thermodynamically unstable in acidic pH values [25]. As soon as the rupture occurs, the soluble species would be released from the trench. Mg ions would diffuse away as they are still soluble in the bulk solution pH. However, Al ions would precipitate as $Al(OH)_3$, covering the cerium precipitate. However, the corrosion still continues to dissolve the surrounding alloy matrix until undercutting the corroding particle. That the S-phase, if covered with the cerium layer, can still liberate some Cu ions into the environment through the ruptured regions of the precipitate. Besides, the undercut might fall out and leave behind surface corrosion pits. During the first 24 h, the electrochemical response of the system is mainly linked to S-phase evolutions. In fact, both the copper enrichment and cerium precipitation cause an increase in OCP and LPR values up to 24 h (see Fig. 9.1a). Fig. 9.16 schematically shows different stages of cerium interaction with S-phase particles.

9.4.2. Inhibition mechanism of θ-phase—Al_2Cu is also an unstable phase that undergoes dealloying but at a slower rate compared to S-phase. Since dealloying is the main reason of the local solution chemistry establishment, the cerium precipitation rate is rather low on θ-phase particles. In fact, the corrosion initiates by dealloying attack at several locations on an Al_2Cu particle, resulting in the formation $Al(OH)_3$ islands. Furthermore, the Cu-rich islands support cathodic reactions which leads to

a local alkalinity required for cerium precipitation. However, since the process progress sluggishly, the precipitation rate is rather low compared to S-phase. As time elapses, the $Al(OH)_3$ islands are covered with cerium (hydr)oxide, causing the particle to appear in a coarse nodular morphology. At moderate stages of inhibition, the dealloying continues to penetrate into the particle and this is associated with the corrosion of the adjacent alloy matrix. At this stage, the underlying corrosion speeds up a bit and the top part of the particle is responsible for accommodating cathodic reactions. This gives rise to an enhanced local alkalinity on the particle which increase the cerium precipitation rate. The process proceeds further until ending up with an undercut particle which is covered with a thin layer of cerium (hydr)oxide and aluminium hydroxide. It should be mentioned that the whole process from initiation to undercutting takes longer as compared to that for S-phase particles.

9.4.3. Inhibition mechanism of constituent phases—$Al_7Cu_2Fe(Mn)$ and $Al_{76}Cu_6Fe_7Mn_5Si_6$ are highly stable phases in the studied cerium-inhibited solution. The latter does not interact with the cerium during a 96-h exposure as it gets slightly dealloyed over a long-term exposure and this cannot induce the required alkalinity for cerium precipitation. However, $Al_7Cu_2Fe(Mn)$ is less stable and it endures the dealloying attack and selective dissolution of aluminium, leading to the formation of $Al(OH)_3$ piles on the particles. At moderate stages of exposure, this comes along with the discrete precipitation of cerium at the dealloyed locations. However, some $Al_7Cu_2Fe(Mn)$ particles can endure a transition due to the copper reprecipitation process. In fact, those particles that are located in the vicinity of S-phase particles may accommodate the released Cu ions. The phenomenon can lead to an accelerated dealloying which establishes a uniform local chemistry over the corroding particle. The covered particle is well protected as it is firstly stable and secondly buried under a thin layer of cerium (hydr)oxide, enhancing the electrochemical stability of constituent phase. This process is schematically shown in Fig. 9.16. It should be mentioned that the interaction of cerium with θ-phase and constituent phases happens rather slow with time; that is why the system evolves slowly and reveals a nearly stable electrochemical response after 24 h of exposure.

9.5. Conclusions

We studied the interaction of cerium nitrate with different intermetallic phases in AA2024-T3 using electrochemical evaluations and also quasi in-situ and ex-situ analytical TEM at different exposure times up to 96 h. We directly evidenced microstructural evolutions of the isolated IMPs during interaction with the inhibited solution. We observed the pivotal role of dealloying in establishing the basic local solution chemistry which triggers cerium precipitation. We here confirm that IMPs, regardless of their conventional categorisation, are in fact simultaneous anodes and cathodes as from the beginning of exposure. The dealloying is the main factor steering the precipitation rate of cerium: the faster it happens the more cerium precipitates. The Cu-rich regions resulting from selective

dissolution of active elements like magnesium and aluminium support cathodic reactions leading to a local alkalinity.

Al_2CuMg as the most unstable phase is found to be covered with a rather thick cerium-based deposit layer. It is established during several stages of interaction with the cerium-inhibited solution. The cerium in fact cannot inhibit dealloying of the S-phase but can delay the process and mitigate the Cu reprecipitation. The precipitation of cerium takes place on S-phase from the beginning of exposure and no nobility inversion happens. As long as the dealloying propagates into depth, the top Cu-rich part of the corroding particles support cathodic reaction, generating the required alkalinity for cerium precipitation. The rupture of the cerium cap is a phenomenon that occurs at moderate stages of exposure due to the underlying corrosion.

Al_2Cu particles also undergo dealloying in the cerium-containing solution, however a sluggish rate of dealloying results in less cerium precipitation compared to that for S-phase particles. Besides, the corrosion of Al_2Cu particles in cerium-containing solution ends up with an undercut dealloyed remnant which is covered with a thin mixed layer of cerium and aluminium (hydr)oxides. Constituent phases are very stable in the solution and slightly endure dealloying over a long-term exposure. $Al_7Cu_2Fe(Mn)$ particles are found either discretely or fully covered with a thin cerium-based layer at prolonged exposure times. The latter is caused by the redeposited copper nanoparticles that accelerate the dealloying rate, effectively enhancing the cerium precipitation. $Al_{76}Cu_6Fe_7Mn_5Si_6$ particles, if slightly dealloyed, do not interact with cerium. The cerium deposit can be a mixture of Ce(IV) and Ce(III) oxides as the valence transformation happens with prolonged exposure time. This phenomenon was linked to an oxidising reaction either due to the presence of H_2O_2 or happing on Cu-rich regions of the corroding IMPs. The early electrochemical response (i.e., the first 24 h) of the systems is attributed merely to the morphological and compositional evolutions of S-phase particles, leading to the elevated OCP and LPR values. After 24 h, AA2024-T3 system experiences a stabilised condition due to sluggish evolutions of Al_2Cu and constituent phase particles after 24 h of exposure.

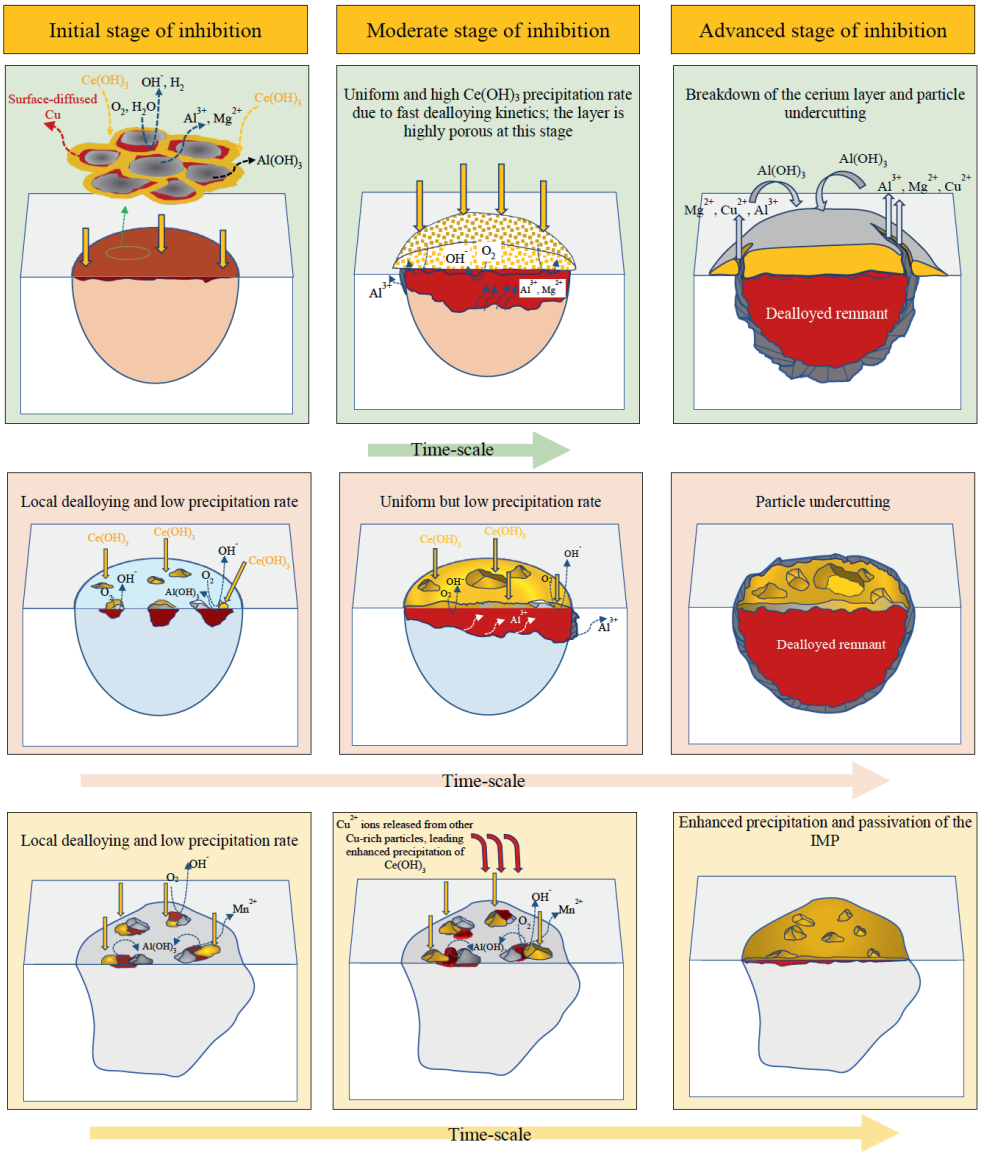


Fig. 9.16. Dealloying-driven cerium deposition on IMPs in AAs. 3D schematic view of mechanism of cerium precipitation mechanisms on individual S-phase (boxed in green; upper row), θ-phase (boxed in pink; middle row) and $Al_7Cu_2Fe(Mn)$ constituent phase (boxed in yellow; lower row) embedded in the alloy matrix. The mechanisms by which the cerium precipitates on IMPs along with the probable corrosion reactions occurring at IMPs are depicted in detail.

References

[1] A.E. Hughes, N. Birbilis, J.M. Mol, S.J. Garcia, X. Zhou, G.E. Thompson, High strength Al-alloys: microstructure, corrosion and principles of protection, Recent Trends in Processing and Degradation of Aluminium Alloys, Recent Trends in Processing and Degradation of Aluminium Alloys, ed. Z. Ahmad, 1 (2011) 223.
[2] C. Örnek, C. Leygraf, J. Pan, Real-Time Corrosion Monitoring of Aluminum Alloy Using Scanning Kelvin Probe Force Microscopy, Journal of The Electrochemical Society, 167 (2020) 081502.
[3] A. Boag, A. Hughes, A. Glenn, T. Muster, D. McCulloch, Corrosion of AA2024-T3 Part I: Localised corrosion of isolated IM particles, Corrosion Science, 53 (2011) 17-26.
[4] N. Birbilis, R. Buchheit, Investigation and discussion of characteristics for intermetallic phases common to aluminum alloys as a function of solution pH, Journal of the Electrochemical Society, 155 (2008) C117.
[5] N. Birbilis, R.G. Buchheit, Electrochemical characteristics of intermetallic phases in aluminum alloys: an experimental survey and discussion, Journal of the Electrochemical Society, 152 (2005) B140.
[6] Y. Zhu, K. Sun, G. Frankel, Intermetallic phases in aluminum alloys and their roles in localized corrosion, Journal of The Electrochemical Society, 165 (2018) C807.
[7] R. Buchheit, M. Martinez, L. Montes, Evidence for Cu ion formation by dissolution and dealloying the Al2CuMg intermetallic compound in rotating ring-disk collection experiments, Journal of the Electrochemical Society, 147 (2000) 119.
[8] G.S. Frankel, R.L. McCreery, Inhibition of Al alloy corrosion by chromates, Interface-Electrochemical Society, 10 (2001) 34-39.
[9] M. Kendig, R. Buchheit, Corrosion inhibition of aluminum and aluminum alloys by soluble chromates, chromate coatings, and chromate-free coatings, Corrosion, 59 (2003) 379-400.
[10] G. Ilevbare, J. Scully, J. Yuan, R. Kelly, Inhibition of pitting corrosion on aluminum alloy 2024-T3: effect of soluble chromate additions vs chromate conversion coating, Corrosion, 56 (2000) 227-242.
[11] O. Gharbi, S. Thomas, C. Smith, N. Birbilis, Chromate replacement: what does the future hold?, npj Materials Degradation, 2 (2018) 1-8.
[12] N. Birbilis, R.G. Buchheit, D. Ho, M. Forsyth, Inhibition of AA2024-T3 on a phase-by-phase basis using an environmentally benign inhibitor, cerium dibutyl phosphate, Electrochemical and Solid State Letters, 8 (2005) C180.
[13] D. Ho, N. Brack, J. Scully, T. Markley, M. Forsyth, B. Hinton, Cerium dibutylphosphate as a corrosion inhibitor for AA2024-T3 aluminum alloys, Journal of the electrochemical society, 153 (2006) B392.
[14] A. Uhart, J.B. Ledeuil, D. Gonbeau, J.-C. Dupin, J.-P. Bonino, F. Ansart, J. Esteban, An Auger and XPS survey of cerium active corrosion protection for AA2024-T3 aluminum alloy, Applied Surface Science, 390 (2016) 751-759.
[15] M. Mouanga, F. Andreatta, M.-E. Druart, E. Marin, L. Fedrizzi, M.-G. Olivier, A localized approach to study the effect of cerium salts as cathodic inhibitor on iron/aluminum galvanic coupling, Corrosion Science, 90 (2015) 491-502.
[16] L. Kasten, J. Grant, N. Grebasch, N. Voevodin, F. Arnold, M. Donley, An XPS study of cerium dopants in sol–gel coatings for aluminum 2024-T3, Surface and Coatings Technology, 140 (2001) 11-15.
[17] D. Arnott, N. Ryan, B. Hinton, B. Sexton, A. Hughes, Auger and XPS studies of cerium corrosion inhibition on 7075 aluminum alloy, Applications of Surface Science, 22 (1985) 236-251.
[18] T. Hu, H. Shi, T. Wei, F. Liu, S. Fan, E.-H. Han, Cerium tartrate as a corrosion inhibitor for AA 2024-T3, Corrosion Science, 95 (2015) 152-161.
[19] T. Matsuda, K.B. Kashi, K. Fushimi, V.J. Gelling, Corrosion protection of epoxy coating with pH sensitive microcapsules encapsulating cerium nitrate, Corrosion Science, 148 (2019) 188-197.
[20] A. Hughes, T. Markley, S. Garcia, J. Mol, Comparative study of protection of AA 2024-T3 exposed to rare earth salts solutions, Corrosion Engineering, Science and Technology, 49 (2014) 674-687.
[21] A. Mishra, R. Balasubramaniam, Corrosion inhibition of aluminum alloy 6061 by rare earth chlorides, Corrosion, 63 (2007) 240-248.

[22] P. Rodič, I. Milošev, Corrosion inhibition of pure aluminium and alloys AA2024-T3 and AA7075-T6 by cerium (III) and cerium (IV) salts, Journal of The Electrochemical Society, 163 (2015) C85.
[23] H. Shi, E.-H. Han, F. Liu, Corrosion protection of aluminium alloy 2024-T3 in 0.05 M NaCl by cerium cinnamate, corrosion science, 53 (2011) 2374-2384.
[24] S. Garcia, T. Markley, J. Mol, A. Hughes, Unravelling the corrosion inhibition mechanisms of bi-functional inhibitors by EIS and SEM–EDS, Corrosion Science, 69 (2013) 346-358.
[25] S.A. Hayes, P. Yu, T.J. O'Keefe, M.J. O'Keefe, J.O. Stoffer, The Phase Stability of Cerium Species in Aqueous Systems: I. E-pH Diagram for the System, Journal of the Electrochemical Society, 149 (2002) C623.
[26] K.A. Yasakau, M.L. Zheludkevich, S.V. Lamaka, M.G. Ferreira, Mechanism of corrosion inhibition of AA2024 by rare-earth compounds, The Journal of Physical Chemistry B, 110 (2006) 5515-5528.
[27] L. Paussa, F. Andreatta, D. De Felicis, E. Bemporad, L. Fedrizzi, Investigation of AA2024-T3 surfaces modified by cerium compounds: a localized approach, Corrosion science, 78 (2014) 215-222.
[28] J. Li, B. Hurley, R. Buchheit, The Effect of $CeCl_3$ as an Inhibitor on the Localized Corrosion of AA2024-T3 as a Function of Temperature, Journal of The Electrochemical Society, 163 (2016) C845.
[29] A.J. Aldykewicz, H.S. Isaacs, A.J. Davenport, The Investigation of Cerium as a Cathodic Inhibitor for Aluminum-Copper Alloys, Journal of The Electrochemical Society, 142 (1995) 3342-3350.
[30] P. Campestrini, H. Terryn, A. Hovestad, J.H.W. de Wit, Formation of a cerium-based conversion coating on AA2024: relationship with the microstructure, Surface and Coatings Technology, 176 (2004) 365-381.
[31] M.L. Zheludkevich, R. Serra, M.F. Montemor, K.A. Yasakau, I.M.M. Salvado, M.G.S. Ferreira, Nanostructured sol–gel coatings doped with cerium nitrate as pre-treatments for AA2024-T3: Corrosion protection performance, Electrochimica Acta, 51 (2005) 208-217.
[32] N.C. Rosero-Navarro, M. Curioni, R. Bingham, A. Durán, M. Aparicio, R.A. Cottis, G.E. Thompson, Electrochemical techniques for practical evaluation of corrosion inhibitor effectiveness. Performance of cerium nitrate as corrosion inhibitor for AA2024T3 alloy, Corrosion Science, 52 (2010) 3356-3366.
[33] A. Kosari, H. Zandbergen, F. Tichelaar, P. Visser, P. Taheri, H. Terryn, J.M.C. Mol, In-situ nanoscopic observations of dealloying-driven local corrosion from surface initiation to in-depth propagation, Corrosion Science, 177 (2020) 108912.
[34] A. Kosari, F. Tichelaar, P. Visser, H. Zandbergen, H. Terryn, J.M.C. Mol, Dealloying-driven local corrosion by intermetallic constituent particles and dispersoids in aerospace aluminium alloys, Corrosion Science, 177 (2020) 108947.
[35] L.A.J. Garvie, P.R. Buseck, Determination of Ce^{4+}/Ce^{3+} in electron-beam-damaged CeO_2 by electron energy-loss spectroscopy, Journal of Physics and Chemistry of Solids, 60 (1999) 1943-1947.
[36] V.J. Keast, A.J. Scott, R. Brydson, D.B. Williams, J. Bruley, Electron energy-loss near-edge structure – a tool for the investigation of electronic structure on the nanometre scale, Journal of Microscopy, 203 (2001) 135-175.
[37] A. Davenport, H. Isaacs, M. Kendig, XANES investigation of the role of cerium compounds as corrosion inhibitors for aluminum, Corrosion Science, 32 (1991) 653-663.
[38] U. Tiringer, A. Durán, Y. Castro, I. Milošev, Self-healing effect of hybrid sol-gel coatings based on GPTMS, teos, SiO_2 nanoparticles and $Ce(NO_3)_3$ applied on aluminum alloy 7075-T6, Journal of the electrochemical society, 165 (2018) C213.
[39] T.K. Shruthi, G.M. Swain, Detection of H_2O_2 from the Reduction of Dissolved Oxygen on TCP-Coated AA2024-T3 : Impact on the Transient Formation of Cr(VI), Journal of The Electrochemical Society, 166 (2019) C3284-C3289.
[40] A. Hughes, A. Boag, A. Glenn, D. McCulloch, T. Muster, C. Ryan, C. Luo, X. Zhou, G. Thompson, Corrosion of AA2024-T3 Part II: Co-operative corrosion, Corrosion Science, 53 (2011) 27-39.
[41] N. Birbilis, T.H. Muster, R.G. Buchheit, Corrosion of Aluminum Alloys, in: P. Marcus (Ed.) Corrosion mechanisms in theory and practice, CRC press, 2011.
[42] T. Sata, M. Yoshimura, Some material properties of cerium sesquioxide, J. Ceram. Assoc. Japan, 76 (1968) 116-122.

Supplementary Materials for Chapter 9

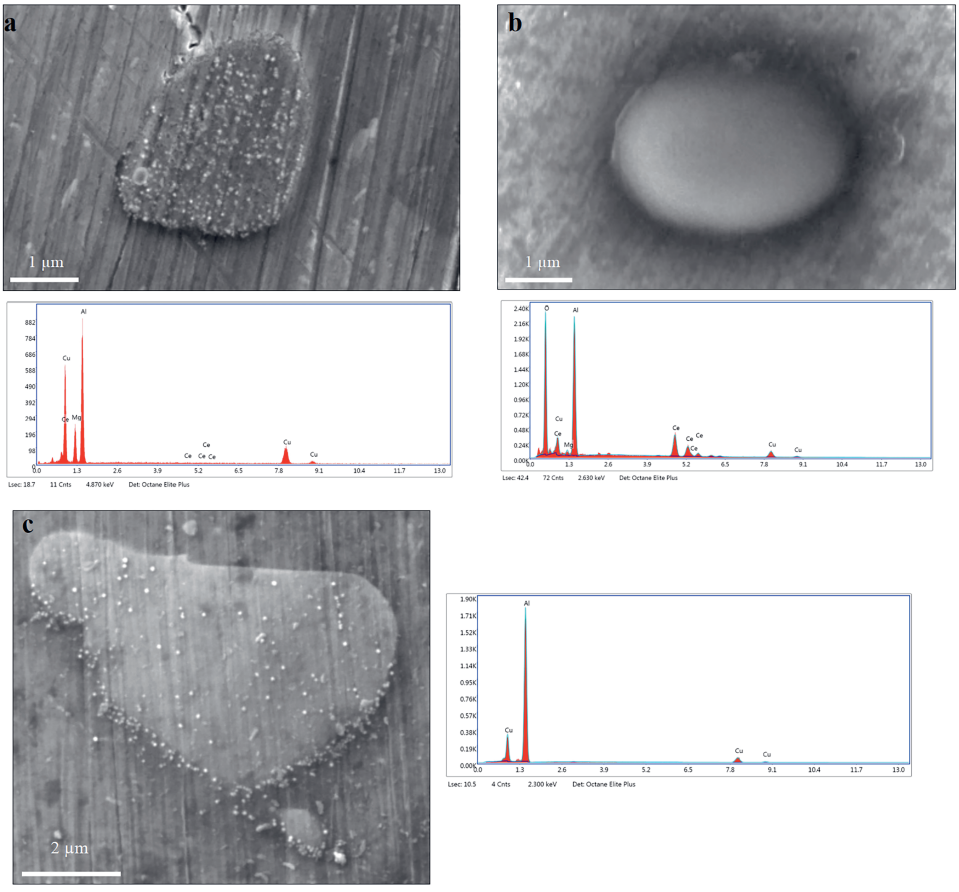


Fig. S9.1. SEM/EDS analysis of exposed particles exposed to 0.01 M NaCl + 0.003 M $Ce(NO_3)_3$ for different times. (a) S-phase after 1.5-h exposure, (b) S-phase after 6-h exposure and θ-phase particles after 6-h exposure.

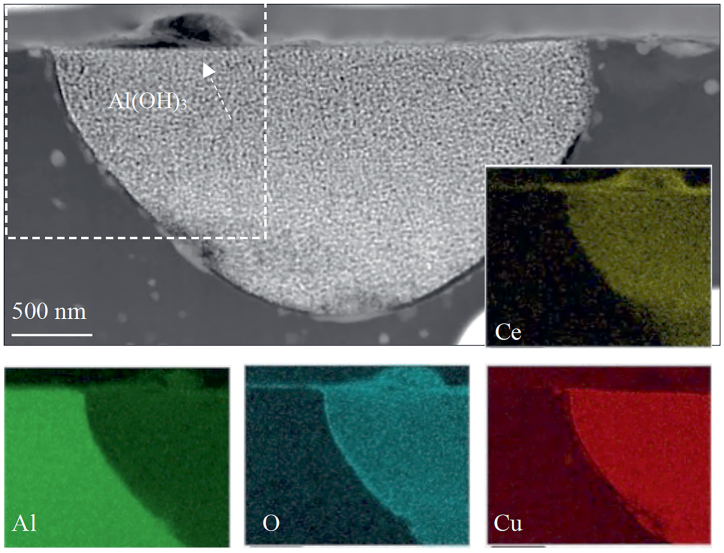


Fig. S9.2. Post-mortem analysis of exposed θ-phase particles after 96 h. Cross-sectional STEM/EDS analysis of an Al_2Cu particle on an AA2024-T3 sheet exposed to 0.01 M NaCl + 0.003 M $Ce(NO_3)_3$.

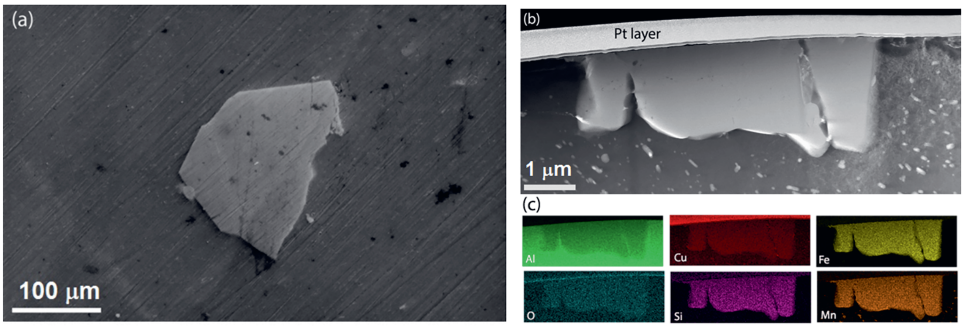


Fig. S9.3. Post-mortem analysis of exposed $Al_{76}Cu_6Fe_7Mn_5Si_6$ particles after 24 h. (a) Top-view SEM and (b) cross-sectional STEM/EDS analysis of the particle on an AA2024-T3 sheet exposed to 0.01 M NaCl + 0.003 M $Ce(NO_3)_3$. The elemental shows no cerium deposition at this stage.

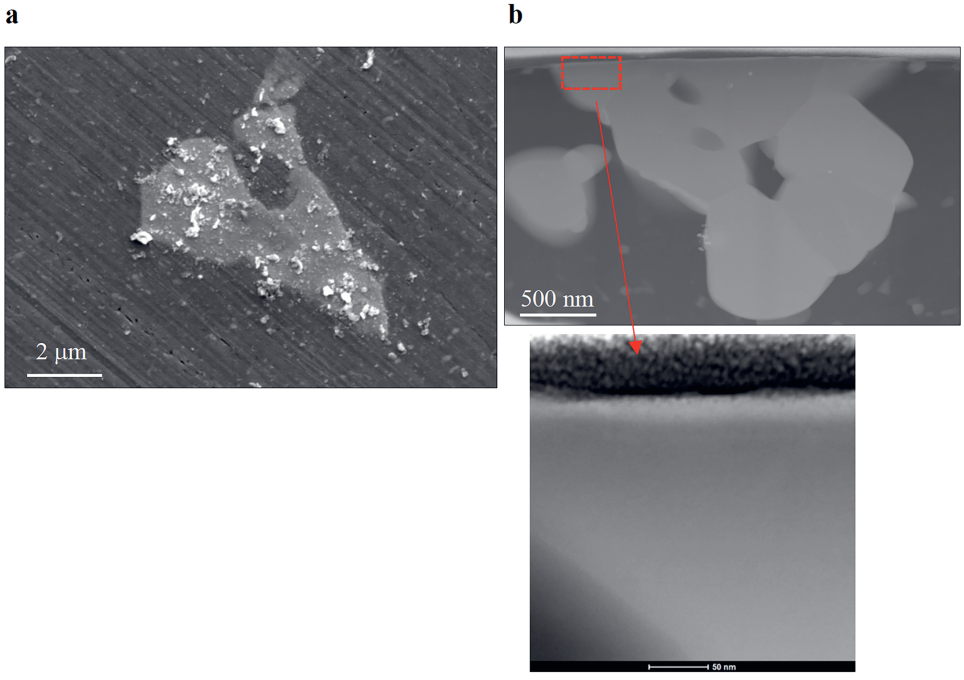


Fig. S9.4. Post-mortem analysis of exposed $Al_7Cu_2Fe(Mn)$ particles after 24 h. (a) Top-view SEM and (b) cross-sectional STEM analysis of an $Al_7Cu_2Fe(Mn)$ particle on an AA2024-T3 sheet exposed to 0.01 M NaCl + 0.003 M $Ce(NO_3)_3$. The inset is the magnified view of the red rectangular region, revealing no cerium precipitation on this particle.

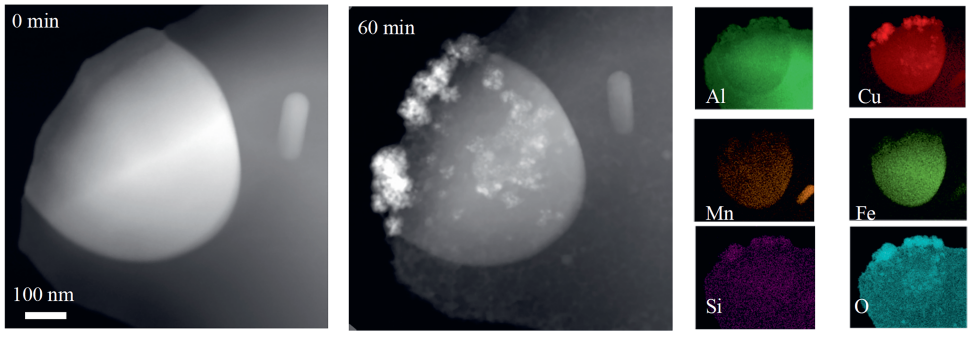


Fig. S9.5. Quasi in-situ studies of $Al_7Cu_2Fe(Mn)$ corrosion in 0.01 M NaCl. STEM images of an $Al_7Cu_2Fe(Mn)$ particle before and after 60 min of exposure. The corresponding EDS map of the particle after 60 reveals appearance of Cu aggregates on the particle. This copper is released from the corroded S-phase particles. The specimen is an Ar ion-milled 3-mm disk.

CHAPTER 10

CONCLUSIONS

10.1. Introduction

Intermetallic phases (IMPs) contribute to both the enhanced mechanical strength and the deteriorated corrosion resistance in aerospace aluminium alloys. Local corrosion in AA2024-T3 is rather complicated due to varying and changing electrochemical reactivity of a complex constellation of IMPs embedded in the alloy matrix during exposure to a corrosive environment. Therefore, local corrosion of this class of structural materials has been studied for decades using a wide variety of combined electrochemical, analytical and microscopic techniques such as SEM, TEM, XPS, SIMS, SKPFM and etc. Overall, microgalvanic coupling has been proposed in the literature as the interaction mechanism between IMPs as well as with their surrounding alloy matrix. However, many of the questions regarding discontinues trenching, copper redeposition, nobility inversion and local chemistry-induced cerium precipitation and etc have not fully been described with this concept of mechanism in their finest details. In this thesis, towards a thorough and spatially well-resolved understanding of corrosion phenomena, nanoscopic analytical TEM studies have been developed, in spite of the challenging implementation. Thus, various analytical TEM investigations including ex-situ TEM, quasi in-situ TEM and in-situ liquid phase TEM were performed to look at corrosion and corrosion inhibition phenomena in AA2024-T3 at the nanoscopic level. This has provided us with new insights into what exactly takes place from initiation towards more advanced stages of in-depth propagation. It has been shown that the intrinsic electrochemical stability of intermetallic compounds is a dominant factor governing the kinetics of local IMP-induced corrosion. In fact, a preceding dealloying drives the local corrosion initiation and this happens to IMPs conventionally defined as anodic as well as cathodic ones. This work elaborates on the early stage dealloying process of different IMPs and how this phenomenon can influence the local solution chemistry surrounding it. Therefore, comprehensive mechanisms explaining the local corrosion and corrosion inhibition of the aerospace AAs at the nano- and microscale are presented.

10.2. On local corrosion mechanisms induced by IMPs in AA2024-T3

In Chapter 4 and 5, a combination of the TEM approaches were dedicated to exploring local corrosion events by major intermetallic phases in AA2024-T3 including Al_2CuMg, Al_2Cu, $Al_7CuFe(Mn)$, $Al_{76}Cu_6Fe_7Mn_5Si_6$ and $Al_{20}Mn_3Cu_2$. With that, direct nanoscopic observations of nano-structural and compositional evolutions from surface initiation to in-depth propagation were acquired, fully describing local corrosion in AA2024-T3. The studied IMPs reveal similarities in triggering local corrosion; however, the associated degradation go through different time scales. Here, the electrochemical reactivity of the IMPs is correlated to their electrochemical stability which is a direct consequence of the chemical composition. Unlike conventional thoughts, IMPs are in fact simultaneous anodic and cathodic sites as from the beginning of exposure. Nanogalvanic interactions between the heterogeneities within the corroding IMPs themselves, and later with the closest neighbouring alloy matrix stabilise the local corrosion. Figure 10.1 shows the progression map of localised corrosion induced by the IMPs in

AA2024-T3 which experience preferential dissolution of active elements and cause galvanic interactions in different length scale. Coming in a chronological order, the degradations events can be broken down into distinct stages of dealloying surface initiation, discontinuous trenching, continuous trenching (depth propagation) and particle undercutting. The last stage is associated with the detrimental Cu redistribution process to which dissimilar intermetallic phases contribute to different extents. Note that $Al_{20}Mn_3Cu$ is not considered in Fig. 10.1 due to the size scale of the dispersoids which is of minor importance to local corrosion.

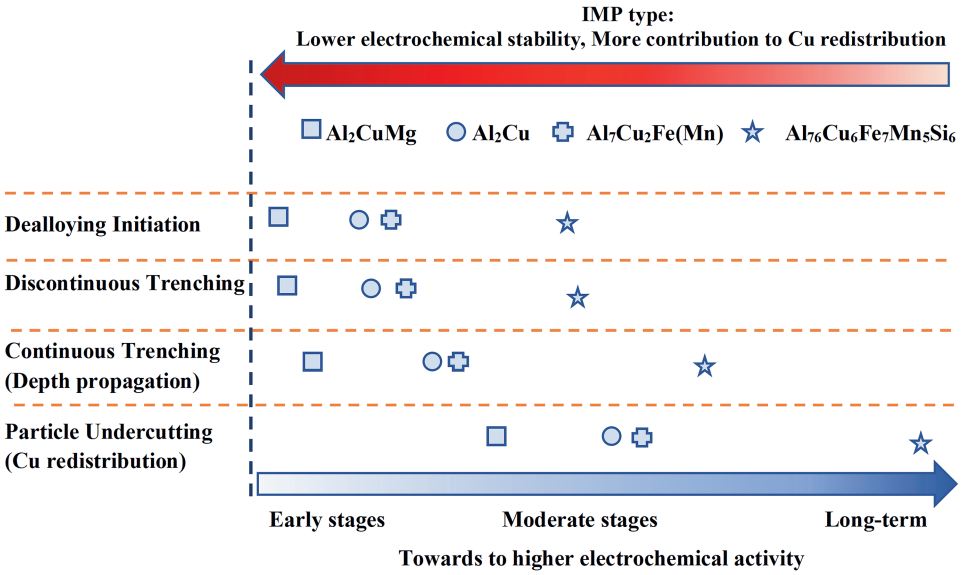


Figure 10.1. Progression map of localised corrosion induced by IMPs. Here, the early stage generally is less than half an hour, moderate stage is between 0.5–6 h, long term is over than 6 h.

Regardless of the IMPs type, local corrosion initiates by dealloying attack to IMPs but stabilises through nanogalvanic interactions between copper-rich regions and the intact areas within IMPs. This condition gives rise to a very local solution chemistry in which the passive layer covering the nearest alloy matrix cannot survive, leading to its local dissolution (discontinuous trenching). Given a low electrochemical stability of S-phase, the surface initiation process occurs rather shortly after exposure through preferential dissolution of aluminium and magnesium. As depicted in Fig. 10.1, the time gap between the surface initiation and discontinuous trenching is rather short for all the IMPs. However, the dealloying-driven initiation and its prompt consequent (i.e., discontinuous trenching) take place at various exposure times for different intermetallic phases owing to their dissimilar electrochemical stability. It should be noted that aluminium is the only element that undergo preferential dissolution in Al_2Cu, while selective dissolution of Al, Mn, and Fe and Si to a lesser extent is observed in the case of

constituent phases and dispersoids. The progression of the dealloying within the corroding particles gives rise to an increased electrochemical reactivity of IMPs. This is associated with an alkaline local solution due to the cathodic activity of the Cu-rich surface of the IMPs, involving the adjacent alloy matrix into the trenching process.

In addition, progressive dealloying controls the electrochemical reactivity of IMPs. For instance, Cu- and Fe-rich locations on a corroding $Al_7CuFe(Mn)$ particle are highly noble, actively supporting cathodic reactions and drive anodic dissolution of the adjacent alloy matrix. In contrast, silicon in a corroding $Al_{76}Cu_6Fe_7Mn_5Si_6$ particle can largely hinder the electrochemical reactivity since during its oxidation, it turns into semiconducting SiO_2. Thus, the local dissolution of the matrix gradually trenches all around the particle and corrosion simultaneously propagates into the matrix and corroding IMP. The more reactive the corroding intermetallic compound is, the deeper corrosion propagates into the depth. The trenching process goes on until the particle undercutting takes place. This is a critical stage at which the corroding particles can differently contribute to the Cu redistribution process. In fact, when a Cu-rich remnant gets detached form the alloy matrix, it can acquire a higher corrosion potential at which copper oxidation is favourable. S-phase contributes to redistribution of copper to the largest extent as the upper part and the periphery of the undercut particles can liberate copper, followed by re-plating at aluminium hydroxide-free parts of the matrix surface. In contrast, the corroded Al_2Cu particles which are largely covered with aluminium hydroxide contribute to a lesser extent. Comparatively, the undercut constituent phase particles release considerably lesser amount of cupper. The replated copper nanoclusters go through a repetitive deposition/dissolution, leading to the progressive degradation of the alloy matrix. Besides, they can also elevate the electrochemical reactivity of Al_2Cu and constituent phase particles which is known as ennoblement process.

10.3. On the formation mechanism of protective conversion layer on AA2024-T3 by lithium-based technology

Direct morphological liquid-phase TEM observations in Chapter 7 along with systematic FIB/SEM studies in Chapter 8 elucidated how the alloy matrix and different IMPs get involved in the conversion process in the lithium carbonate-containing solution. As depicted in Fig. 10.2, the supersaturation of the solution by $Al(OH)_4^-$ ions which needs to be supplied through the active dissolution of the substrate is of critical importance to the conversion process. Since the lithium carbonate-containing solutions are intrinsically alkaline, the alloy matrix cannot acquire passivation at the beginning of exposure and until no more $Al(OH)_4^-$ can be dissolved. In the presence of lithium, the alloy matrix dissolution continues until reaching the required local supersaturation which occurs at lower $Al(OH)_4^-$ concentration as compared to lithium-free solutions. At his stage, the conversion layer appears in a columnar morphology. It should be mentioned that no conversion process occurs in the absence of lithium and it plays a critical role in stabilising the corrosion products. Subsequently, the columnar layer continuously

grows and consequently the kinetics of the dissolution gradually slows down. This is associated with the formation of a porous layer and lastly a dense layer closest to the alloy matrix. This phenomenon results in the full passivation of the alloy matrix. Except for S-phase, the IMPs do not strongly interact with the lithium-based solution; they just endure slight surface dealloying and greatly support cathodic reactions. Thus, the supersaturation caused by the alloy matrix dissolution would lead to the formation of a columnar layer on all the IMPs. In the case of S-phase, a fast dealloying assists the conversion process by local supersaturation. In fact, the columnar firstly appear on Al_2CuMg particles as they locally provide $Al(OH)_4^-$ ions relatively rapidly. Overall, the different morphology of the sublayers is a direct consequence of dissimilar kinetics of the dissolution/precipitations at different stages of the conversion layer formation. It should be noted that the most important thing is the critical role of lithium in making the conversion process happen, otherwise aluminium undergoes sever corrosion in an alkaline lithium-free solution.

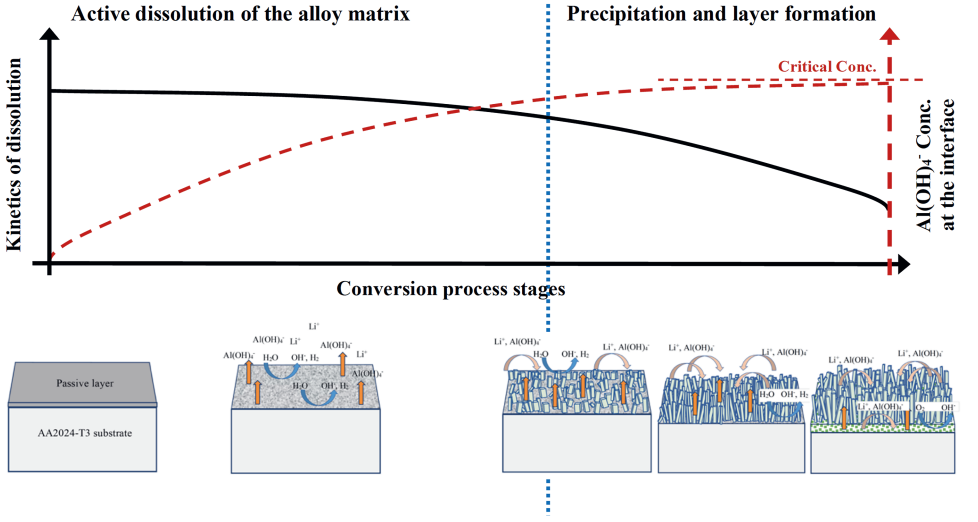


Fig. 10.2. Morphological stages of the lithium-based conversion layer formation. The graph schematically shows the change of the $Al(OH)_4^-$ concentration and the dissolution kinetics while the conversion layer morphologically evolves. The pictures schematically show different stages of the conversion layer formation.

As schematically shown in Fig. 10.3, a typical grown-up conversion layer shows a multi-layered arrangement comprising three distinct sublayers with columnar, porous and dense morphology. In Chapter 6, lithium was found uniformly spread over the different sublayers, although the local phases with no/low concentration of lithium were also detected. The dense layer was specified as amorphous Li-incorporated aluminium hydroxides with a high amount of trapped water (named Li-pseudoboehmite). It was shown that the columnar morphology is composed of single-crystal pillars of

lithium-aluminium double hydroxide (Li-Al LDH). This is a product of CO_3^{2-}, H_2O and even Cl^- intercalation between the $d_{(003)}$ planes which contains Al^{3+}, Li^+ and OH^-. The porous layer residing in between, consists of co-existing amorphous and crystalline compounds. The crystalline products are Li-Al LDH while the amorphous products may comprise different concentration of lithium. The presence of Li-Al LDH was confirmed by XRD analysis on the samples directly exposed to a lithium-containing solution in Chapter 8.

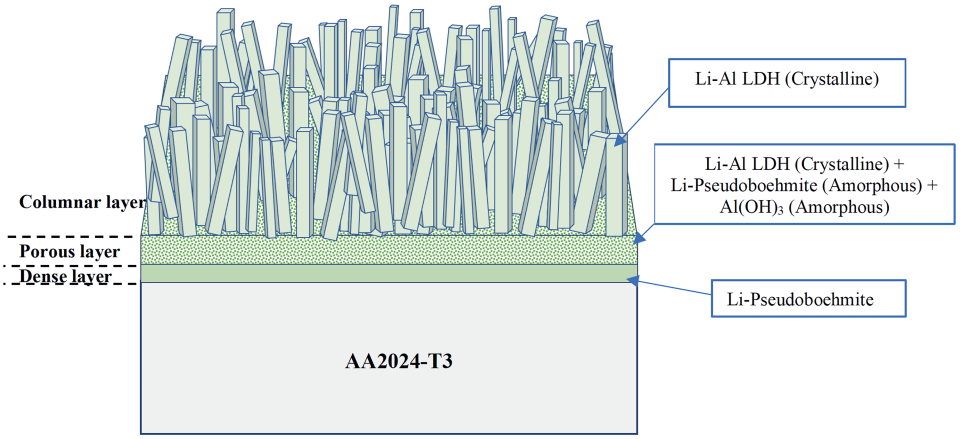


Fig. 10.3. Cross-sectional morphology, structure and chemical composition of the typical lithium-based conversion layer formed in the neutral salts spray (NSS) condition.

10.4. On the local corrosion inhibition mechanisms of AA2024-T3 by a cerium-based compound

In line with the findings in Chapter 4 and 5, it was found out in Chapter 9 that dealloying of IMPs is the main factor governing the rate of local cerium precipitation. This is something in contrast to the conventionally perceived micro-galvanic corrosion between IMPs and the surrounding matrix. By looking at nanoscopic microstructural evolutions of the isolated IMPs during interaction with the inhibited solution, it was observed that the establishment of the local alkaline solution chemistry required for cerium precipitation comes at the expense of IMPs dealloying. In fact, the faster dealloying happens the more cerium precipitates. The Cu-rich regions resulting from selective dissolution of the active elements like magnesium and aluminium support cathodic reactions leading to a local alkalinity.

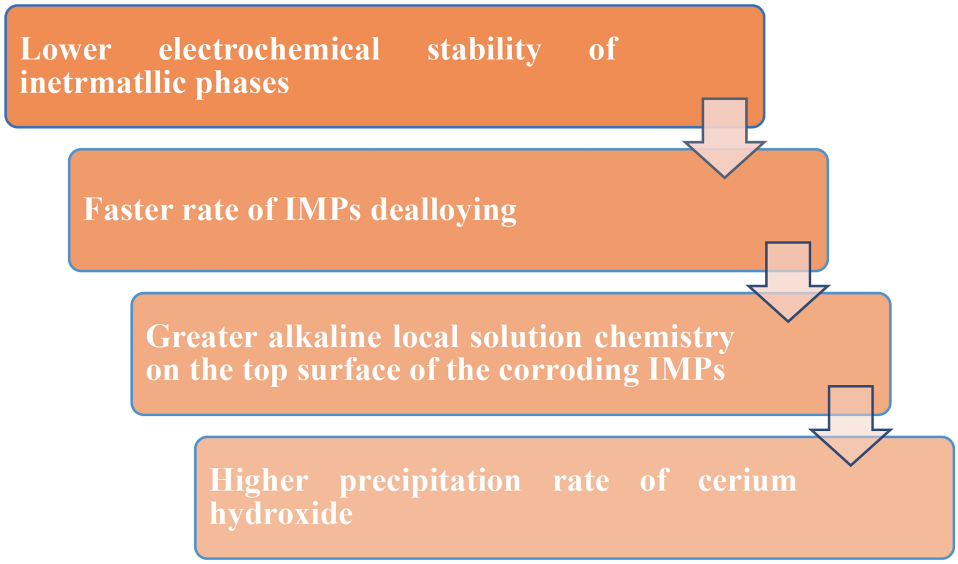


Fig. 10.4. Cerium precipitation as a consequent local electrochemical activity (dealloying) of the IMPs.

Al_2CuMg as the most active phase is covered with a thick cerium-based deposit layer which is established during several stages of the interaction with the cerium-inhibited solution. The precipitation of cerium takes place on S-phase from the beginning of exposure. Besides, as long as the dealloying propagates into depth, the top Cu-rich part of the corroding particles support cathodic reaction, generating the required alkalinity for cerium precipitation. In fact, no nobility inversion happens. The cerium cannot inhibit dealloying of the S-phase, although it can delay the process and mitigate the Cu reprecipitation. At moderate stages of exposure, the rupture of the cerium cap occurs due to the accumulation of massive corrosion products as a result of underlying corrosion. This phenomenon is associated with the coverage of the cerium layer with aluminium hydroxide. Al_2Cu particles endure dealloying at a sluggish rate which results in less cerium precipitation compared to that for S-phase particles. Therefore, they end up with an undercut dealloyed remnant covered with a thin mixed layer of cerium and aluminium hydroxides. Constituent phases are very stable in the cerium-containing solution and slightly endure dealloying over a long-term exposure. Al_7Cu_2Fe(Mn) particles were observed either discretely or fully covered with a thin cerium-based layer at prolonged exposure times. The latter is due to the redistributed Cu nanoparticles that speed up the local dealloying rate and can effectively increase local cerium precipitation. $Al_{76}Cu_6Fe_7Mn_5Si_6$ particles found slightly dealloyed, however they do not interact with cerium. The cerium deposit can be a mixture of Ce(IV) and Ce(III) oxides as the valence transformation happens with prolonged exposure time. This phenomenon was linked to an oxidising reaction either due to the presence of H_2O_2 or happing on Cu-rich regions of the corroding IMPs.

10.5. On applicability of liquid-phase TEM in corrosion science

Recent advances in liquid-phase TEM allows for real-time capturing dynamic processes in materials in contact with liquid environments while the reactions can be electrochemically controlled externally. This unprecedented opportunity has progressively been branched out into many applications like biomaterials, batteries and in particular electrochemical etching of nanoparticles. Promising and exciting years are also ahead of us in corrosion science with the rise and availability of liquid-phase TEM to explore many complicated corroding systems. However, this significant prospect in relation to the approach and its application in corrosion science comes with inherent outstanding challenges and concerns.

TEM specimens are limited to electron-transparency thicknesses and regarding their configuration in the liquid cells, they can merely provide very early stage of surface corrosion not bulk propagation. However, selective masking of the thin specimen can help in this case in order to control oxidation direction for top-view and cross-sectional view observations of corrosion. TEOS is a desire masking material since it has no galvanic effect when deposited on the TEM specimens. Besides, the thin TEM specimens, when sandwiched, can be kept for longer period in corrosive environments. This work took advantage of this approach of doing specimen preparation to observe the lithium conversion layer formation in the AA2024-T3 lamellae in an alkaline environment. Besides, the sandwiched specimens were successfully used here to mimic the bulk scale conditions while the samples are anodically polarised.

Liquid cells are of critical importance and commercial liquid cell need to be designed specifically for corrosion applications. This includes considering the top-bottom effect in order to obtain the highest possible resolutions depending on the imaging mode. HAADF-STEM imaging mode shows a privilege to the TEM imaging as it gives better image contrast corresponding to both the local thickness variations and compositional evolutions caused by corrosion. For electrochemical liquid-phase TEM studies of corrosion, the coverage of Pt WEs on liquid cells with Si_XN_y is necessary and must be taken into account to prevent galvanic coupling and background current effect.

The artefacts like Ga damage can be introduced during the specimen preparation and handling; thus, proper specimen preparation and transfer approaches must be followed to alleviate their potential impact on the corrosion processes. The effect of the electron beam on solution chemistry, in particular for complex solutions, must be minimised to avoid modifying results towards undisturbed corrosion mechanisms and kinetics. The effective ways are to conduct low-dose rate imaging or flowing electrolyte experiments but at the expense of image resolution and corrosion-induced local chemistry, respectively. Given the different challenges and potential artefacts that liquid-phase TEM studies face, a combination of quasi in-situ and ex-situ TEM experiments should be conducted in parallel to obtain detailed chemical and structural analysis, and additionally to validate and support the in-situ results as much as possible. A methodology in this case has schematically been illustrated in Fig. 10.5. Such a

procedure would definitely lead to more profound, comprehensive and reliable insights into interaction behaviour of alloy materials.

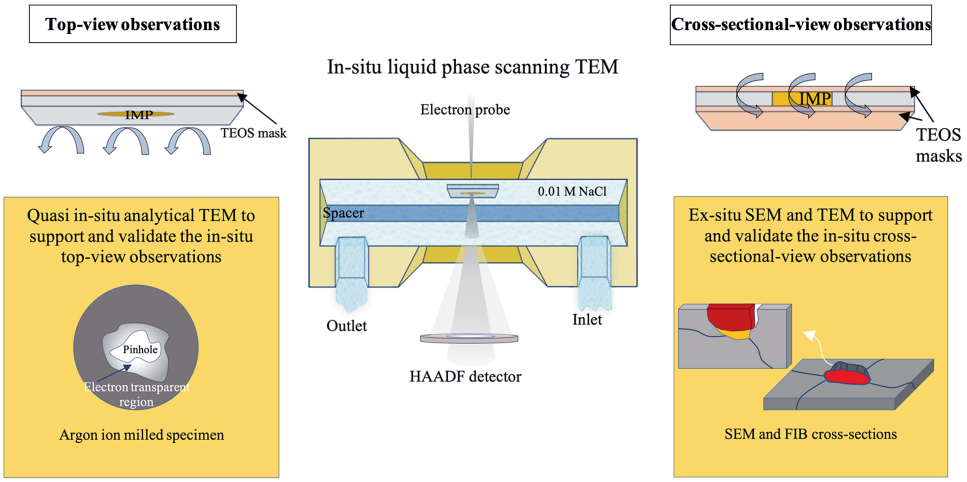


Fig. 10.5. Methodology of acquiring reliable and comprehensive corrosion mechanisms from surface initiation to in-depth propagation at the nanoscale. Liquid-phase TEM results have to be supported by complementary quasi in-situ and ex-situ analytical TEM examinations.

10.6. Future remarks

The future of liquid-phase TEM is on the shoulders of liquid cells. Thus, the relevant technical advances in their design and fabrication can surely enhance the applicability of liquid-phase TEM in many fields of research including corrosion science. Corrosion mechanisms in contemporary alloy systems are very complicated, where a combination of different types of corrosion may occur simultaneously. Thus, liquid-phase TEM studies are more supportive and helpful as long as the thin specimens are studied in working conditions comparable to real life. In this case, liquid cells paly a great role as they are the essential components in order to mimic various environmental conditions such as temperature, mechanical stress, biasing and complex solution chemistry.

For instance, pitting corrosion in majority of the modern stainless steels does not occur at room temperature. Therefore, liquid-phase TEM studies must be conducted at elevated temperatures and in the presence of external bias to encourage pit initiation events. In this regard, the liquid cells with biasing and heating capabilities come in handy to directly observe how pitting initiates at nanoscopic microstructural heterogeneities and in response to elevated temperatures and anodic overpotentials. Stress corrosion cracking (SCC) in alloy materials can be enumerated as a more challenging case for liquid-phase TEM. SCC is normally triggered due to a complicated combination of one or two types of corrosion (e.g., dealloying) in the presence of mechanical stress. Therefore, an experimental

instrumentation (liquid cell) that allows for the quantitative tensile testing of a material in corroding conditions would be key to exploring the mechanism of relevance in various alloy systems.

In liquid-phase TEM, the range of practical alloy specimens is constrained by the scale of the liquid cells. That is why liquid-phase TEM results and real-life testing might reveal discrepancies in terms of kinetics. Thus, more reliable conclusion can be drawn if modelling and simulations are developed in parallel, considering physicochemical conditions within the liquid cells. This is a more pronounced case in Chapter 7 and 8 where the conversion process in the sandwiched thin specimens happens in a shorter time-scale compared to the bulk systems. Certainly, the dedicated thermodynamical and kinetical modelling and simulations regarding a moving boundary condition at the corroding alloy/electrolyte interface in the sandwiched specimen could be very helpful to better cross-corelate between two experimental conditions (i.e., sandwiched thin specimens and bulk systems).

ACKNOWLEDGMENTS, LIST OF PUBLICATIONS AND CURRICULUM VITAE

Acknowledgements

Well, I've come a long way but I can't get through this career without thanking all of the amazing people who have inspired, mentored, and unconditionally supported me throughout my personal and professional life. First and foremost, I would like to thank Netherlands Organisation for Scientific Research (NWO) and AkzoNobel for financially supporting this Ph.D. work as a part of the research program "Understanding Processes using Operando Nanoscopy (UPON)" with project number 14205 (B2).

Arjan and Herman, for me an amazing journey began once I met up with you in Tehran in 2014. I'm glad it finally ended up with the opportunity of working on an advanced and challenging project under the supervision of you both at Delft University of Technology. Arjan, I will be extremely grateful for your continued support throughout this career, in particular in the difficult moments when I had to leave the laboratory empty-handed. I love the way you treat your graduate students; you are always positive and available despite your hectic schedule. I really like the thoughtful process of writing your articles and even emails; I learnt a great deal. Also, thank you for doing a thorough and exhaustive assessment of the manuscripts. Herman, whenever I get advice or remarks from you, I always assume it's from my father; he's hard on the outside but really kind and compassionate on the inside. It's incredible how you organise and rearrange papers to convey a clear-cut scientific point. And I do want to thank you both for all of the exciting, fruitful, and insightful scientific conversations. It was an accomplishment and a great result of our challenging conversations to publish eight pieces of science in prominent journals with very minimal revisions.

Henny, I am grateful to you for introducing me to the gigantic world of transmission electron microscopy in particular Operando TEM. I'm constantly astonished at how motivated and passionate you are in starting and carrying out studies. I find you to be constantly ready to face problems, and I am always amazed by your innovative ideas and scientific brilliance in making the impossible happen. Thank you very much for entrusting me with all of your scientific treasures. Because TEM is a delicate instrument to handle, users require subtle training, and I am extremely fortunate to have received one of the best from you, Frans. I don't know how to thank you for helping me complete my last experimental section of the thesis amid the difficult and confused periods of COVID-19. You were always accessible for interesting talks and assisted me in interpreting complex TEM data and writing papers.

Peyman, I had no idea that we would be officemates two years after our first meeting in Tehran; tiny words! You are a kind-hearted individual who not only assisted me in resolving scientific difficulties but also offered me sound advice in personal matters. I am overjoyed for you since you truly deserve your current position. You are what I refer to as a true friend. Peter, lithium technology is a fantastic advancement toward a greener planet. I am delighted to have the opportunity to work on it. Thank you for the exciting debate about the formation of the lithium conversion layer. We're now on the same page

when it comes to discussing the formation mechanism :-). Majid, I want to thank you for all of the helpful practical ideas and hands-on guidance you gave me. I had a great time spending hours with you discussing science and life; your perspective on affairs is really interesting.

Here, I'd like to thank all of the valued members of the national centre for high resolution electron microscopy (NC-HREM) who welcomed me as a joint member. Thank you for all of your support and advice; Shiv, Sairam, Leo, Yoones, Meng-Yue, Masha and Marijke. Jouk, thank you for sharing your office with me and for assisting me with crystallography and diffraction analyses. T.R. de Kruijff, I appreciate all of your technical support in preparing argon ion milled samples and in-situ TEM setup; you are truly amazing. Hozanna at Kavli Nanolab, thank you very much for training me how to use the FIB/SEM machine. Scientific world requires individuals like you who give time flexibility, freedom and encouragement to users to complete their assignments.

I also want to thank my colleagues in the Corrosion Technology and Engineering (CTE) group, Joost, Mats, Laura-Lynn, Aytac, Shoshan, Agnieszka, Ursa, Bala, Prakash, Maxine, Sven, Ziyu, Eszter, Keer, Khatereh, Can, and especially Sajjad for raising the level of humour in the group. We had a fantastic time attending conferences and social events, and I enjoyed myself pretty much. A particular thanks goes to Yaiza for the suggestion of using TEM to explore cerium-based inhibitor mechanisms. I appreciate you Saskia for kindly arranging meetings and events. Although you had gone by the time I joined the group, Majid Sababi, I will never forget your gracious assistance with my initial accommodation.

Last but not least, I'd want to convey my heartfelt appreciation to my wonderful parents and brothers Mohammad, Ahmad, and Mahdi, who have been tremendously unconditionally supportive of me. Shima, my lovely, warm-hearted and supportive wife, deserves special gratitude for bearing with me during this lengthy journey with all of its ups and downs. I thank you so much for creatively designing the thesis cover. I admire you as much for giving birth to a beautiful angle, Sugol, who is just the apple of our eyes.

Ali Kosari

September 2021, Delft

List of publications

o Ph.D. work

1. **A. Kosari**, H. Zandbergen, P. Visser, H. Terryn, J.M.C. Mol, Challenges to electrochemical evaluation of nanometric sandwiched thin specimens using liquid cells designed for application in liquid-phase TEM corrosion studies, **Corrosion Science** (2021).
2. **A. Kosari**, F. Tichelaar, P. Visser, P. Taheri, H. Zandbergen, H. Terryn, J.M.C. Mol, Nanoscopic and in-situ cross-sectional observations of Li-based conversion coating formation using Liquid-Phase TEM, **npj Materials Degradation**, 5:40 (2021).
3. **A. Kosari**, F. Tichelaar, P. Visser, H. Zandbergen, H. Terryn, J.M.C. Mol, Laterally-resolved formation mechanism of a lithium-based conversion layer at the matrix and intermetallic particles in aerospace aluminium alloys, **Corrosion Science**, 190 (2021) 109651.
4. **A. Kosari**, M. Ahmadi, F. Tichelaar, P. Visser, Y. Gonzalez-Garcia, H. Zandbergen, H. Terryn, J.M.C. Mol, Editors' Choice—Dealloying-Driven Cerium Precipitation on Intermetallic Particles in Aerospace Aluminium Alloys, **Journal of The Electrochemical Society**, 168 (2021) 041505.
5. **A. Kosari**, H. Zandbergen, F. Tichelaar, P. Visser, P. Taheri, H. Terryn, J.M.C. Mol, In-situ nanoscopic observations of dealloying-driven local corrosion from surface initiation to in-depth propagation, **Corrosion Science**, Volume 177, December 202, Page 108912.
6. **A. Kosari**, F. Tichelaar, P. Visser, H. Zandbergen, H. Terryn, A. Mol, Dealloying-driven local corrosion by intermetallic constituent particles and dispersoids in aerospace aluminium alloys, **Corrosion Science**, 177 (2020) 108947.
7. **A. Kosari**, H. Zandbergen, F. Tichelaar, P. Visser, H. Terryn, A. Mol, Application of In Situ Liquid Cell Transmission Electron Microscopy in Corrosion Studies: A Critical Review of Challenges and Achievements, **CORROSION,** 76 (2020) 4-17.
8. **A. Kosari**, P. Visser, F. Tichelaar, S. Eswara, J-N. Audinot, T.Wirtz, H. Zandbergen, H. Terryn, J.M.C. Mol, Cross-sectional characterization of the conversion layer formed on AA2024-T3 by a lithium-leaching coating, **Applied Surface Science,** 512 (2020) 145665.

o Other works

9. E. Rahimi, **A. Kosari**, S. Hosseinpour, A. Davoodi, H. Zandbergen, J.M.C. Mol, Characterization of the passive layer on ferrite and austenite phases of super duplex stainless steel, **Applied Surface Science**, 496 (2019) 143634.
10. D. Nakhaie, **A. Kosari**, J.M.C. Mol, E Asselin, Corrosion resistance of hot-dip galvanized steel in simulated soil solution: A factorial design and pit chemistry study, **Corrosion Science**, 164 (2020) 10831.
11. D. Verkens, R. Revilla, **A. Kosari**, M. Günyüz, C. Işıksaçan, J.M.C. Mol, I. De Graeve, H.Terryn, Effect of simulated brazing on the microstructure and corrosion behavior of twin roll cast AA3003, **Materials and Corrosion**, 71 (1), 60-69.
12. N. Haghdadi, M. Laleh, **A. Kosari**, M.H. Moayed, P. Cizek, P.D. Hodgson, H. Beladi, The effect of phase transformation route on the intergranular corrosion susceptibility of 2205 duplex stainless steel, **Materials Letters,** 238 (2019) 26-30
13. Z. Mirzakhanzadeh, **A. Kosari**, M.H. Moayed, R. Naderi, P. Taheri, J.M.C. Mol, Enhanced corrosion protection of mild steel by the synergetic effect of zinc aluminum polyphosphate and 2-mercaptobenzimidazole inhibitors incorporated in epoxy-polyamide coatings, **Corrosion Science**, 138 (2018) 372-37.

14. M. Seyedi, **A. Kosari**, D. Nakhaie, M.H. Moayed, A. Alagheband, M.Y. Azimi, Effect of quenching after solidification on hardness and electrochemical behavior of a Pb-0.09% Ca-1.23% Sn alloy, **Journal of Energy Storage,** 17 (2018) 441-445.
15. S. Hejazi, S. Mohajernia, M.H. Moayed, A. Davoodi,..., **A. Kosari**, Electrochemical and quantum chemical study of Thiazolo-pyrimidine derivatives as corrosion inhibitors on mild steel in 1 M H2SO4, **Journal of Industrial and Engineering Chemistry,** 25 (2015)112-121.
16. M. Ebrahimzadeh, M. Gholami, M. Momeni, **A Kosari**, M.H. Moayed, A. Davoodi, Theoretical and experimental investigations on corrosion control of 65Cu–35Zn brass in nitric acid by two thiophenol derivatives, **Applied Surface Science,** 332 (2015) 384-392.
17. N. Ebrahimi, M. Momeni, **A. Kosari**, M. Zakeri, M. H. Moayed, A comparative study of critical pitting temperature of stainless steel by electrochemical impedance spectroscopy (EIS), potentiodynamic and potentiostatic techniques, **Corrosion Science**, 59 (2012) 96-10.
18. M. Vakili Azghandi, A. Davoodi, G. A. Farzi, **A. Kosari**, Water-base acrylic terpolymer as a corrosion inhibitor for SAE1018 in simulated sour petroleum solution in stagnant and hydrodynamic conditions, **Corrosion Science**, 64 (2012) 44-54.
19. M. Vakili Azghandi, A. Davoodi, G. A. Farzi, **A. Kosari**, Corrosion inhibitive evaluation of an environmental friendly water-base acrylic terpolymer on mild steel in hydrochloric acid media, **Metallurgical and Materials Transactions A**, 44A (2013) 5493- 5504.
20. S. Pour-Ali, C. Dehghanian, **A. Kosari**, In situ synthesis of polyaniline-camphorsulfonate particles in epoxy matrix for corrosion protection of mild steel in 3.5 wt% NaCl solution, **Corrosion Science**, 85 (2014) 204–214.
21. S. Pour-Ali, C. Dehghanian, **A. Kosari**, Corrosion protection of the reinforcing steel in chloride-laden concrete environment through epoxy/polyaniline-camphorsulfonate nanocomposite coating, **Corrosion Science**, 90 (2015) 239–247.
22. **A. Kosari**, M. H. Moayed, A. Davoodi, R. Parvizi, M. Momeni, H. Eshghi, H. Moradi, Electrochemical and quantum chemical assessment of two organic compounds from pyridine derivatives as corrosion inhibitors for mild steel in HCl solution under stagnant condition and hydrodynamic flow, **Corrosion Science**, Volume 78, January 2014, Pages 138-150.
23. **A. Kosari**, A. Davoodi, M. H. Moayed, R. Gheshlaghi, The response surface method as an experimental design technique to explore and model the corrosion inhibitors performance, **CORROSION**, Volume 71, July 2015, Pages 819-827.
24. **A. Kosari**, M. Momeni, R. Parvizi, M. Zakeri, M.H. Moayed, A. Davoodi, H. Eshghi, Theoretical and electrochemical assessment of inhibitive behaviour of some thiophenol derivatives on mild steel in HCl, **Corrosion Science**, Volume 53, October 2011, Pages 3058-3067.

Conference presentations

1. **A. Kosari**, H. Zandbergen, F. Tichelaar, P. Visser, Y. Gonzalez-Garcia, H. Terryn, J.M.C. Mol, New insights into early-stage local corrosion of aerospace aluminium alloys through time-resolved TEM studies, **EuroCorr 2021**, Online event.
2. **A. Kosari**, H. Zandbergen, F. Tichelaar, P. Visser, P. Taheri, H. Terryn, J.M.C. Mol, In-Situ Liquid Phase TEM Studies of Corrosion Initiation in Aluminium Alloys, **PRiME ECS2020**, Online event.
3. **A. Kosari**, F. Tichelaar, P. Visser, H. Zandbergen, H. Terryn, J.M.C. Mol, Interaction of intermetallic compounds in aluminium alloys with a cerium-based corrosion inhibitor; ex-situ and quasi in-situ TEM studies, **EuroCorr 2020**, Online event.
4. **A. Kosari**, H. Zandbergen, F. Tichelaar, P. Visser, H. Terryn, J.M.C. Mol, In-situ liquid phase and quasi in-situ TEM studies of lithium-based conversion layer formation on aluminum alloys, **EuroCorr 2020**, Online event.
5. **A. Kosari**, H. Zandbergen, F. Tichelaar, P. Visser, P. Taheri, H. Terryn, J.M.C. Mol, In-situ liquid TEM studies of early-stage corrosion of aerospace aluminum alloys, **Gordon Research Conference (GRC)** on liquid phase microscopy2020, Tuscany, Italy.
6. **A. Kosari**, H. Zandbergen, F. Tichelaar, P. Visser, H. Terryn, J.M.C. Mol, Quasi in-situ and in-situ liquid TEM studies of corrosion initiation in aluminium alloys, **Eurocorr 2019**, Seville, Spain.
7. **A. Kosari**, P. Visser, P. Taheri, F. Tichelaar, H. Zandbergen, H. Terryn, J.M.C. Mol, In-situ transmission electron microscopy for corrosion inhibition study of alloys; advantages and challenges, **Eurocorr 2018**, Krakow, Poland
8. **A. Kosari**, P. Visser, M. Ahmadi, P. Taheri, F. Tichelaar, H. Zandbergen, H. Terryn, J.M.C. Mol, TEM characterisation of passive layers on AA2024 formed by leaching of lithium carbonate from an organic coating. **8th Aluminium Surface Science and Technology (ASST) Symposium**, Denmark, 2018.
9. **A. Kosari**, Y. Gonzalez-Garcia, S.K.M. Malladi, H. Zandbergen, F. Tichelaar, H. Terryn, J.M.C. Mol, Quasi in-situ TEM study of Ce-based inhibitor interaction with AA2024, **Eurocorr 2017**, Prague, Czech.

Ali KOSARI

Born on 5th July 1986
Mashhad, Iran



EDUCATION

2016-2020	Delft University of Technology (TU Delft), Delft, The Netherlands Ph.D. of Materials Science and Engineering-Corrosion Technology and Electrochemistry (CTE)-National Centre for High Resolution Electron Microscopy (HREM)
2011-2013	Ferdowsi University of Mashhad (FUM), Mashhad, Iran M.Sc. of Materials Science and Engineering
2006-2011	Ferdowsi University of Mashhad (FUM), Mashhad, Iran B.Sc. of Materials Engineering-Industrial Metallurgy

WORK EXPIERENCE

2020 Aug-Present	**Postdoc Researcher** Delft University of Technology (TU Delft)
2016 Aug-2020 Aug	**Researcher Ph.D. Student** Delft University of Technology (TU Delft)
2015-2016	**Metallurgical and corrosion consultant** NirouGostaran Khorasan (NGKH), Lead-acid battery manufacturer
2016 Jan-2016 Jul	**Lecturer** Corrosion and oxidation in materials-B.Sc. course Sajjad University of Technology
2013-2015	**Researcher and Lab technician** Corrosion and Protection Laboratory of Ferdowsi University of Mashhad (FUM).
2011-2013	**Teaching Assistant (TA)-B.Sc. Courses** Physical Metallurgy I and II, Corrosion and Oxidation of Materials, Heat Transfer Phenomena

Propositions

belonging to the dissertation:
"Corrosion and Corrosion Inhibition Studies of Aerospace Aluminium Alloys at the Nanoscale using TEM Approaches"

[1] Intermetallic particles (IMPs) in aerospace aluminium alloys are simultaneous anodic and cathodic sites as from the beginning of exposure, causing nanogalvanic interactions within the corroding IMPs and with the nearest neighbouring alloy matrix. [This proposition was concluded from Chapter 4 and 5]

[2] Intrinsic electrochemical stability of intermetallic compounds is a dominant factor governing the kinetics of local IMP-induced corrosion. [This proposition was concluded from Chapter 4 and 5]

[3] Dealloying rate of IMPs drives cerium precipitation by inducing very local alkaline solution chemistry. [This proposition was concluded from Chapter 9]

[4] Morphology of the sublayers in the lithium conversion layer is a direct consequence of the kinetics of the dissolution/precipitation process at certain stages. [This proposition was concluded from Chapter 8]

[5] Ex-situ and quasi in-situ investigations provide an important reality check for representativeness of liquid-phase TEM-based mechanistic studies.

[6] Classical approaches to corrosion studies are unable of unravelling mechanisms in contemporary complex corroding systems.

[7] Graduate student must have the courage of reporting his/her findings if against highly cited literature.

[8] Doing in-situ liquid-phase TEM studies of corrosion phenomena is as demanding, exciting as having a new-born baby.

[9] Mechanisms of materials behaviour are intrinsically straightforward in nature, although routes to a thorough understanding can be very complicated.

[10] Rushing to publish early-obtained results is not done since it might end up with next papers rejecting early thoughts.

[11] The peer-review process should typically include a more thorough check of the bibliography to avoid irrelevant papers being referred to.

[12] Defining a research Ph.D. proposal should include a risk mitigation plan for COVID-19 pandemic in the many years to come.

The propositions are regarded as opposable and defendable and have been approved as such by the promotors Prof. dr. ir. J.M.C. Mol and Prof. dr. H. Terryn